STOCHASTIC MULTISCALE MODELING OF POLYCRYSTALLINE MATERIALS

A Dissertation

Presented to the Faculty of the Graduate School

of Cornell University

in Partial Fulfillment of the Requirements for the Degree of

Doctor of Philosophy

by

Bin Wen

January 2013

STOCHASTIC MULTISCALE MODELING OF POLYCRYSTALLINE MATERIALS

Bin Wen, Ph.D.

Cornell University 2013

Mechanical properties of engineering materials are sensitive to the underlying random microstructure. Quantification of mechanical property variability induced by microstructure variation is essential for the prediction of extreme properties and microstructure-sensitive design of materials. Recent advances in high throughput characterization of polycrystalline microstructures have resulted in huge data sets of microstructural descriptors and image snapshots. To utilize these large scale experimental data for computing the resulting variability of macroscopic properties, appropriate mathematical representation of microstructures is needed. By exploring the space containing all admissible microstructures that are statistically similar to the available data, one can estimate the distribution/envelope of possible properties by employing efficient stochastic simulation methodologies along with robust physics-based deterministic simulators. The focus of this thesis is on the construction of low-dimensional representations of random microstructures and the development of efficient physics-based simulators for polycrystalline materials. By adopting appropriate stochastic methods, such as Monte Carlo and Adaptive Sparse Grid Collocation methods, the variability of microstructure-sensitive properties of polycrystalline materials is investigated.

The primary outcomes of this thesis include:

- Development of data-driven reduced-order representations of microstruc-

ture variations to construct the admissible space of random polycrystalline microstructures.

- Development of accurate and efficient physics-based simulators for the estimation of material properties based on mesoscale microstructures.
- Investigating property variability of polycrystalline materials using efficient stochastic simulation methods in combination with the above two developments.

The uncertainty quantification framework developed in this work integrates information science and materials science, and provides a new outlook to multiscale materials modeling accounting for microstructure and process uncertainties. Predictive materials modeling will accelerate the development of new materials and processes for critical applications in industry.

BIOGRAPHICAL SKETCH

The author was born in the city of Shenyang, Liaoning Province, China, in November, 1983. After completing his high school education from Shenyang No. 120 Middle School, the author was admitted into the department of Aeronautical Science and Engineering at Beijing University of Aeronautics and Astronautics (BUAA) in 2002, from where he received his Bachelor's degree in June, 2006, and the Master's degree in June, 2008. In August 2008, the author entered the doctoral program at the Sibley School of Mechanical and Aerospace Engineering, Cornell University, and was awarded another Master's degree in January 2011.

This thesis is dedicated to my parents Guipu Wen and Xiaojie An for their constant support and encouragement towards academic pursuits during my school years.

ACKNOWLEDGEMENTS

I would like to express my most sincere gratitude to my advisor, Professor Nicholas Zabaras, for his constant support, motivation and guidance over the last four years. His invaluable help and care cover not only the academic work, but also the life beyond lab. I would also like to thank Professors Christopher Earls and Derek Warner for serving on my special committee and for their encouragement and suggestions during the course of this work. Their kindly helps are precious to me.

This research was supported by the Computational Mathematics program of AFOSR (grant F49620-00-1-0373), the Materials Design and Surface Engineering program of the NSF (award CMMI-0757824), the Mechanical Behavior of Materials program Army Research Office (proposal to Cornell University No. W911NF0710519), the Computational Mathematics program of NSF (award DMS- 0809062) and an OSD/AFOSR MURI09 award to Cornell University on uncertainty quantification. This research used resources of the National Energy Research Scientific Computing Center, supported by the Office of Science of the U.S. Department of Energy under Contract No. DE-AC02-05CH11231. Additional computing resources were provided by the NSF through TeraGrid resources provided by NCSA under grant number TG-DMS090007. I would like to thank the Sibley School of Mechanical and Aerospace Engineering for having supported me through a teaching assistantship for part of my study at Cornell. The computing codes were developed based on open source scientific computation libraries including PETSc, GSL, and FFTW. The academic license that allowed for these developments is appreciated. Finally, I would like to thank fellow MPDC members and other friends for their support during my days at Cornell.

TABLE OF CONTENTS

LIST OF TABLES

LIST OF FIGURES

CHAPTER 1

INTRODUCTION

In most materials processes (e.g. forging) of polycrystalline materials, the evolution of the material properties is defined through multiple coupled physical phenomena at various length scales. In addition to the multiscale/multiphysics nature of such processes, predictive modeling provides various other challenges as understanding the variability of properties and material structure at the various scales is a complicated high-dimensional data-driven problem. In practice, the only information that is available to quantify these variations is a limited number of experimental samples and/or statistical correlations. This leads to an analysis of the problem assuming that the microstructure and property variations are random fields satisfying certain constraints. To perform any such analysis, one must first construct models of these variations to be used as inputs in the subsequent uncertainty analysis. In addition, a robust physics-based deterministic simulator is needed to estimate the properties/responses of given microstructure realizations. The analysis of the effect of microstructure uncertainties on the material system can be broken down into two major steps: (i) construction of a stochastic microstructure model (preferably a low-dimensional, continuous mapping) that encodes and quantifies the variation of material features in a mathematically rigorous way, and (ii) using this model as an input to the corresponding stochastic partial differential equations (SPDEs) that describe the relevant physical phenomena and solve for the probabilistic evolution of the desired dependant variables (error bars on material properties, probabilistic models for the microstructure evolution, etc.). The goal of this thesis is to develop an efficient computational framework that investigates the effect of polycrystalline microstructure variability on the (homogenized) material properties

during deformation processing.

In the past few years, several investigations were undertaken to study the variation in stress-strain response and elastic properties of single phase metals caused by microstructure uncertainties using a variety of computational methodologies. In [106], the principle of maximum entropy (MaxEnt) was used to describe the grain size distribution of polycrystals given a set of grain distribution moments as constraints. Microstructure realizations were then generated and interrogated using crystal plasticity finite element method (CPFEM) [6]. Orientations were randomly assigned to all constituent grains. The Monte Carlo (MC) method was adopted to compute the error-bars of the effective stress-strain response of FCC aluminum. In [50], the orientation distribution function (ODF) was adopted to describe the polycrystalline microstructure. A number of ODF samples were given as the input data. The Karhunen-Loève expansion (KLE) [77, 30] was utilized to reduce the input complexity and facilitate the high-dimensional stochastic simulation. An adaptive version of the sparse grid collocation strategy [28, 78] was used to obtain the variability of the stress-strain curve and the convex hull of elastic moduli of FCC aluminum after deformation. Recently, an uncertainty quantification of multiscale deformation process was conducted [52]. Each point of the macroscale workpiece was attached with a mesoscale random microstructure, which determines the mechanical property at that point. Since the microstructure is location-specific, the stochastic input is extremely high-dimensional. A bi-orthogonal decomposition approach was introduced to build the reduced-order surrogate space of the stochastic input. The variability of elastic moduli induced by microstructure variation over the workpiece was studied. In this thesis, we are going to extend the previous work on the uncertainty quantification of material properties induced by random mi-

crostructures. Emphasis is given to the development of robust physics-based deterministic solvers and construction of data-driven low-dimensional stochastic input models.

The deterministic physics-based material property estimator is a key factor in uncertainty quantification. The accuracy and efficiency of the deterministic solver have direct impact on the results and performance of the stochastic simulation. Starting with the pioneering works by Sachs [105] and Taylor [122], numerical prediction of effective and local mechanical behavior of polycrystalline materials based on underlying microstructures has received great attention. The Sachs model (also known as the lower bound model) assumes a homogeneous stress field in the microstructure [5]. In contrast, the Taylor model (also known as the upper bound model) assumes uniform strain in the polycrystal [74, 35, 7]. Although it does not account for interactions inside the microstructure, the Taylor model has been widely used for its simplicity and high computational efficiency [39, 40, 17, 51]. To account for intergranular interaction during deformation, self-consistent methods have been developed. The formulation of these models is based on the solution of the problem of an ellipsoidal inclusion (individual grain) embedded in an infinite homogeneous equivalent medium (polycrystalline aggregate). Each inclusion (or grain) is taken as an averaged medium, the heterogeneity within which is not considered. The first attempt to model the overall elasto-plastic behavior of polycrystals was proposed by Kröner [53] based on the use of Eshelby's solution [21]. An improvement was introduced by Hill [33] to account for the plastic interaction between the inclusion and the surrounding matrix using an incremental formulation based on the linearization of the local constitutive equations. Several extensions of this method have been proposed [34, 37, 92, 63, 64, 129, 81, 137]. Improvements taking con-

sideration of the second-order moment of the field fluctuation in grains were also developed in [15, 76, 65] to account for intragrain heterogeneities. Various numerical schemes for the solution of crystal plasticity problems have also been considered that represent the microstructure using probabilistic descriptors. A microstructural descriptor is evolved during processing rather than the actual microstructure itself. The simplest of these descriptors is the one-point probability distribution, namely the orientation distribution function (ODF). Under applied deformation, texturing is simulated by numerically evolving the ODF using conservation laws [16]. Solution schemes are based upon representation of the ODF using a series of harmonics [4, 41] or finite elements (FE) [56, 57], and the Taylor assumption is typically applied. Adopting the spectral representation (Fourier expansion) of the ODF [43], Kalidindi and co-workers [41, 42, 47, 46] efficiently predicted mechanical properties/response as functions of crystallographic orientation and processing parameters. Coefficients of the expansions were calibrated against the results obtained from other simulations such as the finite element method. This spectral approach has been applied to the computation of property closures and design problems [48, 23, 108]. The finite element representation of the ODF, has also been well studied and applied to design problems [117, 118]. This approach was extended in [116] to consider interactions between constituent grains by employing the two-point correlation function.

To accurately estimate the local micromechanical fields, full-field simulations that interrogate polycrystalline microstructures with intracrystalline resolution are receiving increasing attention. The crystal plasticity finite element method is one of the most popular full-field models [96]. A comprehensive review is given in [103]. Several disadvantages are associated with the finite

element approach. The difficulty in finite element meshing coupled with the large number of degrees of freedom limits the size of the microstructure that can be treated. Furthermore, the high computation cost of finite element analysis is a great obstacle in formulating and solving multiscale and/or stochastic problems. Consequently, current research efforts have been devoted in finding viable full-field alternatives. A recent development is the materials knowledge systems (MKS) [61, 24, 22]. This framework is built on the statistical continuum theories developed by Kröner [54] that express the localization of the response field at the microscale using a set of kernels and their convolution with statistical descriptions of local microstructure. The microstructure representative volume element (RVE) is tessellated into a uniform grid of spatial cells (or voxels). Each spatial cell is quantified using a discrete statistical representation. The kernels (or influence coefficients) are estimated by calibrating against a database containing results obtained from other simulations, e.g. FEM. The calibration is simplified by working in Fourier space through discrete Fourier transform (DFT). Another efficient full-field approach based on Green's functions and fast Fourier transform (FFT) has been proposed for solving the governing equations for periodic heterogeneous media [66, 68]. This method was originally developed as a fast algorithm to compute the elastic and elasto-plastic effective and local response of composites with isotropic components [93, 94, 84, 85], and further adapted to deal with polycrystalline microstructures using a visco-plastic constitutive model [66]. Local and homogenized mechanical responses, as well as texture evolution, of 2D and 3D realistic polycrystals were studied in [67, 69, 71]. Comparison with the self-consistent method [62] and finite element simulations [97, 75] were conducted and showed the accuracy and efficiency of the fast Fourier transform scheme. Recent at-

tempts to couple the fast Fourier transform-based model with finite elements is presented in [45]. Two formulations based on infinitesimal-strain theory were recently reported to predict micromechanical fields in polycrystals deforming in the elasto-viscoplastic regime [121, 70, 32]. In contrast to the MKS, the crystal plasticity fast Fourier transform approach directly solves the underlying boundary value problem in the microstructure using the Green's function method. The equilibrium and compatibility conditions are satisfied. The crystal plasticity fast Fourier transform-based method provides several advantages: taking pixelized microstructure images as the input without requiring sophisticated discretization, accurately investigating the global and local mechanical behavior of microstructures by accounting for both intergrain and intragrain interactions, and the high computation efficiency. One of the major tasks of this thesis is to develop robust physics-based solvers for polycrystalline microstructures. A Taylor model is firstly implemented as the deterministic and point simulator in the stochastic and multiscale frameworks, respectively. A more sophisticated FFT-based full-field approach is further developed to study both the macroscopic and local elasto-viscoplastic responses of realistic microstructures subjected to deformation. Both methods are compared with the crystal plasticity finite element method also developed in the current work. Integrating the microstructure estimator in the macroscale processing simulation through appropriate homogenization scheme [86], a multiscale framework that predicts spatial distribution of mechanical responses of the workpiece accounting for underlying microstructure heterogeneities can be established. Since the multiscale simulation requires multiple calls of the local point simulator, the computation of such a multiscale problem can be very time consuming if the point simulator is expensive. In the current work, we embed the Taylor model in the multiscale

solver in order to achieve acceptable efficiency.

Dimensionality reduction techniques have been introduced to the computational materials science to construct efficient low-dimensional surrogate models of the high-dimensional stochastic heterogeneous media. In [27], a linear embedding methodology using principle component analysis (PCA) was developed to model the topological variations of composite microstructures satisfying some experimentally determined statistical correlations. This model was successful in reducing the representation of two-phase microstructures. However, as most of the data sets contain essential nonlinear structures that are invisible to PCA, it cannot be easily extended to the case of polycrystals. In [29], a nonlinear dimensionality reduction (NLDR) strategy was proposed to embed data variations into a low-dimensional manifold that could serve as the input model for subsequent analysis. This methodology was applied to construct a reduced-order model of thermal property variation of two-phase composites. The reduced model was subsequently utilized as a stochastic input model to study the effect of material uncertainty on thermal diffusion. However, this nonlinear strategy does not provide a robust mathematical parametric input model which reveals the inherent patterns. In addition, the mapping between the original and the surrogate space is based on the IsoMap [123] algorithm requiring computation of the geodesic distance matrix among data. In general, this matrix may not be well defined and the computation of the matrix could be expensive. Kernel principal component analysis (KPCA), which first nonlinearly maps the input to a "feature" space and then performs PCA, was therefore introduced to resolve the issues affiliated with linear PCA and Isomap model reduction. Successful application of KPCA to modeling of random permeability field of complex geological channelized structures was provided in [80].

A bi-orthogonal decomposition model reduction approach [8, 128] was employed in [52] to build the reduced-order model of location-specific microstructures in a stochastic multiscale forging simulation. In that work, microstructures were assumed to have different distributions at different spatial points over the workpiece. As a result, the stochastic input was extremely high dimensional, which is known as the "curse of dimensionality". Conventional model reduction schemes that only locally decompose microstructure complexity at a given material point and cannot explore the correlation between the microstructures in the continuum are not sufficient. To this end, the bi-orthogonal KLE was introduced to decompose the multiscale random microstructure into a few modes in both the macro- and meso-scales, so that the dimension of the multiscale random field can be effectively reduced. However, this earlier work limited its stochastic input to two prescribed random variables. In this thesis, we are going to employ the model reduction techniques to construct low dimensional surrogate model of random input polycrystalline microstructure features. For random microstructures associated with a single material point, conventional linear and nonlinear methods such as KLE, Isomap, and PCA/KPCA will be adopted. The bi-orthogonal decomposition will be combined with a second-level KLE to construct the reduced-order surrogate space of the location-specific microstructure in the stochastic multiscale simulation.

Having constructed the reduced-order model of the stochastic input, the stochastic partial differential equations (SPDEs) that define the physics of deformation can be solved subsequently with the repeated calling of the deterministic simulation. The most traditional and popular SPDE solver is the Monte Carlo (MC) method. Its convergence rate does not depend on the number of independent input random variables, and its implementation is very easy if a work-

ing deterministic code is given. However, the MC method becomes quickly intractable for complex problems in multiple random dimensions. This is because the number of realizations required to acquire good statistics is usually quite large. Furthermore, the number of realizations changes with the variance of the input parameters and the truncation errors are hard to estimate. A stochastic collocation method that represents the stochastic solution as a polynomial approximation is later introduced. Its interpolant is constructed via independent function calls to the deterministic problem at different interpolation points which are selected based on the Smolyak algorithm [112]. An adaptive version of this approach, the adaptive sparse grid collocation (ASGC), has been developed [78]. This method utilizes local linear interpolation and uses the magnitude of the hierarchical surpluses as an error indicator to detect the non-smooth region in the stochastic space and thus place automatically more points around this region. This approach results in further computational gains and guarantees that a user-defined error threshold is met. In this thesis, we will use both the MC and ASGC methods to solve the stochastic problem and quantify the variability of material properties.

The following part of the thesis will be divided into three major chapters. The next chapter presents studies of mechanical properties/responses variability of microstructures corresponding to a single material point. In Section 2.1, macroscopic stress-strain response of single-phase FCC nickel microstructures under deformation is studied. Fatigue properties of nickel-based superalloy microstructures are examined in Section 2.2. The uncertainty quantification of multiscale deformation processes is studied in Chapter 3, where the random microstructure is assumed to be location specific, i.e. microstructure distribution varies with spatial location. A bi-orthogonal decomposition scheme is devel-

oped to reduce the dimension of multiscale microstructure input. The variability of strain, stress and strength fields over the workpiece after forging is investigated. The microstructures in the above mentioned two chapters are represented using crystallographic and/or topological features such as grain orientations and sizes. Taylor model is used to approximately estimate the mechanical response of microstructures. For more accurate prediction, we develop a full-field crystal elasto-viscoplasticity fast Fourier transform (CEPFFT) approach in Chapter 4. The high computation efficiency of this model shows great potential in integrating it with stochastic/multiscale materials simulations. In the last section, conclusions of the thesis work and suggestions for future research are summarized.

CHAPTER 2

UNCERTAINTY QUANTIFICATION AT A SINGLE MATERIAL POINT

Our uncertainty quantification work starts with the random microstructure associated with a single material point. Mechanical response variability of single-phase FCC nickel microstructures due to both orientation and grain size uncertainties is studied in Section 2.1. A nonlinear model reduction technique based on Isomap manifold learning [29] is introduced to find the surrogate space of the grain size feature while crystallographic orientations are reduced by KLE. Homogenized stress-strain curve with error bars during deformation and critical stress distribution after deformation are computed. The notation follows the work in [73]. In Section 2.2, a homogenized constitutive model for IN100 nickel-based superalloys [98] is implemented in the Taylor model and FE framework. Variability of fatigue resistance, measured by strain-based fatigue indicator parameters (FIPs) [109] of the two-phase superalloy is studied with the assistance of principal component analysis (PCA) and kernel principal component analysis (KPCA). Distributions of FIPs, as well as their convex hulls showing the extreme values, of microstructures sharing identical statistical features with given samples under cyclic loading are extracted. Most content and notation are from the work in [130].

2.1 Investigating mechanical response variability of single-phase polycrystalline microstructures

2.1.1 Model reduction theory

Features of polycrystals are composed of two aspects: topology and crystallographic texture. The first aspect regards geometry characters, such as grain shape and grain size, while the second is the crystallographic orientation distribution of grains. For a polycrystalline microstructure, its properties are mostly determined by the grain size and orientation distribution. In order to model the uncertainty of microstructures, the two features are considered as random fields. Model reduction techniques are applied to grain size and texture separately, and then their low-dimensional representations are combined to fully represent a microstructure. In this section, focus is given on a nonlinear model reduction scheme performing to the grain size space. The model reduction on texture will be introduced in Section 2.1.3.

Fig. 2.1 shows multiple microstructures that satisfy some specific experimentally determined statistics of grain size distribution. Each microstructure that satisfies the given statistics of the grain size distribution is a point lying on a curve (manifold) embedded in a high-dimensional space. The problem of 'manifold learning' as applied to this situation is as follows: *Given a set of N unordered points belonging to a manifold $\mathcal{M}$ embedded in a high-dimensional space $\mathbb{R}^n$, find a low-dimensional region $\mathcal{A} \subset \mathbb{R}^{d_1}$ that parameterizes $\mathcal{M}$, where $d_1 \ll n$.*

The process of learning the nonlinear low-dimensional structure hidden in a set of unorganized high-dimensional data points is known as the *manifold learn-*

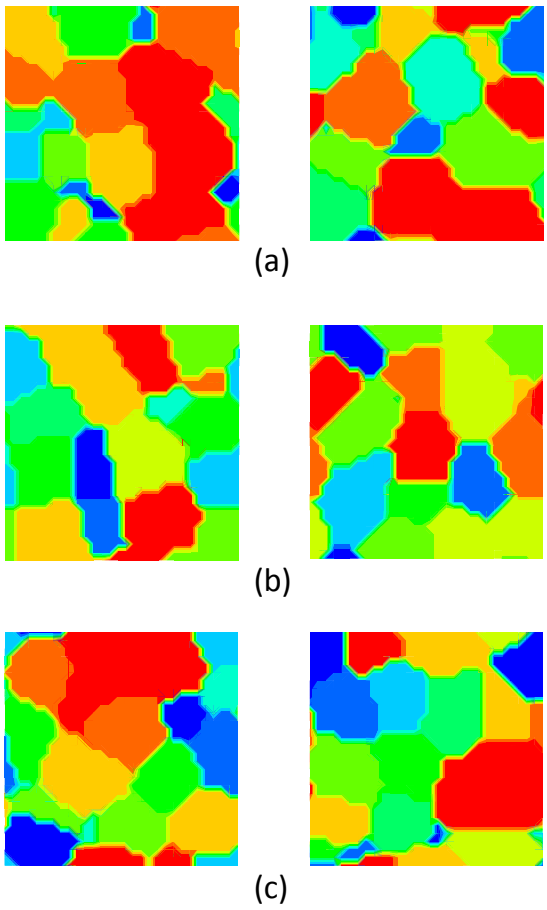

Figure 2.1: Slices of 3D microstructures satisfying different constraints of the grain size (given here in terms of grain volume, the domain of microstructure is $1mm^3$) distribution: (a) constant mean grain volume ($0.0185\ mm^3$), (b) constant mean grain size ($0.0185\ mm^3$) and second-order moment ($3.704 \times 10^{-4}\ mm^6$), and (c) constant grain size ($0.0185\ \ mm^3$), second-order moment ($3.704 \times 10^{-4}\ mm^6$) and third-order moment ($8.637 \times 10^{-6}\ mm^9$).

ing problem. Principle Component Analysis (PCA), Karhunun-Loève expansion (KLE) and multidimensional scaling (MDS) [44] are classical methods in manifold learning. These methods extract optimal mappings when the manifold is embedded linearly or almost linearly in the input space. However, in most cases of interest, the manifold is nonlinearly embedded in the input space, making the classical methods of dimension reduction highly approximate.

Recently, two new approaches have been developed that combine the computational advantages of PCA with the ability to extract the geometric structure of nonlinear manifolds. One set of methods takes a bottom-up approach, i.e they try to preserve the local geometry of the data. They aim to map nearby points on the manifold to nearby points in the low-dimensional representation. Such methods, Locally Linear Embedding (LLE) [104], Laplacian Eigen Maps, Hessian Eigen Maps, essentially construct a homeomorphic mapping between local sets in the manifold to an open ball in a low-dimensional space. The complete mapping is a union of these local maps. On the other hand, the alternate set of approaches towards nonlinear model reduction take a top-down approach [18]. Such global approaches, like the Isomap and its numerous variants, attempt to preserve the geometry at all scales. They ensure that nearby points on the manifold (with distance defined via a suitable metric) map to nearby points in the low-dimensional space and faraway points map to faraway points in the low-dimensional space. The distance between original points is identical to that between their low-dimensional counterparts. Though both approaches are viable, we focus our attention to global methods of non-linear dimension reduction.

The basic premise of the Isomap [123, 1] algorithm is that 'only geodesic distances reflect the true low-dimensional geometry of the manifold'. The geodesic distance (between two points) on a manifold can be intuitively understood to be the shortest distance between the two points *along the manifold* (see Fig. 2.2 for an illustration).

Subsequent to the construction of the geodesic distance between the sample points $\{\mathbf{x}_i\}$ in the high-dimensional space, the Isomap [123] algorithm constructs the low-dimensional parametrization simply as a set of points $\{\mathbf{y}_i\}$ lying in a low-

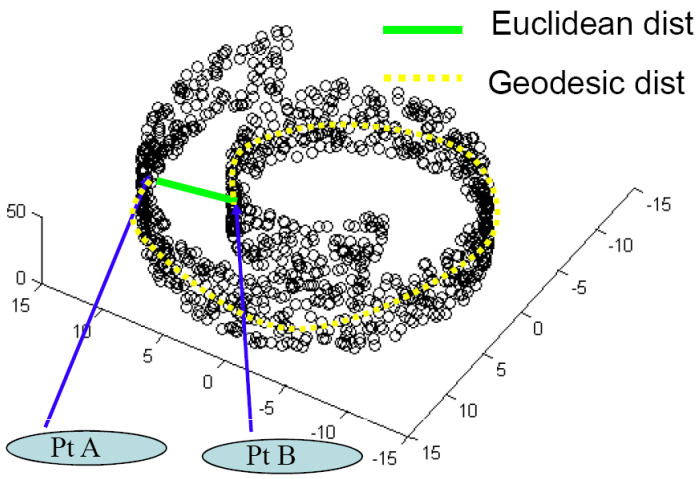

Figure 2.2: A schematic showing the manifold in the high- and low-dimensional spaces. The data points shown here are in 3D but the intrinsic dimensionality of the manifold is 2.

dimensional space that most accurately preserve the geodesic distance. That is, the distance between two points $\mathbf{y}_i$ and $\mathbf{y}_j$ in low-dimensional space should be the same with the geodesic distance between their corresponding points $\mathbf{x}_i$ and $\mathbf{x}_j$ in the high-dimensional space. This property is called isometry. With the Isomap algorithm, *given a set of N-unordered points belonging to a manifold* $\mathcal{M}$ *embedded in a high-dimensional space* $\mathbb{R}^n$, *a low-dimensional region* $\mathcal{A} \in \mathbb{R}^{d_1}$ *is computed which is isometric to* $\mathcal{M}$, *with* $d_1 \ll n$.

Since we have no notion of the geometry of the manifold to start with (hence cannot construct the true geodesic distances), we approximate the geodesic distance using the concept of graph distance $\mathcal{D}_G(i, j)$, thus the distance of points far away is computed as a sequence of small hops. This approximation, $\mathcal{D}_G(i, j)$, asymptotically matches the actual geodesic distance $\mathcal{D}_M(i, j)$ in the limit of large number of samples [29]. As discussed before, the key to a good model reduction and reconstructions is a viable measurement of microstructure. Since the important feature we are looking to embed and recreate is the grain size distribution,

we choose this feature as the measurement (see Section 2.1.2).

Having computed the pairwise distance matrix between the given microstructures, one can compute the location of N points in a reduced-order surrogate space, $\mathbf{y}_i \in \mathbb{R}^{d_1}$ such that the distance between these points is arbitrarily close to the given distance matrix. Multi Dimensional Scaling (MDS) methods allow this mapping [29]. The intrinsic dimension d_1 of an embedded manifold is linked to the rate of convergence of the length-functional of the minimal spanning tree of the geodesic distance matrix of the unordered data points in the high-dimensional space [29]. The rate of change of the length functional as more number of points are chosen is related to the dimensionality of the manifold via a simple relation $log(L) = alog(N) + \epsilon$, where $a = (d_1 - 1)/d_1$. The intrinsic dimensionality, d_1, can be estimated by finding the length functional for different number of samples N and subsequently finding the best fit for a.

The procedure above results in N points in a low-dimensional space $\mathbb{R}^{d_1}$. The geodesic distance and the MDS step result in a low-dimensional convex region $\mathcal{A} \subset \mathbb{R}^{d_1}$. Using the N samples, the reduced space is given as a convex hull $\mathcal{A} = \text{convex hull}(\mathbf{y}_i)$ that parameterizes the grain size space. Since microstructures in $\mathcal{M}$ satisfy all the required grain size properties, they are here taken to be equally probable to occur. That is, every point in the high-dimensional stochastic space $\mathcal{M}$ is equiprobable. The convex hull can be mapped to a unit hypercube with the same dimensionality d_1. Since the microstructures are equiprobable, we consider each of the dimensions of the hypercube as defining an independent uniform random variable. These random variables define our stochastic support space. Since $\mathcal{A}$ serves as the surrogate space of $\mathcal{M}$, we can access the variability in $\mathcal{M}$ by sampling over $\mathcal{A}$, or equivalently the hypercube, which is

the sampling space in the sparse grid collocation method. Unfortunately, this requires not only the mapping $\mathcal{M} \longrightarrow \mathcal{A}$ just described but also the inverse mapping (microstructure reconstruction) $\mathcal{A} \longrightarrow \mathcal{M}$. This microstructure reconstruction will be discussed in Section 2.1.2. The overall steps of the procedure are summarized in Fig. 2.3. Note that here the surrogate space $\mathcal{A}$ is mapped to a unit d_1-dimensional hypercube to allow interfacing this procedure with sparse grid collocation techniques [78]. In such collocation methods, the sampling points are defined on a hypercube. These collocation methods have been shown to be efficient in interfacing with deterministic solvers of e.g. deformation, diffusion, flow, etc. in random media, thus allowing modeling the effect of microstructural uncertainty on material properties.

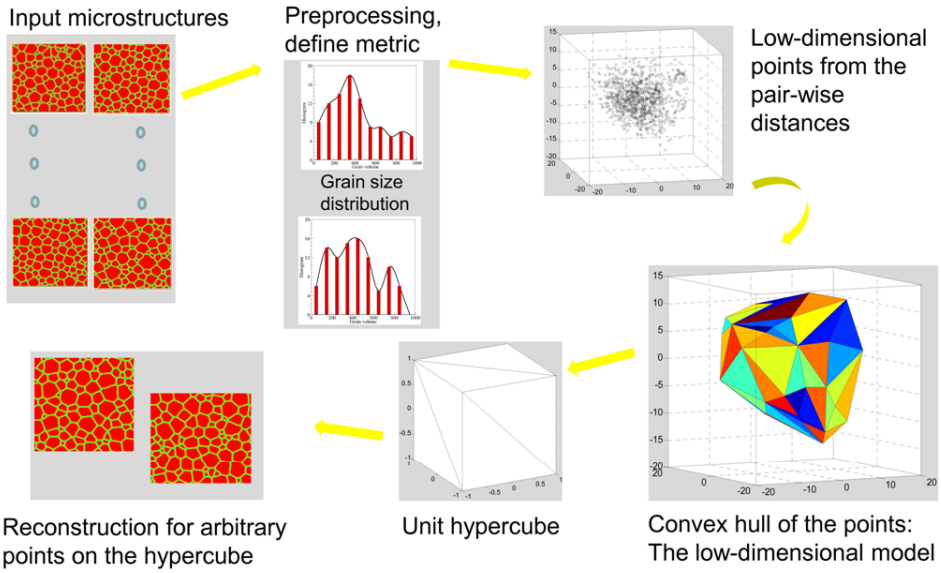

Figure 2.3: The various steps in a data-driven model reduction of polycrystal microstructures. The high-dimensional microstructures are mapped to a low-dimensional region $\mathcal{A}$. This convex region defined by the data points in $\mathcal{A}$ is mapped to a unit hypercube. Each sample point on this hypercube corresponds to a viable microstructure that needs to be reconstructed using the given data.

2.1.2 Microstructure representation and reconstruction methodology

Topology representation: Grain size vector of a microstructure

The high-dimensional representation of a microstructure topology feature in this work is chosen to be the grain size distribution, namely the volume of grains, for its great effect on mechanical properties. A polycrystalline microstructure contains a finite number of grains and each grain has its own size. If the size of each grain is given, the microstructure can be non-uniquely determined. The only differences in geometry of these microstructures are the shapes and arrangement of the grains, which do not have significant effect on microstructure mechanical properties and can be neglected especially when the Taylor homogenization hypothesis is adopted. Here, we treat microstructures having the same grain size distribution to be in the same class. A measurement that uniquely represents this kind of microstructures is needed. Here, the measurement is chosen as the grain size (in terms of volume) vector sorted by ascending order (we refer it as 'sorted grain size vector') and the term 'microstructure' in the following refers to the grain size feature instead of a microstructure realization. For example, consider a cubic microstructure containing $n = 4$ grains whose volumes are given as $\mathrm{S} = \{0.3mm^3, 0.2mm^3, 0.4mm^3, 0.1mm^3\}$. Rearranging the grain size in ascending order, the new representation of this microstructure is $\mathrm{S} = \{0.1mm^3, 0.2mm^3, 0.2mm^3, 0.4mm^3\}$. This resulting vector is chosen as the representation of this kind of microstructure. After being sorted, microstructures belonging to the same class result in the same grain size vector, while different classes give different vectors. This choice is selected as it

is easy to express and satisfy the given constraints on grain size (mean, standard deviation, higher-order moments, etc.) and in addition, the (non-unique) reconstruction of a microstructure with given grain sizes is straightforward. In the meantime, adopting Euclidean distance as the metric, we can measure the difference between microstructres represented by sorted grain size vector. To estimate the difference between two microstructures, $\mathbf{A} \in \mathcal{M}$ and $\mathbf{B} \in \mathcal{M}$, we first sort the grain sizes (effectively, grain volume) by ascending order. The Euclidean distance, $\mathcal{D}_G(\mathbf{A}, \mathbf{B})$, between them is defined as follows:

$$\mathcal{D}(\mathbf{A}, \mathbf{B}) = (\sum_{i}^{n} (S_i^A - S_i^B)^2)^{1/2} \tag{2.1}$$

Fig. 2.4 shows an example of using sorted grain size vector to measure the difference between two 54-grain microstructures. Fig. 2.4(a) depicts the sorted grain volume distribution of two microstructures having the same mean grain size. Fig. 2.4(b) measures the difference in each grain between the microstructures, which also tells how much microstructure **A** is different from microstructure **B**. The dimensionality of this grain size vector is determined by the number of grains of a microstructure. For a microstructure containing 54 grains, its representation is 54-dimensional. As the mean grain size is fixed, there are only 53 independent dimensions. If more constraints are added, the dimensionality will be further reduced.

Microstructure reconstruction

Given a set of samples $\{\mathbf{x}_i\}$, $i = 1, \ldots, N$ in manifold $\mathcal{M}$, the non-linear dimensionality reduction strategy (Section 2.1.1) converts these points into a set of points $\{\mathbf{y}_i\}$, $i = 1, \ldots, N$ belonging to a convex set $\mathcal{A}$. This convex region $\mathcal{A} \subset \mathbb{R}^{d_1}$, defines the reduced representation of the space of microstructures. As $\mathcal{A}$ is the surro-

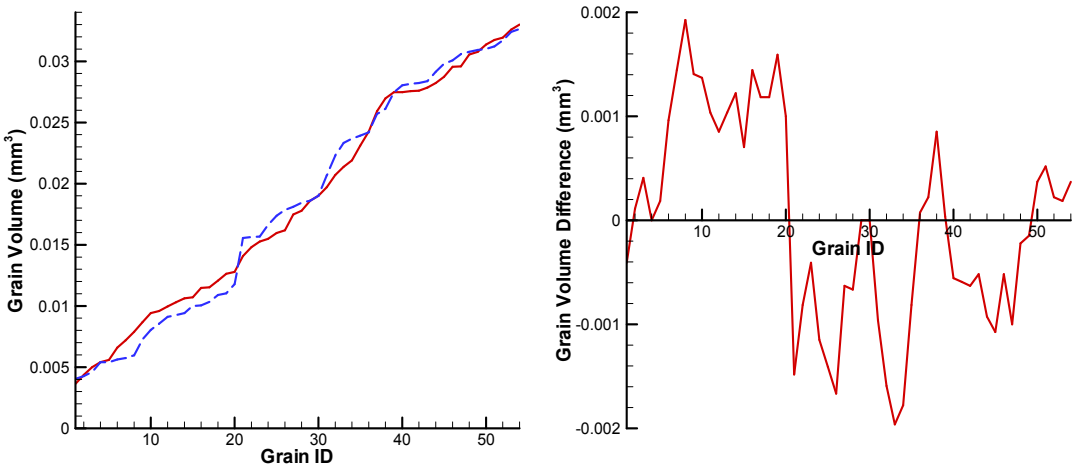

Figure 2.4: (a) Two microstructures represented by sorted grain size vectors. (b) The difference between the two sorted grain size vectors.

gate space of $\mathcal{M}$, one can access the complete variability in the topology and property distribution of grain size in $\mathcal{M}$ by simply sampling over the region $\mathcal{A}$. But we have no knowledge of the image of a point in the microstructural space $\mathcal{M}$ corresponding to an arbitrary point $\mathbf{y} \in \mathcal{A}$. For a usable reduced-order model of the microstructure space, an explicit mapping $\mathcal{F}^{-1}$ from $\mathcal{A}$ to $\mathcal{M}$ has to be constructed.

As shown in Fig. 2.3, the reduced-dimensionality space $\mathcal{A}$ is used as the surrogate space from which acceptable microstructures need to be sampled (at arbitrary points). The procedure of reconstructing a microstructure $\mathbf{x} \in \mathcal{M}$ from the low-dimensional space $\mathcal{A} \subset \mathbb{R}^{d_1}$ is as follows: (1) Generate a point in the low-dimensional space $\mathbf{y} \in \mathcal{A}$. (2) Find the m nearest neighbors of $\mathbf{y}$ and denote them as $\mathbf{y}_i, i = 1, \ldots, m$. (3) Find the microstructures $\mathbf{x}_i, i = 1, \ldots, m$ in the high-dimensional space $\mathcal{M} \subset \mathbb{R}^n$ that are corresponding to $\mathbf{y}_i, i = 1, \ldots, m$. Based on isometry, $\mathbf{x}$ could be computed following a linear interpolation algorithm:

$$\mathbf{x} = \sum_{i=1}^{n} W_i \mathbf{x}_i, \quad W_i = \frac{\frac{1}{\mathcal{D}(\mathbf{y}_i, \mathbf{y})}}{\sum_{j=1}^{n} \frac{1}{\mathcal{D}(\mathbf{y}_j, \mathbf{y})}} \tag{2.2}$$

Note that the metric in the reduced space $\mathcal{A} \subset \mathbb{R}^{d_1}$ is the Euclidean distance and the points $\mathbf{x_i} \in \mathcal{M}$ are the sorted grain size vectors defined earlier. The equation above demonstrates that the new generated microstructure can be interpolated by its nearest neighbors weighed by the reciprocal distances between their corresponding low-dimensional points. The mean grain size of the interpolated microstructure automatically equals the required value because of the linearity of Eq. (2.2). However, when the microstructures on the manifold are constrained by higher-order moments, the resulted microstructure by interpolation cannot satisfy all the constraints, which means it does not lie on the manifold, but has slight deviation. To obtain the microstructure satisfying all the given moments, we need to modify the grain sizes. This procedure is referred to as projecting the image onto the manifold in [29]. An algorithm implemented in the current work that can adjust the grain size distribution to satisfy the second- and third-moments of grain size is briefly described below.

Controlling the grain size distribution to satisfy a given second-order moment of the grain size distribution is straightforward. Given a grain size vector whose mean size is M_1, we would like to adjust the grain sizes so that its second-order moment is M_2. To do this, we first centerize the original grain size vector to one that has zero mean by subtracting M_1 from each component. We next weight each component with the ratio of the expected standard deviation to the current standard deviation. The algorithm is as follows:

Step 1: $E_1 = \frac{1}{n}\sum_{i=1}^{n} S_i = M_1$;

Step 2: $S_i = S_i - M_1$;

Step 3: $E_2 = \frac{\sum_{i=1}^{n} S_i^2}{n}$;

Step 4: $a = \sqrt{\frac{M_2 - M_1^2}{E_2}}$;

Step 5: $S_i = aS_i$.

Having the zero-mean grain size vector satisfying the expected standard deviation, the final grain size vector that satisfies both the mean size and second-order moment can be obtained by adding M_1 to its components, i.e. $S_i = M_1 + aS_i$, for $i = 1, \ldots, n$.

The control of the third-order moment is more complicated. Two iterative processes are needed to accomplish this task. The basic idea is to find an intersection vector of two surfaces. One surface is composed of microstructures satisfying the first two moments and the other one is defined by the third-order moment M_3. Still, the mean size M_1 is subtracted from the grain size vector. The first three target moments of the zero mean grain size vectors are then equal to $\hat{M}_1 = 0, \hat{M}_2 = M_2 - M_1^2$ and $\hat{M}_3 = M_3 - 3M_1M_2 + 2M_1^3$, respectively. The complete algorithm is as follows:

Step 1: $\hat{S}_i = S_i - M_1$;

Step 2: $\hat{S'}_i = \hat{S}_i$, and $E_1 = \frac{1}{n}\sum_{i=1}^{n} S_i$;

Step 3: $\hat{S}_i = \hat{S}_i - E_1$;

Step 4: $E_2 = \frac{1}{n}\sum_{i=1}^{n} S_i^2$;

Step 5: $\hat{S}_i = \hat{S}_i \sqrt{\frac{\hat{M}_2}{E_2}}$;

Step 6: loop

$$\delta_i = \frac{3\hat{S}_i^2}{n};$$
$$d = \sum_{i=1} n\delta_i^2, E_3 = \frac{1}{n}\hat{S}_i^3;$$
$$m = \hat{M}_3 - E_3;$$
$$\hat{S}_i = \hat{S}_i + \frac{m}{d}\delta_i;$$
$$\text{if} |m| < \text{cutoff}, \text{break};$$

Step 7: error = norm($\hat{S'}_i - \hat{S}_i$);

Step 8: if error < cutoff, go to step 9, else go to step 1;

Step 9: $S_i = M_1 + \hat{S}_i$.

The grain size vector $\{S_i, i = 1, \ldots, n\}$ now satisfies all the three given moment constraints.

With a grain size vector, a realistic 3D microstructure can be generated using a grain growth simulation method such as the phase-field method [36], although in the current work the realization of the 3D microstructure is not necessary. An example of a 3D microstructure that satisfies given moment constraints is shown in Fig. 2.5.

Given the methodology discussed in Sections 2.1.1 and 2.1.2, the mapping between high- and low-dimensional stochastic space of grain size feature is constructed based on an isometric nonlinear model reduction methodology. In the next section, the representation and model reduction on texture space will be introduced.

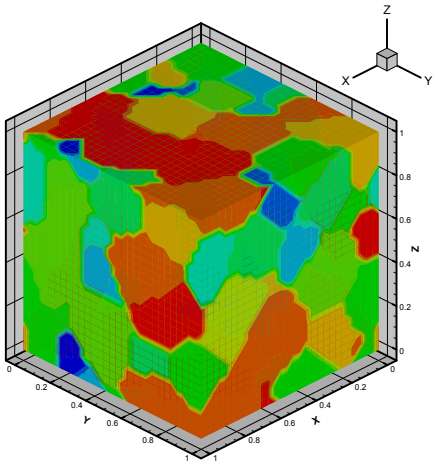

Figure 2.5: A 3D microstructure with 64 grains with prescribed mean grain size value ($0.0185mm^3$). The reconstruction is based on a grain-growth model implemented using a phase-field method.

2.1.3 Texture modeling

Other than grain size, the properties of a polycrystalline microstructure are highly dependent on its crystallographic texture. For the case of a discrete microstructure containing moderate number of grains, the texture effect is usually much more significant than the grain size effect. To examine the effect of variability in initial texture on the final property of the microstructure, the texture is defined as a random field, whose variables are orientation components of individual grains. In this paper, the orientation of a grain is defined by a rotation around an axis and is known as Rodrigues parametrization, an axis-angle representation consisted of three components:

$$\mathbf{r} = \mathbf{w} \tan \frac{\phi}{2} \tag{2.3}$$

where $\mathbf{r} = \{r_1, r_2, r_3\}$ are the three Rodrigues components; $\mathbf{w} = \{w_1, w_2, w_3\}$ gives the direction cosines of the rotation axis with respect to microstructure coordinates; and ϕ is the rotation angle.

In nature, the orientation of a grain should be totally random if no constraint is taken into account. Through certain deformation, the orientation is changed due to grain rotation and distortion, and therefore forms preferred texture throughout the entire microstructure. For a set of independently randomly distributed orientations, it is difficult to perform dimensionality reduction because of lack of intrinsic correlations. However, processed microstructures through certain deformation mode gain preferred texture that are implicitly correlated among orientations. Several linear dimensionality reduction techniques have already been successfully implemented in reducing the Orientation Distribution Function (ODF) to lower-dimensional representations [50, 3]. In those works, the material deformation simulation was conducted using an ODF based scheme, where the microstructure was assumed to be continuous and its macroscopic properties were computed by integrating over the entire fundamental zone of Rodrigues space. The ODF was updated following the ODF conservation equation [55].

In the current work, however, the microstructure is discretely represented by an ensemble of grains, each of which possesses an orientation consisted of three axis-angle parameters (Eq. (2.3)). The update of the texture is obtained by estimating the elastic distortion inside grains [6]

$$\begin{aligned} \mathbf{m}_t^\alpha &= \mathbf{F}^e(t)\mathbf{m}_0^\alpha \\ \mathbf{n}_t^\alpha &= \mathbf{F}^{e-T}(t)\mathbf{n}_0^\alpha \end{aligned} \tag{2.4}$$

where $\mathbf{m}^\alpha$, $\mathbf{n}^\alpha$ are the direction and normal of the slip system α and $\mathbf{F}^e$ is the elastic deformation gradient. In this case, the texture is described by a finite number of orientations (the same with grain number), leading only certain points in Rodrigues space having a non-zero ODF value. Thus, the appropriate method to

reduce the texture dimension should be directly performed on grain orientations, instead of assuming a continuous field in Rodrigues space.

Here, we define the orientation vector representing the microstructure texture as

$$\boldsymbol{\tau}(\mathbf{r}) = \left\{r_1^1, r_2^1, r_3^1, r_1^2, r_2^2, r_3^2, \ldots, r_1^n, r_2^n, r_3^n\right\}^T \tag{2.5}$$

where n is the total number of grains. Texture $\boldsymbol{\tau} \in \mathcal{T}$, in which $\mathcal{T} \subset \mathbb{R}^{3n}$ is the stochastic space of texture. The Rodrigues representation is defined in Eq. (2.3). $\{r_1^i, r_2^i, r_3^i\}$ are the three orientation components of the i-th grain. The initial orientations of grains are provided in the form of Eq. (2.5) through input files. The initial orientation matrix of grain i ($i = 1, \ldots, n$) can be calculated by

$$\mathbf{R}_0^i = \frac{1}{1 + \mathbf{r}_0^i \cdot \mathbf{r}_0^i}\left(\mathbf{I}(1 - \mathbf{r}_0^i \cdot \mathbf{r}_0^i) + 2(\mathbf{r}_0^i \otimes \mathbf{r}_0^i + \mathbf{I} \times \mathbf{r}_0^i)\right) \tag{2.6}$$

where $\mathbf{r}_0^i$ is the initial orientation for the i-th grain. Thus the initial slip system α of grain i, represented in the sample coordinate system, can be determined by

$$\begin{aligned} \mathbf{m}_0^{i,\alpha} &= \mathbf{R}_0^i \mathbf{m}_{local}^{\alpha} \\ \mathbf{n}_0^{i,\alpha} &= \mathbf{R}_0^i \mathbf{n}_{local}^{\alpha} \end{aligned} \tag{2.7}$$

where $\alpha = 1, \ldots, 12$ for FCC materials and $\mathbf{m}_{local}^{\alpha}$ and $\mathbf{n}_{local}^{\alpha}$ are the slip direction and plane normal, respectively, in the local (crystal) coordinate system. $\mathbf{m}_0^{i,\alpha}$ and $\mathbf{n}_0^{i,\alpha}$ define the initial orientation of grain i and are needed for computing the resolved shear stresses and update the plastic deformation in the crystal plasticity simulation.

Although orientations are usually defined within the fundamental zone of Rodrigues space due to the crystal symmetry, the range of Rodrigues components are in essence from negative infinity to positive infinity. Thus, the vector

$\boldsymbol{\tau}$ has no constraint. Our goal is to find a lower-dimensional space $\Gamma \subset \mathbb{R}^{d_2}$ as the surrogate space of $\mathcal{T}$.

For a microstructure that underwent through a sequence of deformation processes controlled by random variables $\boldsymbol{\omega} = \{\omega_1, \omega_2, \ldots\}$, its texture will also depends on $\boldsymbol{\omega}$. While the explicit relationship between $\boldsymbol{\tau}$ and $\boldsymbol{\omega}$ is not easy, neither necessary, to find, we adopt the Karhunen-Loève Expansion (KLE) to represent the random texture using a series of intermediate uncorrelated parameters $\boldsymbol{\eta}$, which are implicitly dependent on $\boldsymbol{\omega}$. Given a set of N texture samples, the unbiased estimate of the covariance matrix of these texture vectors is

$$\tilde{\mathbf{C}} = \frac{1}{N-1} \sum_{i=1}^{N} (\boldsymbol{\tau}_i - \bar{\boldsymbol{\tau}})^T (\boldsymbol{\tau}_i - \bar{\boldsymbol{\tau}}), \bar{\boldsymbol{\tau}} = \frac{1}{N} \sum_{i=1}^{N} \boldsymbol{\tau}_i \tag{2.8}$$

$\boldsymbol{\tau}_i$ is the ith realization of $\boldsymbol{\tau} \in \mathcal{T}$ and N is the total number of known realizations, namely the sample number. The truncated Karhunen-Loève Expansion of the random vector $\boldsymbol{\tau}$ is then written as

$$\boldsymbol{\tau}(\mathbf{r}, \boldsymbol{\omega}) = \bar{\boldsymbol{\tau}}(\mathbf{r}, \boldsymbol{\omega}) + \sum_{i=1}^{d_2} \sqrt{\lambda_i} \boldsymbol{\phi}_i(\mathbf{r}) \eta_i(\boldsymbol{\omega}) \tag{2.9}$$

where $\boldsymbol{\phi}_i$, λ_i are the ith eigenvector and eigenvalue of $\tilde{\mathbf{C}}$, respectively; $\{\eta_i(\boldsymbol{\omega})\}$ is a set of uncorrelated random variables having the following two properties

$$\begin{aligned} E(\eta_i(\boldsymbol{\omega})) &= 0, \\ E(\eta_i(\boldsymbol{\omega})\eta_j(\boldsymbol{\omega})) &= \delta_{ij}, i, j = 1, \ldots, d_2 \end{aligned} \tag{2.10}$$

and their realizations are obtained by

$$\eta_i^{(j)} = \frac{1}{\sqrt{\lambda_i}} \left\langle \boldsymbol{\tau}_j - \bar{\boldsymbol{\tau}}, \boldsymbol{\phi}_i \right\rangle_{l_2}, j = 1, \ldots, N, i = 1, \ldots, d_2. \tag{2.11}$$

where $\langle \cdot, \cdot \rangle_{l_2}$ denotes the scalar product in $\mathbb{R}^N$. Since the covariance function is symmetric and positive definite, all the eigenvalues are positive real numbers

and the eigenvectors are mutually orthogonal and they span the space in which $\boldsymbol{\tau}(\mathbf{r}, \omega)$ belongs to. The summation in Eq. (2.9) is mean square convergent and usually truncated after few dominant terms, which preserve most information of the vector $\boldsymbol{\tau}$.

The truncated realizations of $\{\boldsymbol{\eta}^{(j)}\} \in \Gamma \subset \mathbb{R}^{d_2}$ are treated as reduced texture representations, which is analogous to the reduced grain size samples $\{\mathbf{y}_i\} \in \mathcal{A}$. The only constraint that we know about the random variables $\{\boldsymbol{\eta}^{(j)}\}$ is from Eq. (2.10). This distribution can be easily derived using Maximum Entropy Principle (MaxEnt) [50] to be a Gaussian distribution. Only in a very few special cases, the uncorrelated Gaussian random variables are not independent [83] and our example is not in that category. Therefore, here we treat $\boldsymbol{\eta}$ as a set of independent random variables that are normally distributed around $\mathbf{0}$. A convenient method to transform $\boldsymbol{\eta}$ to random variables $\boldsymbol{\zeta}$ that are uniformly distributed within the hypercube $[0,1]^{d_2}$ is based on the Rosenblatt transformation [102]. The distribution of $\boldsymbol{\zeta}$ is in fact the cumulative distribution functions (CDF) of $\boldsymbol{\eta}$.

$$\begin{aligned}
\zeta_1 &= \Phi_{\eta_1}(\eta_1) \\
\zeta_2 &= \Phi_{\eta_2|\eta_1}(\eta_2|\eta_1) = \Phi_{\eta_2}(\eta_2) \\
&\vdots \\
\zeta_{d_2} &= \Phi_{\eta_{d_2}|\eta_1 \ldots \eta_{d_2}-1}(\eta_{d_2}|\eta_1 \ldots \eta_{d_2}-1) = \Phi_{\eta_{d_2}}(\eta_{d_2})
\end{aligned} \tag{2.12}$$

where $\Phi(\cdot)$ is the standard normal CDF and in the current case is

$$\Phi_{\eta_i}(\eta_i) = \frac{1}{2}\left[1 + erf\left(\frac{\eta_i}{\sqrt{2}}\right)\right] \tag{2.13}$$

For a given point in the hypercube $\boldsymbol{\zeta} \in [0,1]^{d_2}$, its corresponding point $\boldsymbol{\eta}$ from the original distribution is naturally found to be

$$\eta_i = \Phi^{-1}(\zeta_i), i = 1, \ldots, d_2 \tag{2.14}$$

which can immediately give us a texture vector using Eq. (2.9).

Based on the analysis above, each microstructure $\mathbf{h}$ (with both grain size and texture features) that belongs to the high-dimensional stochastic space $\mathcal{H} = \mathcal{M} \times \mathcal{T}$, can be presented by $\mathbf{l}(\mathbf{y}, \boldsymbol{\eta})$ in the low-dimensional surrogate space $\mathcal{L} = (\mathcal{A} \times \Gamma) \subset \mathbb{R}^d$ ($d = d_1 + d_2$).

A mapping from $\mathcal{L}$ to $\mathcal{H}$ can be constructed for sampling allowable microstructure features. Define the stochastic model for the feature variation as $\mathcal{F}^{-1}(\boldsymbol{\xi}) : \mathcal{L} \longrightarrow \mathcal{H}$, where $\boldsymbol{\xi} = \{\xi_1, \ldots, \xi_d\}$ is a random vector chosen from $\mathcal{L}$. This low-dimensional stochastic model $\mathcal{F}^{-1}$ for the microstructure is the input to the SPDEs defining the crystal plasticity problem. For the grain size feature, this mapping is described in Section 2.1.2; for texture, the mapping is directly performed by Eq. (2.9), where $\mathcal{F}^{-1}(\boldsymbol{\eta}) : \boldsymbol{\eta} \longrightarrow \boldsymbol{\tau}$.

Mapping the low-dimensional space to a hypercube having the same dimensionality [29], the uncertainty of the mechanical property of the microstructure can be efficiently investigated using the adaptive sparse grid collocation (ASGC) method. It is a stochastic collocation procedure that solves stochastic partial differential equations (SPDEs) by computing the solution at various sample points, $\boldsymbol{\xi}$, from this space, $\mathcal{L}$. Each of the sample points corresponds to a microstructure that can be interrogated to evaluate its mechanical response. The sparse grid collocation approach will then create an interpolant of the mechanical response in the d-dimensional stochastic space of the random microstructures.

2.1.4 Sparse grid collocation

In the previous subsections, the grain size and texture of a polycrystalline microstructure have been reduced to a set of lower-dimensional representations as the input to stochastic simulation. A highly efficient, stochastic collocation based solution strategy is used to solve for the evolution of mechanical response. This subsection briefly reviews the adaptive sparse grid collocation method for solving SPDEs. For details, the interested reader is referred to [78].

The basic idea of sparse grid collocation is to approximate the multi-dimensional stochastic space $\mathcal{L}$ using interpolating functions on a set of collocation points $\{\boldsymbol{\xi}_i\}_{i=1}^{M} \in \mathcal{L}$. The collocation method collapses the multi-dimensional problem (based on the Smolyak algorithm) to solving M (M is the number of collocation points) deterministic problems. One computes the deterministic solution at various points in the stochastic space and then builds an interpolated function that best approximates the required solution. Notice, during the process, the mapping $\mathcal{F}^{-1}$ from low-dimensional surrogate $\mathcal{L}$ to high-dimensional microstructural space $\mathcal{H}$ needs to be implemented, so that the deterministic solver can work.

In the context of incorporating adaptivity, Newton-Cotes grid is utilized with equidistant support nodes. Hierarchical basis is used in constructing the interpolant. The interested function $u(t, \boldsymbol{\xi})$ can be approximated by

$$\hat{u}_{d,q}(t, \boldsymbol{\xi}) = \sum_{\|\mathbf{i}\| \leq d+q} \sum_{\mathbf{j} \in B_i} \omega_{\mathbf{j}}^{\mathbf{i}}(t) \cdot a_{\mathbf{j}}^{\mathbf{i}}(\boldsymbol{\xi}) \tag{2.15}$$

The mean of the random solution is evaluated as:

$$E(\hat{u}_{d,q}(t)) = \sum_{\|\mathbf{i}\| \leq d+q} \sum_{\mathbf{j} \in B_i} \omega_{\mathbf{j}}^{\mathbf{i}}(t) \cdot \int_{\mathcal{L}} a_{\mathbf{j}}^{\mathbf{i}}(\boldsymbol{\xi}) d\boldsymbol{\xi} \tag{2.16}$$

where q is the depth (level) of sparse grid interpolation and d is the dimensionality of stochastic space. B_i is a multi-index set. $\omega_{\mathbf{j}}^{\mathbf{i}}$ is the hierarchical surplus, which is the difference between the function value u at the current point and interpolation value $\hat{u}$ from the coarser grid in the previous level. $a_{\mathbf{j}}^{\mathbf{i}}$ is the d-dimensional multilinear basis functions defined by tensor product. For the estimation of higher-order moments (k-th order) of the function of interest, we only need to change u to u^k. The function of interest u and its interpolation $\hat{u}$ in the current work are the volume average equivalent stress of a polycrystalline microstructure at an equivalent strain of 0.2.

With increasing level of interpolation, new support nodes are added to the hypercube if the error indicator

$$\gamma_{\mathbf{j}}^{\mathbf{i}} = \frac{\|\omega_{\mathbf{j}}^{\mathbf{i}} \cdot \int_{\mathcal{L}} a_{\mathbf{j}}^{\mathbf{i}}(\boldsymbol{\xi}) d\boldsymbol{\xi}\|_{L_2}}{\|E_{\|\mathbf{i}\|-d-1}\|_{L_2}} \tag{2.17}$$

is larger than a threshold ϵ. The error indicator $\gamma_{\mathbf{j}}^{\mathbf{i}}$ measures the contribution of each term in Eq. (2.16) to the integration value (mean of the interpolated function) relative to the overall integration value computed from the previous interpolation level.

After the ASGC has been performed, the solutions of the SPDEs, namely the mechanical response of the random microstructures has been computed as an interpolant in the stochastic support space that defines the microstructure variability. Using this multi-dimensional interpolant of the mechanical response, one can compute statistical quantities of interest such as realizations, moments and the probability density function (PDF) using kernel density estimation [13].

2.1.5 Deterministic solver

We are interested to compute the variability of the macroscopic mechanical response of polycrystalline microstructures subjected to compression in the presence of uncertainty in grain size and texture. The deterministic solver is based on a rate-independent crystal plasticity constitutive model developed in [6]. A multiplicative decomposition of the deformation gradient into an elastic and plastic part, $\mathbf{F} = \mathbf{F}^e\mathbf{F}^p$, is used. By comparing the resolved shear stress with the slip resistance on specific slip system, active slip systems can be determined, which control the hardening of the crystals. The grain size effect is incorporated by explicitly introducing a grain size parameter into the Taylor hardening law [10]:

$$\hat{\tau} - \hat{\tau}_0 = \alpha\mu\, b\, \sqrt{\rho} \tag{2.18}$$

where

$$\dot{\rho} = \sum_{\kappa} \left\{ \frac{1}{L_g b} + k_1\, \sqrt{\rho} - k_2 \rho \right\} |\dot{\gamma}^{\kappa}| \tag{2.19}$$

The first term in Eq. (2.19) represents a geometric storage due to lattice incompatibility, describing the grain boundary hardening. L_g is the grain size parameter, which is effectively the equivalent diameter of the grain [49]. $\hat{\tau}$ is the single crystal flow strength, $\hat{\tau}_0$ is the initial yield strength, α is a constant usually chosen to be $1/3$, b is the Burgers vector, μ is the shear modulus, ρ is the density of dislocations, $\dot{\gamma}^{\kappa}$ is the strain rate of slip system κ. k_1 and k_2 are constants that can be determined from observations. The second term describes storage through a statistical measure of forest dislocation, describing the dislocation interaction hardening inside grains. The last term represents a dynamic recovery rate that renders dislocation segments inactive as they rearrange themselves [10].

The elastic and plastic deformation gradients can also be updated after calculating the incremental shear strain, which is determined by setting the resolved shear strain equal to the slip resistance. The Cauchy stress for each grain is calculated by

$$\mathbf{T} = \mathbf{F}^e\{[\det\mathbf{F}^e]^{-1}\mathbf{T}^*\}\mathbf{F}^{eT} \text{with} \quad \mathbf{T}^* = \mathbf{C}^e\mathbf{E}^e \tag{2.20}$$

where $\mathbf{E}^e = \frac{1}{2}\left(\mathbf{F}^{eT}\mathbf{F}^e - \mathbf{I}\right)$ is the strain tensor and $\mathbf{C}^e$ is the fourth-order elasticity tensor expressed in the microstructure coordinate system.

The deformation of the microstructure follows the Taylor hypothesis, in which all grains are assumed to be subject to the same deformation gradient. Under Taylor hypothesis, a realization of the microstructure is not necessary and the interactions between grains are neglected. This is a commonly used method for computing the homogenized macroscopic properties of materials in a stochastic simulation due to its high computational efficiency. Macroscopic properties, such as stress and strain, are computed as the volume-average of the microscopic values for different grains. For example, the macroscopic Cauchy stress $\bar{\mathbf{T}}$ and average plastic rate of deformation $\bar{\mathbf{D}}^p$ are calculated in the following form:

$$\bar{\mathbf{T}} = \langle\mathbf{T}\rangle = \frac{1}{V(\mathcal{B})}\int_{V(\mathcal{B})}\mathbf{T}dV \tag{2.21}$$

$$\bar{\mathbf{D}}^p = \langle\mathbf{D}^p\rangle = \frac{1}{V(\mathcal{B})}\int_{V(\mathcal{B})}\mathbf{D}^p dV \tag{2.22}$$

Accordingly, the macroscopic Von-Mises equivalent stress and equivalent strain are calculated in the form of

$$\bar{\sigma}_{eff} = \sqrt{\frac{3}{2}\bar{\mathbf{T}}' \cdot \bar{\mathbf{T}}'} \tag{2.23}$$

where $\bar{\mathbf{T}}'$ is the deviatoric part of $\bar{\mathbf{T}}$, and

$$\bar{\varepsilon}_{eff} = \int_0^t \sqrt{\frac{2}{3}\bar{\mathbf{D}} \cdot \bar{\mathbf{D}}} dt \tag{2.24}$$

where $\bar{\mathbf{D}}$ is the averaged deformation rate that can be directly computed as the symmetric part of the velocity gradient $\mathbf{L}$ in the Taylor hypothesis.

Utilizing this deterministic solver, several cases were considered and compared with available experimental data. The microstructure of interest consists of 64 grains each of which is assigned a random orientation. Nickel is selected as the material with parameters in Eq. (2.19) being $b = 2.49 \times 10^{-7} mm$, $k_1 = 1.15 \times 10^5 mm$, $k_2 = 3.14 mm^2$, and the three independent elastic constants are $C_{11} = 247 GPa$, $C_{12} = 147 GPa$, $C_{44} = 125 GPa$ [10, 72]. By varying the domain size of the microstructure, the effective stress of different mean grain size microstructures subjected to compression are computed and plotted at a series of strains (from 5% to 20%). Comparing with the experimental data [10, 95], we found our results to be consistent with experiments (Fig. 2.6). Although the restricted assumption in the Taylor model raises the material strength to some extent, the superior computation efficiency makes this method highly preferable in stochastic simulations. The variability of the macroscopic equivalent stress at specific strain under the same deformation history is of interest in following subsection.

2.1.6 Numerical examples

In this subsection, several examples are presented to study the statistics of mechanical response of polycrystalline microstructures based on the model reduc-

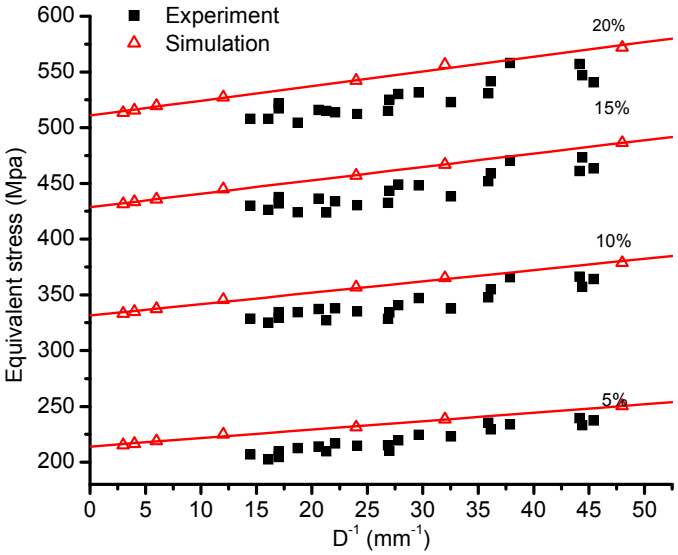

Figure 2.6: A comparison of the simulated and experimental results.

tion techniques and sparse grid collocation method introduced above. The deterministic solver adopts the aforementioned crystal plasticity constitutive model. The macroscopic equivalent stress is averaged over the microstructure domain following the Taylor hypothesis. In the following numerical examples, the mechanical response of FCC nickel microstructures subjected to compression is examined given various grain size and texture information.

The methodologies that are used in solving this stochastic problem are introduced in the previous subsections. Here, we summarize the main procedure of addressing the examples of interest.

1. Generate a number of grain size samples $\{\mathbf{x}_i\} \in \mathcal{M}, i = 1, \ldots, N$ according to certain information (prescribed mean size, 2nd- and 3rd-order moments, etc.). The given input microstructures satisfy the same constraints.
2. Utilize NLDR to reduce the dimensionality of the grain size samples. Their low-dimensional representations are $\{\mathbf{y}_i\} \in \mathcal{A}, i = 1, \ldots, N$. The optimal

dimensionality of the lower space $\mathcal{A}$ is linked to the rate of convergence of the length functional of the minimal spanning tree of the geodesic distance matrix of the unordered data points in the high-dimensional space [29]. A convex hull is constructed as the envelope of the reduced points.

3. Assign a given texture to the given set of microstructures. Put them through a sequence of deformation processes that are controlled by several random processing variables ω. The resultant textures are utilized to construct initial random texture space $\mathcal{T}$ for the stochastic polycrystal plasticity problem.

4. Perform KLE on texture samples, $\{\boldsymbol{\tau}_i(\omega)\}, i = 1, \ldots, N$. The low-dimensional representations $\{\boldsymbol{\eta}^{(i)}\} \in \Gamma$ can be obtained by truncating the eigen-spectrum to a desired level.

5. Combine the reduced grain size and texture to form the low-dimensional surrogate of feature space of microstructures, which is the stochastic input to the sparse grid collocation SPDE solver.

6. Use the ASGC method to construct the stochastic solution. This method solves the deterministic problem at various collocation points $\boldsymbol{\xi}$ on the stochastic space and constructs an interpolation based approximation to the stochastic solution. For a given set of stochastic collocation points, the corresponding microstructures of these points can be reconstructed (by the mapping $\mathcal{F}^{-1} : \mathcal{L} \longrightarrow \mathcal{H}$) and used as inputs in the solution of the corresponding crystal plasticity boundary value problem (compression test). For each of these deterministic problems, the elasto-plastic mechanical response is computed by the Taylor homogenization. The ASGC method constructs the stochastic interpolant of the mechanical response using the deterministic responses for the appropriately selected sparse grid colloca-

tion points.

7. After the corresponding stochastic plasticity problem has been solved, the final equivalent stress for any other microstructure realization in the stochastic support space can be calculated using the hierarchical interpolating functions. The probability distribution of the final equivalent stress at strain 0.2 is constructed using kernel smoothing density estimation on the histogram of realizations.

Example 1

In the first example, 1000 microstructure samples are first generated. Each sample contains 54 grains whose volume is uniformly distributed in the interval between $0.0037mm^3$ and $0.0333mm^3$. The mean grain volume of each microstructure is controlled to be $0.0185mm^3$, while higher-order moments are free to vary. These samples are used as the input database of grain size feature. By applying the NLDR method (Section 2.1.1), we first construct the geodesic distance matrix between points and then map them to a low-dimensional space through Multi-Dimensional Scaling (MDS) and Isomap. The number of nearest neighbors is set to be 10. The intrinsic dimensionality d_1 of the low-dimensional space is estimated by linking to the convergence of the length functional of the minimal spanning tree (MST) of the neighborhood graph defined by geodesic distance matrix [29]. To be specific, for various sizes of samples (varying from 20 to 1000), points are randomly picked from the set of samples. The minimal spanning tree of these sample sets was computed. The length functional of the MST was computed for each of these sample sets. The optimal dimensionality of the low-dimensional set is related to the slope of the line representing the re-

lationship between the length functional and the sample number (in logarithm form). The slope is computed using a least squares fit and rounded to be $d_1 = 3$ (Fig. 2.7). In this way, the original 54 dimensional grain size representation is reduced to 3.

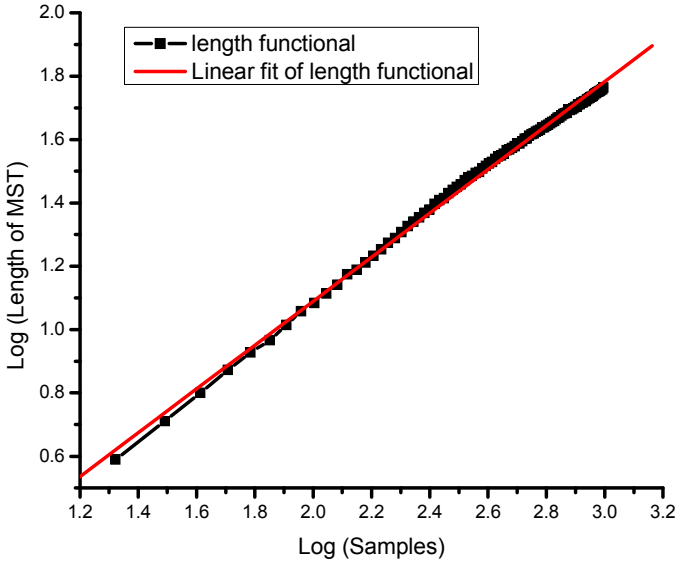

Figure 2.7: Plot of the length functional of the MST with respect to various sample sizes.

The prescribed texture samples are obtained through a series of random processing on an initially arbitrarily generated sample. To be specific, an arbitrary texture consisted of 54 random orientations was first generated and assigned to 1000 microstructure samples. Then, these microstructures were input into a sequence of deformation modes controlled by two independent random variables ω_1 and ω_2.

$$\mathbf{L} = \omega_1 \begin{bmatrix} 0 & 0 & 0 \\ 0 & 1 & 0 \\ 0 & 0 & -1 \end{bmatrix} + \omega_2 \begin{bmatrix} 0 & -1 & 0 \\ 1 & 0 & 0 \\ 0 & 0 & 0 \end{bmatrix} \tag{2.25}$$

where random variables ω_1 and ω_2 determine the deformation rate $\mathbf{L}$ of different modes and vary from $-0.002 sec^{-1}$ to $0.002 sec^{-1}$. At each time step, the

deformation of the microstructure is controlled by the combination of these two modes, but for different samples, the combination is different in terms of the deformation rates ω_1 and ω_2. At the end of $500sec$, the 1000 resultant textures were collected as the input texture database to the stochastic problem. With these texture samples, the unbiased estimate of the covariance matrix $\tilde{\mathbf{C}}$ is constructed. We then apply KLE (Section 2.1.3) on the covariance matrix and set the energy cutoff to be 90% – truncate the eigenvalue and eigenvector number d_2 when the energy captured by the first d_2 eigenvalues is larger than 90%. Fig. 2.8 shows that the first 2 eigenvalues of the covariance matrix captured 93.1% of the total energy (summation of all eigenvalues). Therefore, the dimensionality of the reduced initial texture is chosen to be 2.

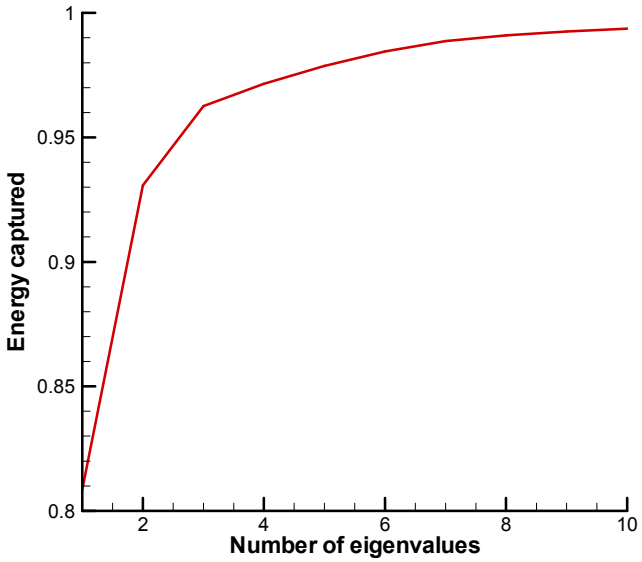

Figure 2.8: The energy captured by the most significant eigenvalues.

A three-dimensional convex hull corresponding to low-dimensional grain size representation is constructed with 88 faces and mapped to unit hypercube $[0,1]^3$ [29], and the low-dimensional texture representation is also mapped to a two-dimensional hypercube $[0,1]^2$. Assuming grain size and texture fea-

tures are independent, the complete low-dimensional surrogate of microstructure is five-dimensional. Therefore, a five-dimensional hypercube can be constructed whose first three dimensions correspond to grain size and the last two dimensions correspond to texture. The adaptive sparse grid collocation (ASGC) method is used with a sparse grid defined on this hypercube $[0,1]^5$ to investigate the mechanical response uncertainty due to the variation of grain size and texture. The cutoff of error indicator Eq. (2.17) controlling the interpolation error is set to be 0.001. Each realization within the hypercube can be transformed to the low-dimensional space and therefore mapped to a microstructure feature set (Sections 2.1.2 and 2.1.3). The mechanical response of the new microstructure was then computed using the Taylor model deterministic solver (Section 2.1.5). In this example, a deformation consisting of compression in the z-direction and stretch in the other two directions is applied to the microstructure. The velocity gradient is

$$\mathbf{L} = 0.002 sec^{-1} \begin{bmatrix} 0.5 & 0 & 0 \\ 0 & 0.5 & 0 \\ 0 & 0 & -1 \end{bmatrix} \tag{2.26}$$

The final equivalent strain is $\varepsilon = 0.2$. The homogenized macroscopic equivalent stresses corresponding to this strain is the primary variable that is interpolated in the stochastic space using a level 8 of interpolation. 1192 collocation points are adaptively generated. The mean final equivalent stress is found to be $539.159 MPa$ and the standard deviation is $10.471 Mpa$. As mentioned, the ASGC method decomposes the multi-dimensional stochastic problem into solving a number of deterministic problems. Thus, the deterministic solver is called at each collocation point. The deterministic solver (here, the Taylor model crystal plasticity solver) estimates the relation between the equivalent stress and equiv-

alent strain and records the history of deformation process in a stress-strain curve. The variation in the stress-strain response is shown in Fig. 2.9 (a), where the bars represent the standard deviation of the equivalent stress for the corresponding equivalent strain. Constructing the interpolant of the final equivalent stress (at strain equal to 0.2), we can obtain the distribution of the final stress by sampling uniformly from the hypercube. According to Eq. (2.15), given a point located in the hypercube, we can find a stress corresponding to it. Generate sufficient samples (in this case, 10000 points are generated from the interpolant), a histogram of the final stress is obtained. Utilizing kernel smoothing density estimation [13], the PDF of the final equivalent stress is plotted in Fig. 2.9(b).

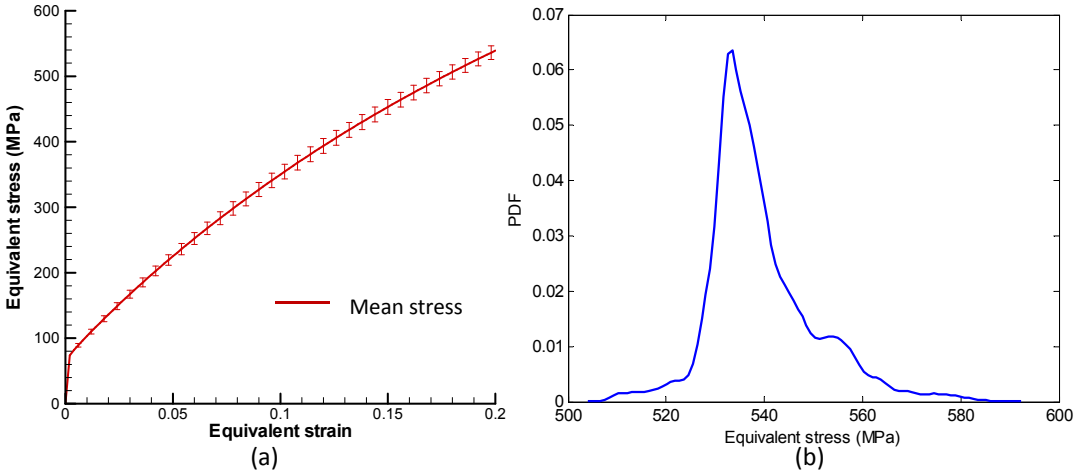

Figure 2.9: (a) Variation in stress-strain response due to uncertainty in grain size and initial texture. The random texture was generated from the deformation process defined in Eq. (2.25). The bars represent the standard deviation of the effective stress for the corresponding effective strain. (b) PDF of the final equivalent stress of the microstructures having the same mean size.

Example 2

In the second example, the initial texture samples are generated through a three-random-variable process, in which a homogeneous compression component is added to the previous two modes (Eq. (2.27)). After KLE, the lower-dimensional representation is cut off at $d_2 = 4$, where 91.8% energy is captured. The grain size samples are the same with Example 1, so that the final low-dimensional space is 7. We aim at investigating the initial texture uncertainty dependence of the mechanical response.

$$\mathbf{L} = \omega_1 \begin{bmatrix} 0.5 & 0 & 0 \\ 0 & 0.5 & 0 \\ 0 & 0 & -1 \end{bmatrix} + \omega_2 \begin{bmatrix} 0 & 0 & 0 \\ 0 & 1 & 0 \\ 0 & 0 & -1 \end{bmatrix} + \omega_3 \begin{bmatrix} 0 & -1 & 0 \\ 1 & 0 & 0 \\ 0 & 0 & 0 \end{bmatrix} \tag{2.27}$$

Following the similar procedure as in Example 1, 7146 nodes are adaptively generated for a level 8 sparse grid collocation. The mean stress was computed to be 540.148MPa and the standard deviation 13.304MPa. It comes to our notice that although the mean stress is almost the same as in the previous example, the standard deviation is increased, which means the variance of the equivalent stress is enlarged. The stress-strain curve variation and final stress distribution are collected and constructed in Fig. 2.10. From this figure, a wider distribution of the mechanical response is observed, which implies that the randomness of the mechanical response increased because of the additional randomness in texture.

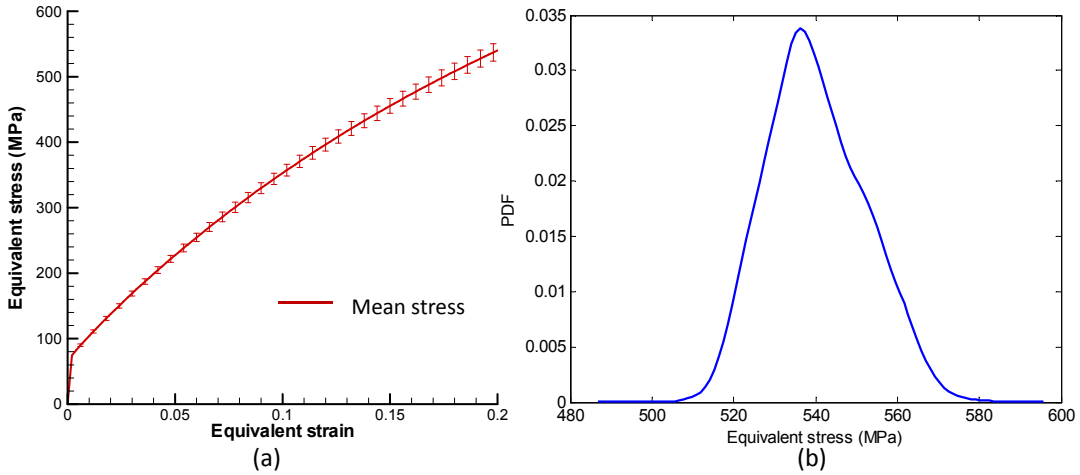

Figure 2.10: (a) Variation in stress-strain response due to the effect of uncertainty in grain size and initial texture. The random texture was generated from the deformation process defined in Eq. (2.27). The bars represent the standard deviation of effective stress for the corresponding effective strain. (b) PDF of the final equivalent stress of the microstructures having the same mean size.

Example 3

The first two examples demonstrated the mechanical response variability due to texture uncertainty. This example considers the grain size effect on mechanical properties. The mean grain volume is preserved at $0.0185mm^3$, whereas the second-order moment is set to be $3.704 \times 10^{-4}mm^6$. Compared with Example 1, where the second-order moment is various and mostly around $4.10 \times 10^{-4}mm^6$, the microstructures in this example have a narrow grain size distribution. Performing NLDR, the best fit dimensionality d_1 of the low-dimensional space is still 3.

We select the initial texture the same as in the first example that was generated from Eq. (2.25). Similar estimation process is conducted and the mechanical response is analyzed up to level 8 with 936 adaptively generated collocation

points. The mean final equivalent stress and standard deviation are 537.918MPa and 8.957MPa, respectively. In the stress-strain response variation (Fig. 2.11 (a)) and final stress distribution (Fig. 2.11 (b)), a sharper distribution is observed. The final stresses corresponding to narrow grain size distribution are more concentrated around the mean value.

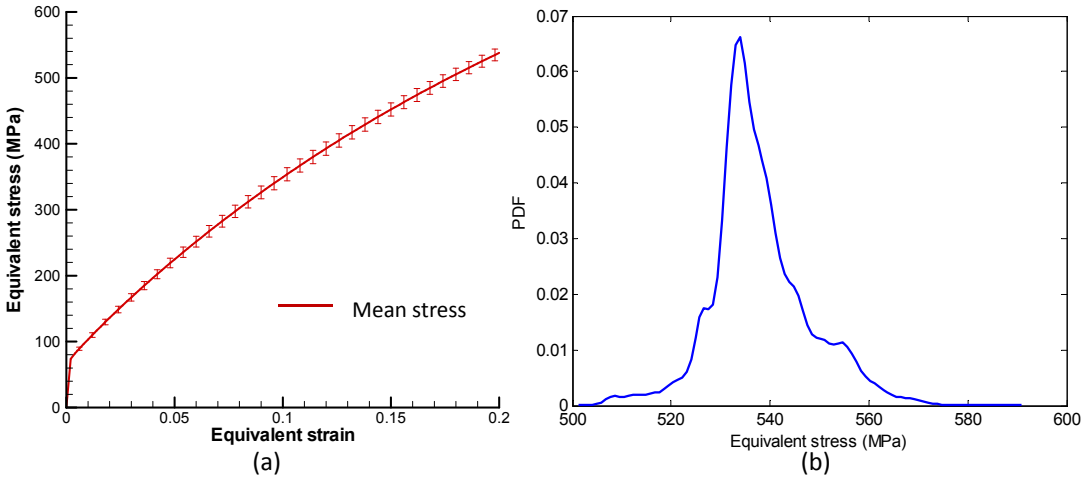

Figure 2.11: (a) Variation in stress-strain response due to the effect of uncertainty in grain size and initial texture. The input microstructures have fixed mean grain size and 2nd order grain size moment, whereas their texture is defined from the process in Eq. (2.25). The bars represent the standard deviation of effective stress for the corresponding effective strain. (b) PDF of the final equivalent stress of the microstructures.

Example 4

In this part, we constrain the grain size distribution of microstructure samples through 3 moments. Keeping the first two moments identical with those in Example 3, the third-order moment constraint is added with the value $8.637 \times 10^{-6} mm^9$. This value is larger than the average third-order moment ($7.86 \times 10^{-6} mm^9$) when only the first two moments are constrained. This variance

results that most grain sizes in a microstructure are close but smaller than the mean size, while a few grain sizes are much larger than the others. If the third-order moment is set to a higher value, the variation of the grain size will be quite small or even cannot be captured among the microstructure samples. The resulting microstructures tend to have the same grain size distribution. A comparison of sorted grain size vectors among three microstructure samples whose grain size distributions are constrained by different number of moments are demonstrated in Fig. 2.12. We can observe that the microstructure constrained by only the mean size tends to have almost evenly distributed grain sizes. Grain sizes of the one constrained by two moments are more concentrated around the mean size. In the case that three moments are constrained, most grain sizes are a little smaller than the mean size, while a couple of grains have unusual large values.

As more constraints are applied to the grain size distribution, the underlying correlation is increased. Performing NLDR on this set of sorted grain size vectors, we obtain the optimal dimensionality of the grain size feature to be 2. Combining the reduced grain size vectors with texture (the same as Example 1), the low dimensional space has only 4 dimensions. The governing stochastic equations for compression are solved through ASGC up to level 8 with 798 collocation points. The mean final equivalent stress is found to be $539.543MPa$ and the standard deviation is $8.974MPa$. The stress-strain curve variance and final stress distribution are plotted in Fig. 2.13. Although the variance is almost the same as in Example 3, the distribution of the final stress is more concentrated. A comparison between the final stress distribution of these three cases are shown in Fig. 2.14.

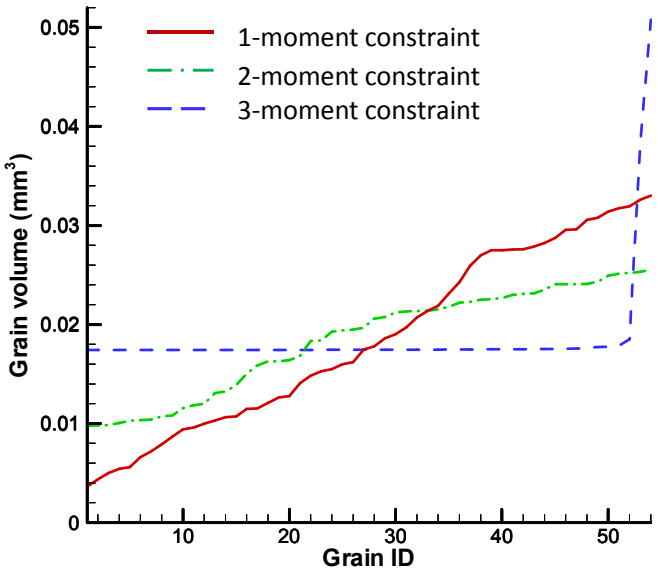

Figure 2.12: Three microstructure samples whose grain size distributions are constrained by different number of moments. The first case is constrained by mean volume $0.0185mm^3$; the second is constrained by the same mean volume and the second-order moment $3.704\times10^{-4}mm^6$; the last case is constrained by a third-order moment $8.637\times10^{-6}mm^9$ in addition to the first two moments.

Example 5

In the last example, the volume of the microstructure is reduced to $0.001mm^3$ (compared to previously $1mm^3$ domain). In this way, the mean effective diameter of grains is decreased to 1/10 of the first example. The volume of individual grains now distributed within $3.7\times10^{-6}mm^3$ to $3.33\times10^{-5}mm^3$ interval. Only the mean grain size is constrained. This example meant to study the microstructure mean grain size effect on the mechanical response distribution. The smaller the grain size, the higher the equivalent stress should be induced at the same strain.

Fig. 2.15 (a) shows the stress-strain curve variation. The mean value of the final stress is $580.996Mpa$ (raised by about $40MPa$) and the standard deviation is

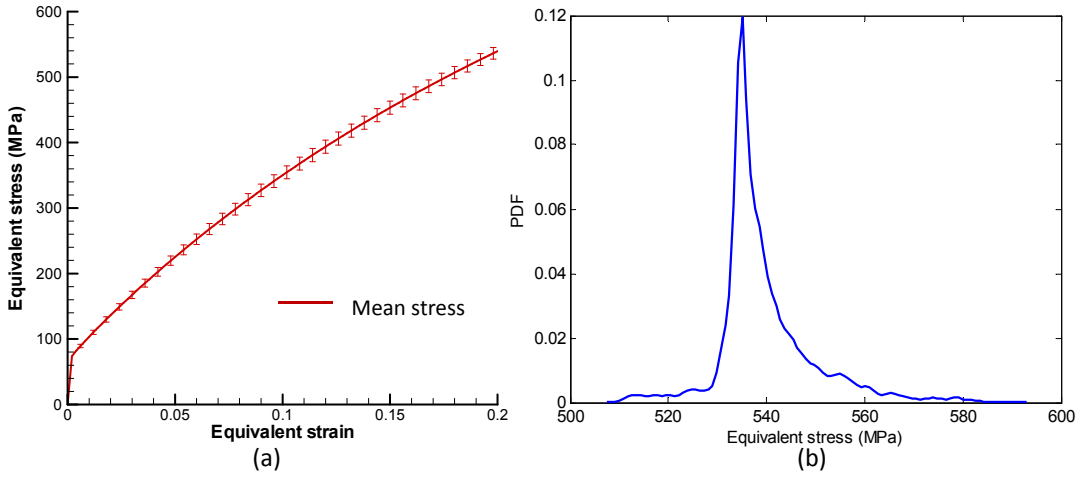

Figure 2.13: Case of microstructures having the same mean size, 2nd-order and 3rd-order moments. Variation in stress-strain response due to the effect of uncertainty in grain size and initial texture. The bars represent the standard deviation of effective stress for the corresponding effective strain. (b) PDF of the final equivalent stress.

10.634MPa (close to the standard deviation 10.471Mpa in Example 1). Fig. 2.15 (b) compares the final stress distributions of different mean grain size. Both cases have similar shape while the one with smaller grain size has higher mean value.

2.1.7 Conclusions

The effect of multiple sources of uncertainty on macroscopic mechanical response is studied. A microstructure was considered as a combination of random fields consisted of grain size and texture. Given a set of microstructure samples as the realization of this random field, dimensionality reduction techniques were applied to find their underlining correlations. A nonlinear model reduction based on Isomap was performed on grain size variables and Karhunen-

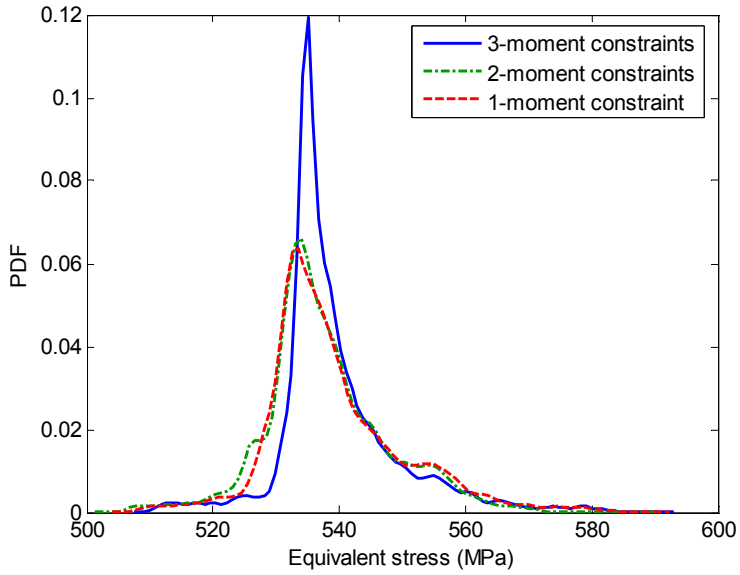

Figure 2.14: Final stress distribution of microstructures whose grain size distributions are constrained by different number of moments: mean grain volume $0.0185mm^3$ (dashed); mean grain volume $0.0185mm^3$ and second order moment $3.704 \times 10^{-4}mm^6$ (dash-dot); mean grain volume $0.0185mm^3$, second order moment $3.704 \times 10^{-4}mm^6$, and third order moment $8.637 \times 10^{-6}mm^9$(solid)

Loève Expansion was adopted to reduce the texture dimensionality. The dimensionality of the random field was successfully reduced from 216 to less than 7. Adaptive sparse grid collocation was then introduced to sample new microstructures from the low-dimensional space. The elasto-viscoplastic mechanical response of the microstructures satisfying given information was computed and its distribution is constructed. The effect of texture and grain size randomness is studied. It shows that the model reduction techniques greatly simplified the representation of random microstructure features, while the significant characters can be preserved. The propagation of uncertainty in microstructure evolution enables one to provide the prediction on macroscopic mechanical response. The distribution of final stress and stress-strain curve provide impor-

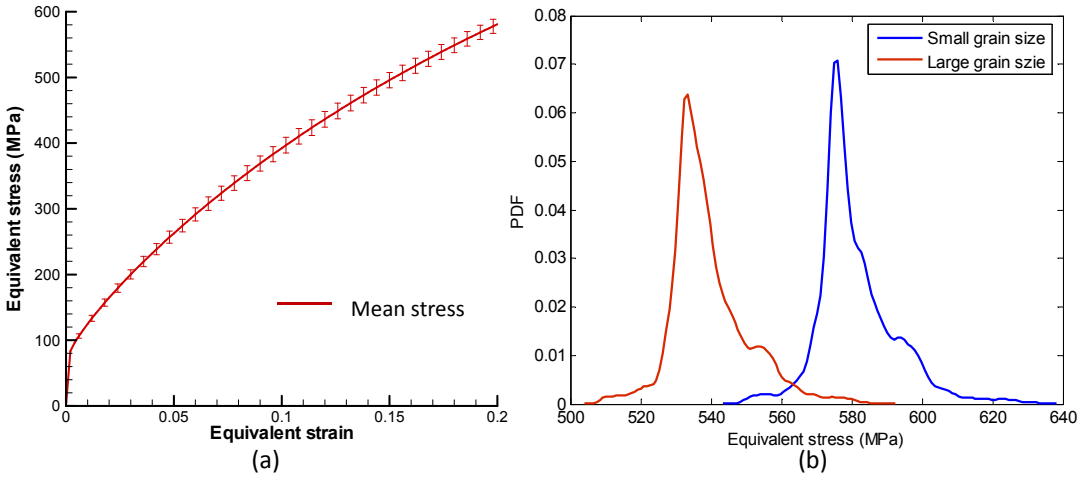

Figure 2.15: (a) Variation in stress-strain response due to the effect of uncertainty in grain size and initial texture. The mean grain size is $1.85 \times 10^{-5} mm^3$. The bars represent the standard deviation of the effective stress for the corresponding effective strain. (b) Final stress distribution of microstructures having different mean grain size.

tant guidance in material design and process, when certain grain size and texture information is known.

The sparse grid approach constructed an interpolant of the mechanical response in the stochastic space of grain size distribution and texture. This interpolant allows the user to compute with controllable interpolation error the response of any other microstructure in the class of the given microstructures. This cannot be possible with alternative approaches as for example when using the Maximum Entropy (MaxEnt) approach with the given data. In addition, modeling the texture uncertainty using MaxEnt is computationally an intractable task.

In this work, the mechanical response is analyzed using Taylor approach which provides fast but less accurate results. In Taylor model, the deformation of the microstructure is constrained to be identical. It leads to an overestimation

on the mechanical response. Development of more accurate full-field crystal plasticity solvers will be introduced later in the thesis.

2.2 Investigating variability of fatigue indicator parameters of two-phase nickel-based superalloy microstructures

2.2.1 Construction of microstructure stochastic input model

Microstructure representation

Features of two-phase polycrystals include topology, crystallographic texture, and volume fraction of each phase. The microstructure topology is defined in terms of grain shape and grain size [119]. For a polycrystalline alloy microstructure, its material properties are mostly determined by these three features. Following the same idea as in Section 2.1, these features are considered as random variables in order to model microstructure uncertainty. Appropriate mathematical descriptions of them are needed. A low-dimensional representation of the microstructure will be used as the stochastic surrogate input model to allow an efficient computation of the variability of the microstructure properties.

The two-phase grain structure is modeled in a homogenized sense in this work. As a result, no γ' particles are explicitly modeled. Each constituent grain of the microstructure is considered as a homogenized single crystal which takes the effective properties of both phases. A schematic of an explicit ($\gamma + \gamma'$) structure of a grain and its equivalent homogenized model is demonstrated in

Fig. 2.16. The effect of the second phase on material properties can be taken into account by introducing particular parameters in the constitutive model, which will be discussed in Section 2.2.4.

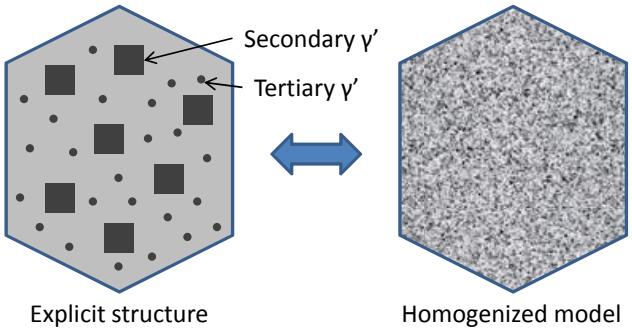

Figure 2.16: Explicit structure of a (γ+γ') grain and its equivalent homogenized model. The gray background on the left grain represents γ matrix, while secondary and tertiary γ' precipitates are depicted as dark particles.

Statistical volume elements (SVEs) of polycrystalline alloy microstructures are represented as aggregates of discrete grains associated with specific orientations and phases (see Fig. 2.17(a)). As we implicitly model the two-phase material in a homogenized sense, each grain in the microstructure is effectively the combination of γ matrix and γ' precipitates aligning in the same orientation. An array containing both sizes and orientations of finite number of grains can be adopted as the descriptor of the microstructure (Fig. 2.17(b)). For a microstructure composed of M grains, the first M components of the feature array are sizes of homogenized grains sorted in ascending order and the rest $3M$ components are the corresponding orientations described by Rodrigues parameters [25], as defined in Eq.(2.3). We will study the effects of each feature separately and determine the one that dominates fatigue properties of superalloy microstructures.

We are given a set of correlated microstructure realizations. In superalloy microstructures resulting from certain (e.g. deformation) process, the grain sizes,

grain orientations (texture) and volume fraction of the γ phase satisfy certain (statistical) constraints. For grain size, the constraints are usually in the form of low-order statistical moments (Section 2.1). The lognormal distribution is often used for describing polycrystalline Ni-based superalloy grain sizes [109]. The γ' phase disperses in the γ phase matrix as precipitates described by their size and volume fraction. Three types of γ', primary, secondary, and tertiary, are usually observed according to their size and other attributes. In the homogenized two-phase superalloy constitutive model, one needs in general to account for the γ'-phase uncertainty in addition to the grain size and orientation variation. The effect of microstructure features on fatigue properties can be studied using the deterministic material point simulator for different microstructure realizations.

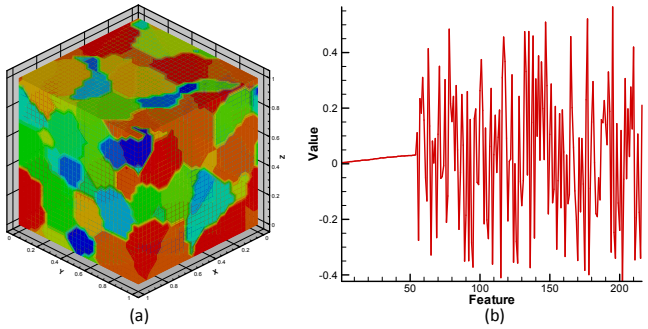

Figure 2.17: (a) A 3D polycrystalline microstructure with 54 grains. (b) The descriptor of the microstructure. The first 54 components are the sizes of grains, and the last 162 components are Rodrigues parameters representing grain orientations.

Principal component analysis based model reduction

Following the idea in Section 2.1, model reduction techniques are introduced exploring the correlation among the data to construct a low-dimensional surrogate representation of the original microstructure space in order to facilitate the stochastic simulation. The samples from this surrogate space need to be

mapped to the original space for this technique to be practical. Uncertainty quantification of the microstructure properties driven by the given microstructure realizations then becomes feasible.

In this work, we introduce PCA/KPCA for model reduction of the homogenized superalloy polycrystalline microstructure. The microstructures are described by the size and orientation attributes of all constituent grains. A set of grain size and orientation samples generated by simulation are given as the initial input. It is assumed that they are obtained through certain random deformation processes and therefore satisfy some statistical constraints. We fix the number of grains to be 54 and the total volume of the microstructure to be $10^{-3}mm^3$. Therefore, the mean grain size is fixed. The initial grain size samples are generated according to a lognormal distribution and the orientations are generated from a sequence of random deformation processes that will be introduced in Section 2.2.5. After that, we will perform model reduction solely on the sample data assuming that no other information is known (no information about what distribution the grain size follows and what are the random variables controlling the process to generate random textures). The algorithm of PCA/KPCA is summarized below. More details of the mathematical formulation can be found in [107, 80, 59]. The notation follows the paper [130].

Define a complete probability space $(\Omega, \mathcal{F}, \mathcal{P})$ with sample space Ω, which corresponds to all microstructures resulted from certain random process, $\mathcal{F} \subset 2^{\Omega}$ is the σ-algebra of subsets in Ω and $\mathcal{P} : \mathcal{F} \to [0, 1]$ is the probability measure. Each sample $\omega \in \Omega$ is a continuum field representing a microstructure that can be described by a discretized representation, $\mathbf{y} = (y_1, \ldots, y_M)^T : \Omega \to \mathbb{R}^M$. M can be regarded as the number of features in a microstructure. So each $y_i, i = 1, \ldots, M$

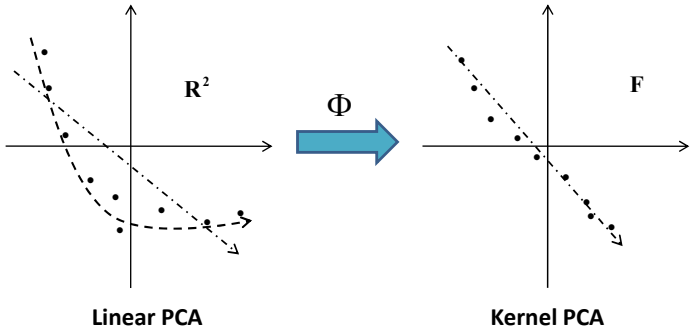

Figure 2.18: Basic idea of KPCA. Left: In this non-Gaussian case, the linear PCA cannot effectively capture the nonlinear relationship among the realizations in the original space. Right: After the nonlinear mapping Φ, realizations become linearly related in the feature space F. Linear PCA can now be performed in F.

is a random variable. The dimensionality of the stochastic input is then the length of the vector $\mathbf{y}$. Any microstructure-sensitive property $\mathcal{A}$ is a function of the microstructure features: $\mathcal{A} = \mathcal{A}(\mathbf{y})$. Therefore, $\mathcal{A}$ is also random. To investigate the variability of $\mathcal{A}$ for microstructures in Ω, we need to be able to compute properties of any sample in Ω. However, only a finite number of realizations $\{\mathbf{y}_1, \ldots, \mathbf{y}_N\}$ of Ω are available. How to explore the space Ω based on a finite number of given microstructure realizations (input data) becomes essential.

The dimensionality of the input, M, is often large. We need to find a reduced order representation of the random field that is consistent with the given data in some statistical sense. To be specific, we want to find a form $\mathbf{y} = f(\boldsymbol{\xi})$, where $\boldsymbol{\xi}$, of dimension much smaller than the original input stochastic dimension M, are a set of independent random variables with a specific distribution. Therefore, by drawing samples $\boldsymbol{\xi}$, we can obtain realizations of the underlying random field, namely, full feature descriptions of microstructures. $KPCA/PCA$ is used for this purpose.

Given N realizations $\{\mathbf{y}_1, \ldots, \mathbf{y}_N\}$ of a random field $\mathcal{Y}(\omega)$, where each realization is represented as a M-dimensional vector $\mathbf{y}_i \in \mathbb{R}^M$ (e.g. $\mathbf{y}_i$ is a feature realization representing a microstructure by grain size and/or texture), we can map them into a "feature" space $\mathbf{Y}_i = \Phi(\mathbf{y}_i),\ i = 1, \ldots, N$. Notice that this "feature" space is in the context of KPCA terminology and different from the microstructure feature input. We will refer the initial microstructure feature input space as the physical space. If $\Phi(\mathbf{y}) = \mathbf{y}$, KPCA is identical to linear PCA. The centered map $\tilde{\Phi}$ is:

$$\tilde{\Phi} = \Phi(\mathbf{y}) - \bar{\Phi}, \tag{2.28}$$

where $\bar{\Phi} = \frac{1}{N}\sum_{i=1}^{N} \Phi(\mathbf{y}_i)$ is the mean of the Φ-mapped data. The covariance matrix $\mathbf{C}$ in the F space is then

$$\mathbf{C} = \frac{1}{N}\sum_{i=1}^{N} \tilde{\Phi}(\mathbf{y}_i)\tilde{\Phi}^T(\mathbf{y}_i). \tag{2.29}$$

The dimension of this matrix is $N_F \times N_F$, where N_F is the dimension of the "feature" space.

A kernel eigenvalue problem is formulated which uses only dot products of vectors in the "feature" space. We first substitute the covariance matrix into the l.h.s. of the eigenvalue problem

$$\mathbf{CV} = \lambda\mathbf{V}, \tag{2.30}$$

to obtain

$$\mathbf{CV} = \frac{1}{N}\sum_{i=1}^{N} \left(\tilde{\Phi}(\mathbf{y}_i) \cdot \mathbf{V}\right) \tilde{\Phi}(\mathbf{y}_i), \tag{2.31}$$

which implies that all solutions $\mathbf{V}$ with $\lambda \neq 0$ lie in the span of $\tilde{\Phi}(\mathbf{y}_1), \ldots, \tilde{\Phi}(\mathbf{y}_N)$. Projecting $\mathbf{V}$ onto sample realizations

$$\mathbf{V} = \sum_{j=1}^{N} \alpha_j \tilde{\Phi}(\mathbf{y}_j), \tag{2.32}$$

and multiplying Eq. (2.30) with $\tilde{\Phi}(\mathbf{y}_i)$ from the left, we obtain

$$\frac{1}{N}\sum_{j=1}^{N}\alpha_j\sum_{k=1}^{N}\Big(\tilde{\Phi}(\mathbf{y}_i)\cdot\tilde{\Phi}(\mathbf{y}_k)\Big)\Big(\tilde{\Phi}(\mathbf{y}_k)\cdot\tilde{\Phi}(\mathbf{y}_j)\Big)=\lambda\sum_{j=1}^{N}\alpha_j\Big(\tilde{\Phi}(\mathbf{y}_i)\cdot\tilde{\Phi}(\mathbf{y}_j)\Big), \tag{2.33}$$

for $i = 1,\ldots,N$. Note here that the vector $\boldsymbol{\alpha}$ is not normalized. Defining the $N\times N$ kernel matrix $\mathbf{K}$ as the dot product of vectors in the "feature" space F:

$$\mathbf{K}: K_{ij}=\Big(\Phi(\mathbf{y}_i)\cdot\Phi(\mathbf{y}_j)\Big), \tag{2.34}$$

the corresponding centered kernel matrix is then:

$$\tilde{\mathbf{K}}=\Big(\tilde{\Phi}(\mathbf{y}_i)\cdot\tilde{\Phi}(\mathbf{y}_j)\Big)=\mathbf{HKH}. \tag{2.35}$$

In the centering matrix $\mathbf{H} = \mathbf{I} - \frac{1}{N}\mathbf{1}\mathbf{1}^T$, $\mathbf{I}$ is the $N \times N$ identity matrix and $\mathbf{1} = [11\ldots1]^T$ is a $N \times 1$ vector. Substituting Eqs. (2.34) and (2.35) into Eq. (2.33), we arrive at the following kernel eigenvalue problem:

$$N\lambda\boldsymbol{\alpha}=\tilde{\mathbf{K}}\boldsymbol{\alpha}, \tag{2.36}$$

where $\boldsymbol{\alpha} = [\alpha_1,\ldots,\alpha_N]^T$. In the following, for simplicity, we will denote λ_i as the eigenvalues of $\tilde{\mathbf{K}}$, i.e. the solutions $N\lambda_i$ in Eq. (2.36). We rewrite Eq. (2.36) in the following matrix form:

$$\tilde{\mathbf{K}}\mathbf{U}=\boldsymbol{\Lambda}\mathbf{U}, \tag{2.37}$$

where, $\boldsymbol{\Lambda} = \mathrm{diag}(\lambda_1,\ldots,\lambda_\mathrm{N})$ and $\mathbf{U} = [\boldsymbol{\alpha}_1,\ldots,\boldsymbol{\alpha}_N]$ is the matrix containing the eigenvectors of the kernel matrix $\tilde{\mathbf{K}}$, where column i is the ith eigenvector $\boldsymbol{\alpha}_i = [\alpha_{i1},\ldots,\alpha_{iN}]^T$.

Therefore, through Eq. (2.32), the ith eigenvector of the covariance matrix $\mathbf{C}$ in the feature space can be shown to be [107, 59]

$$\mathbf{V}_i=\sum_{j=1}^{N}\alpha_{ij}\tilde{\Phi}(\mathbf{y}_j). \tag{2.38}$$

Furthermore, the eigenvector $\mathbf{V}_i$ can be normalized. Since the eigenvectors $\boldsymbol{\alpha}_i$ from the eigenvalue problem Eq. (2.37) are already normalized, the ith orthonormal eigenvector of the covariance matrix $\mathbf{C}$ can be shown to be [107, 59]

$$\tilde{\mathbf{V}}_i = \sum_{j=1}^{N} \tilde{\alpha}_{ij} \tilde{\Phi}(\mathbf{y}_j), \text{ where } \tilde{\alpha}_{ij} = \frac{\alpha_{ij}}{\sqrt{\lambda_i}}. \tag{2.39}$$

Let $\mathbf{y}$ be a realization of the random field, with a mapping $\Phi(\mathbf{y})$ in F. According to the theory of linear PCA, $\Phi(\mathbf{y})$ can be decomposed in the following way:

$$\Phi(\mathbf{y}) = \sum_{i=1}^{N} z_i \tilde{\mathbf{V}}_i + \bar{\Phi}, \tag{2.40}$$

where z_i is the projection coefficient onto the ith eigenvector $\tilde{\mathbf{V}}_i$:

$$z_i = \tilde{\mathbf{V}}_i \cdot \tilde{\Phi}(\mathbf{y}) = \sum_{j=1}^{N} \tilde{\alpha}_{ij} \left(\tilde{\Phi}(\mathbf{y}) \cdot \tilde{\Phi}(\mathbf{y}_j) \right). \tag{2.41}$$

From Eq. (2.34), it is seen that in order to compute the kernel matrix, only the dot products of vectors in the feature space F are required, while the explicit calculation of the map $\Phi(\mathbf{y})$ does not need to be known. As shown in [107], the dot product can be computed through the use of the kernel function. This is the so called "kernel trick". The kernel function $k(\mathbf{y}_i, \mathbf{y}_j)$ calculates the dot product in space F directly from the vectors of the input space $\mathbb{R}^M$:

$$k(\mathbf{y}_i, \mathbf{y}_j) = \left(\Phi(\mathbf{y}_i) \cdot \Phi(\mathbf{y}_j) \right). \tag{2.42}$$

The commonly used kernel functions are polynomial kernel and Gaussian kernel.

We can write all the z_i in a vector form $\mathbf{Z} := [z_1, \ldots, z_N]^T$:

$$\mathbf{Z} = \mathbf{A}^T \mathbf{k}_{\mathbf{y}} + \mathbf{b}, \tag{2.43}$$

where $\mathbf{A} = \mathbf{H}\tilde{\mathbf{U}}$, $\mathbf{b} = -\frac{1}{N}\tilde{\mathbf{U}}^T\mathbf{H}\mathbf{K}\mathbf{1}$ and $\tilde{\mathbf{U}} = [\tilde{\boldsymbol{\alpha}}_1, \ldots, \tilde{\boldsymbol{\alpha}}_N]$ with $\tilde{\boldsymbol{\alpha}}_i := [\tilde{\alpha}_{i1}, \ldots, \tilde{\alpha}_{iN}]^T$ and

$$\mathbf{k}_\mathbf{y} = [k(\mathbf{y}, \mathbf{y}_1), \ldots, k(\mathbf{y}, \mathbf{y}_N)]^T. \tag{2.44}$$

Suppose the eigenvectors are ordered by decreasing eigenvalues and we only work in the low-dimensional subspace which is spanned by the first r eigenvectors. Then the decomposition in Eq. (2.40) can be truncated after the first r terms:

$$\Phi(\mathbf{y}) \approx \sum_{i=1}^{r} z_i \mathbf{V}_i + \bar{\Phi} = \sum_{i=1}^{N} \beta_i \Phi(\mathbf{y}_i), \tag{2.45}$$

where $\boldsymbol{\beta} = \mathbf{A}_r\mathbf{Z}_r + \frac{1}{N}\mathbf{1}$ and β_i is its ith component. Since only the first r eigenvectors are used, $\tilde{\mathbf{U}}_r = [\tilde{\boldsymbol{\alpha}}_1, \ldots, \tilde{\boldsymbol{\alpha}}_r]$. $\mathbf{A}_r = \mathbf{H}\tilde{\mathbf{U}}_r$ is a matrix of size $N \times r$ and $\mathbf{Z}_r = [z_1, \ldots, z_r]^T$ is a r-dimensional column vector. Details on the derivations of these equations can be found in [80].

Thus, given N samples from the original stochastic feature space F, we can find an approximate r-dimensional subspace $\tilde{F}$ of F which is spanned by the orthonormal basis $\tilde{\mathbf{V}}_i, i = 1, \ldots, r$. Similar to K-L expansion, the expansion coefficients $\mathbf{Z}_r$ are a r-dimensional random vector that defines this subspace. By drawing samples of $\mathbf{Z}_r$ from it, we can obtain different realizations of $\Phi(\mathbf{y})$ through Eq. (2.45). The stochastic reduced-order input model in the "feature" space can be defined as: for any realization $\mathbf{Y} \in \tilde{F}$, we have

$$\mathbf{Y}_r = \sum_{i=1}^{N} \beta_i \Phi(\mathbf{y}_i) = \boldsymbol{\Phi}\boldsymbol{\beta}, \text{ with } \boldsymbol{\beta} = \mathbf{A}\boldsymbol{\xi} + \frac{1}{N}\mathbf{1}. \tag{2.46}$$

Here, $\boldsymbol{\Phi} = [\Phi(\boldsymbol{y}_1), \ldots, \Phi(\boldsymbol{y}_N)]$ is a matrix of size $N_F \times N$. The subscript r emphasizes that the realization $\mathbf{Y}_r$ is reconstructed using only the first r eigenvectors. $\boldsymbol{\xi} := [\xi_i, \ldots, \xi_r]^T$ is a r-dimensional random vector. If the probability distribution

of $\boldsymbol{\xi}$ is known, we can then sample $\boldsymbol{\xi}$ and obtain samples of the random filed in $\tilde{F}$.

However, the probability distribution of ξ_i is not known to us. What we know is only the realizations of these random coefficients ξ_i, which can be obtained through Eq. (2.43) by using the available samples:

$$\boldsymbol{\xi}^{(i)} = \mathbf{A}^T \mathbf{k}_{\mathbf{y}_i} + \mathbf{b}, \quad i = 1, \ldots, N. \tag{2.47}$$

Our problem then reduces to identify the probability distribution of the random vector $\boldsymbol{\xi} := [\xi_i, \ldots, \xi_r]^T$, given its N samples $\boldsymbol{\xi}^{(i)} = [\xi_1^{(i)}, \ldots, \xi_r^{(i)}]$, $i = 1, \ldots, N$. A polynomial chaos representation is introduced in the next subsection for representing each component of the random vector $\boldsymbol{\xi}$ in terms of another random vector with known distribution.

Finally, according to the properties of the K-L expansion [77, 30, 113] used in the "feature" space, the random vector $\boldsymbol{\xi}$ satisfies the following two conditions:

$$E[\xi_i] = 0, \quad E[\xi_i \xi_j] = \delta_{ij} \frac{\lambda_i}{N}, \quad i, j = 1, \ldots, r. \tag{2.48}$$

Therefore, the random coefficients ξ_i are uncorrelated but not independent.

By sampling $\boldsymbol{\xi}$, we can reconstruct high-dimensional Φ-mapped features in F space. By applying an appropriate "pre-image" scheme [59], realizations in the original physical space (namely, microstructures) can be obtained. A weighted K-nearest neighbor (KNN) pre-imaging algorithm has been designed in [29, 80] and will be adopted in this work (Section 2.2.3) for KPCA microstructure reconstruction, while for PCA, the pre-imaging is directly performed through Eq. (2.46) as $\Phi(\mathbf{y}) = \mathbf{y}$.

In practice, the form of map $\Phi(\mathbf{y})$ is not known nor required. Only the kernel

function (dot product in the F space) $k(\mathbf{y}_i, \mathbf{y}_j)$ is needed. For linear PCA, the kernel function is simply the dot product in the input space (1st order polynomial)

$$k(\mathbf{y}_i, \mathbf{y}_j) = (\mathbf{y}_i \cdot \mathbf{y}_j), \tag{2.49}$$

implying that $\Phi(\mathbf{y}) = \mathbf{y}$; and for KPCA, various kernels may be chosen. A commonly selected one is the Gaussian kernel (or radial basis function (RBF)):

$$k(\mathbf{y}_i, \mathbf{y}_j) = \exp\left(-\frac{\|\mathbf{y}_i - \mathbf{y}_j\|^2)}{2\sigma^2}\right), \tag{2.50}$$

where $\|\mathbf{y}_i - \mathbf{y}_j\|^2$ is the squared L_2-distance between two realizations. The kernel width parameter σ is computed using the average minimum distance between two realizations in the input space [101]:

$$\sigma^2 = c\frac{1}{N}\sum_{i=1}^{N} \min_{j\neq i}\|\mathbf{y}_i - \mathbf{y}_j\|^2, \quad j = 1, \ldots, N, \tag{2.51}$$

where c is a user-controlled parameter.

2.2.2 Polynomial chaos expansion of stochastic reduced-order model

As explained in the last subsection, we need to draw samples $\boldsymbol{\xi}$ from the reduced space and reconstruct microstructure realizations in order to investigate material property variability of microstructures. To this end, the reduced surrogate space needs to be constructed and mapped to an appropriate distribution in which sampling is convenient. In Section 2.1, Maximum Entropy estimation is used. In this section, we adopt polynomial chaos expansion (PCE) [30, 132, 133] to represent $\boldsymbol{\xi}$ as a function of Gaussian or uniform random variables $\boldsymbol{\eta}$. The

components of $\boldsymbol{\xi}$ are uncorrelated but not necessarily independent. Although Rosenblatt transformation [102] can be used to decompose the problem to a set of independent random variables, this is computationally expensive for high-dimensional problems. Currently, we assume the independence between the components of $\boldsymbol{\xi}$. It has been shown in various applications [113, 31] that this assumption gives rather accurate results.

Following the independence assumption of ξ_i, each of them can be expanded on to an one-dimensional polynomial chaos (PC) basis of degree p:

$$\xi_i = \sum_{j=0}^{p} \gamma_{ij} \Psi_j(\eta_i), \quad i = 1, \ldots, r, \tag{2.52}$$

where the η_i are i.i.d. random variables. The random basis functions $\{\Psi_j\}$ are chosen according to the type of random variable $\{\eta_i\}$ that has been used to describe the random input. For example, if Gaussian random variables are chosen then the Askey based orthogonal polynomials $\{\Psi_j\}$ are chosen to be Hermite polynomials; if η_i are chosen to be uniform random variables, then $\{\Psi_j\}$ must be Legendre polynomials [132].

Gaussian-Hermite and uniform-Legendre formats will be considered for the reconstruction of reduced-order random variables (see Section 2.2.5). The PC coefficients are computed as

$$\gamma_{ij} = \frac{E\left[\xi_i \Psi_j(\eta_i)\right]}{E\left[\Psi_j^2(\eta_i)\right]}. \tag{2.53}$$

If Gaussian-Hermite chaos is chosen, Eq. (2.53) can be expressed as

$$\gamma_{ij} = \frac{1}{\sqrt{2\pi}\, j!} \int_{-\infty}^{+\infty} \xi_i \Psi_j(\eta_i) e^{-\frac{\eta_i^2}{2}} d\eta_i, \quad i = 1, \ldots, r, \quad j = 0, \ldots, p. \tag{2.54}$$

If Uniform-Legendre is chosen, Eq. (2.53) becomes

$$\gamma_{ij} = \frac{2j+1}{2} \int_{-1}^{1} \xi_i \Psi_j(\eta_i) d\eta_i, \quad i = 1, \ldots, r, \quad j = 0, \ldots, p. \tag{2.55}$$

A proper method is needed to evaluate these integrals. However, it is noted that the random variable ξ does not belong to the same stochastic space as η, and we only have a number of N realizations of ξ. The distribution of ξ is invisible. A non-linear mapping $\Gamma : \eta \rightarrow \xi$ is thus needed which preserves the probabilities such that $\Gamma(\eta)$ and ξ have the same distributions. A non-intrusive projection based on empirical cumulative distribution functions (CDFs) of samples developed in [113] is utilized to build the map. The integral in Eq. (2.53) is then computed using Gauss quadrature.

The non-linear mapping $\Gamma : \eta \rightarrow \xi$ can be defined as shown below for each ξ_i:

$$\xi_i \overset{d}{=} \Gamma_i(\eta_i), \quad \Gamma_i \equiv F_{\xi_i}^{-1} \circ F_{\eta_i}, \tag{2.56}$$

where F_{ξ_i} and F_{η_i} denote the CDFs of ξ_i and η_i, respectively. Here, the equalities, "$\overset{d}{=}$" is interpreted in the sense of distribution such that the probability density functions (PDFs) of random variables on both sides are equal. The marginal CDF of the samples ξ_i can be evaluated numerically from the available data. Kernel density estimation is used to construct the empirical CDF of ξ_i. Let $\{\xi_i^{(s)}\}_{s=1}^N$ be N samples of ξ_i obtained from Eq. (2.41). The marginal PDF of ξ_i is then:

$$p_{\xi_i}(\xi_i) \approx \frac{1}{N} \sum_{s=1}^{N} \frac{1}{\sqrt{2\pi}\tau} \exp\left(-\frac{\xi_i - \xi_i^{(s)}}{2\tau^2} \right). \tag{2.57}$$

The marginal CDF of ξ_i is obtained by integrating Eq. (2.57) and the inverse CDF can be computed. Having the map Γ_i, the coefficients γ_{ij} are subsequently computed via Gauss quadrature.

After mapping the reduced space to Gaussian or uniform distribution, Monte Carlo or adaptive sparse grid collocation (ASGC) can be used to sample new realizations. Since the sampling space of ASGC is a unit hypercube

$[0,1]^h$, we need to further map the independent Gaussian ($\mathcal{N}(0,1)$) or uniform ($\mathcal{U}(-1,1)$) variables to the hypercube based on CDF.

$$\eta_i = \Upsilon_i(\nu_i), \Upsilon_i = F_{\eta_i}^{-1}, i = 1, \ldots, r, \tag{2.58}$$

where $\nu_i \sim \mathcal{U}(0,1)$ is the sample space of the i-th component of ASGC, F_{η_i} is the CDF of η_i.

2.2.3 The pre-image problem in KPCA

The sampled random variables after reconstruction (Eq. (2.52)) are reduced-order representations. For linear PCA, the recovery of a microstructure is straightforward using Eq. (2.46), since $\mathbf{Y} = \Phi(\mathbf{y}) = \mathbf{y}$. For KPCA, the reconstructed reduced-order representations are in the "feature" space F. Through Eq. (2.46), we can find the high-dimensional representations, but still, in the "feature" space ($\Phi(\mathbf{y}) \neq \mathbf{y}$). However, what we need are the realizations in the physical input space $\mathbb{R}^M$, which requires the inverse mapping $\mathbf{y} = \Phi^{-1}(\mathbf{X})$. Recall that in order to construct the eigenvalue problem in the feature space, the mapping $\mathbf{Y} = \Phi(\mathbf{y})$ is not necessary as long as the kernel function is provided. Therefore, the inverse mapping needs to be constructed approximately. This inverse mapping problem is known as the "pre-imaging" problem. For each realization $\mathbf{Y}$ in the "feature space', it provides an approximation of the corresponding realization in the physical input space, i.e. $\hat{\mathbf{y}} \approx \Phi^{-1}(\mathbf{Y})$.

A weighted K-nearest neighbor scheme is adopted for finding the pre-images. The basic idea is that for an arbitrary realization $\mathbf{Y}$ in F, we can first compute its distances $\tilde{d}_i, i = 1, \ldots, K$ to the K-nearest neighbors $\mathbf{Y}_i, i = 1, \ldots, K$

in F. Then the distances $d_i, i = 1, \ldots, K$ between its counterpart $\hat{\mathbf{y}}$ and K-nearest neighbors, $\mathbf{y}_i, i = 1, \ldots, K$, in the physical space are recovered. The pre-image $\hat{\mathbf{y}}$ is then computed by

$$\hat{\mathbf{y}} = \frac{\sum_{i=1}^{K} \frac{1}{d_i} \mathbf{y}_i}{\sum_{i=1}^{K} \frac{1}{d_i}}. \tag{2.59}$$

The distance between $\mathbf{Y}$ and $\Phi(\mathbf{y}_i)$ in the feature space is defined as

$$\begin{aligned} \tilde{d}_i^2(\mathbf{Y}, \Phi(\mathbf{y}_i)) &:= \|\mathbf{Y} - \Phi(\mathbf{y}_i)\|^2 \\ &= \|\mathbf{Y}\|^2 + \|\Phi(\mathbf{y}_i)\|^2 - 2\mathbf{Y}_r^T \Phi(\mathbf{y}_i), \end{aligned} \tag{2.60}$$

for $i = 1, \ldots, N$. Recall that for Gaussian kernel, $k(\mathbf{y}_i, \mathbf{y}_i) = 1$ and $\mathbf{Y} = \sum_{i=1}^{N} \beta_i \Phi(\mathbf{y}_i)$. N is the total number of the given data (microstructure realizations). Then each feature distance $\tilde{d}_i^2 (\mathbf{Y}, \Phi(\mathbf{y}_i)), i = 1, \ldots, N$ can be computed in the following matrix form [80] :

$$\tilde{d}_i^2 = 1 + \boldsymbol{\beta}^T \mathbf{K} \boldsymbol{\beta} - 2\boldsymbol{\beta}^T \mathbf{k}_{\mathbf{y}_i}, \tag{2.61}$$

for $i = 1, \ldots, N$.

Denote the vector $\tilde{\mathbf{d}}^2 = [\tilde{d}_1^2, \ldots, \tilde{d}_N^2]^T$ and we can sort this vector in ascending order to identify the K-nearest neighbors of $\mathbf{Y}$ from $\Phi(\tilde{\mathbf{y}}_i), i = 1, \ldots, n$.

On the other hand, the squared feature distance between the Φ-map of the pre-image $\hat{\mathbf{y}}$ and $\Phi(\mathbf{y}_i)$ is given as:

$$\begin{aligned} \hat{d}_i^2 (\Phi(\hat{\mathbf{y}}), \Phi(\mathbf{y}_i)) &= \|\Phi(\hat{\mathbf{y}}) - \Phi(\mathbf{y}_i)\|^2 \\ &= k(\hat{\mathbf{y}}, \hat{\mathbf{y}}) + k(\mathbf{y}_i, \mathbf{y}_i) - 2k(\hat{\mathbf{y}}, \mathbf{y}_j) \\ &= 2\left(1 - k(\hat{\mathbf{y}}, \mathbf{y}_i)\right), \end{aligned} \tag{2.62}$$

for $i = 1, \ldots, N$. Note that in the derivation above, we used that $k(\hat{\mathbf{y}}, \hat{\mathbf{y}}) =$

$k(\mathbf{y}_i, \mathbf{y}_i) = 1$ for a Gaussian kernel. Furthermore, the squared input-space distance can be computed from the following equation:

$$k(\hat{\mathbf{y}}, \mathbf{y}_i) = \exp\left(-\frac{\|\hat{\mathbf{y}} - \mathbf{y}_i\|^2}{2\sigma^2}\right), \tag{2.63}$$

from which we obtain

$$d_i^2 = \|\hat{\mathbf{y}} - \mathbf{y}_i\|^2 = -2\sigma^2 \log(k(\hat{\mathbf{y}}, \mathbf{y}_i)), \tag{2.64}$$

for $i = 1, \ldots, N$. Substituting the expression of $k(\hat{\mathbf{y}}, \mathbf{y}_j)$ from Eq. (2.62) into Eq. (2.64), one arrives at

$$d_i^2 = \|\hat{\mathbf{y}} - \mathbf{y}_i\|^2 = -2\sigma^2 \log(1 - 0.5\hat{d}_i^2), \tag{2.65}$$

for $i = 1, \ldots, N$. Because we try to find an approximate pre-image such that $\Phi(\hat{\mathbf{y}}) \approx \mathbf{Y}$, it is straightforward to identify the relationship $\tilde{d}_i^2 \approx \hat{d}_i^2$. Therefore, the squared input-distance between the approximate pre-image $\hat{\mathbf{y}}$ and the ith input data realization can be computed by:

$$d_i^2 = \|\hat{\mathbf{y}} - \mathbf{y}_i\|^2 = -2\sigma^2 \log(1 - 0.5\tilde{d}_i^2), \tag{2.66}$$

for $i = 1, \ldots, N$ and where $\tilde{d}_i^2$ is given by Eq. (2.61).

Finally, the pre-image $\hat{\mathbf{y}}$ for a feature space realization $\mathbf{Y}$ is given by Eq. (2.59). It is noted that here we use the K-nearest neighbors in the "feature" space. However, they are the same as the K-nearest neighbors in the input space, since Eq. (2.66) is monotonically increasing. Therefore, the pre-image $\hat{\mathbf{y}}$ of an arbitrary realization in the "feature" space is the weighted sum of the pre-images of the K-nearest neighbors of $\mathbf{Y}$ in the "feature" space, where the nearest neighbors are taken from the samples $\mathbf{y}_i, i = 1, \ldots, N$. A unique pre-image can now be obtained using simple algebraic calculations in a single step (no iteration is required) that is suitable for stochastic simulation.

2.2.4 Two-phase crystal plasticity constitutive model

The crystal plasticity constitutive model is critical for predicting the mechanical properties of polycrystalline materials. The previously developed single-phase constitutive model for FCC crystals (Section 2.1) is here extended to two-phase superalloy, IN100. In this material, the second phase, γ', disperses in the γ phase in three forms: primary (large particles that may not exist due to insufficient heat treatment), secondary (medium size particles) and tertiary (particles of small size and low volume fraction) precipitates. The strength of the superalloy is significantly reinforced due to the existence of these particles. The two-phase structure is approximately described by a homogenized model. The second phase configuration is not explicitly modeled. Effects from the second phase are taken into account through particular parameters in the constitutive model. In the homogenized model, we take the effective property of both phases in a single phase medium representation.

Cube slip $\langle 110 \rangle \{100\}$ systems are introduced to take cross slip mechanism at high temperatures into consideration. The rate dependent flow rule which estimates the shearing rate on each slip system includes a back force term for the modeling of the Baushinger effect arising principally from matrix dislocation interaction with γ' phase. The effect of volume and size of γ' precipitates on material strength is taken into account by constitutive parameters. The constitutive equations are summarized below and detailed in [98, 109, 110].

The flow rule of slip system α is

$$\dot{\gamma}^{(\alpha)} = \left[\dot{\gamma}_0^{(\alpha)} \left\langle \frac{|\tau^{(\alpha)} - \chi_\lambda^{(\alpha)}| - \kappa_\lambda^{(\alpha)}}{D_\lambda^{(\alpha)}} \right\rangle^{n_1} + \dot{\gamma}_1^{(\alpha)} \left\langle \frac{|\tau^{(\alpha)} - \chi_\lambda^{(\alpha)}|}{D_\lambda^{(\alpha)}} \right\rangle^{n_2} \right] \mathrm{sgn}(\tau^{(\alpha)} - \chi_\lambda^{(\alpha)}), \qquad (2.67)$$

where $\dot{\gamma}_0^{(\alpha)}$ is the initial shearing rate, $D_\lambda^{(\alpha)}$ is the drag stress assumed to be con-

stant. λ ={oct, cub} refers to the octahedral and cube slip systems, respectively. The function $\langle x \rangle$ returns x if $x > 0$ and returns 0, otherwise. The resolved shear stress on the α slip system $\tau^{(\alpha)}$ is computed by

$$\tau^{(\alpha)} = \bar{\mathbf{T}} : \left(\mathbf{m}_0^{(\alpha)} \otimes \mathbf{n}_0^{(\alpha)} \right), \tag{2.68}$$

where $\bar{\mathbf{T}}$ is the PK-II stress and $\mathbf{m}_0^{(\alpha)}$ and $\mathbf{n}_0^{(\alpha)}$ are vectors in the slip direction and normal to the slip plane, respectively, in the original configuration, since a total Lagrangian algorithm is adopted. $\bar{\mathbf{T}}$ is related to local elastic deformation gradient $\mathbf{F}^e$ via the fourth-order stiffness tensor $\mathbf{C}^e$:

$$\bar{\mathbf{T}} = \mathbf{C}^e \cdot \bar{\mathbf{E}} = \frac{1}{2} \mathbf{C}^e \cdot (\mathbf{F}^{eT} \mathbf{F}^e - \mathbf{I}). \tag{2.69}$$

The evolution of the slip resistance $\kappa_\lambda^{(\alpha)}$ (λ=cub, oct) follows the Taylor strain hardening law determined by dislocation density $\rho_\lambda^{(\alpha)}$:

$$\kappa_\lambda^{(\alpha)} = \kappa_{0,\lambda}^{(\alpha)} + \alpha_t \mu_{mix} b \sqrt{\rho_\lambda^{(\alpha)}}, \tag{2.70}$$

where $\alpha_t = \langle 0.1 - 0.68 f'_{p1} + 1.1 f'^2_{p1} \rangle$, $\mu_{mix} = (f_{p1} + f_{p2} + f_{p3}) \mu_{\gamma'} + f_m \mu_\gamma$. $\mu_{\gamma'}$ and μ_γ are shear moduli for γ' precipitates and γ matrix, respectively. The magnitude of Burgers vector is $b = (f_{p1} + f_{p2} + f_{p3}) b_{\gamma'} + f_m b_\gamma$. f_{p1}, f_{p2}, f_{p3} are volume fractions of primary, secondary, and tertiary γ' precipitates, respectively, and $f_m = 1 - f_{p1} - f_{p2} - f_{p3}$ is the volume fraction of γ matrix phase. $f'_{p1} = \frac{f_{p1}}{f_{p1} + f_m}$, $f_{p2} = \frac{f_{p2}}{f_{p2} + f_m}$ and $f_{p3} = \frac{f_{p3}}{f_{p3} + f_m}$. For different slip systems, the initial slip resistance can be evaluated by

$$\begin{aligned} \kappa_{0,oct}^{(\alpha)} &= \left[(\tau_{0,oct}^{(\alpha)})^{n_k} + \psi_{oct}^{n_k} \right]^{1/n_k} + (f_{p1} + f_{p2}) \tau_{ns}^{(\alpha)}, \\ \kappa_{0,cub}^{(\alpha)} &= \left[(\tau_{0,cub}^{(\alpha)})^{n_k} + \psi_{cub}^{n_k} \right]^{1/n_k}, \end{aligned} \tag{2.71}$$

where

$$\psi_\lambda = c_{p1} \sqrt{w \frac{f'_{p1}}{d_1}} + c_{p2} \sqrt{w \frac{f'_{p2}}{d_2}} + c_{p3} \sqrt{w f'_{p3} d_3} + c_{gr} d_{gr}^{-0.5}, \; w = \frac{\Gamma_{APB}}{\Gamma_{APB-ref}}, \tag{2.72}$$

and

$$\tau_{ns}^{(\alpha)} = h_{pe}\tau_{pe}^{(\alpha)} + h_{cb}|\tau_{cb}^{(\alpha)}| + h_{se}\tau_{se}^{(\alpha)}, \tag{2.73}$$

in which Γ_{APB} is the anti-phase boundary energy density here taken be equal to $\Gamma_{APB-ref}$, $d_i, i = 1, 2, 3$ are the sizes of precipitates, and d_{gr} is the grain size.

The dislocation density evolution has the following form:

$$\dot{\rho}_{\lambda}^{(\alpha)} = h_0 \left\{ Z_0 + k_{1,\lambda}\sqrt{\rho_{\lambda}^{(\alpha)}} - k_{2,\lambda}\rho_{\lambda}^{(\alpha)} \right\} |\dot{\gamma}^{(\alpha)}|,$$
$$Z_0 = \frac{k_\delta}{b d_{\delta eff}},\ d_{\delta eff} \approx \left(\frac{2}{d_{2\delta}}\right)^{-1}. \tag{2.74}$$

The evolution of the back stress $\chi_{\lambda}^{(\alpha)}$ is also based on dislocation density and shear rate:

$$\dot{\chi}_{\lambda}^{(\alpha)} = C_\chi \left\{ \eta\mu_{mix} b \sqrt{\rho_{\lambda}^{(\alpha)}}\, sgn(\tau^{(\alpha)} - \chi_{\lambda}^{(\alpha)}) - \chi_{\lambda}^{(\alpha)} \right\} |\dot{\gamma}^{(\alpha)}|, \tag{2.75}$$
$$\eta = \frac{\eta_{0,\lambda} Z_0}{Z_0 + k_{1,\lambda}\sqrt{\rho_{\lambda}^{(\alpha)}}},$$

where $C_\chi = 123.93 - 433.98 f'_{p2} + 384.06 f'^2_{p2}$.

An implicit iterative algorithm is used for the solution of the non-linear constitutive equations. In initial slip resistance $\kappa_{0,\lambda}$, the grain size effect is introduced in the form of the Hall-Petch law $\kappa \propto d_{gr}^{-0.5}$.

The parameters in the constitutive model can be calibrated by experimental results for specific superalloys (e.g. IN100). In the current work, the same parameters for superalloys at $650°C$ listed in [98] are adopted. For additional information about the constitutive model refer to [109, 134].

Strain based fatigue indicator parameters (FIPs) related to small crack formation and early growth are extracted as the measure of fatigue resistance, or more precisely as a measure of driving forces for fatigue crack formation [82]. The four FIPs of interest are the cumulative plastic strain per cycle (P_{cyc}), which correlates to the crack incubation life; the cumulative net plastic shear strain measure (P_r), which correlates with dislocations pile-up on grain boundaries; the Fatemi-Socie parameter (P_{FS}), which relates to the small crack growth; and the maximum range of cyclic plastic shear strain parameter (P_{mps}) [109]. The definitions of these FIPs are as follows.

The cumulative plastic strain per cycle (P_{cyc}):

$$P_{cyc} = \int_{cyc} \sqrt{\frac{2}{3}}\dot{p}dt = \int_{cyc} \sqrt{\frac{2}{3}\mathbf{D}^p : \mathbf{D}^p}dt, \tag{2.76}$$

where $\mathbf{D}^p$ is the plastic rate of deformation tensor. The crack incubation life (N_{inc}) is related to a critical value, p_{crit}, i.e.,

$$P_{cyc}N_{inc} = p_{crit}. \tag{2.77}$$

The cumulative net plastic shear strain measure (P_r):

$$P_r = \max\left(\int_{cycle} \dot{\epsilon}^p_{ij} n_i m_j dt\right), \tag{2.78}$$

where $\mathbf{m}$ is the direction along any given plane with normal $\mathbf{n}$. The maximum value of this parameter is obtained along all possible slip directions over all possible planes for one cycle.

The Fatemi-Socie parameter (P_{FS}):

$$P_{FS} = \frac{\Delta\gamma^p_{max}}{2}\left[1 + k^\star \frac{\sigma^{max}_n}{\sigma_y}\right], \tag{2.79}$$

where $\Delta\gamma^p_{max}$ is the maximum range of cyclic plastic shear strain, σ_n^{max} is the peak tensile stress normal to the plane associated with this maximum shear range and σ_y is the cyclic yield strength estimated by the Von-Mises stress at the yield strain ϵ_y. Here, we choose $\epsilon_y = 0.77\%$. The parameter $k^\star$ could be a function of several material properties in addition to the multiaxial strain state. In the current work, a constant value $k^\star = 0.5$ is used as suggested in [109].

The maximum range of cyclic plastic shear strain parameter (P_{mps}):

$$P_{mps} = \frac{\Delta\gamma^p_{max}}{2}. \tag{2.80}$$

This parameter is used when the incubation life is completely controlled by the irreversible motion of the dislocations with no assist of normal stress, namely, $k^\star = 0$ in Eq. (2.79).

An example of nickel-based superalloy microstructure consisting of 54 grains having random orientations in a $10^{-3}mm^3$ volume subjected to cyclic loading (tension and compression along z-direction) is demonstrated below. The volume fractions and sizes of γ' precipitates are given by $f_{p1} = 0$, $f_{p2} = 0.42$, $d_2 = 108nm$, $f_{p3} = 0.11$, $d_3 = 7nm$. Mechanical behavior of the microstructure is controlled by the constitutive model introduced above. All the FIPs are computed throughout the third deformation loop. The last non-Schmid term $\tau_{ns}^{(\alpha)}$ in $\kappa_{0,oct}^{(\alpha)}$ is assumed to be 0. This is an approximation as its contribution to threshold stress is not insignificant. The stress-strain response of cyclic loading condition with 3 loops and the normalized distributions of the FIPs are plotted in Fig. 2.19. Note that the x-axis in both Figs. 2.19(a) is true strain, not plastic strain. The maximum FIPs over the entire microstructure are $maxP_{cyc} = 1.51 \times 10^{-2}$, $maxP_r = 1.12 \times 10^{-4}$, $maxP_{FS} = 6.50 \times 10^{-3}$, and $maxP_{mps} = 5.98 \times 10^{-3}$.

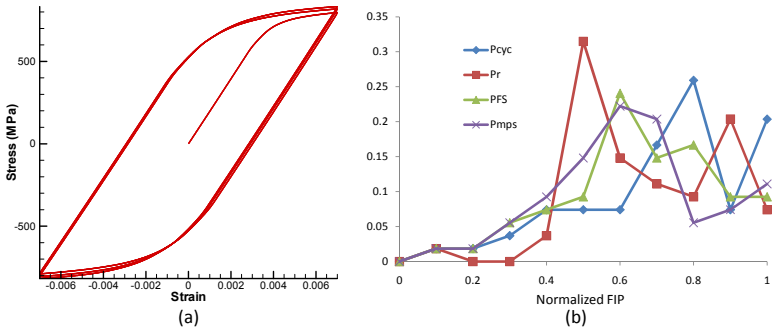

Figure 2.19: (a) Stress-strain response during 3 loops of cyclic loading. The strain rate is $0.001s^{-1}$. (b) Distribution of normalized FIPs at a strain amplitude of $\epsilon = 0.007$.

It is worth mentioning that the Taylor model is used to control the deformation of the microstructure to allow efficient stochastic simulation to be discussed next. As a result, the distributions of FIPs in the microstructure predicted in this model may not be very accurate but they serve as reasonable fatigue indicators for one grain. We also conducted a $3D$ finite element (FE) analysis on a cubic polycrystalline microstructure with 54 grains (Fig. 2.20(a)). The microstructure is discretized using $7 \times 7 \times 7$ brick elements. The maximum and average values of FIPs over all the Gauss points of all elements within an individual grain are evaluated as the representatives of the fatigue driving force of the corresponding grain. The maximum of the grain level FIPs over the entire microstructure are $maxP_{cyc,max} = 1.99 \times 10^{-2}$, $maxP_{r,max} = 8.16 \times 10^{-4}$, $maxP_{FS,max} = 7.90 \times 10^{-3}$, $maxP_{mps,max} = 6.76 \times 10^{-3}$, $maxP_{cyc,ave} = 1.49 \times 10^{-2}$, $maxP_{r,ave} = 4.46 \times 10^{-4}$, $maxP_{FS,ave} = 6.21 \times 10^{-3}$, and $maxP_{mps,ave} = 5.44 \times 10^{-4}$. Here, $P_{x,max}/P_{x,ave}$ denotes the maximum/average P_x over all Gauss points within one grain, and $maxP_{x,max}/maxP_{x,ave}$ is the maximum of $P_{x,max}/P_{x,ave}$ over all grains in the microstructure. The contour plot of the maximum range of cyclic plastic shear strain parameter, P_{mps}, is plotted in Fig. 2.20(b).

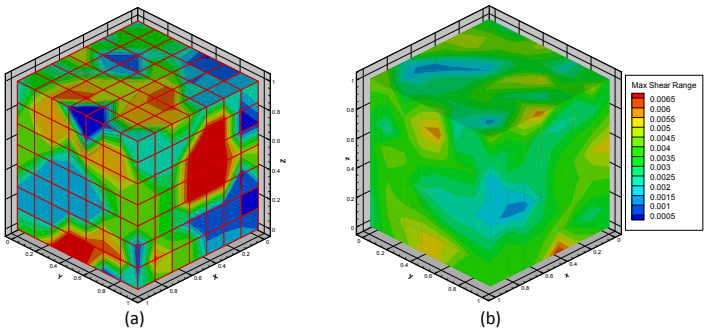

Figure 2.20: (a) A 3D finite element realization of polycrystalline microstructure. Each color represents an individual grain. (b) The field of the maximum range of cyclic plastic shear strain parameter at the end of the 3rd loop.

The true stress-strain curve and normalized distributions of FIPs are demonstrated in Fig. 2.21. We see that the Taylor simulation gives similar stress-strain response and distributions of FIPs as the FE model. Most of the FIPs obtained from the Taylor model are close to the grain level average FIPs obtained in the FE model. Considering the computational cost that the Taylor model takes only 3 minutes for one simulation while the FE model takes about 9 hours (the efficiency is evaluated here for one processor), we will adopt the Taylor model as the deterministic solver in the further investigation of the variability of FIPs. The fatigue property of a microstructure under cyclic loading can be measured by the maximum FIPs over all grains.

2.2.5 Numerical examples

Numerical examples are presented to study the probabilistic distribution of the FIPs of nickel-based superalloy polycrystalline microstructures using PCA-based model reduction techniques, PC representation, and sparse grid collocation and MC methods. The deterministic solver adopts the two-phase polycrys-

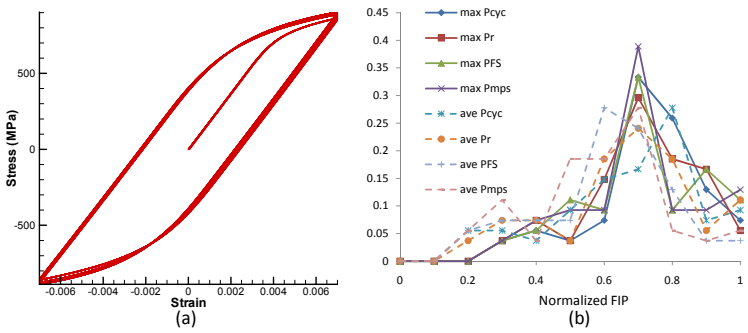

Figure 2.21: Finite element simulation results: (a) Stress-strain response during 3 loops of cyclic loading. (b) Distributions of normalized FIPs at a strain amplitude of $\epsilon = 0.007$.

tal plasticity constitutive model introduced earlier. The maximum FIPs over all grains are used to measure fatigue properties of microstructures. In the following subsections, variability of FIPs due to topological and orientational microstructure uncertainties are examined.

The available information of microstructure features is often given as a limited number of samples that are obtained through a sequence of preprocessing. Similar as in Section 2.1, we randomly generate 1000 microstructures through simulation. This operation mimics the industrial random preprocessing and is only for the generation of inherently correlated samples, based on which model reduction would work. After that, the sample data will serve directly as the initial input to the stochastic simulation. The knowledge about how the data was generated will not be known or used in this part of the analysis. Each microstructure is composed of 54 grains in a $V = 1 \times 10^{-3} mm^3$ domain. The mean grain volume is therefore $1.85 \times 10^{-5} mm^3$. By assuming cubic shape of all grains, the mean size is $\langle d_{gr} \rangle = 0.0265mm$. As indicated in many works, the grain size can be well described by a lognormal distribution. Therefore, we generate grain

sizes of a microstructure according to a lognormal distribution defined as

$$p(d_{gr}) = \frac{1}{d_{gr}\sqrt{2\pi\sigma^2}} \exp(-\frac{\ln(d_{gr}) - \mu}{2\sigma^2}), \tag{2.81}$$

where d_{gr} is the grain size, and μ, σ refer to the mean and standard deviation of $\ln(d_{gr})$. The mean grain size is $\langle d_{gr}\rangle = \exp(\mu + \sigma^2/2)$, which takes the value 0.0265 mm as mentioned above. The procedure of generating grain size samples is as follows. For a single microstructure sample, we first generate 54 approximate grain sizes $\{\hat{d}_{gr,i}, i = 1, \ldots, 54\}$ from the lognormal distribution with $\mu = \ln\langle d_{gr}\rangle - \sigma^2/2$, where $\langle d_{gr}\rangle = 0.0265mm$ and $\sigma = 0.025$. To avoid extreme large or small grains, all grain sizes are constrained within the range $0.4\langle d_{gr}\rangle < \hat{d}_{gr,i} < 2.5\langle d_{gr}\rangle$. If a grain size falls beyond that range, a new one will be generated until it satisfies the inequality. After obtaining all the 54 grain sizes, we will compute the corresponding volumes (cube root) $\hat{V}_{gr,i} = \hat{d}^3_{gr,i}, i = 1, \ldots, 54$, by assuming spherical grains. Then, the volume fraction $f_{gr,i}$ of each grain i will be obtained after normalization: $f_{gr,i} = \hat{V}_{gr,i}/\sum_j^{54} \hat{V}_{gr,j}$. The grain volume $V_{gr,i}$ will be updated by multiplying the volume fraction by the total volume of the microstructure $V = 0.001$ (namely, $V_{gr,i} = V \times f_{gr,i}$, for $i = 1, \ldots, 54$). The grain sizes can be therefore determined by the resultant grain volumes. Repeating this procedure 1000 times, we can obtain 1000 microstructure grain size samples. Assigning an arbitrary texture to all grain size samples and putting them into a sequence of random deformation process, we can derive 1000 random texture using the same manner as in Section 2.1. To be specific, an arbitrary texture consisted of 54 orientations is firstly assigned to 1000 microstructure samples. Then, these microstructures are input into a sequence of deformation modes controlled by three independent random variables ω_1, ω_2 and ω_3 (Eq.(2.27)). The random variables ω_1, ω_2 and ω_3 determine the deformation rate $\mathbf{L}$ of different modes and vary uniformly from $-0.002sec^{-1}$ to $0.002sec^{-1}$. At each time step,

the deformation of the microstructure is controlled by the combination of these three modes, but for different samples, the combination is different in terms of the deformation rates ω_1, ω_2 and ω_3. At the end of 500 *secs*, the 1000 resultant textures were collected as the input texture database to the stochastic problem. Since our model only updates orientations of grains but leaves their sizes untouched, the resultant microstructures would have the same grain sizes as the input while the texture becomes random. Moreover, the texture evolution is not significantly affected by the grain size according to the constitutive model. Therefore, the correlation of texture and grain size features is quite weak.

After generating the 1000 grain size and texture samples, we take them as the given input data to the following stochastic simulation investigating material properties due to initial microstructure uncertainties. They are the only accessible information, while the knowledge of how they are generated is blind to the uncertainty quantification process. The correlation within the feature samples will be exploited by the construction of correlation matrix through PCA/KPCA model reduction. Inserting random grain size or orientation features to the model reduction, the surrogate microstructure representation is derived. Then, polynomial chaos expansion (PCE) is used to map the reduced-order space to a known distribution, form which samples can be easily drawn and ASGC or/and MC can be conveniently introduced to solve for the variability of FIPs. Distributions and convex hulls and FIPs will be constructed according to the solution. Simulations using different models (i.e. linear/non-linear PCA, Uniform-Legendre/Gaussian-Hermite PCE, ASGC/MC) are conducted and compared. The effect of the selected dimensionality of the reduced space is also studied.

Here, we need to point out that grain sizes have to be greater than zero after

reconstruction from reduced order realizations. To guarantee this, we perform model reduction on the logarithm of grain volume fractions, $\ln(f_{gr,i})$ rather than on $(f_{gr,i})$. To generate a new grain size feature, we draw a sample $\boldsymbol{\xi}$ in the surrogate space, and find its original representation $\mathbf{y}$ in the physical space, which is an array of logarithms of grain volume fractions $\mathbf{y} = \ln(\mathbf{f}_{gr})$. The real grain volume of the microstructure is then $\mathbf{V}_{gr} = V \exp(\mathbf{y})$, where V is the total volume of the microstructure.

Monte Carlo validation

Monte Carlo simulation is conducted to validate various models on computing the variability of FIPs. The purpose of MC is to validate the performance of the PCA/KPCA model reduction and reconstruction, as well as of the PC expansion. We will see from this subsection that sampling from the reduced-order space is approximately equivalent to sampling in the physical input space, while the obtained efficiency is significant. We will first project the given microstructure snapshots (input data) to a reduced-order space through PCA/KPCA and then map this reduced-order space through PCE to a set of standard Gaussian ($\mathcal{N}(0, I)$) or independent uniform ($\mathcal{U}(-1, 1)$) random variables. To generate new microstructure samples, we thus sample from Gaussian or uniform distributions. These samples are mapped back to the reduced space derived by PCA/KPCA. Microstructures in the physical input space are then recovered via pre-imaging. The FIPs are evaluated for many randomly generated microstructures and the distributions of these properties will then be constructed through kernel density method and compared with the distributions constructed based on the 1000 initially given samples. The MC results will also

be used to verify the ASGC simulations performed later on in this section.

First, we would like to examine which microstructure feature is more substantially affecting the variability of FIPs. To this end, we compute the statistics of FIPs of the 1000 initial samples in three ways.

- Case A: a constant grain size vector is assigned to all the 1000 samples, and the texture varies from sample to sample. Without loosing generality, we assume all grains have the same size ($d_{gr} = 0.0265mm$, cube root), while the texture is randomly generated as described above.
- Case B: the grain sizes of different microstructure samples are randomly generated with mean size being $0.0265mm$ as mentioned before. A deterministic texture is randomly selected from the 1000 initial samples and assigned to all the microstructures. Therefore, the grain size is the sole source of uncertainty.
- Case C: the 1000 texture samples are one to one linked to the 1000 grain size vectors to define microstructure samples, so that the uncertainty of the two features can be considered simultaneously.

For each of the above cases, we call the deterministic solver 1000 times and extract the values of the FIPs. The volume fraction of primary γ' is 0 and that of secondary and tertiary γ' is set to be 0.42 and 0.11, respectively. The range of the cyclic strain is from -0.007 to 0.007. The strain rate is selected to be $0.001s^{-1}$. By comparing the distributions of the FIPs of these three cases, we find that most of the distributions from Case A are very close to the corresponding distributions from Case C. Also, the variance of FIPs caused by grain size uncertainty (Case B) is much smaller than that caused by orientational uncertainty (Case A).

Fig. 2.22 shows the PDFs of maximum FIPs over microstructure domain constructed based on 1000 initial samples for Case A and Case C, respectively. It is seen that most of the PDFs for the two cases are very close except that $maxP_{cyc}$ shows certain difference.

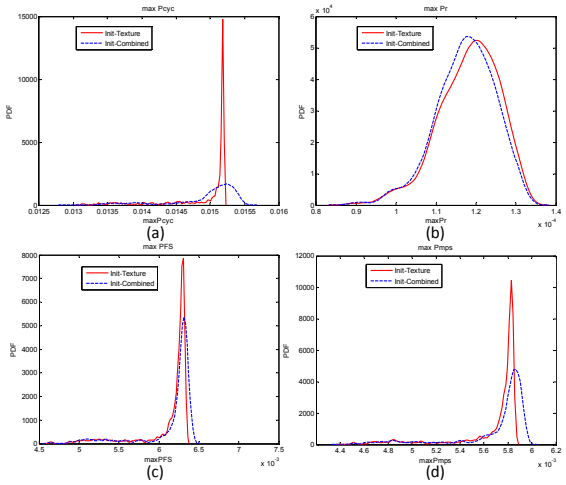

Figure 2.22: Distributions of maximum FIPs extracted from the 1000 initial sample microstructures. The solid curves are obtained by considering both grain size and texture features as random sources. The dashed curves are for the case with random texture but with fixed sizes assigned to all grains in the microstructure. (a) $MaxP_{cyc}$; (b) $MaxP_r$; (c) $MaxP_{FS}$; (d) $MaxP_{mps}$.

Comparing the statistics of the three cases (Table 2.1), we can see that the mean and standard deviation (std) of Cases A and C are very close to each other, while the variance of Case B is much smaller than the other two cases. Therefore, we ignore the grain size uncertainty while putting our focus on the texture uncertainty. This treatment further reduces the dimensionality of the input space without significantly influencing the evaluation of the distribution of the FIPs. As we will see shortly, the reduced dimensionality of the grain size feature is larger than that of texture. However, the variation induced in FIPs is insignificant.

Table 2.1: Statistics of the maximum FIPs computed from three cases of initial samples: "Texture" means only texture uncertainty is considered; "Grain size" means only that only grain size uncertainty is considered; and "Combined" means that both grain size and texture uncertainties are considered.

	Texture	Grain size	Combined
$MaxP_{cyc}$ mean	1.49×10^{-2}	1.50×10^{-2}	1.49×10^{-2}
$MaxP_{cyc}$ std	5.02×10^{-4}	2.92×10^{-5}	5.21×10^{-4}
$MaxP_r$ mean	1.18×10^{-4}	1.17×10^{-4}	1.17×10^{-4}
$MaxP_r$ std	7.53×10^{-6}	6.50×10^{-7}	7.34×10^{-6}
$MaxP_{FS}$ mean	6.13×10^{-3}	6.33×10^{-3}	6.15×10^{-3}
$MaxP_{FS}$ std	3.41×10^{-4}	1.41×10^{-5}	3.60×10^{-4}
$MaxP_{mps}$ mean	5.67×10^{-3}	5.88×10^{-3}	5.70×10^{-3}
$MaxP_{mps}$ std	3.03×10^{-4}	6.67×10^{-6}	3.28×10^{-4}

We next examine the model reduction of the input texture space. The randomness will only be assigned to grain orientations, while the volume of all grains is fixed at $V_{gr,i} = 1.85 \times 10^{-5} mm^3, i = 1, \ldots, 54$. The total dimensionality of the input microstructure feature is $54 \times 4 = 216$, in which 54 dimensions are fixed grain sizes and the rest 162 dimensions are random orientations. We first construct the reduced model for the 1000 initial microstructure samples. Then, we arbitrarily choose the reduced coordinates for one of the 1000 samples. After that, we reconstruct the microstructure feature (texture) using the chosen reduced coordinates. The reconstructed and the original features are plotted and compared in Fig. 2.23. We first apply the PCA method to reduce the input space to 4 dimensions driven by the given samples. The total energy proportion, defined by Eq. (2.82) captured by the largest 4 eigenvalues is $0.918 > 90\%$.

$$\text{Energy}(r) = \frac{\sum_{i=1}^{r} \lambda_i}{\sum_{j=1}^{N} \lambda_j}, \tag{2.82}$$

where r is the number of preserved largest eigenvalues λ_i and N is the number of given samples. A reconstructed realization compared with the original texture is depicted in Fig. 2.23(a). We next repeat the above calculations using KPCA to perform the nonlinear model reduction of the input texture samples. The parameter c in the kernel width σ estimation Eq. (2.51) is chosen to be 10. The total energy captured by the largest 4 eigenvalues is 0.815, which is lower than that captured in linear PCA. A reconstructed realization compared with the original microstructure feature is depicted in Fig. 2.23(b). Both of the two model reduction techniques demonstrate good capability of reducing and reconstructing microstructure features.

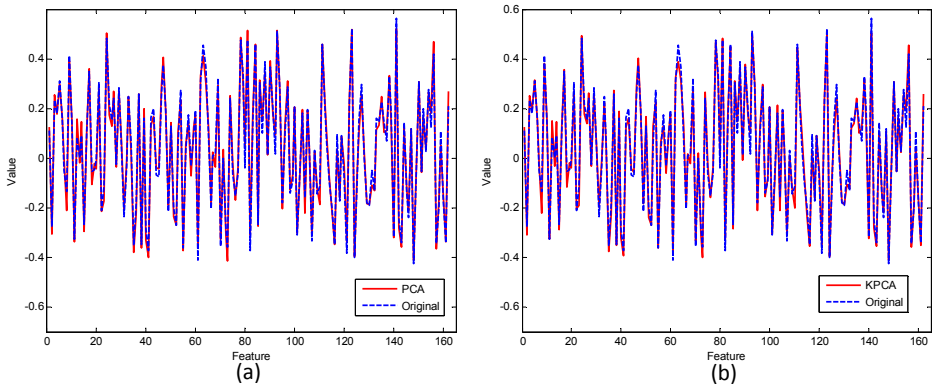

Figure 2.23: (a) A PCA reconstructed texture feature compared with the original test sample. The dimensionality of the reduced-order representation is 4, which captures 91.8% of the total "energy". (b) A KPCA reconstructed texture feature compared with the original test sample. The dimensionality of the reduced-order representation is 4, which captures 81.5% of the total "energy".

The energy spectrum of both linear PCA and kernel PCA are plotted. It is observed that the first few eigenvalues capture the majority of the total energy

and PCA eigenvalues capture more energy than KPCA at the same dimension (Fig. 2.24).

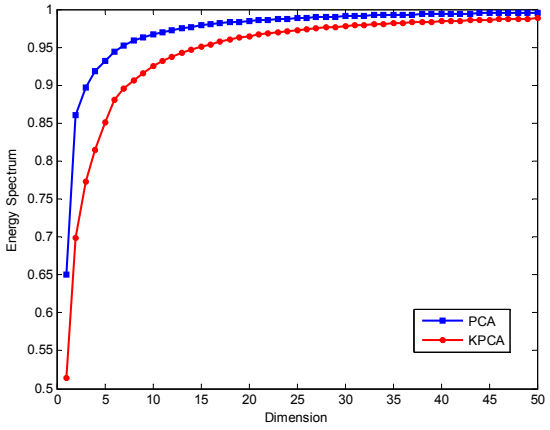

Figure 2.24: Plots of the energy spectrum for PCA and KPCA on texture feature. The value of y-axis is the total energy proportion captured by the first x principal components.

We next conduct a 10-fold cross validation on the 1000 initial samples to test the performance of the two model reduction schemes on the texture microstructure feature. For the first fold, 100 out of 1000 samples are used as the testing set to test the reconstructed features from the PCA/KPCA model trained by the remaining 900 samples. Then, we select another (different) 100 samples as the testing set, and the rest 900 to be the training set. The process is repeated 10 times until we have used all the 1000 samples as testing sample once. The average of the relative errors between testing and reconstructed features is defined as

$$\begin{aligned} Err_{\text{test}} &= \frac{1}{N'}\sum_{i=1}^{N'}\epsilon_i, \\ \epsilon_i &= \frac{\|\mathbf{y}_i - \hat{\mathbf{y}}_i\|_{L_2}}{\|\mathbf{y}_i\|_{L_2}}, \end{aligned} \tag{2.83}$$

where $\mathbf{y}_i$ and $\hat{\mathbf{y}}_i$ are the testing samples and predicted features, respectively, and N' is the size of the testing set. The averaged relative errors for texture are

plotted in Fig. 2.25. The mean error is 0.1201 for PCA and 0.1462 for KPCA. It is observed that the error of PCA is smaller than that of KPCA, while both of them are below 15% when 4 principal components are preserved.

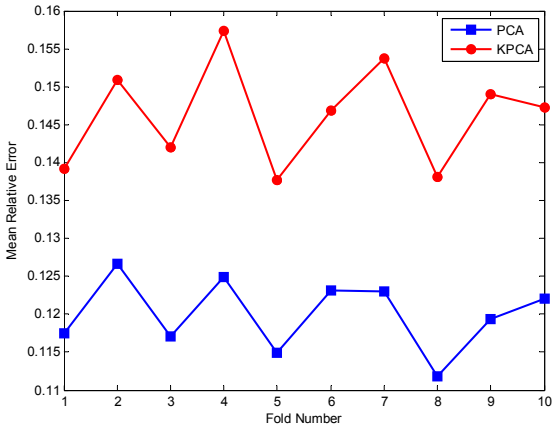

Figure 2.25: Averaged relative errors of testing texture samples in 10-fold cross validation for PCA and KPCA.

We next need to establish the mapping between the low-dimensional surrogate space and a well-defined probabilistic distribution. By the independence assumption between the random variables in the reduced-order representation, each component can be approximated using one-dimensional PC basis of degree p. If Gaussian random variables are to be mapped then Hermite polynomials are chosen to be the PC basis. On the other hand, if the reduced space is mapped to a uniform distribution, Legendre polynomials must be selected for Eq. (2.52). We here use the Gaussian-Hermite and uniform-Legendre PCs, respectively, for different model reduction schemes and compare the reconstructed features. The order of PC basis is set to be 12, which gives accurate estimation to the reduced-order representation distributions (Figs. 2.26 and 2.27). The distributions of the initial reduced variables of microstructure features are computed from the given 1000 initial samples based on the histogram of the reduced samples derived by PCA/KPCA (Eq. (2.41)). Alternatively, 10000 random variables are

randomly sampled from the uniform or Gaussian distribution and mapped to the surrogate space via PCE (Eq. (2.52)). It is noticed that Uniform-Legendre PCs give accurate representation to all four reduced-order random variables, while Gaussian-Hermite cannot fit the random variable ξ_2 corresponding to the second principal component very well. Thus, we will next perform further stochastic simulations using only Uniform-Legendre PCs.

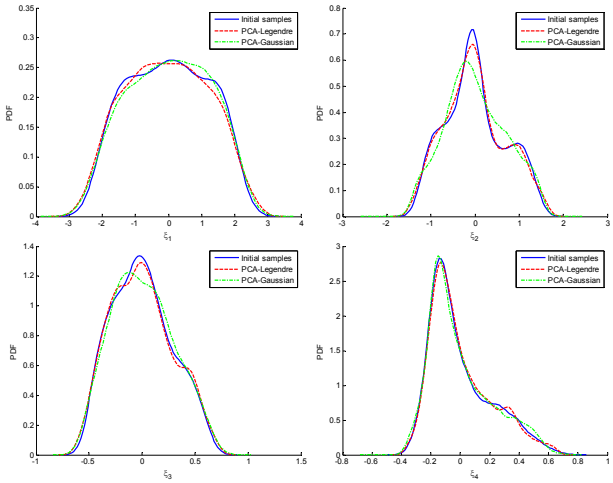

Figure 2.26: Marginal PDFs of the initial random variables (the reduced representations obtained after performing PCA on the 1000 given texture samples) and identified random variables obtained using PCE (reconstructed through PCE (Eq. (2.52)) on 10000 randomly generated samples from Gaussian or Uniform distribution). The distributions are constructed through kernel density based on data.

The marginal PDFs of the maximum FIPs of microstructures satisfying given texture constraints computed by Monte Carlo using 10000 samples from the reduced space are plotted in Fig. 2.28, as well as the distributions of the FIPs computed directly from the 1000 initial samples with various texture and fixed grain size (the same distribution obtained in Case A). Uniform-Legendre PCs are used to represent the reduced random variables. The agreement of MC simulated PDFs using 10000 samples and the PDFs obtained using the given initial

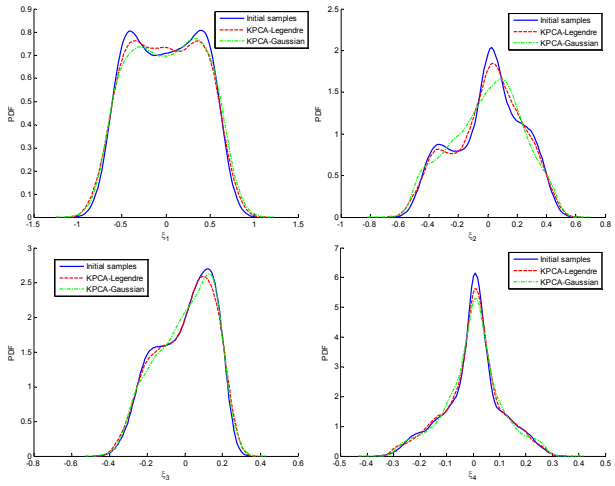

Figure 2.27: Marginal PDFs of the initial random variables (the reduced representations obtained after performing KPCA on the 1000 given texture samples) and identified random variables obtained using Hermite or Legendre PCE. The distributions are constructed through kernel density based on data.

1000 samples is achieved, which validates the performance of model reduction. Both PCA and KPCA capture the main features of the PDFs of the FIPs. The PCA results seem to be more consistent with the initial samples.

The sampled mean and standard deviation of the maximum FIPs obtained from different methods (some to be discussed later on) are listed in Table 2.2. Most of the MC simulated statistics, especially the means, agree quite well with the ones computed directly from the 1000 initial data considering that only 4 random variables are used to generate new samples. The PCA simulation gives closer prediction to the sampled mean and variance obtained using only the initial samples.

Following the same idea as for the texture, model reduction of the grain size

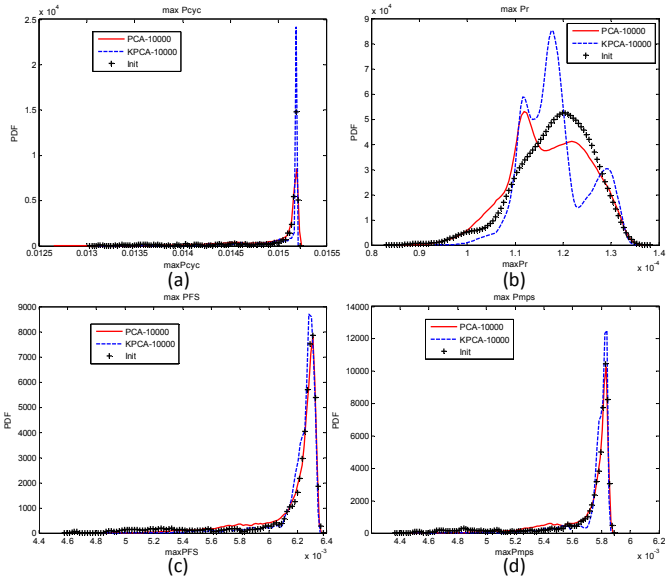

Figure 2.28: Distributions of the maximum FIPs computed by different methods. The PDFs marked as 'Init' are computed using the initial given data. For MC, 10000 samples are drawn in the reduced space and mapped back to the texture input space. A fixed grain volume $V_{gr} = 1.85 \times 10^{-5} mm^3$ is assigned to all grains. FIPs are computed using the deterministic solver on these reconstructed microstructures and kernel density function is constructed based on data. The dimensionality of the low-dimensional space is 4. (a) $MaxP_{cyc}$; (b) $MaxP_r$; (c) $MaxP_{FS}$; (d) $MaxP_{mps}$.

feature is also studied. Again, we assume only secondary and tertiary γ' precipitates dispersed in the γ matrix with fixed volume fractions (setting $f_{p1} = 0$, $f_{p2} = 0.42$ and $f_{p3} = 0.11$), so that the grain size effect can be captured. An arbitrary but deterministic texture is assigned to all 1000 initial samples, whose grain sizes are generated using the procedure described earlier with mean size $0.0265mm$. The dimensionality of the random input is now 54. To guarantee that the grain sizes are positive, we first transform all grain volume fractions to logarithms. PCA/KPCA is then used to compute the low-dimensional surrogate space of the transformed grain sizes. New grain size samples are generated by sampling in the reduced space and mapped back to the physical space. The

Table 2.2: Statistics of the maximum FIPs computed by different model reduction techniques with different dimensions. Uniform-Legendre PCs are adopted to map the reduced surrogate space of texture to a uniform distribution $\mathcal{U}(0, I)$. In the table, "Init" refers to the initial 1000 samples, "PCA-4dim" refers to 10000 MC samples generated in the 4-dimensional reduced space constructed by linear PCA, and "KPCA-4dim" refers to 10000 MC samples generated in the 4-dimensional reduced space constructed by KPCA. Similar notation is used for the rest of the acronyms.

	Init	PCA-4dim	PCA-5dim	PCA-6dim	KPCA-4dim	KPCA-5dim	KPCA-6dim
$MaxP_{cyc}$ mean	1.49×10^{-2}	1.49×10^{-2}	1.49×10^{-2}	1.49×10^{-2}	1.51×10^{-2}	1.51×10^{-2}	1.50×10^{-2}
$MaxP_{cyc}$ std	5.02×10^{-4}	4.38×10^{-4}	4.23×10^{-4}	4.35×10^{-4}	2.74×10^{-4}	2.71×10^{-4}	3.29×10^{-4}
$MaxP_{r}$ mean	1.18×10^{-4}	1.17×10^{-4}	1.17×10^{-4}	1.17×10^{-4}	1.18×10^{-4}	1.19×10^{-4}	1.19×10^{-4}
$MaxP_{r}$ std	7.53×10^{-6}	7.97×10^{-6}	7.97×10^{-6}	8.24×10^{-6}	6.49×10^{-6}	6.68×10^{-6}	6.73×10^{-6}
$MaxP_{FS}$ mean	6.13×10^{-3}	6.16×10^{-3}	6.16×10^{-3}	6.16×10^{-3}	6.22×10^{-3}	6.22×10^{-3}	6.21×10^{-3}
$MaxP_{FS}$ std	3.41×10^{-4}	2.34×10^{-4}	2.27×10^{-4}	2.26×10^{-4}	1.55×10^{-4}	1.54×10^{-4}	1.77×10^{-4}
$MaxP_{mps}$ mean	5.67×10^{-3}	5.69×10^{-3}	5.70×10^{-3}	5.70×10^{-3}	5.76×10^{-3}	5.76×10^{-3}	5.75×10^{-3}
$MaxP_{mps}$ std	3.03×10^{-4}	2.12×10^{-4}	2.03×10^{-4}	2.08×10^{-4}	1.33×10^{-4}	1.32×10^{-4}	1.59×10^{-4}

grain volume vector $\mathbf{V}_{gr}$ corresponding to a low-dimensional representation $\boldsymbol{\xi}$ is computed as

$$\mathbf{V}_{gr} = V \exp(\Gamma^{-1}(\boldsymbol{\xi})), \tag{2.84}$$

where Γ is the PCA/KPCA model reduction map of the logarithmic volume fraction to the low-dimensional space as defined in Eq. (2.41), and $V = 0.001mm^3$ is the total volume of the microstructure. We first apply the PCA method to reduce the dimensionality of the stochastic input space. The correlation between grain size samples is weak since they are generated in a very random way. This correlation is still captured by PCA even though the grain size generation procedure is not known during model reduction. We must keep the first 10 principal

components to capture more than 90% of the "energy". The total energy proportion captured by the largest 10 eigenvalues is 0.912. Using KPCA, the nonlinear model reduction captures 0.892 of the total energy by the largest 10 eigenvalues. The energy captured by the same number of eigenvalues in PCA is close to that in KPCA for the grain size feature. Reconstructed realizations by PCA and KPCA compared with the original grain size feature are depicted in Fig. 2.29(a). The newly sampled grain size features are smoother than the initial samples. Both model reduction techniques demonstrate good capability of reducing and reconstructing the grain size feature. The energy spectrums of both PCA and KPCA are shown in Fig. 2.29(b). It is observed that the first few eigenvalues capture the majority of the total energy and PCA eigenvalues capture a little more energy than KPCA at the same dimensionality.

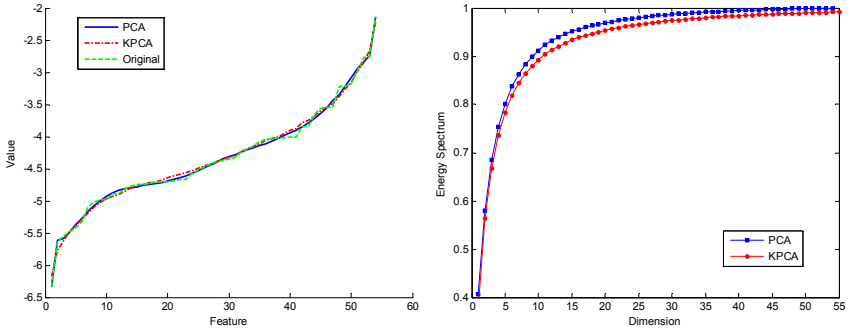

Figure 2.29: (a) PCA and KPCA reconstructed grain size feature compared with an original test sample. The dimensionality of the reduced-order representation for both cases is 10, which captures 91.2% and 89.2% of the total "energy", respectively. (b) Plots of the energy spectrum for PCA and KPCA. The value of the y-axis is the total energy proportion captured by the first x principal components.

The 10-fold cross validation for grain size feature is shown in Fig. 2.30. The relative error for both cases is smaller than 1.6% with PCA performing better than KPCA.

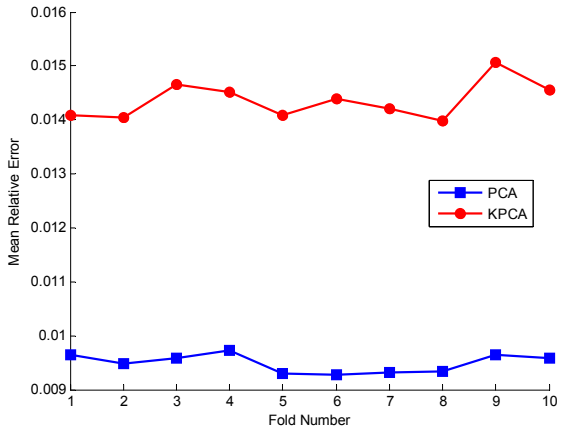

Figure 2.30: Averaged relative errors of testing grain size samples in 10-fold cross validation for PCA and KPCA.

Polynomial chaos representation on reduced random variables is also tested with 10000 random samples in the reduced space. The order $p = 12$ can accurately capture the distributions of all the reduced random variables derived from the initial samples. In Fig. 2.31, we show PC expansion of the first 2 random variables who have the largest variance for both PCA and KPCA. The agreement between identified and initial random variables distributions is observed. Both Unform-Legendre and Gaussian-Hermite PCs give accurate estimation on the distributions. To be consistent with the texture computation, we adopt Uniform-Legendre PCE to map the reduced space to a uniform distribution where new samples will be generated.

The reconstructed distributions of the FIPs and those directly extracted from the initial samples (Case B: fixed texture, random grain sizes) are plotted in Fig. 2.32. We notice that the variance of FIPs induced by the grain size effect is very small just as we discussed earlier (one order of magnitude smaller than texture induced standard deviation as shown in Table 2.1). The PCA gives very accurate prediction to the initial data, while KPCA captures well the main characters but provides slightly different estimation to the variance.

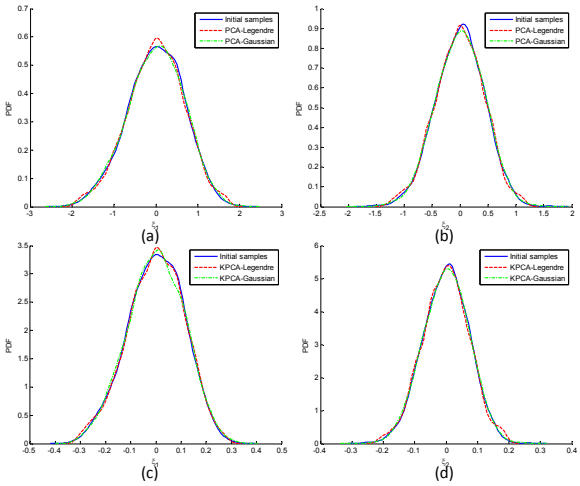

Figure 2.31: (a,b) Marginal PDFs of the first 2 PCA reduced initial random variables (the reduced representations obtained after performing PCA on the 1000 given grain size samples) and identified random variables using PCE (reconstructed through PCE (Eq. (2.52)) on 10000 randomly generated samples from Gaussian or Uniform distribution). (c,d) Marginal PDFs of the first 2 KPCA reduced random variables and identified random variables using PCE on 10000 randomly generated samples from Gaussian or Uniform distribution. The distributions are constructed through kernel density based on data.

We also discover that the reduced dimensionality of the grain size feature is 10, which is much larger than the texture feature (4 dimensions were enough for texture reduction in capturing 90% energy). It is inefficient to explore high-dimensional stochastic input space to capture very small variability in the properties. Therefore, we will focus on texture uncertainty in the following examples.

Convergence tests as the dimension of the reduced order space increases are performed for PCA and KPCA on the texture feature. The Uniform-Legendre PCs are used. We plot the marginal PDFs of maximum and volume averaged FIPs extracted from 10000 MC samples when 4, 5 and 6 principal components are preserved in Figs. 2.33 and 2.34, respectively, for PCA and KPCA. Placed in

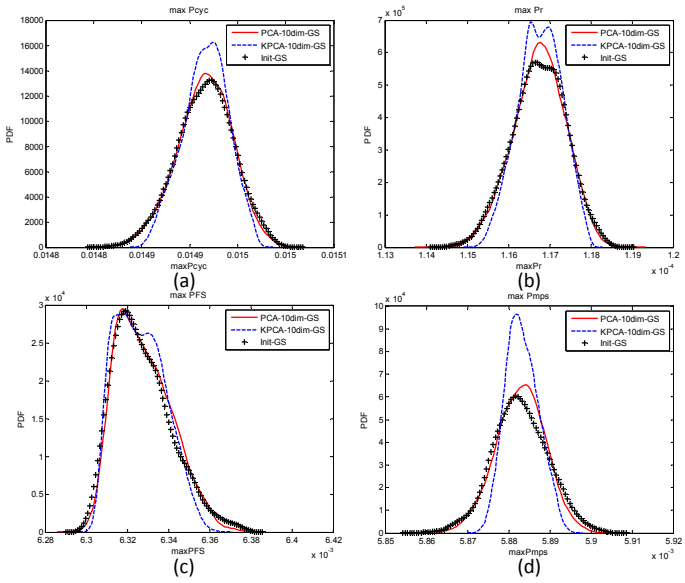

Figure 2.32: Distributions of the maximum FIPs due to grain size uncertainty computed by different methods. For MC, 10000 samples are drawn in the 10-dimensional reduced space and mapped back to the grain size input space. (a) $MaxP_{cyc}$; (b) $MaxP_r$; (c) $MaxP_{FS}$; (d) $MaxP_{mps}$.

the figures are also the distributions of FIPs obtained using only the initial samples (Case A: random texture and fixed grain sizes). We observe great consistence of the simulations with increasing dimensionality of both PCA and KPCA.

The sampled mean and standard deviation of the maximum FIPs computed using different methods and different reduced dimensions are listed in Table 2.2. It is observed that all the examples (from $r = 4$ to $r = 6$) give consistent prediction, while the PCA predictions are closer to the FIPs obtained using only the initial samples. Improvement on the predicted FIPs is observed as the dimensionality of the reduced space increases, especially for $maxP_r$.

The convergence test of MC simulations as we increase the number of samples is conducted at $r = 6$ (Figs. 2.35 and 2.36). Good convergence is achieved using 10000 random samples.

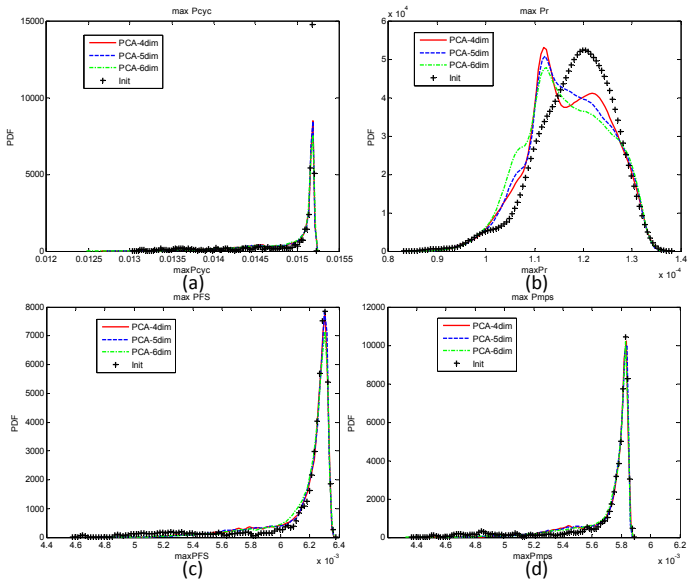

Figure 2.33: Distributions of maximum FIPs of 10000 MC samples computed based on PCA and Uniform-Legendre PCE. The dimensionality of the reduced space varies from 4 to 6. The distributions of FIPs of 1000 initial samples are also plotted as a reference. (a) $MaxP_{cyc}$; (b) $MaxP_r$; (c) $MaxP_{FS}$; (d) $MaxP_{mps}$.

It was shown that both PCA and KPCA provide good prediction on FIPs distributions and low-order statistics. In most cases, PCA gives closer prediction on mean and standard deviation of FIPs than KPCA at the same reduced dimensionality for the current microstructure data set. This is a bit surprising result considering that KPCA is a non linear dimensionality reduction method. The reasons for this outcome may include: (1) the variation of the initial samples is too small to show the nonlinear nature of the microstructure data; (2) the accuracy of the K nearest neighborhood pre-imaging strategy adopted is not good enough to provide precise microstructure reconstruction; (3) the kernel selected here could not effectively reduce the nonlinearity of the data. Moreover, the MC prediction of the mean FIPs is consistent with the initial samples, while the standard deviation prediction contains small deviation.

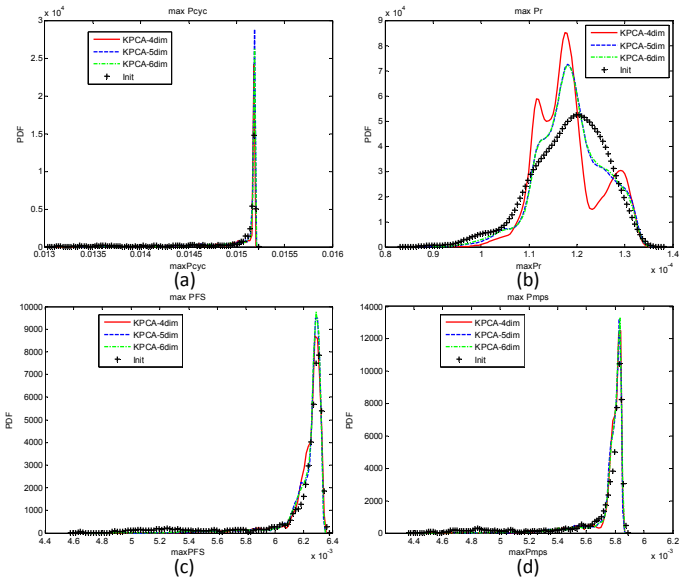

Figure 2.34: Distributions of maximum FIPs of 10000 MC samples computed based on KPCA and Uniform-Legendre PCE. The dimensionality of the reduced space varies from 4 to 6. The distributions of FIPs of 1000 initial samples are also plotted as a reference. (a) $MaxP_{cyc}$; (b) $MaxP_r$; (c) $MaxP_{FS}$; (d) $MaxP_{mps}$.

Adaptive sparse grid collocation

The variability of FIPs is also examined through the adaptive sparse grid collocation (ASGC) method (Section 2.1.4), which has been proved to be more efficient then Monte Carlo method for stochastic problems of moderately high dimensionality and at the same time provides control of the interpolation error in the stochastic support space [78]. As before, Uniform-Legendre PCs are adopted to expand the reduced-order texture features as they produce better reconstruction of the reduced random variable distributions. Both PCA and KPCA are employed. The uncertainty source is assumed to be texture whose reduced dimensionality varies from 4 to 6. The function of interest u and its interpolation $\hat{u}$ in the current work are the maximum and volume averaged FIPs of the microstructure. The threshold of the error indicator, defined in Eq. (2.17),

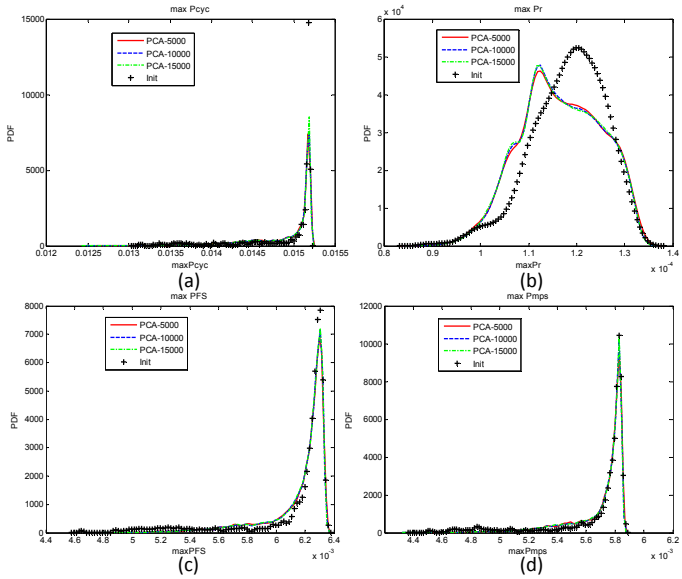

Figure 2.35: Convergence test of the distributions of maximum FIPs computed by PCA. 5000, 10000, and 15000 samples are generated in the 6-dimensional reduced space. Comparison with 1000 initial samples is shown. (a) $MaxP_{cyc}$; (b) $MaxP_r$; (c) $MaxP_{FS}$; (d) $MaxP_{mps}$.

for adaptivity is set to be 10^{-4} for all computations.

We first focus only on texture uncertainty induced variability of the FIPs. When PCA is adopted, the ASGC error converges below 10^{-4} at level 8, namely, no new collocation nodes will be needed after level 8. Total number of 1399, 3059, and 6220 collocation nodes are generated, respectively, for reduced space of dimensionality 4, 5, and 6. Note that each collocation point requires the solution of the material point simulator for given realizations of the random variables.

The marginal PDFs of maximum FIPs when different number of principal components are preserved are plotted in Fig. 2.37. The construction of the distributions of the FIPs is a post processing operation in the ASGC method. After performing the ASGC simulation, we uniformly sample 10000 random points in

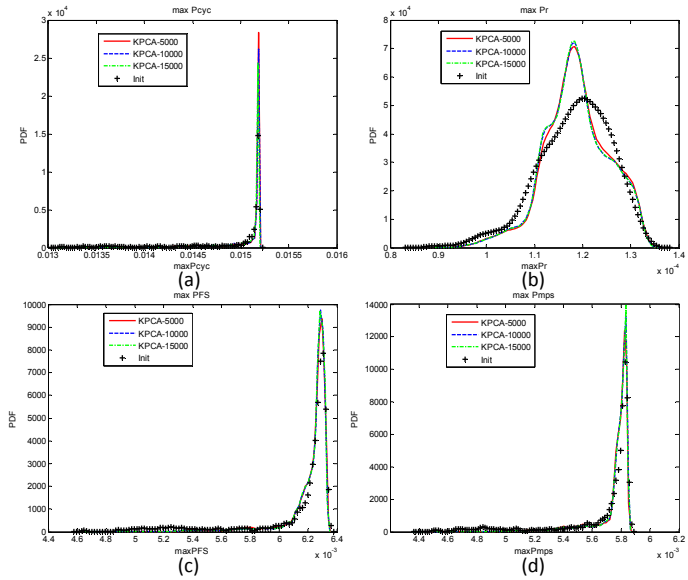

Figure 2.36: Convergence test of the distributions of the maximum FIPs computed by KPCA. 5000, 10000, and 15000 samples are generated in the 6-dimensional reduced space. Comparison with 1000 initial samples is shown. (a) $MaxP_{cyc}$; (b) $MaxP_r$; (c) $MaxP_{FS}$; (d) $MaxP_{mps}$.

the hypercube where the sparse grid is defined. The FIPs corresponding to each point are computed by interpolation using the basis obtained from ASGC. Kernel density functions based on histograms of the samples of the FIPs are therefore constructed. Comparison with MC simulation when the reduced-order space is 6-dimensional is demonstrated. We would like to point out that the data of MC used here are identical with those in the earlier examples. They are re-plotted here just for comparison purposes. ASGC distributions show similar shapes with the results of MC simulations. However, distributions of the FIPs predicted by ASGC are broadened (larger variance) as we increase the dimensionality of the reduced space.

Using KPCA, the marginal PDFs of maximum FIPs with different number of retained principal components are also extracted and presented in Fig. 2.38.

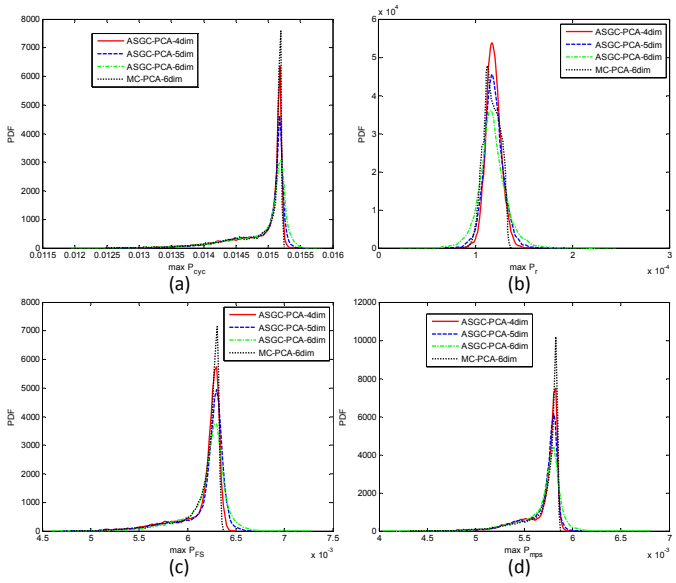

Figure 2.37: Distributions of maximum FIPs obtained with ASGC based on linear PCA and Uniform-Legendre PCE. Comparison with 10000 MC samples at $r = 6$ is demonstrated. (a) $MaxP_{cyc}$; (b) $MaxP_r$; (c) $MaxP_{FS}$; (d) $MaxP_{mps}$.

The number of collocation points for $r = 4$ and $r = 5$ after convergence at level 9 is 1647, 3633, respectively. For $r = 6$, 7921 collocation points are generated up to level 10.

The statistics of the maximum FIPs evaluated by ASGC combined with Uniform-Legendre PCE are tabulated in Table 2.3. Again, the ASGC simulations provide close estimation of mean values with MC, while the standard deviation demonstrates some small difference.

The distributions of the FIPs (Figs. 2.37 and 2.38) become slightly broader as the dimensionality of the reduced space increases. However, the predicted standard deviation (Table 2.3) does not show this trend. Moreover, most MC

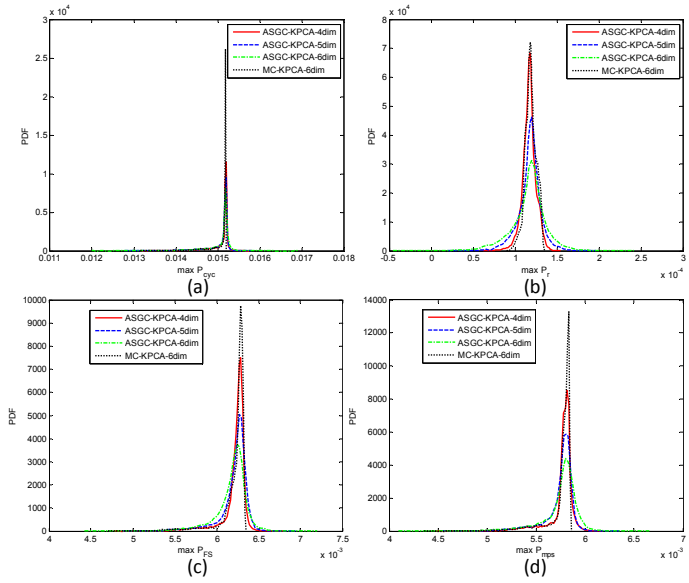

Figure 2.38: Distributions of the maximum FIPs obtained with ASGC based on KPCA and Uniform-Legendre PCE. Comparison with 10000 MC samples at $r = 6$ is demonstrated. (a) $MaxP_{cyc}$; (b) $MaxP_r$; (c) $MaxP_{FS}$; (d) $MaxP_{mps}$.

predicted PDFs of FIPs are narrower than the ASGC constructed FIPs. However, the MC computed standard deviation of certain FIPs is larger than that evaluated through ASGC. This possible inconsistency may arise from insufficient samples at the tails of the distributions and a need for a higher depth of interpolation in ASGC. For this problem, the ASGC estimation balances computational accuracy and efficiency.

All the above examples assume constant volume fractions of secondary and tertiary γ' precipitates, and the primary precipitates are not considered. Next, we take volume fractions of secondary and tertiary γ' precipitates as sources of uncertainty. The formulation of the current constitutive model adopts volume fractions of different types of γ' precipitates as explicit parameters. Therefore, the randomness of γ' can be easily dealt without the assistance of model reduction. We assume that the volume fractions of the secondary and tertiary γ'

Table 2.3: Mean and standard deviation of the maximum FIPs evaluated by ASGC. Uniform-Legendre PCE is employed.

	PCA-4dim	PCA-5dim	PCA-6dim	KPCA-4dim	KPCA-5dim	KPCA-6dim
$MaxP_{cyc}$ mean	1.49×10^{-2}	1.49×10^{-2}	1.49×10^{-2}	1.51×10^{-2}	1.50×10^{-2}	1.50×10^{-2}
$MaxP_{cyc}$ std	4.13×10^{-4}	3.92×10^{-4}	4.29×10^{-4}	2.61×10^{-4}	2.48×10^{-4}	3.09×10^{-4}
$MaxP_{r}$ mean	1.18×10^{-4}	1.19×10^{-4}	1.17×10^{-4}	1.17×10^{-4}	1.17×10^{-4}	1.17×10^{-4}
$MaxP_{r}$ std	9.29×10^{-6}	1.09×10^{-5}	1.17×10^{-5}	5.57×10^{-6}	1.01×10^{-5}	1.09×10^{-5}
$MaxP_{FS}$ mean	6.17×10^{-3}	6.19×10^{-3}	6.20×10^{-3}	6.22×10^{-3}	6.21×10^{-3}	6.18×10^{-3}
$MaxP_{FS}$ std	2.33×10^{-4}	2.31×10^{-4}	2.07×10^{-4}	1.26×10^{-4}	1.31×10^{-4}	9.17×10^{-5}
$MaxP_{mps}$ mean	5.70×10^{-3}	5.70×10^{-3}	5.70×10^{-3}	5.76×10^{-3}	5.74×10^{-3}	5.74×10^{-3}
$MaxP_{mps}$ std	1.86×10^{-4}	1.69×10^{-4}	1.30×10^{-4}	1.11×10^{-4}	6.75×10^{-5}	9.77×10^{-5}

particles follow uniform distributions $\mathcal{U}(0.3, 0.5)$ and $\mathcal{U}(0.11, 0.14)$, respectively. The volume fractions are assumed independent from each other as well as from other features (e.g. texture). The reduced space of texture is chosen to be 4. Therefore, the total dimensionality of the sampling space will be 4 + 2 = 6. The PDFs of FIPs computed by both ASGC and MC based on PCA and Uniform-Legendre PCE are plotted in Fig. 2.39. For a level of interpolation 8, 2939 deterministic problems are solved up in ASGC and 10000 simulations are conducted in MC. It is seen that the mean and standard deviation of FIPs are different from previous examples because of the varying volume fraction of γ' phase.

Convex hull of FIPs

To better understand the extreme values of FIPs and learn the correlation between them, convex hulls that serve as envelopes of the values of the FIPs in the presence of uncertainties are constructed. From Eqs. (2.79) and (2.80), we see that P_{FS} and P_{mps} are closely correlated, since the latter is a special situation

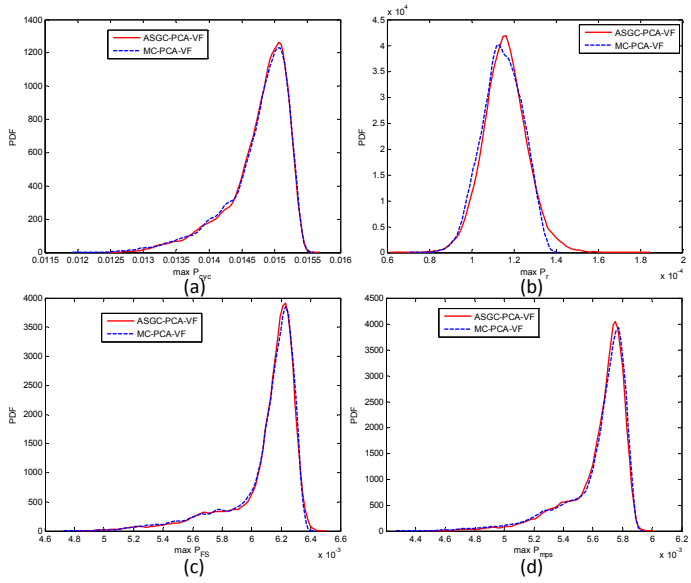

Figure 2.39: Distributions of the maximum FIPs obtained by ASGC and 10000 MC samples when the volume fractions of secondary and tertiary γ' precipitates are random. (a) $MaxP_{cyc}$; (b) $MaxP_r$; (c) $MaxP_{FS}$; (d) $MaxP_{mps}$.

of the former (when $\sigma_n^{max} = 0$, $P_{FS} = P_{mps}$). Therefore, only the 3D visualization of the convex hulls consisting of P_{cyc}, P_r and P_{FS} are shown in Fig. 2.40. For all the figures, Uniform-Legendre PCs are used to represent the 4-dimensional reduced-order random variables. The points in the FIP coordinate system are the ones that have been used for the construction of the PDFs. The Q-Hull [9] MatLab package is used to construct the convex hull.

It is observed that the volume of the convex hulls predicted by ASGC is greater than the corresponding volume constructed by MC, while the shapes of the convex hulls are similar (Fig. 2.40). We also recall from the marginal PDFs of FIPs (e.g. Figs. 2.37 and 2.38) that the ASGC provides some predictions that are away from the MC predictions but with very low probability (the tails of those PDFs). These less-probable values are the cause of the wide range of the obtained convex hulls. To better demonstrate and understand this phenomenon,

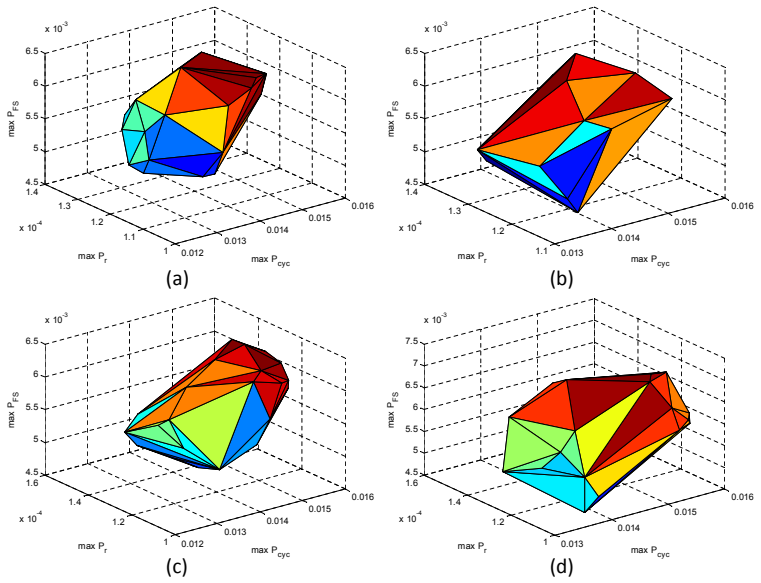

Figure 2.40: Convex hulls of maximum FIPs constructed by 10000 samples. The random source is texture and the reduced dimensionality is 4. (a) MC-PCA; (b) MC-KPCA; (c) ASGC-PCA; (d) ASGC-KPCA.

we further plot planar convex hulls of two FIPs along with the sample points and PDFs of each dimension (Fig. 2.41). The correspondence of the low probability and the extreme values predicted by ASGC are clearly captured.

It is seen that most of the data fall within the range where both ASGC and MC give high probability. Finally, 3D and 2D convex hulls when volume fractions of secondary and tertiary γ' precipitates are taken as uncertainty sources are presented in Figs.2.42 and 2.43. PCA in combination with Uniform-Legendre PCE is employed. The range and shapes of the convex hulls are much different from the cases where γ' volume fractions are taken as constant.

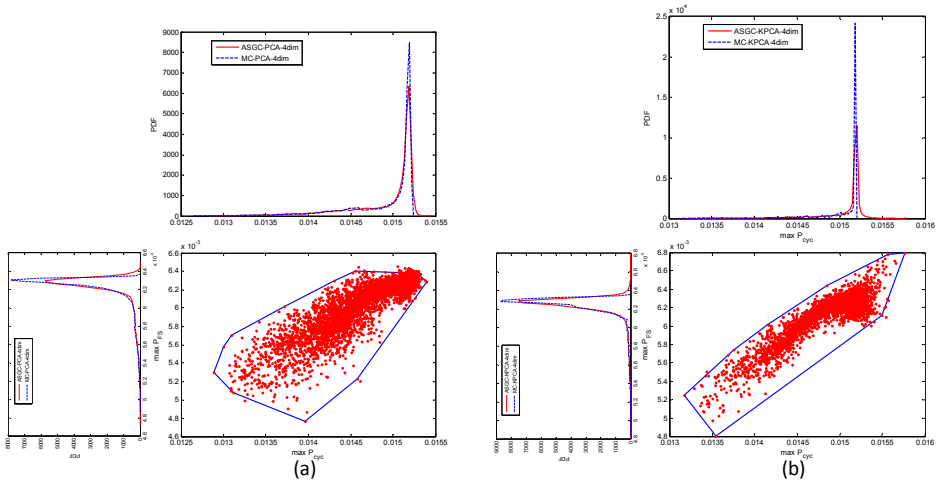

Figure 2.41: 2D convex hull with enclosed sample points obtained by ASGC. Both ASGC and MC distributions corresponding to the chosen FIPs are also plotted to show the probability of occurrence of specific values. The random source is texture and the reduced dimensionality is 4. (a) $MaxP_{cyc}$ vs. $MaxP_{FS}$ when PCA is adopted; (b) $MaxP_{cyc}$ vs. $MaxP_{FS}$, when KPCA is adopted.

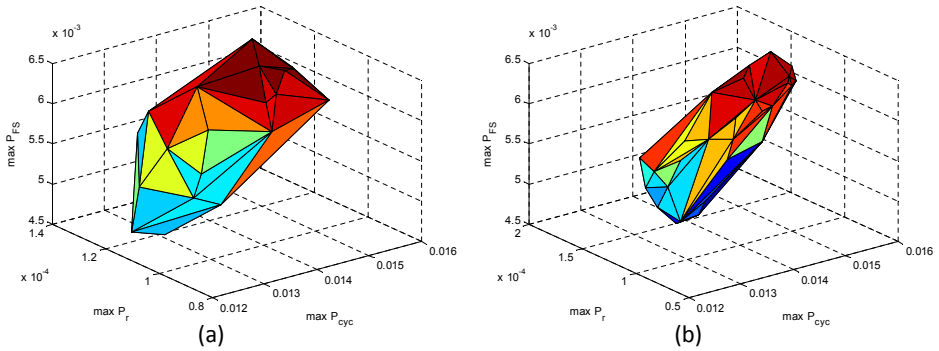

Figure 2.42: Convex hulls of maximum FIPs constructed by 10000 samples from ASGC. The random sources are texture and volume fractions of secondary and tertiary γ' precipitates. The reduced dimensionality of texture is 4, and the volume fractions are sampled from $\mathcal{U}(0.3, 0.5)$ and $\mathcal{U}(0.11, 0.14)$, respectively, for secondary and tertiary precipitates. (a) 3D convex hull of MC results; (b) 3D convex hull of ASGC results.

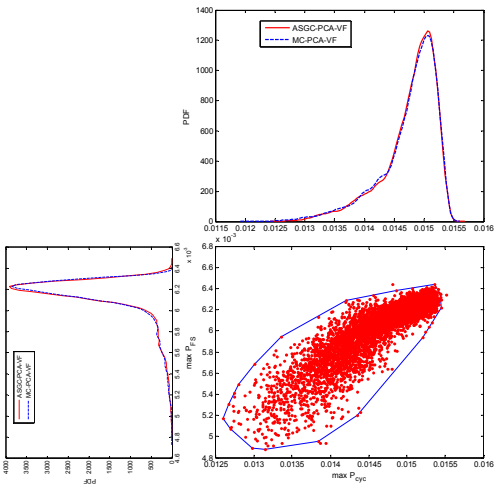

Figure 2.43: 2D convex hull with enclosed sample points obtained by ASGC. The random sources are texture and volume fractions of secondary and tertiary γ' precipitates. The reduced dimensionality of texture is 4, and the volume fractions are sampled from $\mathcal{U}(0.3, 0.5)$ and $\mathcal{U}(0.11, 0.14)$, respectively, for secondary and tertiary precipitates.

2.2.6 Conclusions

In this work, the effect of multiple sources of uncertainty on two-phase superalloy microstructure fatigue properties is studied. A two-phase microstructure is considered as a combination of random features consisting of grain size, texture, and volume fraction of the γ' phase. Given a set of microstructure samples, PCA based dimensionality reduction techniques are applied to find their underlining correlations. Both linear and nonlinear (kernel) PCA methods are examined. The reduced-order representations are mapped to uniform distributions by PC expansion. Adaptive sparse grid collocation is then introduced to sample new microstructures from the low-dimensional space. The strain-based fatigue indicator parameters of superalloy microstructures satisfying given information are computed and their distributions are constructed. The significance of different feature effect on FIPs is examined. It is shown that texture and volume

fraction of γ' precipitates are the primary factors determining FIPs in the problems and data considered. The model reduction techniques greatly simplified the representation of random microstructure features, while important characteristics of microstructures are preserved. Convergence with the dimensionality of the reduced-order variables is shown. Comparisons with MC results are also provided. The propagation of uncertainty in microstructure evolution enables one to provide the prediction on FIPs. The correlation between distributions of FIPs and their convex hulls are demonstrated. Distributions and convex hulls of FIPs provide important guidance in materials design, when certain grain size and texture information is known.

From the numerical examples we found that both PCA and KPCA provide reasonable predication to distributions of FIPs as well as their convex hulls. In the current work, however, PCA is more accurate than KPCA. As discussed earlier, two main reasons may apply: (1) the variation of initial samples is too small to show the nonlinear nature of the microstructure input data; (2) the accuracy of the K nearest neighbor pre-imaging strategy adopted is not good enough to provide precise microstructure reconstruction; (3) the kernel selected here could not effectively reduce the nonlinearity of the data. ASGC produces consistent predictions with MC but is computationally more efficient. Furthermore, the independence assumption of low-dimensional random variables may also be a source of inaccuracy for all stochastic simulations.

In the current stochastic simulation, the modeling of the Ni-based superalloy microstructure does not take into account the interaction between grains as the crystal plasticity constitutive model is implemented using the Taylor approach for the purpose of efficiency. The predictions can be improved by adopting finite

element (FE) model. However, this approach will be computationally very expensive. In a later chapter (Chapter 4), we will introduce an efficient FFT-based full field model as the alternative to the FEM to accurately study the fatigue properties of IN100. Model reduction on realistic microstructures represented in the form of images is also interested.

CHAPTER 3

UNCERTAINTY QUANTIFICATION OF MULTISCALE DEFORMATION PROCESS

In general, microstructures are location-specific (meaning that microstructures associated with different spatial points may have different distributions, see Fig.3.1) [38]. As a result, the stochastic input to a multiscale deformation process simulator will be extremely high dimensional, which prevents one from quantifying uncertainties of properties of interest in the final product. This problem is usually referred to as the "curse of dimensionality". Conventional model reduction schemes only locally decompose microstructure complexity at a given material point and cannot explore the correlation between the microstructures in the continuum. To resolve this problem, we present a bi-orthogonal KLE strategy [8, 128] to the multiscale random microstructure into a few modes in the macro- and meso-scales [52]. A second-level KLE is then conducted to further reduce the dimensionality of the stochastic space after bi-orthogonal decomposition. The optimal dimensionality of the final reduced-order space will be determined based on the energy proportion captured by the principal components in the two-step decomposition. A non-intrusive strategy is used to project the reduced random variables to the space of random variables with known probability distribution. Low order statistics of equivalent stress, strain, and strength fields of disks after forging are studied by repeatedly calling the multiscale forging solver using microstructures sampled in the reduced space. We use Monte Carlo (MC) sampling to construct the stochastic solution.

In the following, we will first formulate the bi-orthogonal KL decomposition within the context of polycrystals. Its application to multiscale forging problems

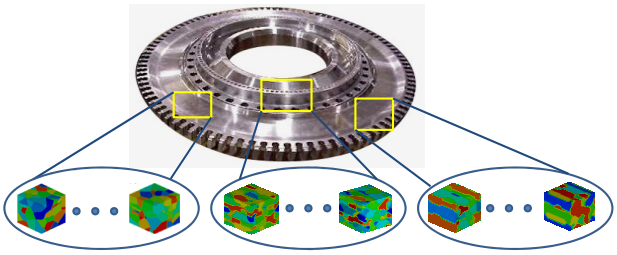

Figure 3.1: Microstructure dependence on spatial location. At different locations $\mathbf{x}$ in the workpiece, the microstructure may have different features due to pre-processing. The random microstructure field, $\mathbf{A}(\mathbf{x}, \mathbf{s}, \omega)$, denotes features of the microstructure indexed by $\mathbf{s}$ at the location $\mathbf{x}$ of the workpiece. In this paper, a fixed number of grains N_{gr} is taken for all microstructures and the orientational features (three Rodrigues parameters per grain) are indexed by $s = 1, \ldots, 3 \times N_{gr}$. ω signifies the random nature of the field $\mathbf{A}$.

will be introduced afterwards. This chapter closely follows the work in [131].

3.1 Microstructure representation

Before introducing the model reduction theory, it is important to define the input data. The goal of the current work is to quantify the variability of mechanical responses of forging disks induced by microstructure uncertainty. The stochastic input are a set of random microstructures associated with workpieces. In the general continuum representation, the location specific random microstructure is defined as a random field $\mathbf{A}(\mathbf{x}, \mathbf{s}, \omega)$. The value of $\mathbf{A}$ can be the orientation of point $\mathbf{s}$ in the microstructure located at $\mathbf{x}$. In numerical simulation, a discrete form of representation is needed. Currently, we mesh the macroscale workpiece using finite elements, and employ an array of topological and orientational features of constituent grains to represent the microstructure at each Gauss point of the finite element discretization (the same representation as used

in Section 2.2.1). For a microstructure (e.g. FCC nickel) composed of M grains, the first M components of the feature array are sizes of individual grains sorted in ascending order and the rest $3M$ components are the corresponding orientations described by Rodrigues parameters. As a result, the location dependent random microstructure becomes $A(\mathbf{x}_i, s_j, \omega)$, which is the s_j-th feature of the microstructure located at the point $\mathbf{x}_i$.

The polycrystalline microstructure representation is high-dimensional, which makes the stochastic simulation intractable. For example, a 20-dimensional vector is needed to store the grain size feature of a microstructure containing 20 grains. The vector will end up to be 80-dimensional when Rodrigues parametrization orientations are considered as well. The dimensionality of the random microstructure increases significantly when microstructure dependence on spatial location $\mathbf{x}$ is introduced. If the correlation between microstructures at different points on the macroscale is not explored, the dimensionality of the random microstructure field explodes. For a random 2D workpiece discretized by n_{el} quadrilateral elements each of which has n_{int} Gauss points, the total dimensionality of the microstructure descriptor ends up to be $4 \times M \times n_{el} \times n_{int}$, where M is the number of grains in the microstructure. This is referred to as the "curse of dimensionality". In practice, not all of the microstructure features have to be treated as random. For example, the source of microstructure uncertainty in the current work is assumed to be only the grain orientations, while the grain sizes are kept fixed. The total dimensionality of the microstructure stochastic space is therefore $3 \times M \times n_{el} \times n_{int}$, which is still very large. A reduced-order surrogate microstructure model of the location dependent random microstructure is needed. By sampling from the low-dimensional surrogate space, uncertainty quantification of the product properties driven

by random microstructures becomes computationally feasible. The surrogate model of the location specific microstructure is built using a bi-orthogonal decomposition (BOD) strategy.

3.2 Bi-orthogonal Karhunen-Loève decomposition

We model the location specific random microstructure as a random field $\mathbf{A}(\mathbf{x}, \mathbf{s}, \omega)$, which is defined as:

$$\mathbf{A}(\mathbf{x}, \mathbf{s}, \omega) : \mathcal{D} \times \mathcal{M} \times \Omega \rightarrow \mathbb{R}, \tag{3.1}$$

where $\mathcal{D}$ is the macroscale spatial domain and $\mathcal{M}$ the microstructure space. We introduce here a complete probability space $(\Omega, \mathcal{F}, \mathcal{P})$ with sample space Ω which corresponds to the outcomes of some experiments, $\mathcal{F} \subset 2^{\Omega}$ is the σ-algebra of subsets in Ω and $\mathcal{P} : \mathcal{F} \rightarrow [0, 1]$ is the probability measure. The definition of the space $\mathcal{M}$ depends on the adopted representation of the microstructures. If a microstructure is represented by a general continuous representative volume element (RVE), $\mathcal{M}$ could be the microstructure domain represented in terms of local spatial coordinates. In the current work, a microstructure is described by discrete orientation features of the constituent grains as introduced in the last subsection. Therefore, $\mathcal{M}$ is taken as the space of grain feature indices. For example, if a microstructure is represented by M feature components (M orientation parameters for all grains), $\mathcal{M}$ will be represented by a vector of dimension M. One can use the idea of Karhunen-Loève expansion to project the field $\mathbf{A}$ to a set of bi-orthogonal bases in the form of:

$$\mathbf{A}(\mathbf{x}, \mathbf{s}, \omega) \quad = \quad \bar{\mathbf{A}}(\mathbf{x}, \mathbf{s}) + \tilde{\mathbf{A}}(\mathbf{x}, \mathbf{s}, \omega)$$

$$= \quad \bar{\mathbf{A}}(\mathbf{x}, \mathbf{s}) + \sum_{i=1}^{\infty} \sqrt{\rho_i} \Psi_i(\mathbf{s}) \mathbf{\Phi}_i(\mathbf{x}, \boldsymbol{\omega}), \tag{3.2}$$

in which ρ_i are the eigenvalues of the underlying eigenvalue problem to be derived shortly (see Eq. (3.9)), Ψ_i are mesoscale modes strongly orthogonal in the microstructure space $\mathcal{M}$, and $\mathbf{\Phi}_i$ are spatial modes weakly orthogonal in the macroscale space $\mathcal{D}$ with respect to the macroscale inner product. Note that the term "mesoscale" refers to the grain-level scale, where heterogeneous grain structure is considered. And the "macroscale" is the scale of the workpiece on which the grain structure is not considered. A single point in the macroscale corresponds to a microstructure defined in the mesoscale.

We denote by $(,)$ the inner product in the microstructure space and by $\{,\}$ the inner product in the macroscale spatial domain [128]. These inner products are defined as:

$$(\Psi_i, \Psi_j) := \int_{\mathcal{M}} \Psi_i(\mathbf{s}) \Psi_j(\mathbf{s}) \mathrm{d}\mathbf{s}, \tag{3.3}$$

and

$$\{\mathbf{\Phi}_i, \mathbf{\Phi}_j\} \quad := \quad \int_{\mathcal{D}} \langle \mathbf{\Phi}_i \cdot \mathbf{\Phi}_j \rangle \mathrm{d}\mathbf{x}, \tag{3.4}$$

where $\langle \cdot \rangle$ here denotes expectation. The integral in Eq. (3.3) is for general continuous representation of microstructures. In this work, a microstructure is described by a vector with components corresponding to grain orientations. Therefore, the inner product (Ψ_i, Ψ_j) in the mesoscale is effectively computed by the dot product of the two corresponding vectors.

The strong orthogonality of Ψ_i can be written as:

$$(\Psi_i, \Psi_j) = \delta_{ij}, \tag{3.5}$$

and the weak orthogonality of $\mathbf{\Phi}_i$ as

$$\{\mathbf{\Phi}_i, \mathbf{\Phi}_j\} = \delta_{ij}. \tag{3.6}$$

Notice that the macroscale modes $\mathbf{\Phi}_i$ are referred to be weakly orthogonal, because the macroscale inner product defined in Eq. (3.4) requires the computation of expectations of the macromodes. The orthogonality is satisfied in an average sense.

By minimizing the distance (based on the norm defined in Eq. (3.4)) between the Karhunen-Loève expansion and the original random field, one ends up with [128]

$$\Psi_i(\mathbf{s}) = \frac{1}{\sqrt{\rho_i}}\{\tilde{\mathbf{A}}, \mathbf{\Phi}_i\}, \tag{3.7}$$

and from the orthogonality conditions (Eqs. (3.5) and (3.6)) as well as the expansion Eq.(3.2), we obtain

$$\mathbf{\Phi}_i(\mathbf{x}, \boldsymbol{\omega}) = \frac{1}{\sqrt{\rho_i}} \int_{\mathcal{M}} \tilde{\mathbf{A}}(\mathbf{x}, \mathbf{s}, \boldsymbol{\omega}) \Psi_i(\mathbf{s}) \mathrm{d}\mathbf{s}. \tag{3.8}$$

These last two Eqs. (3.7) and (3.8) lead to the following eigenvalue problem

$$\rho_i \Psi_i(\mathbf{s}) = \int_{\mathcal{M}} \mathbf{C}(\mathbf{s}, \acute{\mathbf{s}}) \Psi_i(\acute{\mathbf{s}}) \mathrm{d}\acute{\mathbf{s}}, \tag{3.9}$$

from which, the eigenvalues ρ_i and eigenvectors (mesoscale modes) $\Psi_i(\mathbf{s})$ can be computed. The covariance matrix $\mathbf{C}$ is

$$\mathbf{C}(\mathbf{s}, \acute{\mathbf{s}}) = \{\tilde{\mathbf{A}}(\mathbf{x}, \mathbf{s}, \boldsymbol{\omega}), \tilde{\mathbf{A}}(\mathbf{x}, \acute{\mathbf{s}}, \boldsymbol{\omega})\}. \tag{3.10}$$

In discrete form, the covariance can be written as

$$\mathbf{C}(\mathbf{s}, \acute{\mathbf{s}}) = \frac{1}{N} \sum_{j=1}^{N} \sum_{i_n=1}^{n_{el}} \sum_{i_m=1}^{n_{int}} \tilde{\mathbf{A}}_j(\mathbf{x}_{i_m}^{i_n}, \mathbf{s}) \tilde{\mathbf{A}}_j^T(\mathbf{x}_{i_m}^{i_n}, \acute{\mathbf{s}}) \tilde{W}_{i_m} |J_{i_n}| \tag{3.11}$$

We here assume that microstructure data are available for N different realizations of the workpiece. For simplicity of the presentation, we assume that complete microstructure data are available at all integration points in a finite element discretization of the workpiece. In the above equations, N is the number of realizations, n_{el} is the number of the finite elements in the macroscale, n_{int} is the number of integration points in each element, $|J_{i_n}|$ is the Jacobian determinant of the element i_n, $\tilde{W}_{i_m}$ is the integration weight associated with the integration point i_m and $\tilde{\mathbf{A}}$ is a matrix containing centered microstructural features associated with integration points, and $\mathbf{x}_{i_m}^{i_n}$ represents global coordinates of the integration point i_m of element i_n in the macroscale.

The mean field $\bar{\mathbf{A}}$ in Eq. (3.2) is defined by

$$\bar{\mathbf{A}}(\mathbf{x}, \mathbf{s}) = \langle \mathbf{A} \rangle := \int_{\Omega} \mathbf{A}(\mathbf{x}, \mathbf{s}, \boldsymbol{\omega}) p(\boldsymbol{\omega}) \mathrm{d}\boldsymbol{\omega}, \tag{3.12}$$

where $p(\boldsymbol{\omega})$ is the multivariate joint probability density of $\boldsymbol{\omega}$. In practice, the random field $\mathbf{A}(\mathbf{x}, \mathbf{s}, \boldsymbol{\omega})$ is given by N realizations $\{\mathbf{A}_i(\mathbf{x}, \mathbf{s}, \boldsymbol{\omega}_i)\}_{i=1}^{N}$. As a consequence, the mean field is here computed as the average of all given samples. The initial samples (we also refer to them as the training data for the reduced-order model) can be acquired by a variety of ways, such as experiments and numerical simulation. The generation of the training data set for our particular example will be introduced in Section 3.3.

For model reduction, the sum in Eq. (3.2) is usually approximated by the first finite number of, say d, principal components (modes) that capture most of the "energy":

$$\mathbf{A}(\mathbf{x}, \mathbf{s}, \boldsymbol{\omega}) \approx \bar{\mathbf{A}}(\mathbf{x}, \mathbf{s}) + \sum_{i=1}^{d} \sqrt{\rho_i} \Psi_i(\mathbf{s}) \boldsymbol{\Phi}_i(\mathbf{x}, \boldsymbol{\omega}). \tag{3.13}$$

The random energy of the k-th macro-random coupled mode is defined by [128]

$$E_k(\boldsymbol{\omega}) := \int_{\mathcal{D}} \rho_k \boldsymbol{\Phi}_k(\mathbf{x}, \boldsymbol{\omega}) \cdot \boldsymbol{\Phi}_k(\mathbf{x}, \boldsymbol{\omega}) \mathrm{d}\mathbf{x}, \tag{3.14}$$

The energy captured by the $k-$th mode is determined by the expectation of the random energy:

$$\bar{E}_k = \langle E_k \rangle. \tag{3.15}$$

Computing the expectation of the energy of all spatial modes, the energy proportion captured by the first d modes is defined as

$$P_{\text{Energy}}(d) = \frac{\sum_{i=1}^{d} \bar{E}_i}{\sum_{j=1}^{M} \bar{E}_j}, \tag{3.16}$$

where the energy expectations are sorted in descending order.

The macroscale modes $\boldsymbol{\Phi}_k(\mathbf{x}, \boldsymbol{\omega})$ resulted by the bi-orthogonal decomposition are functions of both the random $\boldsymbol{\omega}$ and spatial $\mathbf{x}$ variables, leading to the fact that they are still high-dimensional random vectors. We hereby, propose two reasonable assumptions to simplify the problem and employ a second-level KLE to separate the random variables from the spatial coordinates, so that the dimensionality of the input can be further reduced. The assumptions are:

- The inherent controlling random variables $\boldsymbol{\omega}$ can be separated from the mesoscale and macroscale coordinates $(\mathbf{s}, \mathbf{x})$, meaning that the randomness is independent of the microstructure feature and its spatial location.
- The macroscale modes, $\{\boldsymbol{\Phi}_i\}$, are independent from each other.

The first assumption is natural and rather fundamental to the bi-orthogonal KLE decomposition. The second assumption is strong for arbitrary stochastic

processes, since only the weak orthogonality condition between the macroscale modes holds (Eq. (3.6)). However, it is important for the further decomposition of the spatial modes $\mathbf{\Phi}_i(\mathbf{x}, \boldsymbol{\omega})$ and we will see later on in this paper that this assumption leads to rather accurate results.

Having the above two assumptions, we can next perform a second-level KLE independently on each macro-random coupled mode $\mathbf{\Phi}_i$ (refer to Eq.(2.9) for KLE). The r_i largest eigenvalues $\{\lambda_i^j\}_{j=1}^{r_i}$ that capture most of the "energy" of the ith macro-mode are retained. In this way, the macro-random coupled modes $\{\mathbf{\Phi}_i\}$ are decomposed into basis functions denoted by $\{\psi_i^j(\mathbf{x})\}$ depending only on the macroscale coordinates $\mathbf{x}$ and uncorrelated random variables $\{\boldsymbol{\phi}_i^j\}$. Note that the dimensionality of the stochastic input space is reduced for the second time. The dimensionality, r, of the final reduced random space of microstructures over the workpiece is the sum of the principal dimensions that are preserved for representing macro-random modes:

$$r = \sum_{i=1}^{d} r_i, \tag{3.17}$$

where d is the truncated number terms in the bi-orthogonal KLE (Eq. (3.13)). The reduced stochastic space can now be constructed and mapped to well-known probability distributions through a polynomial chaos expansion as introduced next.

After the second-level KLE, we denote $\{\boldsymbol{\phi}_i^j\}_{j=1}^{r_i}$, with $i = 1, \ldots, d$, to be the uncorrelated reduced representations of the original multiscale microstructures [30]. We need to construct the reduced-order stochastic space of these samples. The Uniform-Legendre PCE with non-intrusive projection as introduced in Section 2.2.2 is adopted to map the reduced representations to the uniform distribution $\mathcal{U}(-1, 1)$, from which additional microstructure realizations (samples)

can be easily generated. Since KLE and PCE have been introduced in previous chapters, we do not repeat them here. For details, readers are referred to [131].

3.3 The multiscale deterministic solver and input data set

The problem of interest in this chapter is the variability of mechanical properties of forged disks due to (initial) microstructure uncertainties. In this section, we will first briefly introduce the multiscale determinisic solver that is used to simulate the forging process and evaluate mechanical properties of the forging disk based on the features of the underlying initial microstructure. The procedure for generating correlated microstructure data over the preform will then be described. These training data will be used in Section 3.4 to produce a reduced-order model for the initial microstructure over the preform using the biorthogonal-KLE approach. This reduced model will be used as the input to the stochastic multiscale simulation. The propagation of uncertainty from the initial microstructures (sampled from the reduced-order model) to the properties of the final disk will be performed with the Monte Carlo method using the deterministic multiscale simulator in Section 3.4. Given the microstructures in the initial workpiece, the multiscale forging analysis returns the disk properties (such as the equivalent stress and strain fields, microstructure features of the deformed disk, etc.). It is important to emphasize that in this work we assume that no model error comes in the picture and that the only source of property variabilities is induced by the uncertainty in the initial microstructure.

3.3.1 The multiscale deterministic solver

A multiscale framework which couples a crystal plasticity constitutive model [6] to a finite element (FE) large deformation simulator is employed. Each integration point on the macroscale workpiece is linked to a mesoscale polycrystalline microstructure described by its grain size and orientation features (Section 3.1). The mechanical properties of a material point are computed by homogenization of the corresponding microstructure properties. In this subsection, the linking between the two scale simulations are summarized to show the dependence of macroscale properties on microstructures. For modeling details, readers are referred to [52, 136, 72].

An updated Lagrangian implicit FE model is employed for the analysis of forging processes [136]. Due to the nonlinear nature of large deformation, a Newton-Raphson scheme is adopted to solve the problem, which requires the constitutive model to compute the PK-I stress $\mathbf{P}_M$ and its increment $\mathrm{d}\mathbf{P}_M$ given the local deformation gradient $\mathbf{F}_M$ [136]. The subscript "M" indicates macroscale variables computed via homogenization of the corresponding properties at the mesoscale [52, 86]. The macroscale PK-I stress is linked to the mesoscale Cauchy stress $\mathbf{T}_m$ by

$$\mathbf{P}_M = \langle \mathbf{P}_m \rangle_h = \langle \det \mathbf{F}_m^r \mathbf{T}_m \mathbf{F}_m^{r-T} \rangle_h = \det \mathbf{F}_M^r \langle \mathbf{T}_m \rangle_h \mathbf{F}_M^{r-T}, \tag{3.18}$$

where $\mathbf{F}_m^r = \mathbf{F}_m \mathbf{F}_m^{n-1}$ is the mesoscale relative deformation gradient measuring the relative deformation from the previous time step $t = t_n$ to the current ($t = t_{n+1}$) deformation $\mathbf{F}_m$. The subscript "m" indicates mesoscale variables. Under Taylor hypothesis, all points in the microstructure associated with a spatial point $\mathbf{x}$ are subjected to the same deformation gradient $\mathbf{F}_m$, which is equal to the macro-

scopic deformation gradient $\mathbf{F}_M$ at $\mathbf{x}$. In the following, we will omit the subscript and use $\mathbf{F}$ for both scales. $\langle \mathbf{T}_m \rangle_h$ is the homogenized Cauchy stress at the macro point $\mathbf{x}$, which can be computed as the volume average of the mesocale stresses, $\mathbf{T}_m$, over the microstructure attached to $\mathbf{x}$:

$$\langle \mathbf{T}_m \rangle_h = \bar{\mathbf{T}}_m = \frac{1}{V} \int_{\mathcal{V}(\mathbf{x})} \mathbf{T}_m \mathrm{d}\mathbf{s}, \tag{3.19}$$

where V is the volume of the microstructure. The increment of the macroscale PK-I stress can be computed as:

$$\begin{aligned} \mathrm{d}\mathbf{P}_M = \mathrm{d}\langle \mathbf{P}_m \rangle_h &= \det \mathbf{F}^r \Big(tr(\mathrm{d}\mathbf{F}^r \mathbf{F}^{r-1}) \langle \mathbf{T}_m \rangle_h \\ &- \langle \mathbf{T}_m \rangle_h (\mathrm{d}\mathbf{F}^r \mathbf{F}^{r-1})^T + \langle \mathrm{d}\mathbf{T}_m \rangle_h \Big) \mathbf{F}^{r-T}. \end{aligned} \tag{3.20}$$

The crystal plasticity model as introduced in Section 2.1.5 is used to compute the mechanical responses (including $\langle \mathbf{T}_m \rangle_h$, $\mathbf{P}_M$, $\mathrm{d}\mathbf{P}_M$, etc.) based on microstructure features (grain size and crystallographic orientation) for a given deformation gradient $\mathbf{F}$.

Macroscopic quantities, such as stress and strain, are computed as the volume-average of the mesoscale values over all grains (e.g. Eq. (3.19)). The macroscopic von-Mises equivalent stress and equivalent strain can then be calculated. The equivalent strength $\bar{\kappa}_{\text{eff}}$ is evaluated as the average slip resistance $\kappa^{(\alpha)}$ of all slip systems of all grains in the microstructure:

$$\bar{\kappa}_{\text{eff}} = \left\langle \frac{1}{n_{\text{slip}}} \sum_{\alpha}^{n_{\text{slip}}} \kappa^{(\alpha)} \right\rangle_h. \tag{3.21}$$

The homogenized properties and response are returned to the macroscale for updating the deformation and response fields of the workpiece. The material of interest in the current work is FCC nickel. Parameters that are being used, as

well as the verification of this particular crystal plasticity constitutive model, are given in Section 2.1.

3.3.2 Initial sample generation

The initial workpiece samples are a set of cylindrical ingots, each point of which is linked to a distinct microstructure (Fig. 3.2).

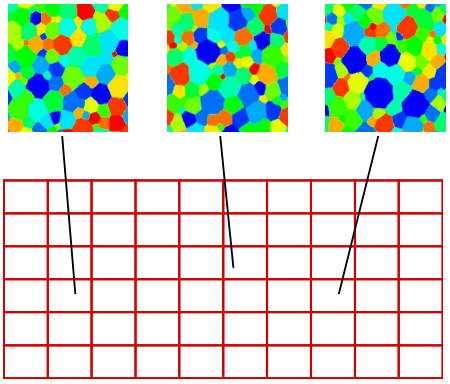

Figure 3.2: Input to the multiscale deformation simulator in Section 3.4. The simulations are done using a $2D$ axisymmetric Lagrangian finite element framework. The ingots are discretized by 10×6 quadrilateral elements, each of which contains 4 Gauss points for the integration in the element domain. Each Gauss point is linked to a microstructure consisting of 20 grains.

To generate the training data set of microstructures, we are using a pre-processing that deforms a set of raw ingots with random upper surfaces into regular cylinders. One thousand raw ingots whose upper surfaces (Fig. 3.3) are represented by degree 6 Bezier curves (Eq. (3.22)) are firstly created as follows:

$$z_\beta(a, \boldsymbol{\omega}) = 0.5 \times \left(1 + \sum_{i=1}^{6} \beta_i(\boldsymbol{\omega}) \varphi_i(a)\right), \tag{3.22}$$

where $\varphi_i(a)$ are Bernstein polynomials that can be found in [52], $a = x/L$ is the

normalized x-coordinate, $\beta_i(\omega)$ are Bezier coefficients, which are i.i.d. randomly sampled from the uniform distribution $\mathcal{U}(-0.1, 0.1)$. For a single initial microstructure at one material point, the volume of its constituent grains is taken as $V_{gr} = 1mm^3/N_{gr}$, where N_{gr} is the number of grains and a random texture is assigned. Microstructures at different locations for all preform samples are duplicates of this microstructure. The only difference between the ingot samples is the random shape of the upper surface. All raw ingots are then used as an input to a deterministic flat-die forging process, during which, their wavy surfaces are flattened under strain rate $v = 0.01s^{-1}$ (Fig. 3.3). Since all workpieces go through distinct deformation processes due to their unique surface shapes, the resultant microstructures will vary from point to point and from sample to sample. These microstructures after this pre-processing are collected to form the database for the stochastic multiscale simulation of Section 3.4. They will be used as the stochastic input (training data) for building the reduced-order surrogate microstructure model and at that stage the information about the pre-process discussed above of generating these microstructure samples will be assumed not known. The flattened ingots in the pre-process of Fig. 3.3 will have slightly distorted shape (or grid) due to their originally wavy upper surfaces. To avoid introducing additional uncertainties to those induced by the initial microstructure, we extract the random microstructures computed in the the forging pre-process of Fig. 3.3 and assign them to the corresponding material points of a set of cylindrical ingots similar to the preform in Fig. 3.3 but with a regular shape (Fig. 3.2). This operation is to make sure that the only random input source in the analysis of Section 3.4 is the initial microstructure.

Since the crystal plasticity constitutive model adopted here only updates grain orientations while keeping the grain sizes constant, the uncertainty source

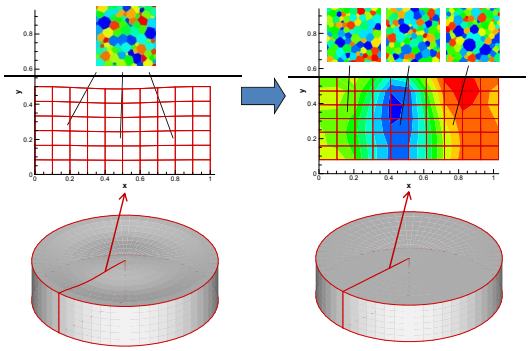

Figure 3.3: Left: Initial ingot with random upper surface and identical initial microstructures. Right: Flattened ingot having various resultant microstructures.

of the stochastic simulation is the texture of microstructures, which has been proven to have great effect on the mechanical response and properties of polycrystals [73]. The dimensionality of the stochastic input is $n_{el} \times n_{int} \times n_{feature} = 60 \times 4 \times 60 = 14400$, where n_{el} is the number of elements in the macroscale discretization, n_{int} is the number of Gauss points of an element, and $n_{feature}$ is the dimensionality of the random feature that describes each microstructure (in this example, 20 sets of 3-dimensional Rodrigues parameters). We will adopt the aforementioned two-step KLE to reduce the dimensionality of the stochastic input space driven by the 1000 sets of microstructure samples. The information of how these samples are generated is not known to the model reduction process. The reduced random variables will be mapped to standard multivariate uniform distribution ($\mathcal{U}(-1, 1)$) following the PC expansion through the non-intrusive projection. New samples will be drawn from the reduced space and reconstructed to be taken as the microstructure input to the multiscale deformation simulator. In this work, Monte Carlo simulation is employed to solve the underlying stochastic equations in conjunction with the multiscale deterministic forging solver.

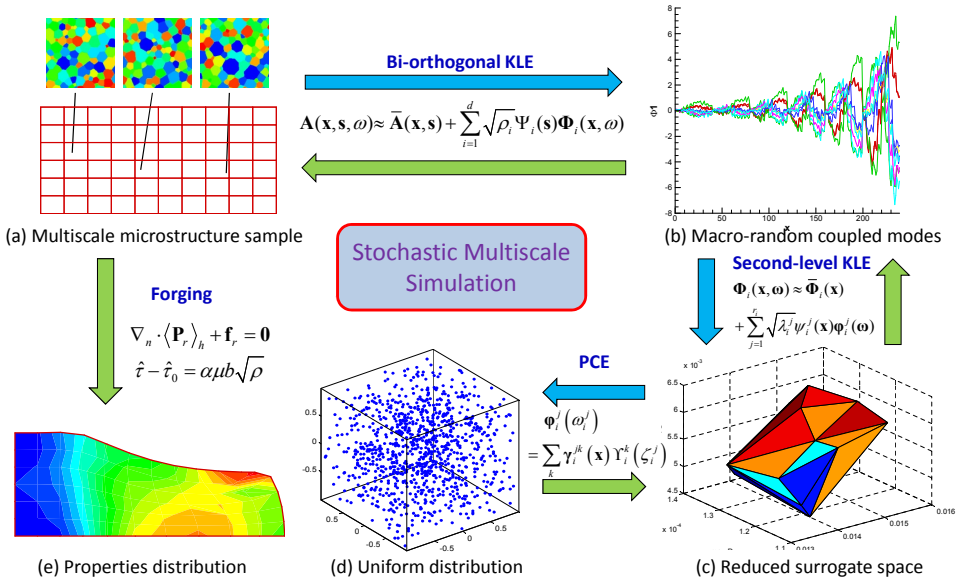

Figure 3.4: Procedure of the stochastic multiscale simulation for quantifying variability of properties of forging disks due to initial microstructure uncertainty.

The complete uncertainty quantification procedure is illustrated in Fig. 3.4. Fig. 3.4(a) refers to the initial preform with the random (high-dimensional) microstructure data. Fig. 3.4(b) denotes the macro-random coupled modes obtained after applying the bi-orthogonal KLE to the training data. The x-axis gives indices of spatial points (numbered points in the spatial domain) and the y-axis is the value of the macromodes $\mathbf{\Phi}_i(\mathbf{x})$ (note that here we present these functions as 1D plots, i.e. the values of $\mathbf{\Phi}_i(\mathbf{x}_j)$ at the finite element integration points $j = 1,\ldots,n_{el}\times n_{int} = 240$). Only a few macromodes that resulted from the initial samples are depicted in the figure. Fig. 3.4(c) refers to the surrogate stochastic microstructure space obtained with a KL expansion of each of the macroscale random modes. Fig. 3.4(d) maps the stochastic support space to a hypercube through PCE allowing sampling of microstructures from the multi-dimensional uniform distribution. Finally, Fig. 3.4(e) refers to the computation of the properties of the forged product for each microstructure sample. The flow

steps in the algorithm shown in Fig. 3.4 are as follows: (a) to (b): Given a number of initial ingot samples, compute the mesoscale and macro-random coupled modes using the bi-orthogonal KLE. (b) to (c): Project the macro-random coupled modes to low-dimensional space through a second-level KLE. (c) to (d) Map the reduced stochastic space to a known (e.g. uniform) distribution using PCE. (d) to (c): Generate new samples in the known low-dimensional distribution, and find their counterparts in the reduced surrogate space through PCE. (c) to (b) Recover macroscale modes via KLE. (b) to (a): Reconstruct the physical representation of new microstructure samples using the bi-orthogonal KLE after obtaining the macroscale modes. (a) to (e): Perform multiscale forging simulations to obtain the properties of the reconstructed samples. Repeating (d)-(c)-(b)-(a)-(e) multiple times, the statistics of the properties of the final forged product can be evaluated.

3.4 Numerical examples

We will next validate the bi-orthogonal decomposition strategy for reducing the complexity of the random microstructure input. Examples showing the evaluation of the reconstruction error of test microstructure features will be considered. By sampling in the reduced microstructure space and using the deterministic multiscale forging simulator we will next compute the variability of the mechanical properties of the forged product induced by microstructure randomness.

3.4.1 Construction and validation of the reduced-order model

The purpose of this subsection is to build the reduced-order model and validate the model reduction scheme on high-dimensional multiscale random microstructures. The input to stochastic forging simulation are 1000 sets of preforms with correlated microstructures (textures) that resulted from the same pre-process. Since each integration point in the workpiece is associated with a 20-grain microstructure, the total dimensionality of the input is 14400 according to the calculation in the previous section. The bi-orthogonal decomposition, followed by a second-level KLE, is applied to the one thousand 14400-dimensional microstructure samples. The model reduction procedure follows the illustration given in Fig.3.4.

The training microstructure samples are used to compute the mesoscale and macroscale modes. The spectrum of the energy expectation for macroscale modes defined by Eq. (3.16) is plotted in Fig. 3.5, along with the eigenvalue spectrum defined by

$$P_{Eigenvalue}(d) = \frac{\sum_{i=1}^{d} \rho_i}{\sum_{j=1}^{M} \rho_j}, \tag{3.23}$$

where ρ_i are the eigenvalues of the covariance matrix Eq. (3.10). It is observed that the first few energy components capture most of the total energy and the energy spectrum overlaps with the eigenvalue spectrum.

To effectively reduce the complexity while preserving most of the features of the initial samples, we truncate the bi-orthogonal KLE expansion keeping only the first 3 modes, which captures about 95% of the total energy.

Each of the three reduced spatial modes $\{\mathbf{\Phi}_1, \mathbf{\Phi}_2, \mathbf{\Phi}_3\}$ is represented by 1000 realizations of 240-dimensional vectors (recall that we present the mesoscale

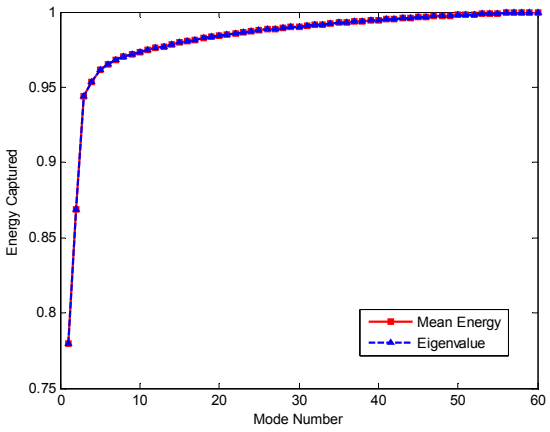

Figure 3.5: The energy and eigenvalue spectrums resulting from the initial microstructure data. The value of y-axis is the total energy proportion captured by the first x principal components.

modes with an one-dimensional vector form). The next task is to separate the random variables from spatial coordinates using a second-level KLE, which results in further reduction of the random space. For each $\mathbf{\Phi}_i$ $(i = 1, 2, 3)$, we perform an independent KLE and keep the largest r_i components that capture more than 95% of the total energy of $\mathbf{\Phi}_i$. The energy spectrum for each of the three modes is plotted in Fig. 3.6. The number of preserved components are $r_1 = 2, r_2 = 3, r_3 = 3$, respectively. The dimensionality of the final reduced space is therefore $r = r_1 + r_2 + r_3 = 8$.

Remark: It is interesting to note the difference in the asymptotic behavior of $\mathbf{\Phi}_i$ as i increases. To capture 95% of the total energy, only the largest 2 eigenvalues are needed for $\mathbf{\Phi}_1$, while for $\mathbf{\Phi}_2$ and $\mathbf{\Phi}_3$ three eigenvalues are needed. We also examined the macro-modes that correspond to lower energy in the bi-orthogonal KLE and discovered that 7, 9, 35, and 108 principal components are needed to capture 95% of the energy of macro modes from $\mathbf{\Phi}_4$ to $\mathbf{\Phi}_7$, respectively. The increase of the dimensions (e.g. number of principal components) that are necessary to capture the same proportion of the total energy is dramatic,

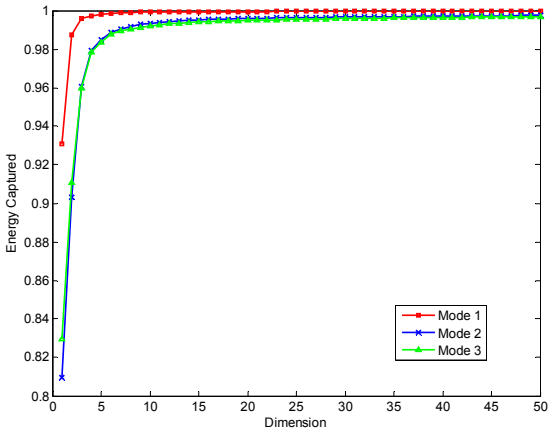

Figure 3.6: The eigenvalue spectrum of three macro-random coupled modes. The value of the y-axis is the total energy proportion captured by the first x principal components. Only the first 50 dimensions are shown.

when the energy captured by the macro-modes $\mathbf{\Phi}_i$ decreases. For this reason, keeping a small number of $\mathbf{\Phi}_i$ is of great importance in reducing the dimensionality of the stochastic space. In the current example, $d = 3$ is the optimal choice.

For the convenience of drawing samples in the subsequent stochastic simulation, the reduced-order variables are projected to the uniform distribution $\mathcal{U}(-1, 1)$ using PCE. The order of the PC basis is set to be 12, which gives accurate estimation to the distributions of the reduced representations. We plot and compare the PDFs of the reduced representations of the training samples and new samples in Figs. 3.7-3.9. The distributions of reduced representations of the training data $\phi_i^j, i = 1, \ldots, d, j = 1, \ldots, r_i$ are computed from the histogram of the given 1000 initial samples derived by the two-step KLE. On the other hand, 10000 new samples are randomly sampled from the uniform distribution and mapped to the surrogate ϕ_i^j space via PCE. A great consistence of the two distributions is observed.

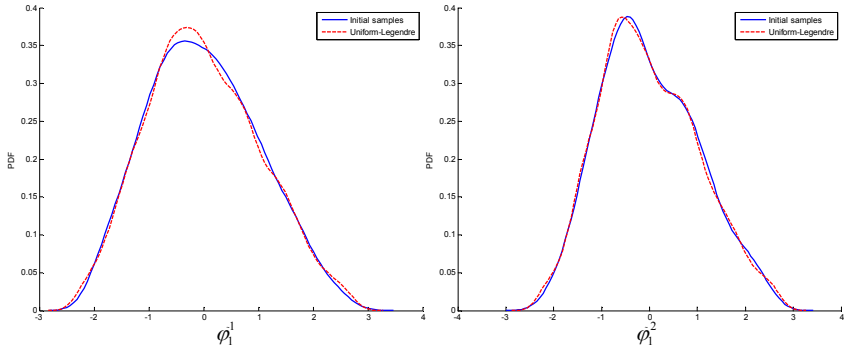

Figure 3.7: Marginal PDFs of the low-dimensional representations ϕ_1^j, $j = 1, 2$, corresponding to the first spatial mode Φ_1 (the reduced representations obtained after two-step KLE on the 1000 given texture samples) and identified random variables obtained using PCE (reconstructed through PCE on 10000 randomly generated samples from the uniform distribution). The distributions are constructed through kernel density based on data.

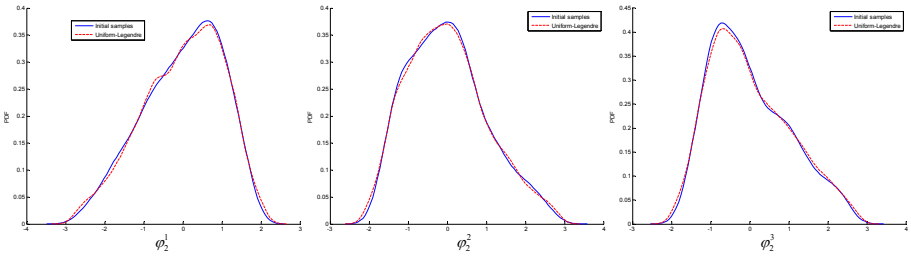

Figure 3.8: Marginal PDFs of the low-dimensional representations ϕ_2^j, $j = 1, 2, 3$, corresponding to the second spatial mode Φ_2 (the reduced representations obtained after two-step KLE on the 1000 given texture samples) and identified random variables obtained using PCE (reconstructed through PCE on 10000 randomly generated samples from the uniform distribution). The distributions are constructed through kernel density based on data.

To check the performance of the multiscale model reduction, we generate a random test sample (containing all microstructures at all integration points within the workpiece) and compare it with its reconstruction from its reduced-order representation. The 14400-dimensional array, $\mathbf{A}$, containing the texture information of all initial microstructures is projected to the 8-dimensional uni-

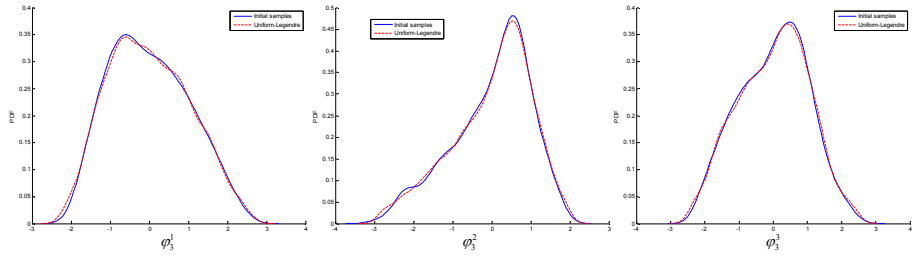

Figure 3.9: Marginal PDFs of the low-dimensional representations ϕ_3^j, $j = 1, 2, 3$, corresponding to the third spatial mode Φ_3 (the reduced representations obtained after two-step KLE on the 1000 given texture samples) and identified random variables obtained using PCE (reconstructed through PCE on 10000 randomly generated samples from the uniform distribution). The distributions are constructed through kernel density based on data.

form distribution through the two-step KLE-PCE process (we first compute the macroscale modes through the bi-orthogonal KLE Eq. (3.8); then we compute the reduced-order representations through the second-level KLE; and finally we map the reduced-order representations to the uniform distribution through the non-linear mapping as introduced in Eq. (2.56)). The realizations of the 8 random variables within $(-1, 1)$ are then mapped back to the 14400-dimensional texture array through the inverse PCE and KLE. We first compare the restored spatial modes from the reduced variables with the modes obtained through the bi-orthogonal KLE on the test sample. The 3 modes capturing most of the energy are shown. It is observed in Fig. 3.10 that the restored $\{\mathbf{\Phi}_i\}_{i=1}^3$ are close to the ones derived from the test sample.

We further reconstruct the texture realization in the physical space based on the restored spatial modes through Eq. (3.13). The restored texture is compared with the test sample. Figure 3.11 shows the pole figures of microstructures associated with two different points of the workpiece. The test microstructure sample and its reconstruction are compared. It is observed that the reconstruction

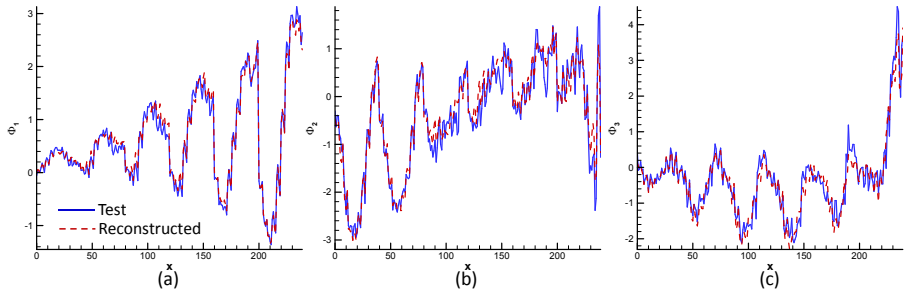

Figure 3.10: Comparison of spatial modes of a given texture sample and its reconstruction. The modes of the given sample are the macromodes $\mathbf{\Phi}$ obtained after performing the bi-orthogonal KLE on the texture sample. The reconstructed modes are recovered from the low-dimensional representations via PCE and second-level KLE. The dimensionality of the reduced representations of Φ_1, Φ_2, and Φ_3 are 2, 3, and 3, respectively. In the figure, the x-axis gives indices of spatial points (numbered points in the spatial domain) and the y-axis is the value of the macromodes $\Phi_i(\mathbf{x})$. The macromodes are given again as one-dimensional plots, i.e. the corresponding values at the indexed finite element integration points.

error for the test microstructure is small.

The reconstruction error for the test microstructure textures throughout the entire workpiece can be quantified by

$$\varepsilon = \frac{1}{S \times M} \sum_{i=1}^{S \times M} \left| \frac{A_i - \hat{A}_i}{A_i} \right|, \tag{3.24}$$

where $S \times M$ is the dimension of the microstructure feature array of the workpiece with S being the number of integration points and M being the number of microstructure parameters (here, $S \times M = 240 \times 60 = 14400$). A_i and $\hat{A}_i$ are the microstructure parameters of the test sample and its reconstruction, respectively. The relative error for this comparison is $\sim 4.26\%$. This example verifies that the multiscale model reduction scheme has very good performance in the application to high-dimensional multiscale random microstructures.

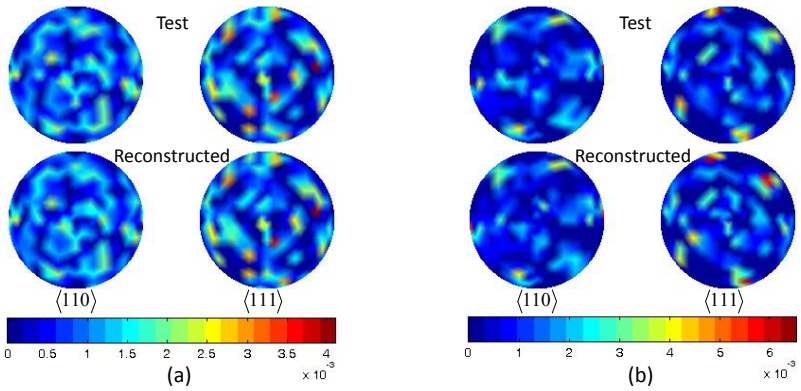

Figure 3.11: (a) Pole figures of the reconstructed and test textures of a microstructure at a single point located at the bottom of the workpiece. (b) Pole figures of the reconstructed and test textures of a microstructure at a single point located at the top of the workpiece. The reconstructed textures are obtained from an eight-dimensional representation.

3.4.2 Stochastic multiscale forging simulation

After establishing the connection between the microstructure space and the reduced surrogate microstructure space, we are ready to draw random microstructure samples and compute the variability of the mechanical properties of workpieces whose microstructures are statistically similar to the given data. The mean and standard deviation of the equivalent strain, stress, and strength fields of the forged workpiece are of interest. The simulation results are taken to be exact. No model error is considered. The mean and standard deviation fields computed based on 4032 MC samples randomly generated from the reduced-space are plotted in Figs. 3.12 and 3.13. The fields computed directly from the 1000 initial samples are also plotted (in the same figures) in comparison with the reconstructed results. The mean fields of properties computed from reconstructed samples are close to the ones computed from the initial samples. This is consistent with the bi-orthogonal decomposition setup. The standard devia-

tion of the properties of reconstructed samples, however, shows deviation from that computed using the initial samples. This is because the limited given samples are not enough to represent the entire random microstructure space (especially the higher order statistics). On the other hand, the reconstructed samples are generated from the surrogate space which is built to efficiently represent the complete microstructure space. Random samples from the reduced-order model reveal features that cannot be captured by the given initial samples. The gained efficiency in sampling in the low-dimensional surrogate microstructure space is prominent.

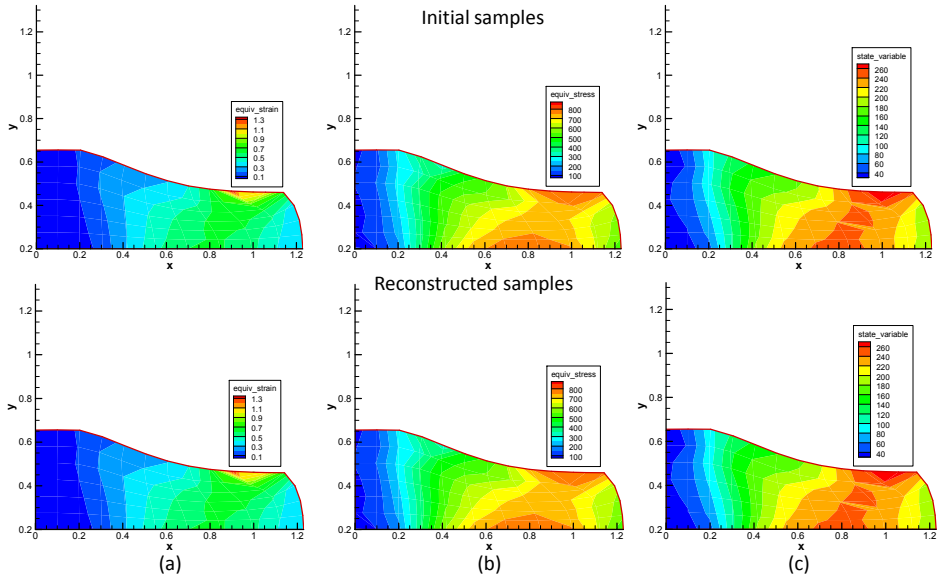

Figure 3.12: Mean field of the properties of the forged product. Upper: results extracted from 1000 initial samples; lower: results evaluated through 4032 MC samples randomly generated from the 8-dimensional reduced space: (a) effective strain, (b) effective stress, (c) effective strength.

A convergence test is also conducted using 8064 random MC samples. The comparison of the mean and standard deviation between 4032 and 8064 samples is given in Figs. 3.14 and 3.15, respectively. The relative difference of quantities between the two sets of simulations defined as $(P_{8064} - P_{4032})/P_{8064}$, where P_N

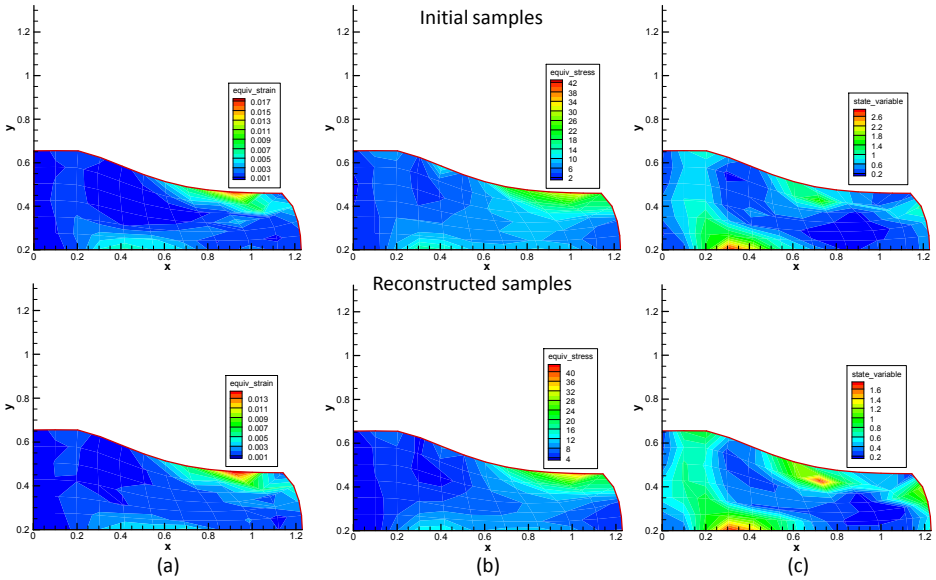

Figure 3.13: Standard deviation field of the properties of the forged product. Upper: results extracted from 1000 initial samples; lower: results evaluated through 4032 MC samples randomly generated from the 8-dimensional reduced space: (a) effective strain, (b) effective stress, (c) effective strength.

is the quantity evaluated using N MC samples, is plotted in Fig. 3.16. From the difference we see that the mean fields of the two simulations are almost the same. The relative error of standard deviation fields is larger than that of the mean field. The largest error is around 0.05.

In order to test the convergence of the bi-orthogonal decomposition model reduction scheme, we next keep more components in the second-level KLE so that they capture 99% energy of the macro-modes. The dimension of the reduced-order space becomes $r = r_1 + r_2 + r_3 = 3 + 7 + 8 = 18$. Using the same test microstructure for verification as in the previous subsection, we observe that the reconstructed macro-modes are as expected closer to the ones extracted from the test sample as shown in Fig. 3.17. Similarly, the test microstructure texture and its reconstruction at two points in the workpiece are shown in Fig. 3.18 to be

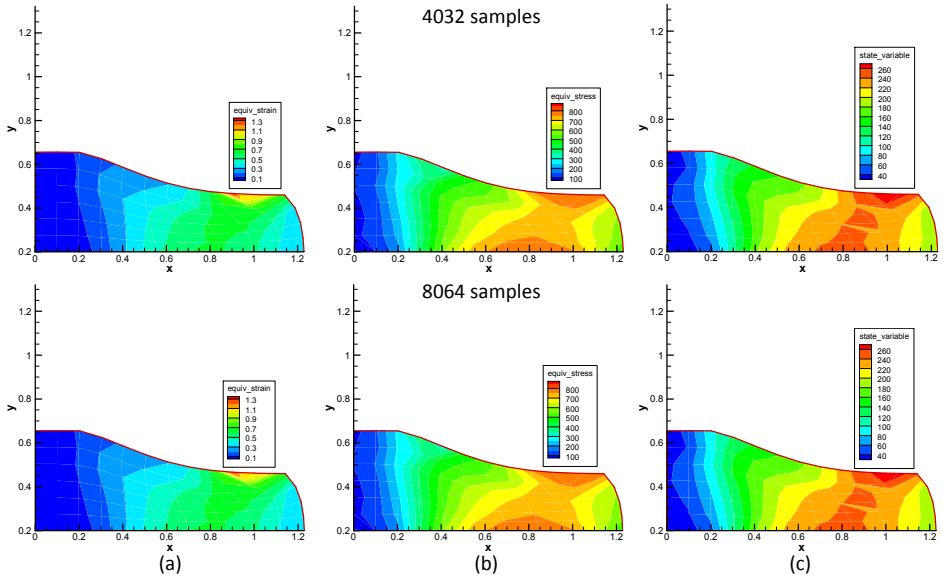

Figure 3.14: Convergence test of the mean field of the properties of the forged product. Upper: results extracted from 4032 MC samples randomly generated from the 8-dimensional reduced space; lower: results evaluated through 8064 MC samples randomly generated from the 8-dimensional reduced space. (a) effective strain, (b) effective stress, (c) effective strength.

in great agreement. The error of reconstruction of the texture over the entire workpiece for this case is reduced to $\varepsilon = 0.0398$.

The mean and standard deviation of effective strain, stress and strength fields are plotted in Fig. 3.19. The relative difference of fields defined as $(P_{18} - P_8)/P_{18}$, where P_d is the quantity evaluated from d-dimensional reduced space, is shown in Fig. 3.20. It is observed that keeping 18 reduced variables gives very similar results as keeping 8 low-dimensional representations, since the total energy captured by the two cases is close. The number of samples used here is 8064.

The distributions of properties of any point on the workpiece can also be computed. In Fig. 3.21, we plot the equivalent strain, stress, and strength dis-

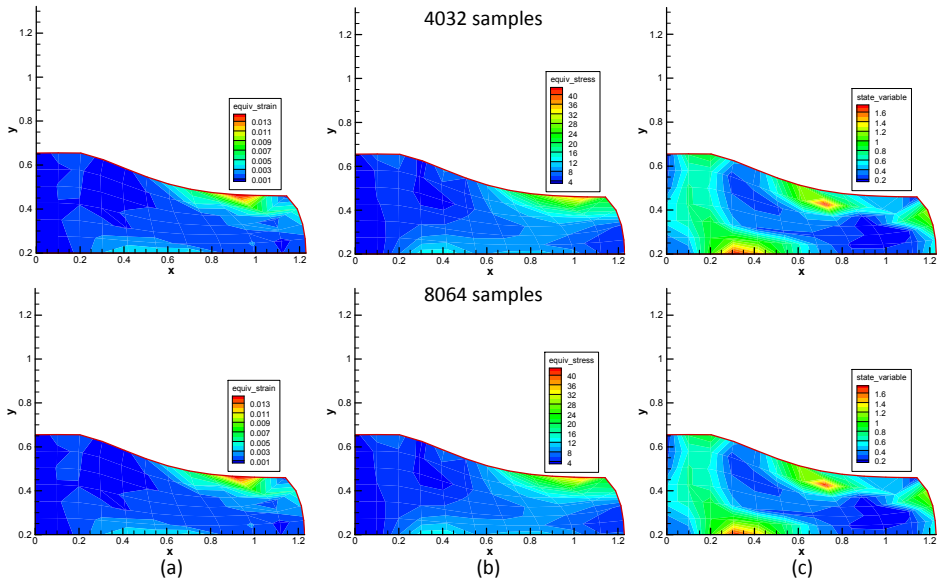

Figure 3.15: Convergence test of the standard deviation field of the properties of the forged product. Upper: results extracted from 4032 MC samples randomly generated from the 8-dimensional reduced space; lower: results evaluated through 8064 MC samples randomly generated from the 8-dimensional reduced space. (a) effective strain, (b) effective stress, (c) effective strength.

tributions, as well as the convex hull of these three quantities, at a single point in the workpiece, where the equivalent strain is large. All distributions and the convex hull [9] are evaluated according to the results of 4032 randomly generated samples from the 8-dimensional reduced space in the MC simulation just discussed.

3.5 Conclusions

A multiscale model reduction scheme based on the bi-orthogonal KLE was presented. The basic idea is to decompose the location-specific random microstructure field into a few orthogonal modes in different (macro and meso) scales.

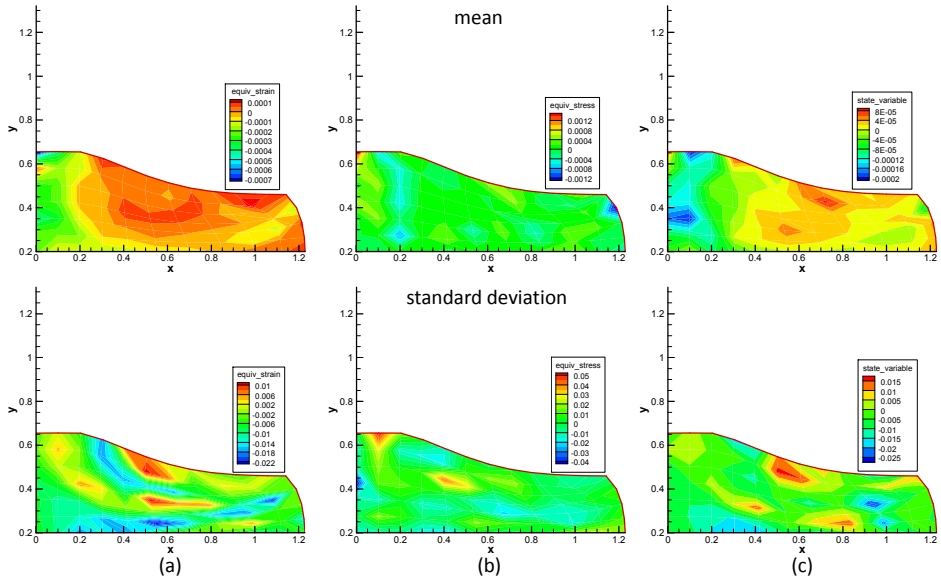

Figure 3.16: Relative difference of the mean and standard deviation field of the properties of the forged product computed by 8064 and 4032 MC samples drawn from the 8-dimensional reduced space. Upper: difference of mean fields; lower: difference of standard deviation fields. (a) effective strain, (b) effective stress, (c) effective strength.

The dimension of the input data is reduced by two-step KLE. A non-intrusive projection strategy along with PCE was employed to map the reduced representations after the two-step KLE to a multivariate uniform distribution. The reconstructed microstructure realizations show agreement with the initial microstructure samples that are given as the known information.

Properties of a continuum workpiece subjected to forging are evaluated by a multiscale solver which couples a finite element large deformation simulator with a crystal plasticity constitutive model. The mean and standard deviation of the equivalent strain, stress, and strength of the final product are computed using Monte Carlo. It is seen that the reduced model captures most of the features of the full model making it feasible to perform large scale stochastic multiscale simulations. Future studies will focus on the model reduction of realistic mi-

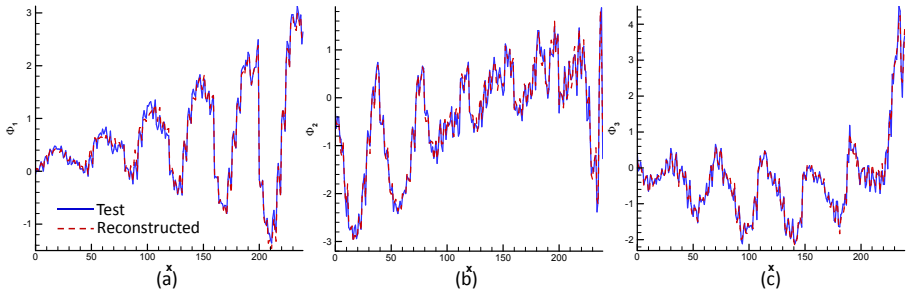

Figure 3.17: Comparison of the reconstructed and spatial modes of a test microstructure. The spatial modes are obtained by projecting the test texture to the eigenbasis through the bi-orthogonal KLE. The reconstructed modes are recovered from the low-dimensional representations using via PCE and second-level KLE. The dimensionality of the reduced representations of Φ_1, Φ_2, and Φ_3 are 3, 7, and 8, respectively. The macromodes are presented as before with 1D plots.

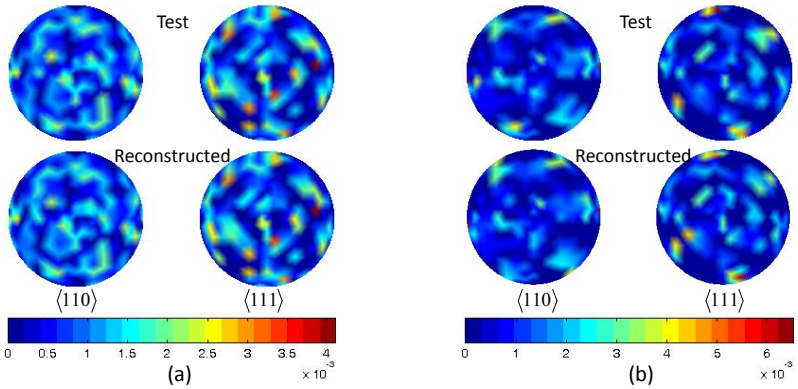

Figure 3.18: (a) Pole figures of the reconstructed and test textures of a microstructure at a single point located at the bottom of the workpiece. (b) Pole figures of the reconstructed and test textures of a microstructure at a single point located at the top of the workpiece. The reconstructed textures are obtained from an 18-dimensional representation.

crostructures described by pixels rather than statistical features as in the present work.

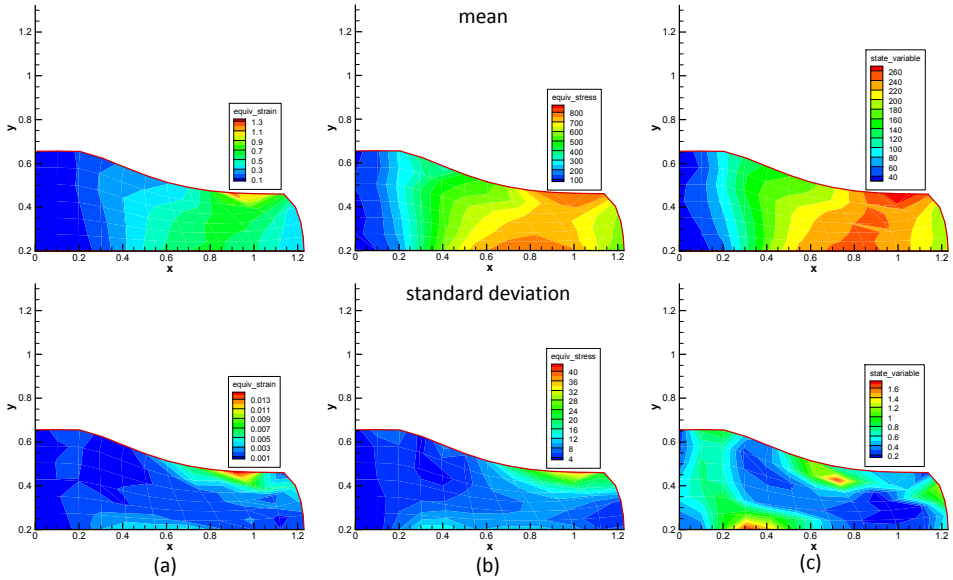

Figure 3.19: The mean and standard deviation fields of effective strain, stress, and strength computed based on random microstructures reconstructed from 18-dimensional reduced-order representations.

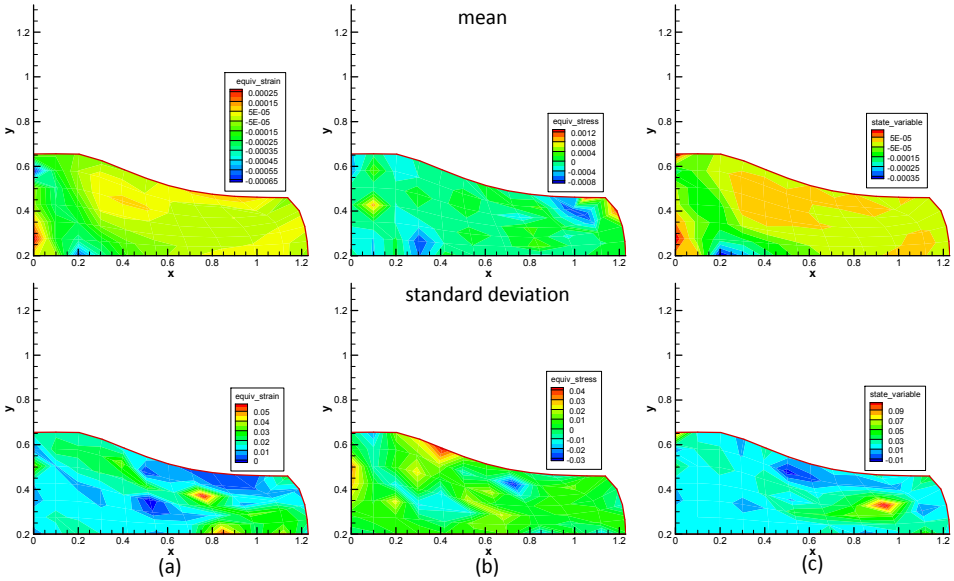

Figure 3.20: The relative error of mean and standard deviation fields of effective strain, stress, and strength computed based on random microstructures reconstructed from 8-dimensional and 18-dimensional reduced-order representations.

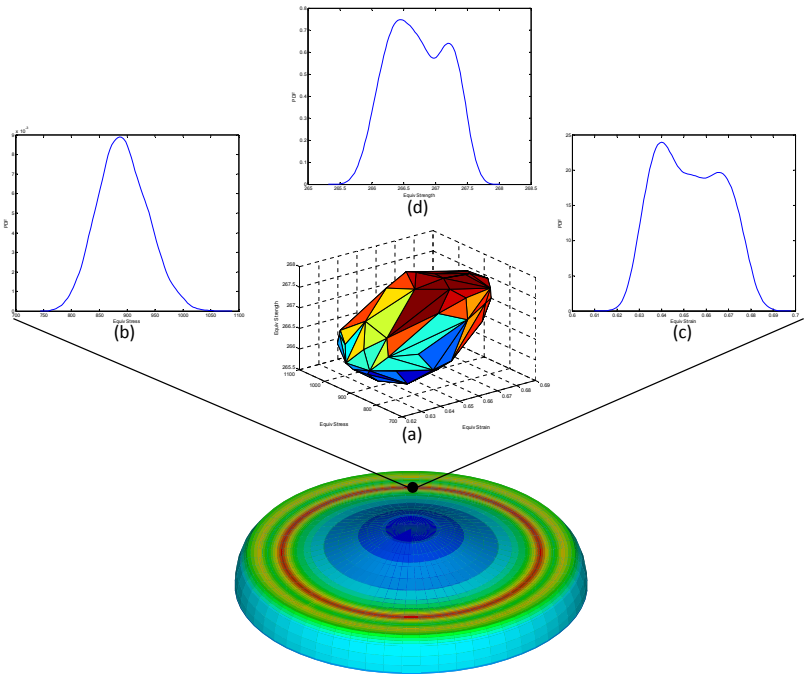

Figure 3.21: Variability of properties at one single point of the forged disk with random microstructures. (a) A convex hull showing the envelope of the three properties. (b) Equivalent stress distribution. (c) Equivalent strength distribution. (d) Equivalent strain distribution.

CHAPTER 4

AN EFFICIENT IMAGE-BASED METHOD FOR MODELING THE ELASTO-VISCOPLASTIC BEHAVIOR OF REALISTIC POLYCRYSTALLINE MICROSTRUCTURES

The above studies use topological and crystallographic features to approximately represent polycrystalline microstructures. The crystal plasticity constitutive model is implemented with the Taylor assumption. The main reasons are (1) the realistic representation of microstructures can be extremely high dimensional; (2) the full-field deterministic solver, such as finite element methods, interrogating realistic microstructure is usually very time consuming. However, realistic microstructure is important for the accurate estimation of microstructure-sensitive properties. In this chapter, we introduce an efficient full-field crystal plasticity simulator based on Green's function method and fast Fourier transform (FFT). This approach takes pixelized microstructure image as the input without requiring sophisticated discretization, and has better numerical performance than the crystal plasticity finite element method for the same spatial resolution without sacrificing accuracy. The high efficiency of this FFT-based method shows significant potential in integrating it with stochastic and/or multiscale materials simulations. This work is an extension to the crystal visco-plasticity FFT approach as described in [68]. We introduce a novel fast Fourier transform-based crystal plasticity model with the incorporation of elasto-viscoplastic constitutive relations (CEPFFT). The elastic and viscoplastic responses are computed separately using the fast Fourier transform-based method and combined to update the stress field. This allows us to take advantage of the pure elastic and rigid viscoplastic formulations, and avoid the difficulty in constructing the stiffness tensor of the reference medium. Through a

series of benchmark examples, we demonstrate that the homogenized and local elasto-viscoplastic responses can be predicted by the CEPFFT model. The constitutive model of IN100 (Ni-based superalloy) [98] is also employed to study the microstructure-sensitive fatigue indicator parameters. Comparison with finite element and rigid viscoplasticity FFT solutions shows great consistence of these methods. Furthermore, we analyzed the performance of the fast Fourier transform based simulator with a rigid visco-plastic model implemented in two different ways (basic formulation [94] and augmented Lagrangian [69]). A multi-grid strategy separating the computation and material grids based on the particle-in-cell method [60] is also employed and the obtained results are compared with those using a single grid strategy [97]. The notation follows the work in [2].

4.1 Crystal elasto-viscoplastic fast Fourier transform simulator

In this section, we address the solution of the boundary value problem defining the deformation of elasto-viscoplastic polycrystalline microstructures using the Green's function method, in which any point in the domain can be considered as an inclusion embedded in a homogeneous reference medium. The local mechanical response of the heterogeneous polycrystal can be calculated as a convolution integral between the Green's function associated with the linear reference homogeneous medium (the homogeneous equivalent microstructure in which grains are embedded) and the actual heterogeneous field [68]. All the local quantities can be written as the summation of a mean value and a fluctuation indicated by a "~" symbol. Usually, the representative volume element of bulk microstructures (not on the surface) is modeled to be periodic and periodic

boundary conditions are applied to control its deformation. In this case, the Fourier transform can be employed to efficiently solve the problem in Fourier space, where the convolution in real space is reduced to a simple product. An iterative scheme is needed to ensure that the solution converges to the micromechanical responses satisfying equilibrium and compatibility conditions.

For clarity, we will start with brief presentation of the solutions of pure elastic and rigid visco-plastic problems. Then, the solution strategy of elasto-viscoplastic problems will be introduced as the extension of the above two cases. For elasto-viscoplastic problems, the strain rate is coupled with stress and stress rate leading to challenges in using the Green's function method. To address this, we will introduce a solution strategy in which the elastic and plastic responses are computed simultaneously but separately.

4.1.1 Solution of crystal elastic boundary value problems

In pure crystal elastic problems, the total strain rate $\dot{\boldsymbol{\varepsilon}}$ is equal to the elastic strain rate $\dot{\boldsymbol{\varepsilon}}^e$, and the stress rate is linearly related to the strain rate through the generalized Hooke's law:

$$\dot{\boldsymbol{\sigma}}(\mathbf{x}) = \mathbf{C}^e(\mathbf{x}) : \dot{\boldsymbol{\varepsilon}}^e(\mathbf{x}), \tag{4.1}$$

where $C^e_{ijkl}(\mathbf{x}) = R_{im}(\mathbf{x})R_{jn}(\mathbf{x})R_{ko}(\mathbf{x})R_{lp}(\mathbf{x})\check{C}^e_{mnop}$ is the local elastic stiffness tensor represented in the sample coordinate system that relates the crystal lattice frame via a rotation matrix $\mathbf{R}(\mathbf{x}) = \mathbf{R}(\mathbf{r}(\mathbf{x}))$ determined by the orientation $\mathbf{r}(\mathbf{x})$ of the crystal at position $\mathbf{x}$. $\check{\mathbf{C}}^e$ is the elastic stiffness modulus in the lattice coordinate system.

For a microstructure subjected to periodic boundary conditions with an imposed average velocity gradient $\mathbf{L} = \nabla\mathbf{V}$, the local equilibrium equation, represented in terms of stress rate, needs to be satisfied at any point $\mathbf{x}$ within the microstructure domain $\mathcal{B}$. The complete boundary value problem is defined as:

$$\begin{aligned} \nabla \cdot \dot{\boldsymbol{\sigma}}(\mathbf{x}) &= \nabla \cdot \tilde{\dot{\boldsymbol{\sigma}}}(\mathbf{x}) = 0 \quad \forall \mathbf{x} \in \mathcal{B}, \\ \tilde{\mathbf{v}}^{e+} = \tilde{\mathbf{v}}^{e-}, &\qquad \dot{\boldsymbol{\tau}}^{+} = -\dot{\boldsymbol{\tau}}^{-} \text{ on } \partial\mathcal{B}, \end{aligned} \tag{4.2}$$

where $\tilde{\mathbf{v}}^e(\mathbf{x}) = \mathbf{v}^e(\mathbf{x}) - \mathbf{L}\cdot\mathbf{x}$ is the velocity fluctuation (deviation of the local velocity $\mathbf{v}^e(\mathbf{x})$ from the mean velocity $\mathbf{V}$) at $\mathbf{x}$ induced by the microstructure heterogeneity. The superscript e indicates that the response stems from elastic deformation. $\dot{\boldsymbol{\tau}}$ is the traction rate on the microstructure boundary. Here, we have decomposed the boundary $\partial\mathcal{B}$ of the microstructure into two parts $\partial\mathcal{B} = \partial\mathcal{B}^- \cup \partial\mathcal{B}^+$ with outward normals $\mathbf{n}^+ = -\mathbf{n}^-$ at two associated points $\mathbf{x}^- \in \partial\mathcal{B}^-$ and $\mathbf{x}^+ \in \partial\mathcal{B}^+$. Quantities on $\mathcal{B}^-$ are indicated by the superscript $-$ and those on $\mathcal{B}^+$ are indicated by superscript $+$. In periodic boundary conditions, the velocity fluctuation $\tilde{\mathbf{v}}^e$ is periodic, and the traction rate $\dot{\boldsymbol{\tau}}$ is anti-periodic in order to meet the equilibrium equations on the boundary between two neighboring cells. Our goal is to compute the velocity and its gradient for all material points that satisfy the above governing equations and use them to evaluate the strain and stress responses over the microstructure domain. To this end, we can write the local stress rate $\dot{\boldsymbol{\sigma}}(\mathbf{x})$ as the sum of two terms:

$$\dot{\boldsymbol{\sigma}}(\mathbf{x}) = \mathbf{C}^0 : \dot{\boldsymbol{\varepsilon}}^e(\mathbf{v}^e(\mathbf{x})) + \boldsymbol{\phi}^e(\mathbf{x}). \tag{4.3}$$

In Eq. (4.3), $\mathbf{C}^0$ is the stiffness modulus of the microstructure, if it were homogeneous, in which point $\mathbf{x}$ is embedded. In this elastic problem, $\mathbf{C}^0$ is selected as

the averaged elastic modulus $\mathbf{C}^e$ over the microstructure domain:

$$\mathbf{C}^0 = \mathbf{C}^{e0} = \langle \mathbf{C}^e \rangle_h = \frac{1}{V_{\mathcal{B}}} \int_{\mathcal{B}} \mathbf{C}^e(\mathbf{x}) \mathrm{d}\mathbf{x}, \tag{4.4}$$

where subscript h means homogenization and $V_{\mathcal{B}}$ is the volume of the microstructure domain $\mathcal{B}$.

The second term, $\boldsymbol{\phi}^e(\mathbf{x})$, in Eq. (4.3) is the periodic polarization field defined as

$$\boldsymbol{\phi}^e(\mathbf{x}) = \dot{\boldsymbol{\sigma}}(\mathbf{x}) - \mathbf{C}^{e0} : \dot{\boldsymbol{\varepsilon}}^e(\mathbf{v}^e(\mathbf{x})) = \tilde{\dot{\boldsymbol{\sigma}}}(\mathbf{x}) - \mathbf{C}^{e0} : \tilde{\dot{\boldsymbol{\varepsilon}}}^e(\tilde{\mathbf{v}}^e(\mathbf{x})). \tag{4.5}$$

Substituting Eq. (4.3) into the equilibrium equation (Eq. (4.2)), we obtain

$$C^{e0}_{ijkl} \dot{\varepsilon}^e_{kl,j} + \phi^e_{ij,j} = 0 \quad \text{or} \quad C^{e0}_{ijkl} \tilde{\dot{\varepsilon}}^e_{kl,j} + \phi^e_{ij,j} = 0. \tag{4.6}$$

Assuming that the elastic strain is small, the elastic strain rate can be approximately taken as the symmetric part of the velocity gradient $\dot{\varepsilon}^e_{ij} \approx D^e_{ij} = \frac{1}{2}\left(v^e_{i,j} + v^e_{j,i}\right)$. Therefore, we obtain:

$$C^{e0}_{ijkl} v^e_{k,lj} + \phi^e_{ij,j} = 0 \quad \text{or} \quad C^{e0}_{ijkl} \tilde{v}^e_{k,lj} + \phi^e_{ij,j} = 0. \tag{4.7}$$

The differential Eq. (4.7) can be solved by means of the Green's function method. Introducing the Green's function $\mathbf{G}^e(\mathbf{x}, \mathbf{x}')$, the solution $\tilde{v}^e_k(\mathbf{x})$ takes the form of

$$\tilde{v}^e_k(\mathbf{x}) = -\int_{\mathcal{B}} G^e_{km}(\mathbf{x} - \mathbf{x}') \phi^e_{mn,n}(\mathbf{x}') \mathrm{d}\mathbf{x}'. \tag{4.8}$$

Substituting Eq. (4.8) into Eq. (4.7), leads to:

$$-C^{e0}_{ijkl} \int_{\mathcal{B}} G^e_{km,lj}(\mathbf{x} - \mathbf{x}') \phi^e_{mn,n}(\mathbf{x}') \mathrm{d}\mathbf{x}' + \int_{\mathcal{B}} \delta_{im} \phi^e_{mj,j}(\mathbf{x}') \delta(\mathbf{x} - \mathbf{x}') \mathrm{d}\mathbf{x}' = 0, \tag{4.9}$$

which can be rearranged as

$$\int_{\mathcal{B}} \left[-C^{e0}_{ijkl} G^{e}_{km,lj}(\mathbf{x}-\mathbf{x}') + \delta_{im}\delta(\mathbf{x}-\mathbf{x}') \right] \phi^{e}_{mn,n}(\mathbf{x}')\mathrm{d}\mathbf{x}' = 0. \tag{4.10}$$

Taking $\phi^{e}_{mn,n}$ to be arbitrary, we arrive at the local equilibrium equation in the Green's function form:

$$-C^{e0}_{ijkl} G^{e}_{km,lj}(\mathbf{x}-\mathbf{x}') + \delta_{im}\delta(\mathbf{x}-\mathbf{x}') = 0. \tag{4.11}$$

We transform this equation to Fourier space where the convolutional solution in real space (Eq. (4.8)) is represented by a simple product. The equilibrium equation in Fourier space is then:

$$\xi_l \xi_j C^{e0}_{ijkl} \hat{G}^{e}_{km}(\boldsymbol{\xi}) = -\delta_{im}, \tag{4.12}$$

where $\boldsymbol{\xi}$ is a point (frequency) in Fourier space. Solving the linear system Eq. (4.12), we obtain the Green's function in Fourier space $\hat{G}^{e}_{km}$ to be

$$\hat{\mathbf{G}}^{e} = \mathbf{A}^{e-1}, \quad \text{with} \quad A^{e}_{ik} = -\xi_l \xi_j C^{e0}_{ijkl}. \tag{4.13}$$

Defining

$$\hat{\Gamma}^{e}_{ijkl} = -\xi_l \xi_j \hat{G}^{e}_{ik}, \tag{4.14}$$

and integrating Eq. (4.8) by parts while assuming that the boundary terms vanish [66], we can compute the velocity fluctuation as:

$$\tilde{v}^{e}_{k}(\mathbf{x}) = \int_{\mathcal{B}} G^{e}_{km,n}(\mathbf{x}-\mathbf{x}')\phi^{e}_{mn}(\mathbf{x}')\mathrm{d}\mathbf{x}'. \tag{4.15}$$

The velocity and its gradient fluctuations in Fourier space are

$$\begin{aligned} \hat{\tilde{v}}^{e}_{i}(\boldsymbol{\xi}) &= \mathrm{i}\xi_j \hat{G}^{e}_{im}(\boldsymbol{\xi})\hat{\phi}^{e}_{mj}(\boldsymbol{\xi}), \\ \hat{\tilde{v}}^{e}_{i,k}(\boldsymbol{\xi}) &= \hat{\Gamma}^{e}_{ikmj}(\boldsymbol{\xi})\hat{\phi}^{e}_{mj}(\boldsymbol{\xi}). \end{aligned} \tag{4.16}$$

After transforming them back to real space (e.g. $\tilde{\mathbf{v}}^e(\mathbf{x}) = FFT^{-1}(\hat{\tilde{\mathbf{v}}}^e(\boldsymbol{\xi}))$), the strain (stretch) rate and spin fluctuations can be evaluated, respectively, by

$$\begin{aligned} \tilde{\tilde{\varepsilon}}^e_{ij}(\mathbf{x}) &= \frac{1}{2}(\tilde{v}^e_{i,j} + \tilde{v}^e_{j,i}), \\ \tilde{\tilde{\omega}}^e_{ij}(\mathbf{x}) &= \frac{1}{2}(\tilde{v}^e_{i,j} - \tilde{v}^e_{j,i}). \end{aligned} \tag{4.17}$$

The stress rate can be updated according to the Hooke's Law (Eq. (4.1)). With the updated stress rate and strain rate, we can perform the next iteration (recompute the polarization and then the velocity gradient) until converged results are reached.

4.1.2 Solution of crystal visco-plastic boundary value problems

If the deformation is assumed to be rigid visco-plastic (i.e. the elastic response is completely neglected), $\dot{\boldsymbol{\varepsilon}} = \dot{\boldsymbol{\varepsilon}}^p$. A nonlinear constitutive model is employed to link stress to strain rate in the form of

$$\dot{\boldsymbol{\varepsilon}}^p(\mathbf{x}) = \mathbf{M}^p(\boldsymbol{\sigma}(\mathbf{x})) : \boldsymbol{\sigma}(\mathbf{x}), \tag{4.18}$$

where $\dot{\boldsymbol{\varepsilon}}^p(\mathbf{x}) = \frac{1}{2}\left(v^p_{i,j} + v^p_{j,i}\right)$ is the plastic stretch rate $\mathbf{D}^p$ (we are using the notation $\dot{\boldsymbol{\varepsilon}}^p(\mathbf{x})$ for consistency with other FFT-based developments [70]) and $\mathbf{M}^p(\boldsymbol{\sigma}(\mathbf{x}))$ is a plastic compliance tensor that is nonlinearly dependent on stress $\boldsymbol{\sigma}(\mathbf{x})$.

The solution procedure for the visco-plastic problem is similar to the pure elastic problem, except that this time the equilibrium equation is written in terms of stress rather than stress rate:

$$\begin{aligned} \nabla \cdot \boldsymbol{\sigma}(\mathbf{x}) &= \nabla \cdot \tilde{\boldsymbol{\sigma}}(\mathbf{x}) = 0 \quad \forall \mathbf{x} \in \mathcal{B}, \\ \tilde{\mathbf{v}}^{p+} = \tilde{\mathbf{v}}^{p-}, &\qquad \boldsymbol{\tau}^+ = -\boldsymbol{\tau}^- \text{ on } \partial\mathcal{B}, \end{aligned} \tag{4.19}$$

where the superscript p indicates plastic deformation induced response and $\boldsymbol{\tau}$ is the traction on the boundary. Incompressibility of plastic deformation also needs to be satisfied. In an earlier developed Fourier transform-based algorithm [66], the incompressibility condition was satisfied by introducing explicitly the constraint $v^p_{k,k} = 0$. In the current work, we account for the incompressibility condition by computing the polarization $\boldsymbol{\phi}^p(\mathbf{x})$ using a strain rate updated iteratively as $\dot{\boldsymbol{\varepsilon}}^p \leftarrow \dot{\boldsymbol{\varepsilon}}^p - \frac{1}{3} tr(\dot{\boldsymbol{\varepsilon}}^p)$ as follows:

$$\boldsymbol{\phi}^p(\mathbf{x}) = \boldsymbol{\sigma}(\mathbf{x}) - \mathbf{C}^{p0} : \dot{\boldsymbol{\varepsilon}}^p(\mathbf{v}^p(\mathbf{x})) = \tilde{\boldsymbol{\sigma}}(\mathbf{x}) - \mathbf{C}^{p0} : \tilde{\dot{\boldsymbol{\varepsilon}}}^p(\tilde{\mathbf{v}}^p(\mathbf{x})), \tag{4.20}$$

where the stiffness modulus of the linear homogeneous reference medium is taken to be the averaged plastic modulus $\mathbf{C}^p = \mathbf{M}^{p-1}$ over the microstructure domain:

$$\mathbf{C}^{p0} = \langle \mathbf{C}^p \rangle_h = \frac{1}{V_{\mathcal{B}}} \int_{\mathcal{B}} \mathbf{C}^p(\boldsymbol{\sigma}(\mathbf{x})) \mathrm{d}\mathbf{x}. \tag{4.21}$$

The plastic modulus $\mathbf{C}^p$ or equivalently the plastic compliance $\mathbf{M}^p$ is determined by the specific plastic constitutive model that is adopted (see Section 4.3). The plastic problem can be solved following the steps from Eq. (4.6) to Eq. (4.17) simply by replacing the superscript e to p and using stress instead of stress rate.

4.1.3 Solution of crystal elasto-viscoplastic boundary value problems

For elasto-viscoplastic problems, the total strain rate $\dot{\boldsymbol{\varepsilon}}$ is additively decomposed into elastic $\dot{\boldsymbol{\varepsilon}}^e$ and plastic $\dot{\boldsymbol{\varepsilon}}^p$ terms with $tr(\dot{\boldsymbol{\varepsilon}}^p) = 0$:

$$\dot{\boldsymbol{\varepsilon}}(\mathbf{x}) = \dot{\boldsymbol{\varepsilon}}^e(\mathbf{x}) + \dot{\boldsymbol{\varepsilon}}^p(\mathbf{x}). \tag{4.22}$$

Following the constitutive relations given above, we observe both stress $\boldsymbol{\sigma}$ and stress rate $\dot{\boldsymbol{\sigma}}$ are entangled with strain rate:

$$\dot{\boldsymbol{\varepsilon}}(\mathbf{x}) = \mathbf{M}^e(\mathbf{x}) : \dot{\boldsymbol{\sigma}}(\mathbf{x}) + \mathbf{M}^p(\boldsymbol{\sigma}(\mathbf{x})) : \boldsymbol{\sigma}(\mathbf{x}), \tag{4.23}$$

where $\mathbf{M}^e = \mathbf{C}^{e-1}$ is the elastic compliance tensor. The local mechanical response at time t depends on the entire loading history of the specimen. The current stress $\boldsymbol{\sigma}$ can be updated by $\boldsymbol{\sigma} = \boldsymbol{\sigma}_n + \Delta t \dot{\boldsymbol{\sigma}}$, where $\boldsymbol{\sigma}_n$ is the stress at the previous time step.

To follow a Green's function approach to the elasto-viscoplastic boundary value problem, a proper modulus $\mathbf{C}^0$ needs to be designed for the homogeneous reference medium that can directly link either stress or stress rate to strain rate. However, to design such an effective modulus is not trivial [121], and the constitutive formulation is not unique. Therefore, we here propose a scheme that solves separately for the elastic and plastic velocity fluctuations using the fast Fourier transform-based algorithm, and thus avoid the construction of the homogeneous moduls. The total velocity gradient at a single point is then computed by adding the two fluctuations to the mean value $\nabla \mathbf{V}$. After that, a nonlinear constitutive model is designed to update the stress and stress rate given the total strain rate. We will refer to this approach that separates the elastic and plastic velocity fluctuations as the main CEPFFT formulation.

The key of this CEPFFT approach is that we solve simultaneously the two forms of the equilibrium equations defined in Eqs. (4.2) and (4.19) for elastic and plastic velocity (and their gradient) fluctuations. The total velocity gradient can then be obtained by

$$\nabla \mathbf{v}(\mathbf{x}) = \nabla \mathbf{V} + \nabla \tilde{\mathbf{v}}^e(\mathbf{x}) + \nabla \tilde{\mathbf{v}}^p(\mathbf{x}), \tag{4.24}$$

from which, the total strain rate $\dot{\boldsymbol{\varepsilon}}$ can be calculated as the symmetric part of $\nabla \mathbf{v}$. However, the portion of elastic strain rate $\dot{\boldsymbol{\varepsilon}}^e$ and plastic strain rate $\dot{\boldsymbol{\varepsilon}}^p$ in $\dot{\boldsymbol{\varepsilon}}$ is not known. As a result, one can not directly compute the stress and stress rate corresponding to a given total strain rate.

An iterative scheme is designed to linearize the nonlinear relations among stress, stress rate, and strain rates, in order to find the elastic and plastic strain rates given the total strain rate. We first rewrite Eq. (4.22) as

$$\mathbf{f} = \dot{\boldsymbol{\varepsilon}}^e(\mathbf{x}) + \dot{\boldsymbol{\varepsilon}}^p(\mathbf{x}) - \dot{\boldsymbol{\varepsilon}}(\mathbf{x}) = \mathbf{0}. \tag{4.25}$$

We aim at solving this equation for the elastic strain rate $\dot{\boldsymbol{\varepsilon}}^e$ with known $\dot{\boldsymbol{\varepsilon}}$ using the Newton-Raphson scheme. To this end, Eq. (4.25) can be linearized as follows:

$$\mathbf{f}^{(i+1)}(\dot{\boldsymbol{\varepsilon}}^{e(i+1)}) = \mathbf{f}^{(i)}(\dot{\boldsymbol{\varepsilon}}^{e(i)}) + \frac{\mathrm{d}\mathbf{f}}{\mathrm{d}\dot{\boldsymbol{\varepsilon}}^e}\left(\dot{\boldsymbol{\varepsilon}}^{e(i+1)} - \dot{\boldsymbol{\varepsilon}}^{e(i)}\right). \tag{4.26}$$

According to the elastic and plastic constitutive models, as well as the stress incremental equation $\boldsymbol{\sigma} = \boldsymbol{\sigma}_n + \Delta t\dot{\boldsymbol{\sigma}}$, we can write the following relations:

$$\begin{aligned}
\frac{\mathrm{d}\dot{\boldsymbol{\varepsilon}}^p}{\mathrm{d}\boldsymbol{\sigma}} &= \mathbf{M}_t^p, \\
\frac{\mathrm{d}\boldsymbol{\sigma}}{\mathrm{d}\dot{\boldsymbol{\sigma}}} &= \frac{\mathrm{d}\left(\boldsymbol{\sigma}_n + \Delta t\dot{\boldsymbol{\sigma}}\right)}{\mathrm{d}\dot{\boldsymbol{\sigma}}} = \Delta t\mathbf{II}, \\
\frac{\mathrm{d}\dot{\boldsymbol{\sigma}}}{\mathrm{d}\dot{\boldsymbol{\varepsilon}}^e} &= \mathbf{C}^e,
\end{aligned} \tag{4.27}$$

where $\mathbf{II}$ is the fourth-order identity tensor and the tangent plastic compliance $\mathbf{M}_t^p$ is specified by the particular plastic constitutive model used (see Section 4.3). Using these relations, we can expand Eq. (4.27) as:

$$\mathbf{f}^{(i+1)}(\dot{\boldsymbol{\varepsilon}}^{e(i+1)}) = \mathbf{f}^{(i)}(\dot{\boldsymbol{\varepsilon}}^{e(i)}) + \left(\frac{\mathrm{d}\dot{\boldsymbol{\varepsilon}}^e}{\mathrm{d}\dot{\boldsymbol{\varepsilon}}^e} + \frac{\mathrm{d}\dot{\boldsymbol{\varepsilon}}^p}{\mathrm{d}\dot{\boldsymbol{\varepsilon}}^e}\right) : \left(\dot{\boldsymbol{\varepsilon}}^{e(i+1)} - \dot{\boldsymbol{\varepsilon}}^{e(i)}\right)$$

$$
\begin{aligned}
&= \mathbf{f}^{(i)}(\dot{\boldsymbol{\varepsilon}}^{e(i)}) + \left(\frac{\mathrm{d}\dot{\boldsymbol{\varepsilon}}^{e}}{\mathrm{d}\dot{\boldsymbol{\varepsilon}}^{e}} + \frac{\mathrm{d}\dot{\boldsymbol{\varepsilon}}^{p}}{\mathrm{d}\boldsymbol{\sigma}}\frac{\mathrm{d}\boldsymbol{\sigma}}{\mathrm{d}\dot{\boldsymbol{\sigma}}}\frac{\mathrm{d}\dot{\boldsymbol{\sigma}}}{\mathrm{d}\dot{\boldsymbol{\varepsilon}}^{e}}\right) : \left(\dot{\boldsymbol{\varepsilon}}^{e(i+1)} - \dot{\boldsymbol{\varepsilon}}^{e(i)}\right) \\
&= \mathbf{f}^{(i)}(\dot{\boldsymbol{\varepsilon}}^{e(i)}) + (\mathbf{II} + \Delta t \mathbf{M}_t^p : \mathbf{C}^e) : \left(\dot{\boldsymbol{\varepsilon}}^{e(i+1)} - \dot{\boldsymbol{\varepsilon}}^{e(i)}\right). \qquad (4.28)
\end{aligned}
$$

Setting $\mathbf{f}^{(i+1)} = \mathbf{0}$, the elastic strain rate at iteration $i+1$ is computed by

$$
\dot{\boldsymbol{\varepsilon}}^{e(i+1)} = \dot{\boldsymbol{\varepsilon}}^{e(i)} - (\mathbf{II} + \Delta t \mathbf{M}_t^p : \mathbf{C}^e)^{-1} : \mathbf{f}^{(i)}. \qquad (4.29)
$$

With the elastic strain rate $\dot{\boldsymbol{\varepsilon}}^{e(i+1)}$ at the $(i+1)$th iteration computed from the equation above, the stress rate $\dot{\boldsymbol{\sigma}}^{(i+1)}$ can be obtained using Eq. (4.1). Therefore, the stress is updated as $\boldsymbol{\sigma}^{(i+1)} = \boldsymbol{\sigma}_n + \Delta t \dot{\boldsymbol{\sigma}}^{(i+1)}$, with which the plastic strain rate $\dot{\boldsymbol{\varepsilon}}^{p(i+1)}$ can be computed using the plastic constitutive relation Eq. (4.18). The impressibility is enforced by setting $\dot{\boldsymbol{\varepsilon}}^{p(i+1)} \leftarrow \dot{\boldsymbol{\varepsilon}}^{p(i+1)} - \frac{1}{3} tr(\dot{\boldsymbol{\varepsilon}}^{p(i+1)})$. Iteratively updating the above equations, the final elastic as well as the plastic strain rates can be computed until convergence is achieved (i.e. when $\mathbf{f}^{i+1}$ in Eq. (4.28) approaches $\mathbf{0}$). The result is not sensitive to the magnitude of Δt. After that, we can construct the elastic and plastic polarization fields, respectively, following Eqs. (4.5) and (4.20), respectively. By transforming them to Fourier space, the fluctuations of velocity gradients induced by elastic and plastic deformation can be updated using Green's functions. Inversely transforming these fluctuations to real space, a new strain rate field as well as stress and stress rate can be obtained. The algorithm can then proceed to the next iteration. The overall CEPFFT algorithm is summarized next.

4.1.4 CEPFFT algorithm

We adopt a basic fast Fourier transform-based algorithm to implement the CEPFFT simulator [66, 93, 94]. This method is based on the exact expression

of Green's function for linear elastic, homogeneous reference material.

Algorithm:

1. At the first iteration, start with an initial guess of the total velocity gradient field at time step $n+1$: ${}^0\nabla\mathbf{v}_{n+1}(\mathbf{x}) = \nabla\mathbf{v}_n(\mathbf{x}), \forall\mathbf{x} \in \mathcal{B}$, from which the local strain rate can be computed $\dot{\boldsymbol{\varepsilon}}(\mathbf{x}) = sym(\nabla\mathbf{v}(\mathbf{x}))$. Then evaluate the elastic portion $\dot{\boldsymbol{\varepsilon}}^e(\mathbf{x})$ and plastic portion $\dot{\boldsymbol{\varepsilon}}^p(\mathbf{x})$ of the strain rate using the Newton-Raphson algorithm (Eqs. (4.25)-(4.29)). At the same time, compute the initial stress ${}^0\boldsymbol{\sigma}(\mathbf{x})$ and stress rate ${}^0\dot{\boldsymbol{\sigma}}(\mathbf{x})$.

2. Compute the elastic and plastic polarization fields, ${}^i\boldsymbol{\phi}^e(\mathbf{x})$ and ${}^i\boldsymbol{\phi}^p(\mathbf{x})$, respectively, for the i iteration given the stress, stress rate and strain rate fields:

$$
\begin{aligned}
{}^i\boldsymbol{\phi}^e(\mathbf{x}) &= {}^i\,\dot{\boldsymbol{\sigma}}(\mathbf{x}) - \mathbf{C}^{e0} :^i\, \dot{\boldsymbol{\varepsilon}}^e(\mathbf{x}),\\
{}^i\boldsymbol{\phi}^p(\mathbf{x}) &= {}^i\,\boldsymbol{\sigma}(\mathbf{x}) - \mathbf{C}^{p0} :^i\, \dot{\boldsymbol{\varepsilon}}^p(\mathbf{x}).
\end{aligned}
\tag{4.30}
$$

3. Transform the polarizations to Fourier space via fast Fourier transform: ${}^i\hat{\boldsymbol{\phi}}^e(\boldsymbol{\xi}) = FFT\left({}^i\boldsymbol{\phi}^e(\mathbf{x})\right)$ and ${}^i\hat{\boldsymbol{\phi}}^p(\boldsymbol{\xi}) = FFT\left({}^i\boldsymbol{\phi}^p(\mathbf{x})\right)$.

4. Compute the velocity gradient fluctuation fields induced by elastic and plastic deformation, respectively, in the Fourier space for the $(i+1)$-th iteration.

$$
\begin{aligned}
{}^{i+1}\nabla\hat{\tilde{\mathbf{v}}}^e(\boldsymbol{\xi}) &= \hat{\boldsymbol{\Gamma}}^e(\boldsymbol{\xi}) :^i\, \hat{\boldsymbol{\phi}}^e(\boldsymbol{\xi}), \forall\boldsymbol{\xi} \neq \mathbf{0};\ \text{ and }\ {}^{i+1}\nabla\hat{\tilde{\mathbf{v}}}^e(\mathbf{0}) = \mathbf{0},\\
{}^{i+1}\nabla\hat{\tilde{\mathbf{v}}}^p(\boldsymbol{\xi}) &= \hat{\boldsymbol{\Gamma}}^p(\boldsymbol{\xi}) :^i\, \hat{\boldsymbol{\phi}}^p(\boldsymbol{\xi}), \forall\boldsymbol{\xi} \neq \mathbf{0};\ \text{ and }\ {}^{i+1}\nabla\hat{\tilde{\mathbf{v}}}^p(\mathbf{0}) = \mathbf{0}.
\end{aligned}
\tag{4.31}
$$

5. Transform the current velocity gradient fluctuation fields back to real space through inverse fast Fourier transform, i.e. ${}^{i+1}\nabla\tilde{\mathbf{v}}^e(\mathbf{x}) = FFT^{-1}\left({}^{i+1}\nabla\hat{\tilde{\mathbf{v}}}^e(\boldsymbol{\xi})\right)$ and ${}^{i+1}\nabla\tilde{\mathbf{v}}^p(\mathbf{x}) = FFT^{-1}\left({}^{i+1}\nabla\hat{\tilde{\mathbf{v}}}^p(\boldsymbol{\xi})\right)$.

6. Compute the total strain rate ${}^{i+1}\dot{\boldsymbol{\varepsilon}} = \dot{\mathbf{E}} + {}^{i+1}\tilde{\dot{\boldsymbol{\varepsilon}}}^{e} + {}^{i+1}\tilde{\dot{\boldsymbol{\varepsilon}}}^{p}$ and then the stress ${}^{i+1}\boldsymbol{\sigma}(\mathbf{x})$ and stress rate ${}^{i+1}\dot{\boldsymbol{\sigma}}(\mathbf{x})$ fields according to the constitutive model.

7. Check the error (equilibrium condition) [94]:

$$e = \frac{\left\langle \|\nabla \cdot {}^{i+1}\boldsymbol{\sigma}\|^2 \right\rangle_h^{1/2}}{\|{}^{i+1}\boldsymbol{\sigma}\|} = \frac{\left\langle \|\boldsymbol{\xi} \cdot {}^{i+1}\hat{\boldsymbol{\sigma}}\|^2 \right\rangle_h^{1/2}}{\|{}^{i+1}\hat{\boldsymbol{\sigma}}(\mathbf{0})\|}. \tag{4.32}$$

   If e is smaller than a prescribed error tolerance, the iteration process stops. Otherwise, return to step (2) and proceed to the next iteration.

Upon convergence, the grain orientations and the positions of the microstructure pixel points are updated according to the spin and velocity gradient fields, respectively (see Section 4.2.2 for details).

Remark 1: The error of the equilibrium condition (Step 7) is mostly determined by the resolution of the image (as it will be shown later in the examples). For images with coarse resolution, the error may converge to a value larger than 0. This error is inherently associated with the FFT-based methodology. Therefore, a practical way to check the convergence is to examine the relevant difference between the error at the current and last iterations:

$$\eta = \frac{|{}^{i+1}e - {}^{i}e|}{{}^{i+1}e}. \tag{4.33}$$

4.1.5 An integrated formulation

It is clear that the computational cost of one iteration step of the algorithm discussed above is approximately doubled that corresponding to either the pure elastic or rigid visco-viscoplastic scenario. A more straightforward thinking of

solving the elasto-viscoplastic problem may be constructing the connection between stress (or stress rate) and total strain (or strain rate) directly, and compute the mechanical responses using only one set of governing equations. This requires one to design a proper modulus $\mathbf{C}^0$ of the reference medium, which determines the convergence rate and the accuracy of the algorithm.

In [121, 70], an integrated formulation based on stress and total strain was proposed:

$$\boldsymbol{\sigma}(\mathbf{x}) = \mathbf{C}^0 : \boldsymbol{\varepsilon}(\mathbf{x}) + \boldsymbol{\phi}(\mathbf{x}). \tag{4.34}$$

The same basic scheme as introduced in the current work was adopted by [121] to solve the problem, while an augmented Lagrangian scheme was used in [70]. A semi-empirical $\mathbf{C}^0$ was chosen for the reference medium [121].

In the current work, we also propose a similar integrated strategy for solving the elasto-viscoplasticity problem. An incremental form is chosen to represent the local stress $\boldsymbol{\sigma}(\mathbf{x})$ in terms of the total strain rate $\dot{\boldsymbol{\varepsilon}}(\mathbf{v}(\mathbf{x}))$:

$$\boldsymbol{\sigma}(\mathbf{x}) = \mathbf{C}^0 : \dot{\boldsymbol{\varepsilon}}(\mathbf{v}(\mathbf{x})) + \boldsymbol{\phi}(\mathbf{x}), \tag{4.35}$$

where the strain rate $\dot{\boldsymbol{\varepsilon}}(\mathbf{v}(\mathbf{x}))$ can be additively decomposed into the elastic strain rate $\dot{\boldsymbol{\varepsilon}}^e(\mathbf{v}(\mathbf{x}))$ and the plastic strain rate $\dot{\boldsymbol{\varepsilon}}^p(\mathbf{v}(\mathbf{x}))$ as given in Eq. (4.22). The reference modulus $\mathbf{C}^0 = \langle \mathbf{C}^{ep} \rangle_h$ is taken as the volume average of the local elasto-viscoplastic modulus $\mathbf{C}^{ep}$ approximately derived as follows:

$$\mathbf{C}^{ep} = \left(\frac{\mathrm{d}\dot{\boldsymbol{\varepsilon}}}{\mathrm{d}\boldsymbol{\sigma}} \right)^{-1} = \left(\frac{\mathrm{d}\dot{\boldsymbol{\varepsilon}}}{\mathrm{d}\dot{\boldsymbol{\varepsilon}}^e} \frac{\mathrm{d}\dot{\boldsymbol{\varepsilon}}^e}{\mathrm{d}\boldsymbol{\sigma}} + \frac{\mathrm{d}\dot{\boldsymbol{\varepsilon}}}{\mathrm{d}\dot{\boldsymbol{\varepsilon}}^p} \frac{\mathrm{d}\dot{\boldsymbol{\varepsilon}}^p}{\mathrm{d}\boldsymbol{\sigma}} \right)^{-1} \approx \left(\frac{\mathbf{M}^e}{\Delta t} + \mathbf{M}^p \right)^{-1}. \tag{4.36}$$

The plastic compliance $\mathbf{M}^p$ is chosen to be the secant compliance that depends on the specifics of the constitutive model adopted. With the construction of

the elasto-viscoplastic modulus, the problem is solved following the same procedure as for the visco-plastic problem. Following the steps from Eq. (4.6) to Eq. (4.17) by removing the superscript e and using stress instead of stress rate, we can solve for the total velocity fluctuation $\tilde{\mathbf{v}}$ and its gradient $\nabla\tilde{\mathbf{v}}$. The convergence rate of this particular algorithm is slower than the main algorithm presented earlier, especially at the transient elasto-viscoplastic regime. A more sophisticated design of $\mathbf{C}^0$ is of great interest. In the following, we will refer to this model as the modified CEPFFT.

It is worth mentioning that the averaged elastic modulus $\mathbf{C}^{e0}$ (Eq.(4.4)) and plastic modulus $\mathbf{C}^{p0}$ (Eq.(4.21)) adopted by the main separate form are also not proven to be optimal for their reference media. However, these moduli have been widely used in pure elastic and visco-plastic problems, respectively, and shown to provide very good convergence rates. It is thus favorable that the separate form directly takes advantage of the existing elastic and visco-plastic formulations. Furthermore, using the main (separate) formulation, we avoid the issue of the non-unique constitutive formulation as seen in the modified (integrated) form.

4.2 Microstructure model

The solution strategy of computing the deformation of polycrystalline microstructures under periodic boundary conditions was discussed in Section 4.1. The main procedure is: (1) compute polarization field; (2) transform the polarization field to Fourier space using fast Fourier transform; (3) update velocity gradient in Fourier space and transform it back to real space; (4) update real-

space fields (e.g. strain rate, spin tensor, stress rate, etc.) accordingly. An iterative scheme is adopted to obtain convergence. In this section, we introduce the digital microstructure model that is used as the input to FFT-based simulations. The update strategy of the microstructure and crystal orientation during deformation is also described.

4.2.1 Discretization

The input to the FFT-based (including pure elastic, rigid visco-plastic, and elasto-viscoplastic) simulators is a pixelized image with orientation parameters associated with each pixel (or voxel for 3D). The pixels or voxels are the discretization of the input image, which essentially requires no effort.

To apply the FFT-based algorithm and solve the underlying boundary value problem, the microstructure is discretized by a regular grid consisting of $N_1 \times N_2$ pixels (2D problem) or $N_1 \times N_2 \times N_3$ voxels (3D problem). Denote L_i to be the period (edge length) of the microstructure in the ith direction ($i = 1, 2$ for 2D and $i = 1, 2, 3$ for 3D). The coordinates of the points in the i-th direction are therefore:

$$x_i = 0, \frac{L_i}{N_i}, 2\frac{L_i}{N_i}, \ldots, (N_i - 1)\frac{L_i}{N_i}. \tag{4.37}$$

In Fig. 4.1, examples of 2D and 3D grids of polycrystalline microstructures are shown in comparison with their image views. Different colors in the microstructure represent grains with distinct orientations. We use a Voronoi tessellation scheme to generate grain structures. The positions of centroids are adjusted to minimize the interaction forces [106].

The regular discretization grid of the microstructure determines a regular

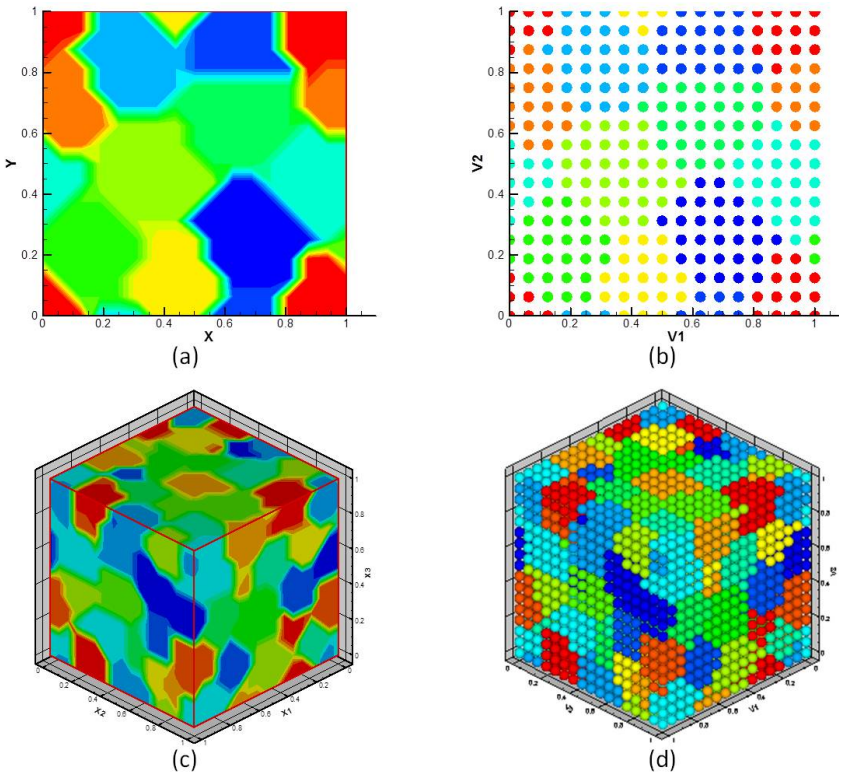

Figure 4.1: (a) The image representation of a 2D polycrystalline microstructure containing 10 grains. (b) The pixel grid of the 10-grain 2D microstructure. The microstructure is discretized by 16×16 pixels. (c) The image representation of a 3D polycrystalline microstructure containing 64 grains. (b) The voxel grid of the 64-grain 3D microstructure. The microstructure is discretized by $16 \times 16 \times 16$ voxels.

reciprocal grid in Fourier space, which makes the fast Fourier transform convenient. The i-th direction coordinates of the points in the reciprocal grid, namely frequencies, are

$$\begin{aligned} \xi_i = &\left(-\frac{N_i}{2}+1\right)\frac{1}{L_i}, \left(-\frac{N_i}{2}+2\right)\frac{1}{L_i}, \ldots, \\ &-\frac{1}{L_i}, 0, \frac{1}{L_i}, \ldots, \left(\frac{N_i}{2}-1\right)\frac{1}{L_i}, \left(\frac{N_i}{2}\right)\frac{1}{L_i}, \end{aligned} \tag{4.38}$$

where $i = 1, 2$ for 2D and $i = 1, 2, 3$ for 3D. In the current work, the number of points in each dimension is selected to be a power of 2 in order to facilitate the

fast Fourier transform that is conducted using the FFTW libraries [26].

4.2.2 Grid and texture update

The grid after deformation may become irregular as material points move according to local velocities. The new position of material point $\mathbf{X}$ is

$$\mathbf{x}(\mathbf{X}) = \mathbf{X} + (\mathbf{L}\mathbf{X} + \tilde{\mathbf{v}}(\mathbf{X}))\,\Delta t, \tag{4.39}$$

where $\mathbf{L} = \nabla\mathbf{V}$ is the homogeneous (average) velocity gradient of the microstructure and $\nabla\tilde{\mathbf{v}}(\mathbf{X})$ is the velocity gradient fluctuation at point $\mathbf{X}$.

To model the deformation of the microstructure, an irregular material grid is expected. However, this irregular grid in the real space results in difficulties on conducting Fourier transform in the next time step in a time-dependent simulation, because that fast Fourier transform requires a regular grid. To resolve this complexity, we introduce a strategy of using two grids, a regular computation grid and an irregular material configuration grid, proposed in [60] based on the Particle-In-Cell (PIC) method [114, 115]. On one hand, the computation grid is used for applying the fast Fourier transform method to evaluate the strain related fields. It is a regular grid but not necessarily rectangular. The material grid, on the other hand, is attached to material particles, on which constitutive relations are carried out.

Each grid carries its own set of unknowns. Information needs to be transferred back and forth between the two grids during computation. At the beginning of each time step, the initial guess of local stress and polarization are computed on the material grid given the initial strain rate. The polarization

field is transferred to the computation grid, on which fast Fourier transform is performed. The updated velocity gradient is then transferred back to the material grid so that the stress related fields can be updated using the constitutive model. At the end of the time step, the computation and material grids are deformed. The material particles move according to local velocity (Eq. (4.39)) and the regular computation grid evolves with the average velocity gradient:

$$\mathbf{x}(\mathbf{X}) = (\mathbf{I} + \mathbf{L}\Delta t)\,\mathbf{X}. \tag{4.40}$$

A schematic showing the operation of the multi-grid strategy is depicted in Fig. 4.2.

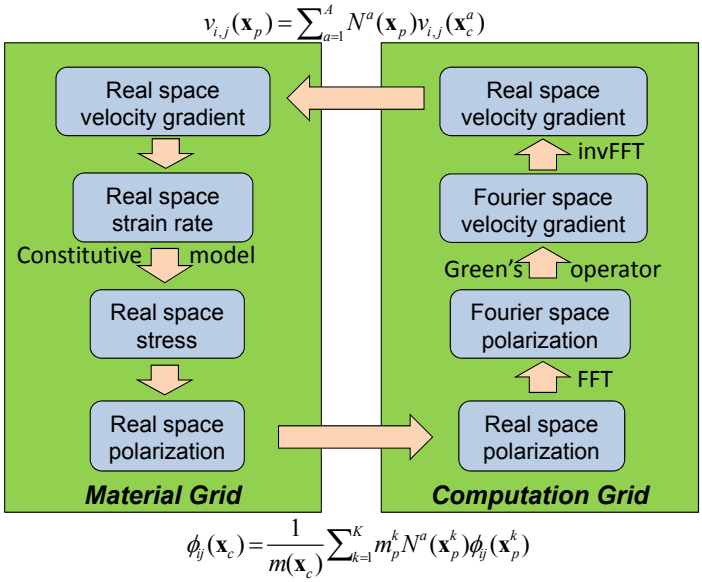

Figure 4.2: A schematic description of the multi-grid CEPFFT strategy. The constitutive model is applied only on the material grid, whereas fast Fourier transform operates on the computation grid.

Given nodal values $f_c(\mathbf{x}_c^a)$ of a function $f(\mathbf{x})$ on the computation grid (denoted by subscript c), the interpolated value at any material point $\mathbf{x}_p$ in the mi-

crostructure (denoted by subscript p) is given as

$$f_p(\mathbf{x}_p) = \sum_a^A N^a(\mathbf{x}_p) f_c(\mathbf{x}_c^a), \tag{4.41}$$

where $N^a(\mathbf{x}_p), a = 1, \ldots, A$ are the finite element basis functions for the element that contains particle $\mathbf{x}_p$. Quadrilateral (in 2D) and brick (in 3D) elements are used for the computation grid.

The inverse transfer from the material grid to the computation grid is performed using the same interpolation functions [60]. We assume that all material particles have the same 'mass' m_p. The 'mass' of a computational node is defined as

$$m_c(\mathbf{x}_c) = \sum_{k=1}^K m_p^k N^a(\mathbf{x}_p^k). \tag{4.42}$$

The sum is over all material particles that are contained in the elements that share a common computation node $\mathbf{x}_c$. N^a is the basis function that is associated with the node $\mathbf{x}_c$, and defined in the element which contains particle $\mathbf{x}_p^k$. The function value f_c of f at any computation node $\mathbf{x}_c$ is therefore:

$$f_c(\mathbf{x}_c) = \frac{1}{m_c(\mathbf{x}_c)} \sum_{k=1}^K m_p^k N^a(\mathbf{x}_p^k) f_p(\mathbf{x}_p^k). \tag{4.43}$$

A 2D illustration of the initial and deformed computation and material grids is shown in Fig. 4.3, where big red dots represent material particles and small black dots are the nodes of the computation grid. The deformed computation grid remains regular so that fast Fourier transform can be conducted, while material particles move heterogeneously. In most PIC studies, the material grid is finer than the computation grid. In the current work, however, we employ the same resolution of the two grids.

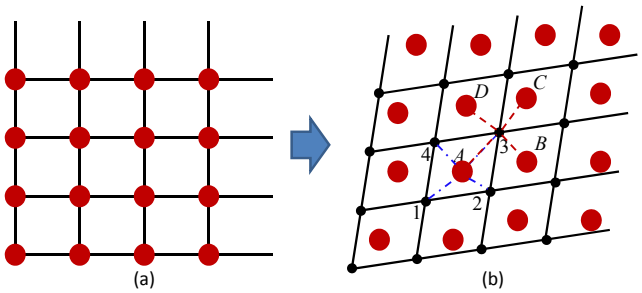

Figure 4.3: (a) Initial computation and material grids. (2) Deformed computation and material grids. The red dots denote material particles and the black dots denote nodes of the computation grid. The blue dash-dot lines show the connection between one material particle (A) and computation nodes and the red dashed lines are the connections between one computation node (3) and surrounding material particles.

This multi-grid strategy requires extra computation time. In the literature, one regular grid is used and the material grid is assumed to coincide with the computation grid at all times [69, 97]. For numerical examples, we will conduct simulations primarily using this single-grid simplification. Comparison with the results obtained from the multi-grid approach will be reported. It will be shown that for the examples considered, the mechanical responses computed from the multi- or single-grid approaches do not vary significantly, although the deformed microstructures have distinct geometry.

The orientations of crystals also evolve with deformation. Upon convergence, the local crystallographic lattice rotations can be updated by the spin tensor calculated by

$$\dot{\omega}(\mathbf{x}) = \dot{\mathbf{\Omega}} + \tilde{\dot{\omega}}(\mathbf{x}) - \dot{\omega}^{slip}(\mathbf{x}), \tag{4.44}$$

where $\dot{\mathbf{\Omega}} = antisym(\nabla \mathbf{V})$ is the average spin tensor over the microstructure domain. $\tilde{\dot{\omega}}(\mathbf{x}) = \tilde{\dot{\omega}}^e(\mathbf{x}) + \tilde{\dot{\omega}}^p(\mathbf{x})$ is the spin fluctuation induced by elastic and plastic rotation. The last term that is subtracted is the rotation rate due to plastic shear

(slip) that does not distort the crystal lattice. It is calculated by

$$\dot{\boldsymbol{\omega}}^{slip}(\mathbf{x}) = \sum_{\alpha}^{N_s} \boldsymbol{\beta}^{(\alpha)} \cdot \dot{\gamma}^{(\alpha)}, \tag{4.45}$$

where $\dot{\gamma}^{(\alpha)}$ is the shearing rate on slip system α, $\boldsymbol{\beta}^{(\alpha)}$ is the anti-symmetric Schmid tensor, $\boldsymbol{\beta}^{(\alpha)} = antisym(\mathbf{S}^{(\alpha)}) = \frac{1}{2}(\mathbf{s}^{(\alpha)} \otimes \mathbf{n}^{(\alpha)} - \mathbf{n}^{(\alpha)} \otimes \mathbf{s}^{(\alpha)})$, and $\mathbf{s}^{(\alpha)}$, $\mathbf{n}^{(\alpha)}$ are the slip direction and normal to the slip plane of the α-th slip system, respectively.

4.3 Numerical examples

In this section, we present numerical examples conducted using the fast Fourier transform based approach. Comparison between different formulations (visco-plasticity vs. elasto-viscoplasticity) and between different methods (finite element method vs. fast Fourier transform based methods) are conducted to validate the current developments. In addition, the basic formulation introduced in this paper is compared with the augmented Lagrangian approach formulated in [68, 97]. Mechanical response and fatigue properties measured by strain based fatigue indicator parameters [82] of IN100 microstructures are studied using the novel CEPFFT method. The computational efficiency of CEPFFT and crystal plasticity finite element method are presented to show the merit of the CEPFFT method. The use of the multi-grid strategy is also discussed.

4.3.1 Basic formulation versus the augmented Lagrangian formulation

We will start with a benchmark plane strain example of 3D polycrystalline microstructure simulated using the crystal visco-plasticity fast Fourier transform method (elastic response is neglected). The single-grid strategy is adopted. The crystal visco-plastic constitutive model proposed in [7] along with a Voce type hardening model described in [97] are implemented in the basic framework highlighted earlier in this paper as well as in the augmented Lagrangian formulation [68, 97]. Through this particular constitutive law, the stress-strain rate relation formulated in Eq.(4.18) is specified as follows:

$$\dot{\boldsymbol{\varepsilon}}^p(\mathbf{x}) = \mathbf{M}_s^p(\boldsymbol{\sigma}(\mathbf{x})) : \boldsymbol{\sigma}(\mathbf{x}), \tag{4.46}$$

where the secant plastic compliance $\mathbf{M}_s^p$ is taken as:

$$\mathbf{M}_s^p\left(\boldsymbol{\sigma}(\mathbf{x})\right) = \dot{\gamma}_0 \sum_{\alpha}^{N_s} \frac{\mathbf{m}^{(\alpha)}(\mathbf{x}) \otimes \mathbf{m}^{(\alpha)}(\mathbf{x})}{\kappa^{(\alpha)}(\mathbf{x})} \left| \frac{\mathbf{m}^{(\alpha)}(\mathbf{x}) : \boldsymbol{\sigma}(\mathbf{x})}{\kappa^{(\alpha)}(\mathbf{x})} \right|^{(1/m-1)}. \tag{4.47}$$

In the equation above, $\dot{\gamma}_0$ is a reference rate of shearing, m characterizes the material rate sensitivity, $\kappa^{(\alpha)}(\mathbf{x})$ is the slip resistance of system α, N_s is the number of active slip systems, and $\mathbf{m}^{(\alpha)}$ denotes the symmetric Schmid tensor of slip system α:

$$\mathbf{m}^{(\alpha)} = sym(\mathbf{S}^{(\alpha)}) = \frac{1}{2}\left(\mathbf{s}^{(\alpha)} \otimes \mathbf{n}^{(\alpha)} + \mathbf{n}^{(\alpha)} \otimes \mathbf{s}^{(\alpha)}\right), \tag{4.48}$$

where $\mathbf{s}^{(\alpha)}$ and $\mathbf{n}^{(\alpha)}$ are the slip direction and slip plane normal of the system α, respectively.

The volume average of the local secant plastic modulus is taken to be the modulus of the reference medium defined by Eq. (4.21) ($\mathbf{C}^{p0} = \langle \mathbf{M}_s^{p-1} \rangle_h$). The

corresponding tangent plastic compliance in Eq. (4.29) at this specific case is $\mathbf{M}_t^p = \frac{1}{m}\mathbf{M}_s^p$. The plastic compliance in Eq. (4.36) for the integrated method highlighted in Section 4.1.5 is $\mathbf{M}^p = \mathbf{M}_s^p$.

FCC aluminum is considered. A cubic polycrystalline microstructure composed of 64 grains is generated using the Voronoi tessellation scheme [106] in an $1mm^3$ domain. The microstructure is discretized by $16 \times 16 \times 16$ equally spaced voxels. The macroscale velocity gradient is

$$\mathbf{L} = \nabla\mathbf{V} = \begin{bmatrix} 0.0 & 0.0 & 0.0 \\ 0.0 & 1.0 & 0.0 \\ 0.0 & 0.0 & -1.0 \end{bmatrix} \times 10^{-3}(s^{-1}). \tag{4.49}$$

The rate-dependent flow rule as given in [97] is used with $\dot{\gamma}_0 = 1s^{-1}$ and $m = 0.1$. The parameters in the Voce type hardening law are selected according to [97]: $\kappa_0 = 47.0MPa$, $\kappa_1 = 86.0MPa$, $\theta_0 = 550.0Mpa$, and $\theta_1 = 16.0MPa$. An arbitrary random texture is assigned to the microstructure. The initial microstructure configuration and pole figures showing the random orientation distribution are shown in Fig. 4.4.

This example is aiming at validating the implementation of the basic FFT framework by providing a comparison with the alternative augmented Lagrangian implementation. After the thickness of the microstructure reduces by 50%, the deformed microstructure and its stress and strain fields are plotted in Fig. 4.5. For both implementations, the stress distribution over the microstructure is consistent with the grain geometry. The local mechanical responses of the two simulations are very close. Both intergranular and intragranular heterogeneities of the stress and strain rate fields are captured.

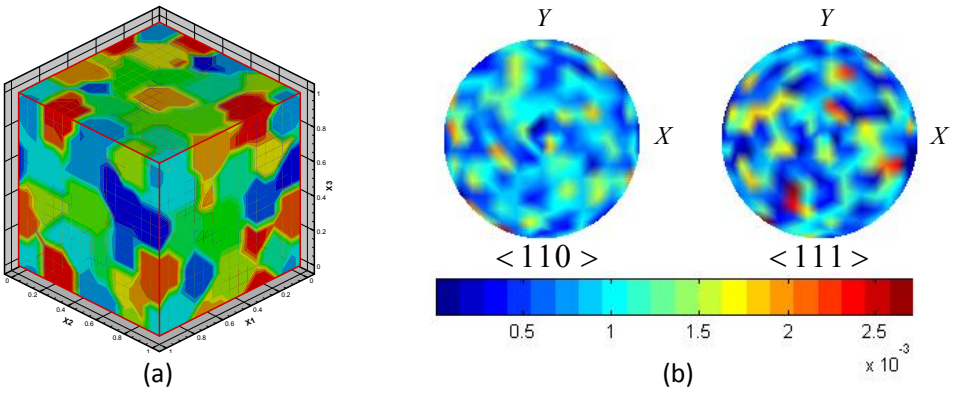

Figure 4.4: (a) The image representation of a 3D polycrystalline microstructure containing 64 grains. (b) Pole figures of the microstructure with randomly assigned orientations.

The homogenized (i.e. volume-averaged) effective stress-strain responses of the entire microstructure computed by the two different algorithms are shown in Fig. 4.6(a). The two curves almost overlap. Pole figures showing the orientation distribution of deformed microstructure are depicted in Fig. 4.6(b), from which we observe the typical plane strain deformation texture pattern for both cases. From the above comparison of the local and effective mechanical responses, we conclude that consistent results are obtained from the two algorithms.

An error analysis is also conducted to reveal the performance of the two formulations. The convergence error, as a function of iteration steps, of the basic formulation (defined by Eq. (4.33)) and of the augmented Lagrangian formulation (the larger value of the strain error $err(\boldsymbol{\varepsilon})$ and stress error $err(\boldsymbol{\sigma})$ as defined in [62]) are depicted in Fig. 4.7(a), while the equilibrium error (Eq. (4.32)) of both algorithms is shown in Fig. 4.7(b). The error is captured at the first time step with $\Delta t = 0.1$. It was observed that the convergence rate of the basic formulation is comparable with the augmented Lagrangian formulation for the cur-

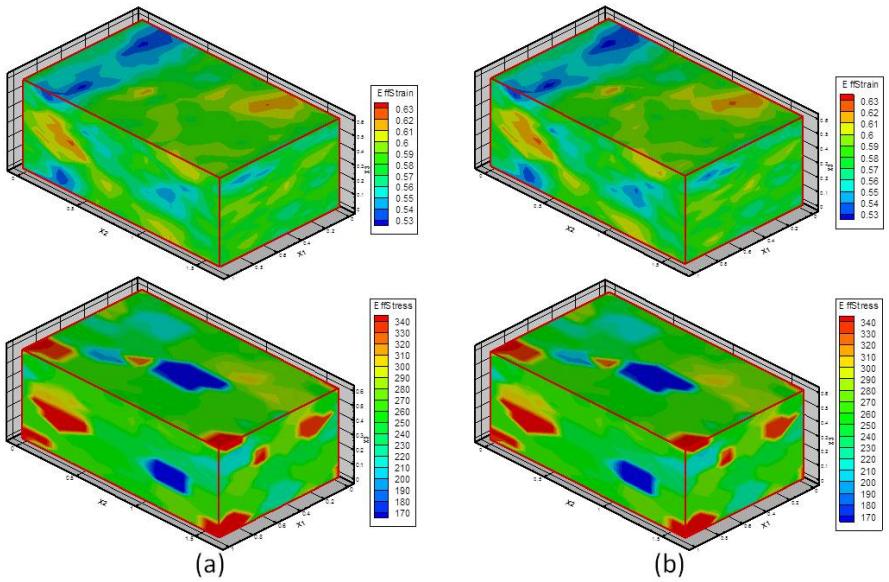

Figure 4.5: Contour plots of plane strain deformed microstructures evaluated by different algorithms. The top layer is the equivalent (plastic) strain field, and the bottom layer is the equivalent stress field. (a) Crystal visco-plasticity fast Fourier transform approach implemented in the basic formulation (b) Crystal visco-plasticity fast Fourier transform approach implemented in the augmented Lagrangian formulation.

rent example. The equilibrium error of the two formulations approaches a very close value as the number of iterations increases, although the fluctuation of the basic formulation is larger than that of the augmented Lagrangian case. The basic formulation performances sufficiently well for the current polycrytalline plasticity problem. The main reason is that the contrast between grains with different orientations is mild. For problems with high contrast, the augmented Lagrangian is expected to offer better convergence, while the basic formulation may even fail to converge [84, 85, 120]. Considering the simple structure of the basic formulation, we are employing it for the CEPFFT implementation.

It is also worth mentioning that the equilibrium error is mostly determined by the resolution of the microstructure. For high resolution, the equilibrium

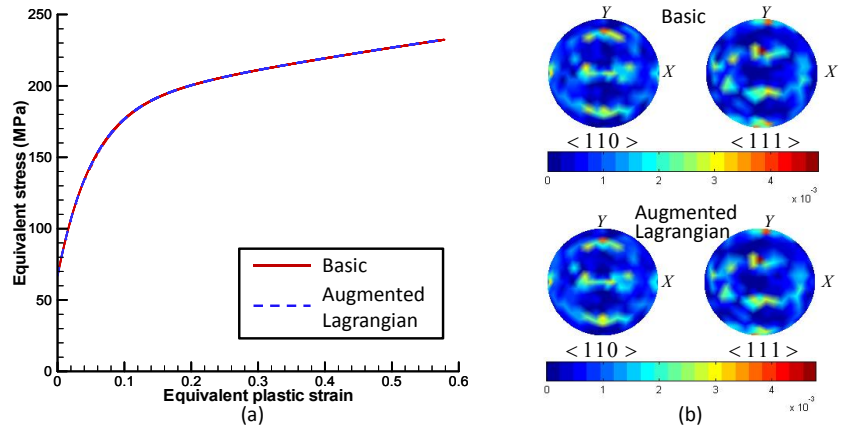

Figure 4.6: (a) The homogenized effective stress-strain responses computed by the basic and augmented Lagrangian crystal viscoplasticity FFT algorithms. (b) Pole figures of the deformed microstructure texture.

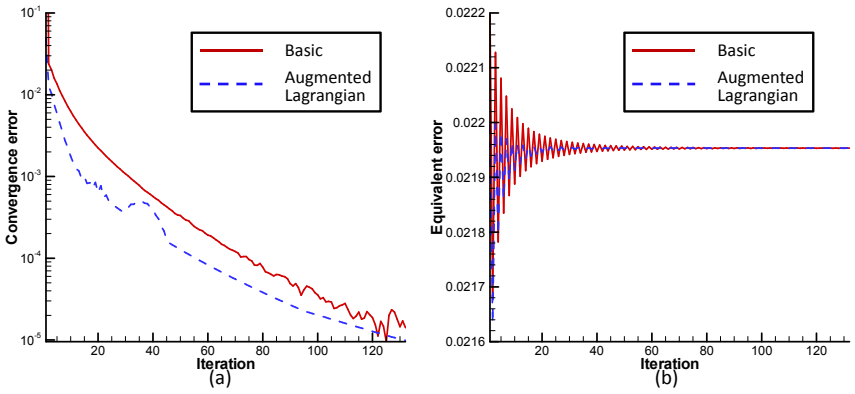

Figure 4.7: (a) Evolution of the convergence error as a function of the number of iterations of the augmented Lagrangian formulation in comparison with the convergence error of the basic formulation. The error axis uses logarithmic scale. (b) Evolution of the absolute (equilibrium) error as a function of the number of iterations of the two formulations. The error axis uses normal scale.

condition is fulfilled with smaller error (see Fig. 4.8). When the number of pixels per side is doubled, the equilibrium error is approximately halved.

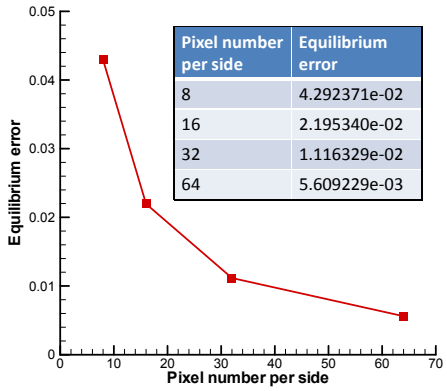

Figure 4.8: Equilibrium error as a function of resolution (number of pixels per side) computed by the basic formulation. The equilibrium error is evaluated when the convergence error reaches below 10^{-7}.

4.3.2 Crystal elasto-viscoplastic FFT simulations for polycrystalline microstructures

We consider here the same problem using the CEPFFT method. Both the microstructure configuration and material parameters are identical to the previous example. The elastic constants in the elasto-viscoplastic model are chosen to be $C_{11} = 110 \times 10^3 MPa$, $C_{12} = 59 \times 10^3 MPa$, $C_{44} = 26 \times 10^3 MPa$. The CEPFFT results are compared with the rigid visco-plastic computation as well as the results obtained from the crystal plasticity finite element method. Both multi-grid and single-grid strategies are adopted and compared.

In the finite element simulation, homogeneous boundary condition is applied to the microstructure to drive its deformation while the boundary conditions of FFT-based simulations are periodic. The homogeneous boundary condition enforces all boundary nodes to have the same deformation/velocity gradient (e.g. Eq. (4.49) for the current plane strain problem), but heterogeneous nodal response inside the microstructure is allowed. This homogeneous

boundary condition will result in different local mechanical responses on the microstructure from those obtained using the periodic boundary condition, but the homogenized effective response should be comparable. The FEM simulation is conducted using our in-house solver extended based on Section 2.1.5 [72]. The constitutive model is the same as used in CEPFFT. The microstructure is discretized by $16 \times 16 \times 16$ elements to be consistent with the voxel model by CEPFFT.

We first adopt the main CEPFFT proposed in Section 4.1.3 with a single-grid strategy. The total strain, plastic strain, and stress fields of the deformed microstructure after 50% thickness reduction computed by different models are plotted in Fig. 4.9. It is seen that CEPFFT gives very consistent prediction to both strain and stress fields with the rigid visco-plastic results obtained in the last example. The magnitude of the plastic strain field prediction by CEPFFT is slightly smaller than the one predicted by visco-plastic approach. On the other hand, the fields predicted by the FFT-based simulations show differences (especially for strain fields) from those predicted by crystal plasticity finite element simulations. The major causes of the differences between the FFT-based methods and the FEM approach include: (1) the different boundary conditions (periodic by the FFT-based methods and homogeneous by FEM), (2) the grain in the FFT-based simulation is assigned to the digital model in the unit of "point", while it is assigned to the finite element model in the unit of "element" (each element contains 8 points), (3) the fast Fourier transform results are computed directly on the voxel points while the finite element results are computed on integration points and extrapolated to nodes using a least squares method, and (4) algorithmic differences. However, we notice that the stress fields exhibit similar patterns. This is because the mean strain predicted by the two methods is about

the same and much larger in value than the fluctuations.

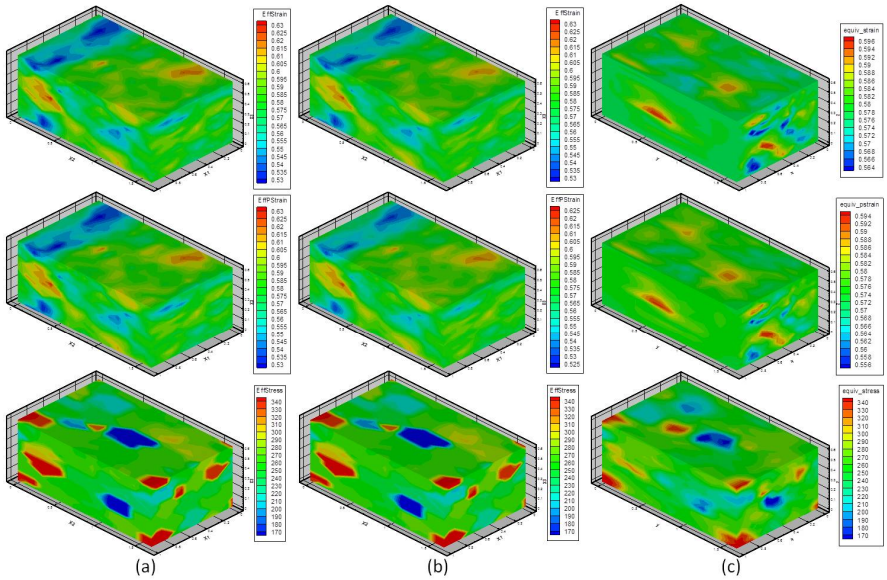

Figure 4.9: Contour plots of plane strain deformed microstructures evaluated by different methods. The first row is the equivalent total strain field, the second row is the equivalent plastic strain field, and the bottom row is the equivalent stress field. (a) Crystal visco-plasticity fast Fourier transform method. The total strain and plastic strain are identical here since the elastic response is ignored in this model. (b) Crystal elasto-viscoplasticity fast Fourier transform method (CEPFFT) (c) Crystal plasticity finite element method.

The homogenized effective stress-strain responses of the entire microstructure are compared in Fig. 4.10. The elastic response is successfully captured by the CEPFFT model and is comparable to the finite element prediction. It is observed that CEPFFT gives close prediction to the homogenized response with the finite element approach even though the boundary conditions for the two approaches are different.

The textures predicted by the three models are plotted using pole figures in Fig. 4.11. It is observed that all the three sets of predicted pole figures are very similar. The typical plane strain pattern is obtained.

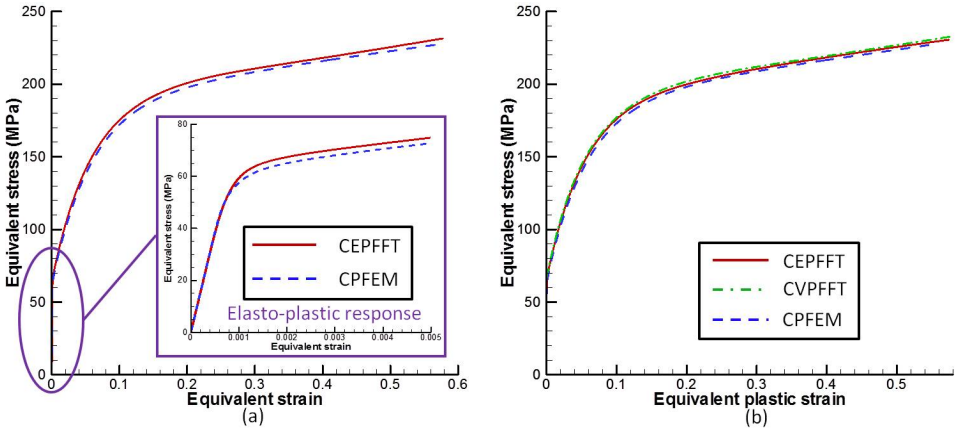

Figure 4.10: The homogenized effective stress-strain responses of plane strain deformed microstructures predicted by different models. (a) Effective stress-total strain responses by CEPFFT and crystal plasticity FEM; (b) The effective stress-plastic strain responses by the three methods. Note that here CVPFFT denotes crystal visco-plasticity fast Fourier method, and CPFEM refers to crystal plasticity finite element method.

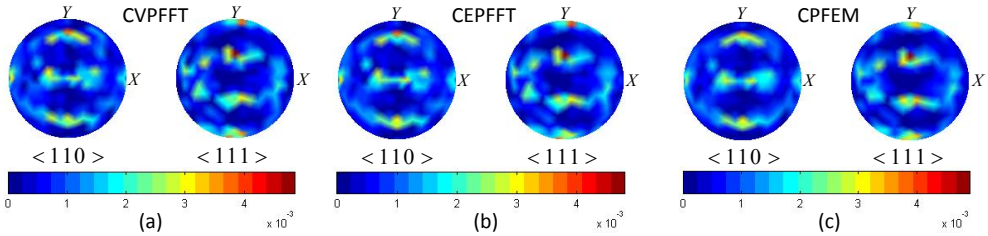

Figure 4.11: Crystallographic textures, represented in pole figures, of plane strain deformed microstructures predicted by three models. (a) Crystal visco-plasticity fast Fourier transform method (CVPFFT) (b) Crystal elasto-viscoplasticity fast Fourier transform method (CEPFFT) (c) Crystal plasticity finite element method (CPFEM).

To check the convergence of the results with respect to increasing resolution, we performed the same simulation on the same microstructure but discretized by 32×32×32 voxels using CEPFFT. The local and effective mechanical responses are compared in Figs. 4.12 and 4.13, respectively. It is observed that the two sets of results are consistent. Plotted in the two figures are also the predictions using

the modified CEPFFT approach introduced at the last of Section 4.1.5, where stress is linked to total strain rate through an elasto-viscoplastic modulus. We observe that the results from this modified implementation are close to the main formulation (that computes elastic and plastic fluctuations separately), although with milder spatial variation. The stress-strain curves predicted by the main and modified CEPFFT almost coincide in the elasto-viscoplastic transition region (as shown in Fig.4.13 (a)), indicating that the two formulations provide consistent prediction to this example. It should be mentioned that the iteration of modified formulation is cut after 100 steps at the elasto-viscoplastic transition part, where the convergence rate becomes slow.

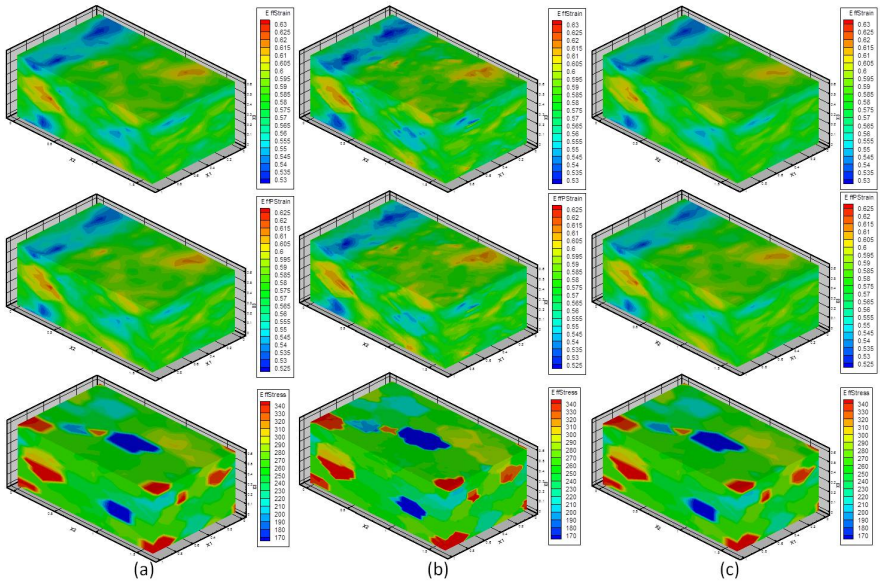

Figure 4.12: Contour plots of plane strain deformed microstructures with different resolution and methods. The first row is the equivalent total strain field, the second row is the equivalent plastic strain field, and the bottom row is the equivalent stress field. (a) The main CEPFFT method using $16 \times 16 \times 16$-voxel microstructure. (b) The main CEPFFT method using a $32 \times 32 \times 32$-voxel microstructure. (c) The modified CEPFFT using a $16 \times 16 \times 16$-voxel microstructure.

We also studied the equilibrium error of the main CEPFFT approach for mi-

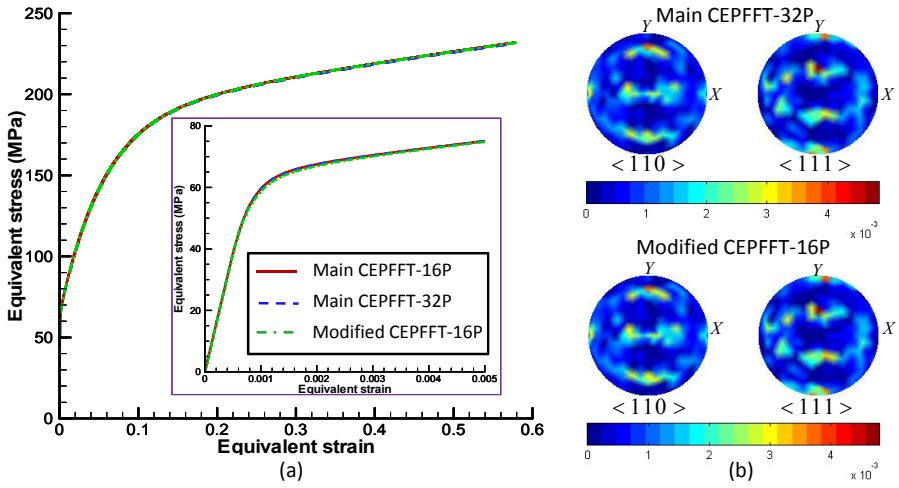

Figure 4.13: (a) The homogenized effective stress-total strain responses for a $16 \times 16 \times 16$-voxel microstructure and a $32 \times 32 \times 32$-voxel microstructure obtained using different formulations. (b) Crystallographic textures represented in pole figures. Main CEPFFT refers to the main crystal elasto-viscoplasticity FFT method implemented using the separate formulation and Modified CEPFFT refers to the integrated formulation using the homogeneous elasto-viscoplastic medium approach Section 4.1.5.

crostructures with different resolution. The improvement of error with refining the image is seen from Fig. 4.14(a), which is similar to the visco-plasticity case. The convergence of the CEPFFT model as a function of iteration number is shown in Fig. 4.14(b). We observe a fast convergence rate for all tests.

In order to study the effect of heterogeneous deformation on mechanical responses, we next repeat the above simulations using the CEPFFT implemented with the multi-grid strategy. The deformed material grid obtained by the multi-grid strategy and the homogeneous approximation are plotted in Fig. 4.15. Contour plots of local mechanical responses are shown in Fig. 4.16. Comparing with the single-grid results, we find that the predicted mechanical responses do not vary much, although the deformed microstructures becomes irregular. The ef-

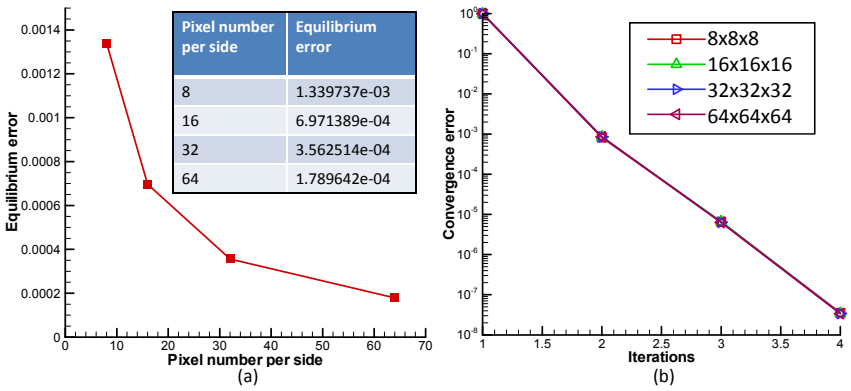

Figure 4.14: (a) Equilibrium error as a function of resolution (number of pixels per side). The equilibrium error is evaluated using the basic formulation when the convergence error reaches below 10^{-7}. (b) Convergence error versus number of iterations.

fective stress-strain curve and grain orientation distribution predicted by the multi-grid strategy are almost identical with the corresponding results obtained by the single-grid prediction and are not repeated here.

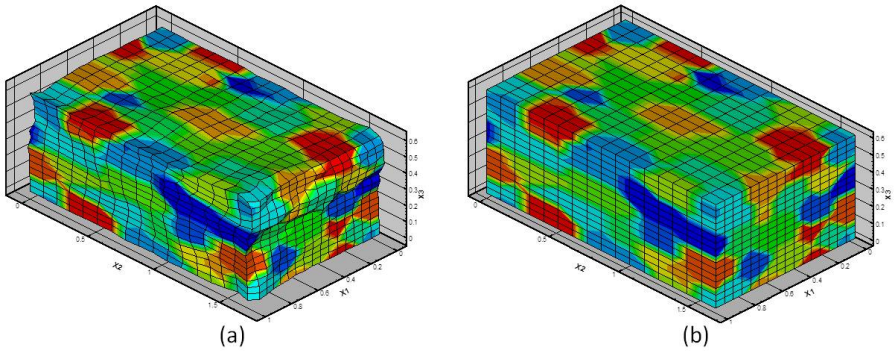

Figure 4.15: (a) Deformed microstructure predicted by multi-grid CEPFFT. (c) Deformed microstructure predicted by single-grid CEPFFT.

We next examine an example of simple shear of the microstructure using different models in order to better validate the current development, especially for the texture evolution. The same polycrystalline microstructure containing 64 grains and material parameters are used, while the imposed velocity gradient

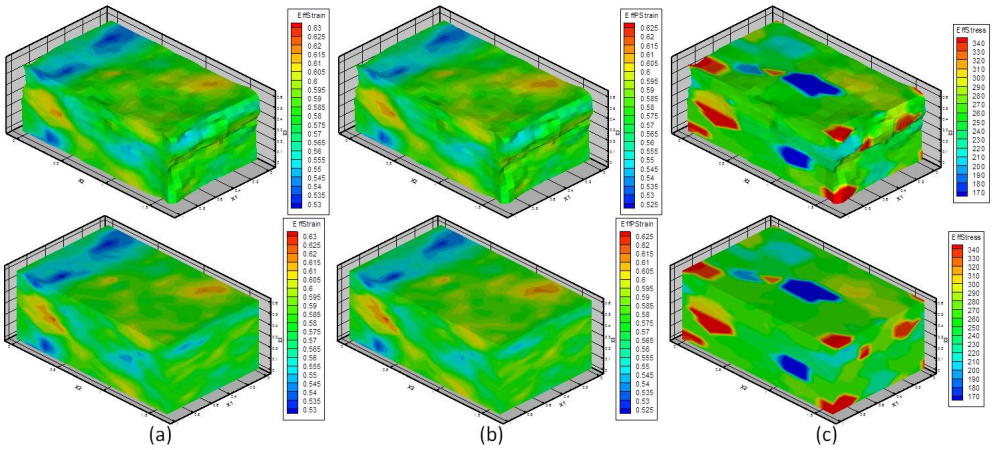

Figure 4.16: Contour plots of plane strain deformed microstructures computed using different strategies. The first row shows results obtained from the multi-grid CEPFFT, and the bottom row shows results obtained from the single-grid CEPFFT. (a) Equivalent total strain (b) Equivalent plastic strain (c) Equivalent stress.

becomes

$$\mathbf{L} = \nabla \mathbf{V} = \begin{bmatrix} 0.0 & -1.0 & 0.0 \\ 0.0 & 0.0 & 0.0 \\ 0.0 & 0.0 & 0.0 \end{bmatrix} \times 10^{-3}(s^{-1}). \tag{4.50}$$

The single-grid strategy along with the main CEPFFT formulation is firstly adopted. The homogenized effective stress-strain responses of the entire microstructure are compared with the rigid visco-plasticity FFT and finite element simulation in Fig. 4.17. The elastic response is successfully captured by the CEPFFT model.

The crystallographic textures described by pole figures are depicted in Fig. 4.18. We can see once more that different models give very close prediction of the texture evolution of the simple shear mode.

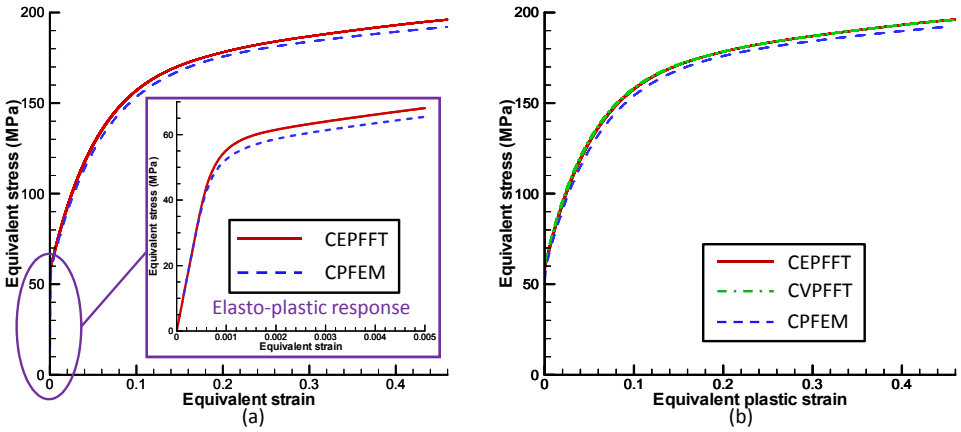

Figure 4.17: The homogenized effective stress-strain responses of sheared microstructures predicted by different models. (a) Effective stress-total strain responses by CEPFFT and crystal plasticity finite element method (CPFEM); (b) Effective stress-plastic strain responses by three methods. CVPFFT refers to crystal visco-plasticity fast Fourier transform method.

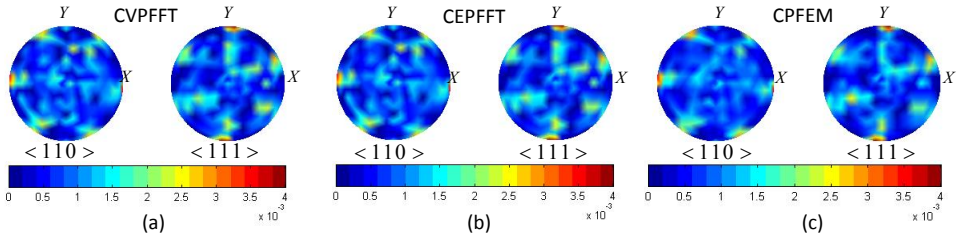

Figure 4.18: Crystallographic textures, represented in pole figures, of sheared microstructures predicted by three models. (a) Crystal visco-plasticity fast Fourier transform method (CVPFFT). (b) Crystal elasto-viscoplasticity fast Fourier transform method (CEPFFT). (c) Crystal plasticity finite element method (CPFEM).

To check the convergence of the results with respect to increasing resolution for simple shear deformation, we also performed the same simulation on the same microstructure but discretized by $32 \times 32 \times 32$ voxels. The homogenized effective stress-strain responses are compared in Fig. 4.19, along with the crystallographic texture after shearing. The results computed using the modified CEPFFT formulation discussed at the last of Section 4.1.5 are also demon-

strated. The stress-strain curves predicted by the main and modified CEPFFT shows small difference in the elasto-viscoplastic transition region (as shown in Fig.4.19 (a)). This is because the convergence rate of the modified formulation becomes very slow at the transition part. The iteration is cut after 100 steps for modified formulation.

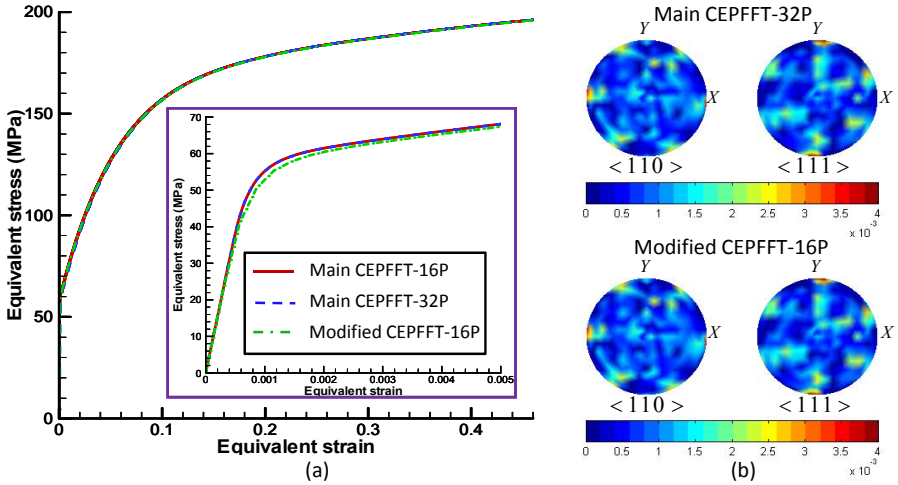

Figure 4.19: (a) The homogenized effective stress-total strain responses by a 16 × 16 × 16-voxel microstructure and a 32 × 32 × 32-voxel microstructure under simple shear obtained using different formulations. (b) Crystallographic textures represented in pole figures. Main CEPFFT refers to the main crystal elasto-viscoplasticity FFT method implemented using the separate formulation and Modified CEPFFT refers to the crystal elasto-viscoplasticity implementation using the integrated formulation.

The local mechanical responses are also estimated. Plotted in Fig. 4.20 are the stress fields computed by (a) the rigid visco-plasticity FFT on a 16 × 16 × 16-voxel microstructure, (b) the main CEPFFT algorithm on a 16 × 16 × 16-voxel microstructure, (c) the modified CEPFFT algorithm on a 32 × 32 × 32-voxel microstructure, (d) the modified CEPFFT algorithm on a 16 × 16 × 16-voxel microstructure, (e) the multi-grid CEPFFT on a 16 × 16 × 16-voxel microstructure with irregular deformation, and (f) the finite element method on the microstruc-

ture discretized by $16 \times 16 \times 16$ elements. Consistent results are observed.

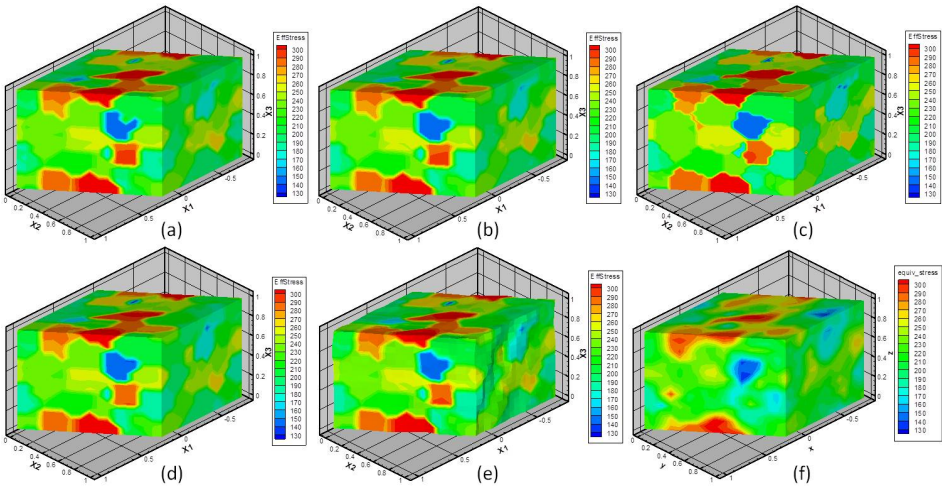

Figure 4.20: Stress contour plots of sheared microstructures evaluated by different methods. (a) Crystal visco-plasticity fast Fourier transform method (CVPFFT). (b) Crystal elasto-viscoplasticity fast Fourier transform method (CEPFFT) implemented with the main formulation with single-grid strategy. (c) CEPFFT implemented in the modified formulation with single-grid strategy on a $32 \times 32 \times 32$-voxel microstructure. (d) CEPFFT implemented in the modified formulation with single-grid strategy. (e) CEPFFT implemented in the main formulation with multi-grid strategy. (f) Crystal plasticity finite element method (CPFEM).

4.3.3 Investigation of fatigue indicator parameters of IN100

In this subsection, we adapt the CEPFFT method to study fatigue properties of Ni-based superalloys. The homogeneous constitutive model developed in [98] for IN100 at high temperature (650°C) is employed. The constitutive model has been summarized in Section 2.2.4. According to this constitutive model, the tangent plastic compliance as required by Eq. (4.29) can be derived as

$$\mathbf{M}_t^p(\mathbf{x}) = \frac{\mathrm{d}\dot{\boldsymbol{\varepsilon}}^p}{\mathrm{d}\boldsymbol{\sigma}} = \sum_{\alpha}^{N_s} \left(\frac{\mathrm{d}\dot{\boldsymbol{\varepsilon}}^p}{\mathrm{d}\dot{\gamma}^{(\alpha)}} \frac{\mathrm{d}\dot{\gamma}^{(\alpha)}}{\mathrm{d}\tau^{(\alpha)}} \frac{\mathrm{d}\tau^{(\alpha)}}{\mathrm{d}\boldsymbol{\sigma}} \right)$$

$$
\begin{aligned}
&= \sum_{\alpha}^{N_s} \mathbf{m}^{(\alpha)}(\mathbf{x}) \otimes \mathbf{m}^{(\alpha)}(\mathbf{x}) \left[\dot{\gamma}_1 \frac{n_1}{D_\lambda^{(\alpha)}} \left\langle \frac{|\tau_\lambda^{(\alpha)} - \chi_\lambda^{(\alpha)}| - \kappa_\lambda^{(\alpha)}}{D_\lambda^{(\alpha)}} \right\rangle^{n_1 - 1} \right. \\
&+ \left. \dot{\gamma}_2 \frac{n_2}{D_\lambda^{(\alpha)}} \left\langle \frac{|\tau_\lambda^{(\alpha)} - \chi_\lambda^{(\alpha)}|}{D_\lambda^{(\alpha)}} \right\rangle^{n_2 - 1} \right],
\end{aligned} \tag{4.51}
$$

where $\dot{\gamma}_1$ and $\dot{\gamma}_2$ are constants related to the initial shearing rate, while n_1 and n_2 quantify the inverse of the material rate sensitivity. $\tau_\lambda^{(\alpha)}$, $\chi_\lambda^{(\alpha)}$, and $D_\lambda^{(\alpha)}$ are the resolved shear stress, back force, and drag stress of slip system α, respectively, with $\lambda = \{\text{oct}, \text{cub}\}$ referring to the octahedral and cube slip systems, respectively. The function $\langle x \rangle$ returns x if $x > 0$ and returns 0, otherwise.

The secant plastic modulus required by Eqs. (4.21) and (4.36) is taken to be $\mathbf{C}^p = \mathbf{M}_s^{p-1}$ with

$$
\begin{aligned}
\mathbf{M}_s^p(\mathbf{x}) &= \sum_{\alpha}^{N_s} \mathbf{m}^{(\alpha)}(\mathbf{x}) \otimes \mathbf{m}^{(\alpha)}(\mathbf{x}) \left[\dot{\gamma}_1 \frac{1}{D_\lambda^{(\alpha)}} \left\langle \frac{|\tau_\lambda^{(\alpha)} - \chi_\lambda^{(\alpha)}| - \kappa_\lambda^{(\alpha)}}{D_\lambda^{(\alpha)}} \right\rangle^{n_1 - 1} \right. \\
&+ \left. \dot{\gamma}_2 \frac{1}{D_\lambda^{(\alpha)}} \left\langle \frac{|\tau_\lambda^{(\alpha)} - \chi_\lambda^{(\alpha)}|}{D_\lambda^{(\alpha)}} \right\rangle^{n_2 - 1} \right].
\end{aligned} \tag{4.52}
$$

With these relations, the algorithm proposed in Section 4.1 can be applied to IN100 superalloy. The constitutive equations and parameters are the same as Section 2.2 and detailed in [98, 109, 110]. The fatigue indicator parameters defined in [109] are computed to measure the fatigue properties.

The same microstructure configuration as in the previous examples is used and the initial texture is random. The volume fractions and sizes of γ' precipitates are given by $f_{p1} = 0$, $f_{p2} = 0.42$, $d_2 = 108nm$, $f_{p3} = 0.11$, $d_3 = 7nm$. The microstructure is subjected to a 3-loop cyclic loading (tension and compression along the z-direction). The stress-strain response in the z-direction during the 3 loading loops is plotted in Fig. 4.21 with comparison to an FEM simulation that adopts the same constitutive model. The CEPFFT models implemented in

both the separate formulation and the integrated formulation are tested. The single-grid update strategy is adopted. The microstructure input to the CEPFFT simulation is discretized by $16 \times 16 \times 16$ voxels to be consistent with the finite element input ($16 \times 16 \times 16$ cubic elements). The CEPFFT simulations give similar prediction to the stress-strain "loop" with the finite element model. Note that the loop predicted by the main CEPFFT algorithm is wider than the loops obtained from the FEM or the modified CEPFFT algorithm. The difference is resulted from the different choice of the modulus for the homogeneous reference medium.

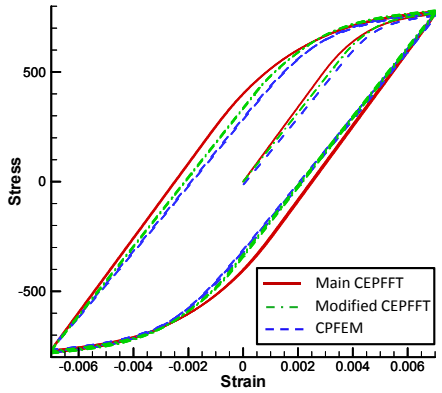

Figure 4.21: Stress-strain responses of three loops of cyclic loading computed by CEPFFT and CPFEM. Main CEPFFT refers to the main crystal elasto-viscoplasticity FFT method implemented using the separate formulation, modified CEPFFT refers to the crystal elasto-viscoplasticity implementation using the homogeneous elasto-viscoplastic medium approach, and CPFEM is the crystal plasticity finite element method.

We next compute strain based fatigue indicator parameters (FIPs) related to small crack formation and early growth [82]. The three fatigue indicator parameters of interest are the cumulative plastic strain per cycle (P_{cyc}), the Fatemi-Socie parameter (P_{FS}), and the maximum range of cyclic plastic shear strain parameter (P_{mps}). The definitions of these fatigue indicator parameters can be

found in [109] and described in Section 2.2.4. Contour plots of fatigue indicator parameters over the microstructure are plotted in Fig. 4.22. All fatigue indicator parameters are computed for the last (3rd) loading loop. We observe that the fatigue indicator parameters contour plots demonstrate similar patterns in CEPFFT and crystal plasticity finite element simulations. The results predicted by the main CEPFFT approach show more heterogeneity and are closer to finite element results than the modified CEPFFT model. Again, the difference between the main and modified CEPFFT results comes from the fact that the convergence rate of the latter is slower than the former, especially at the elasto-viscoplastic transient region. During the simulation, we stop the iterative operation of the modified CEPFFT and continue to the next time step after it reaches 100 iterations.

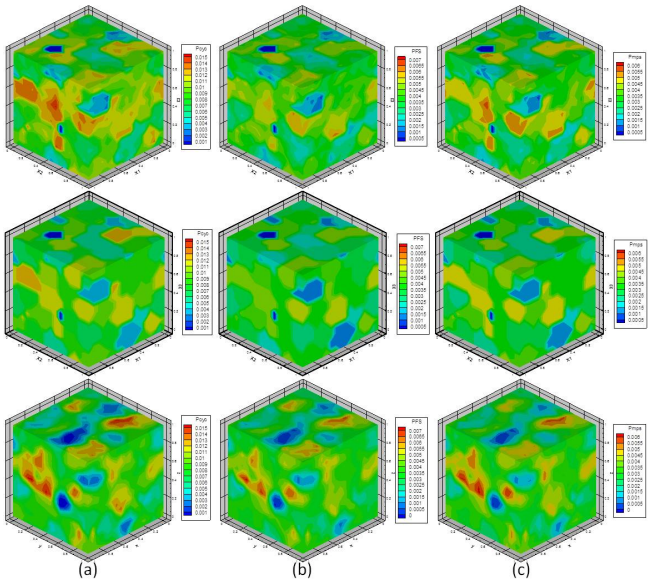

Figure 4.22: Contour plots of fatigue indicator parameters fields. Main CEPFFT results are placed in the top row, results from the modified CEPFFT formulation are placed in the middle row, and crystal plasticity finite element results are located in the bottom row. (a) P_{cyc}, (b) P_{FS}, (c) P_{mps}.

The convergence of the CEPFFT simulation with respect to resolution and

the multi-grid effect are also tested for this fatigue problem. The fatigue indicator parameters are plotted in Fig. 4.23. It is observed that the deformation heterogeneity does not affect significantly the fatigue indicator parameters fields and the distortion of the microstructure is small since the total strain is small for this problem. The finer microstructure ($32 \times 32 \times 32$ voxels) gives consistent prediction to local fatigue indicator parameters with the coarse grid prediction, while larger heterogeneity is captured.

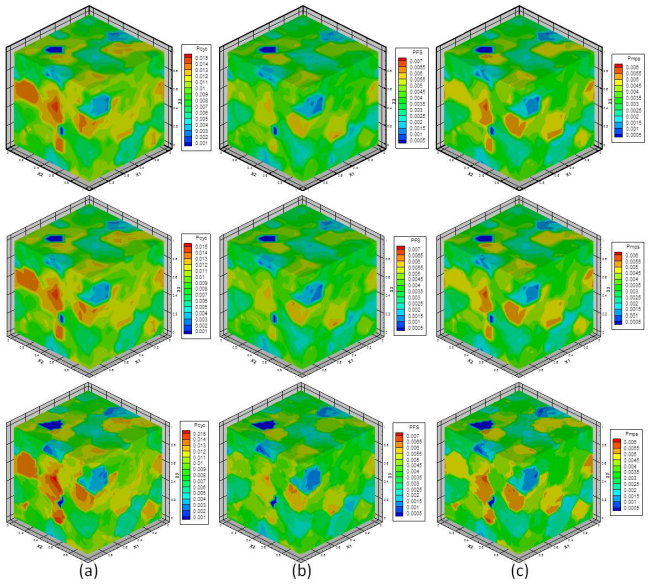

Figure 4.23: Contour plots of fatigue indicator parameters fields evaluated by the multi-grid CEPFFT on coarse microstructure (top row), single-grid CEPFFT on coarse microstructure (middle row), and single-grid CEPFFT on fine microstructure (bottom row). (a) P_{cyc}, (b) P_{FS}, (c) P_{mps}.

Grain level fatigue indicator parameters, namely the maximum and average fatigue indicator parameters of voxels within individual grains [109] are also extracted. Their distributions are shown in Fig. 4.24. The distributions computed using the main CEPFFT based on the $16 \times 16 \times 16$-voxel microstructure are shown in (a). The ones computed using the main CEPFFT on the $32 \times 32 \times 32$-voxel microstructure are plotted in (b). The results of the integrated formulation

of CEPFFT are depicted in (c), and the crystal plasticity finite element results are given in (d). These results are obtained using the single-grid strategy. In the figure, the FIP with "max" prefix means the maximum value of the FIP of voxels within an individual grain. The one with "ave" prefix indicates that it is the average FIP over voxels within an individual grain. The distributions are normalized by the maximum value of each FIP over all grains of the microstructure. It is seen that the distributions of grain level fatigue indicator parameters predicted by the main CEPFFT on the finer microstructure are closer to the finite element results. The ones predicted by the main CEPFFT on coarse microstructure are also close to the fine microstructure estimations.

The maximum and average FIP distributions predicted by the modified CEPFFT (Fig.4.24 (c)) do not exhibit major difference, which is observed in the main CEPFFT prediction (Fig.4.24 (a)). This is consistent with the contour plots of the FIP fields (Fig. 4.22). The close maximum and average FIP distributions shown in Fig. 4.24(c) imply that the intragranular heterogeneity of FIPs predicted by the modified CEPFFT formulation is weak. The main reason is that, since the modulus for the modified formulation defined in Eq. (4.36) (with $\mathbf{M}^p$ given by Eq. (4.52)) does not provide sufficiently good convergence rate, the computation is stopped at each time step at the 100-th iteration. A more sophisticated modulus of the reference medium is therefore needed to resolve this problem.

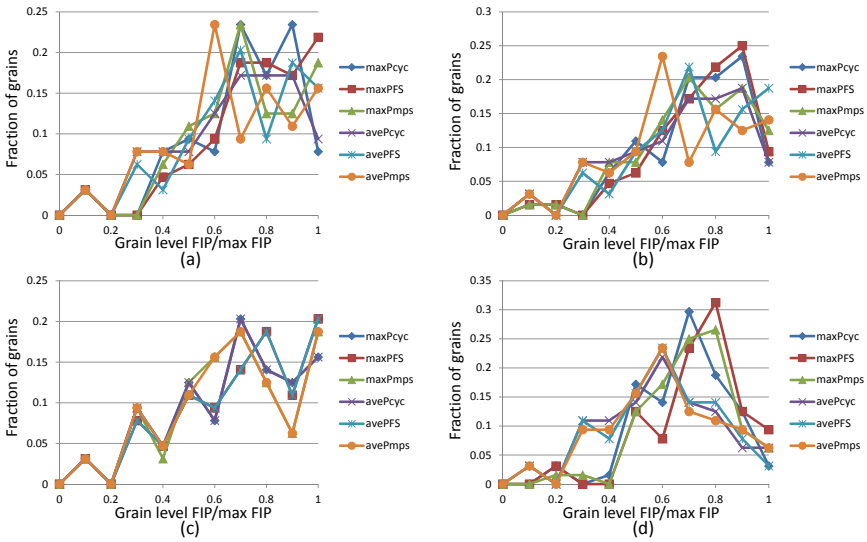

Figure 4.24: Distribution of the fatigue indicator parameters among grains computed by (a) Main CEPFFT with coarse microstructure, (b) Main CEPFFT with fine microstructure, (c) Modified CEPFFT with coarse microstructure and (d) crystal plasticity finite element method. These distributions are normalized by the maximum values of each FIP over all grains.

4.3.4 Computational efficiency

The computational efficiency of the CEPFFT method is important since our goal is to develop a highly efficient full-field simulator that can be adopted in stochastic simulations as the deterministic solver to further study the probabilistic nature of material properties. As mentioned before, with the employment of fast Fourier transform to solve for local mechanical responses, the cumbersome matrix inversion in finite element simulation is circumvented, which leads to great improvement in the computation speed. The computation times for microstructures subjected to plane strain deformation up to 0.02 and 1 complete loop of cyclic loading are reported in Table 4.1 and Fig. 4.25. The performance of the simple shear simulation is very similar to the plane strain example and is not demonstrated. In the plane strain test, the time increment adopted for

the finite element simulation is $\Delta t = 0.25$, which is smaller than that for the fast Fourier transform simulation ($\Delta t = 0.5$), in order to reach convergence of the time integration. In the cyclic loading test, the time step is reduced to $\Delta t = 0.1$ for both cases considering the small strain range. All tests were run on the Teragrid TACC Lonestar Linux Cluster. Each computation node contains two Xeon Intel Hexa-Core 64-bit Westmere processors, the core frequency of which is $3.33GHz$. Single-grid morphology evolution strategy and main formulation are adopted by all CEPFFT tests. The examples are conducted in both serial and parallel computation. We observe that the CEPFFT simulation is much faster than the crystal plasticity finite element method. Similar report on the computation efficiency of FFT-based crystal plasticity methodology can be found in [97].

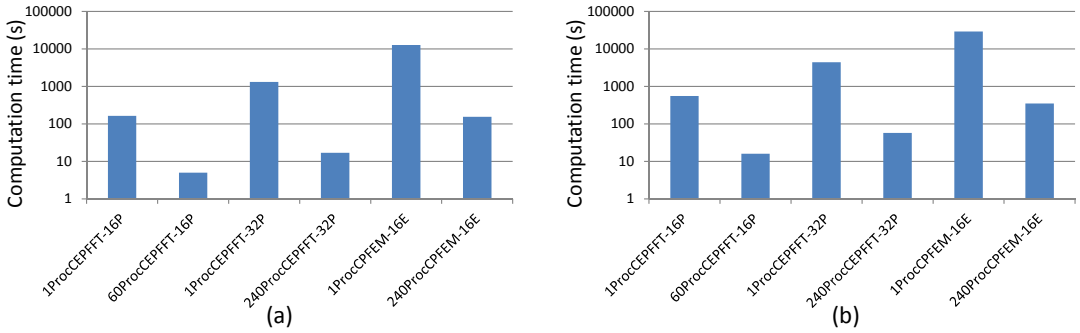

Figure 4.25: Computation times of simulations using different methods on microstructures with different resolutions. (a) Plane strain deformation to 0.02 strain. (b) One complete loop of cyclic loading of the IN100 microstructure. The computation times are shown in logarithmic scale. In the figure, 1ProcCEPFFT-16P means the CEPFFT simulation of a microstructure discretized by $16 \times 16 \times 16$ voxels using 1 processor and 1ProcCPFEM-16E means the crystal plasticity finite element simulation of a microstructure discretized by $16 \times 16 \times 16$ elements using 1 processor.

Table 4.1: Computation times for microstructures under plane strain and cyclic deformations simulated using different methods. CPFEM refers to crystal plasticity finite element method.

	1-processor, CEPFFT, 16^3-voxels	60-processors, CEPFFT, 16^3-voxels	1-processor, CEPFFT, 32^3-voxel	240-processors, CEPFFT, 32^3-voxels	1-processor, CPFEM, 16^3-elements	240-processors, CPFEM, 16^3-elements
Plane strain	164s	5s	1309s	17s	12687s	154s
Cyclic loading	554s	16s	4385s	57s	29026s	348s

4.4 Conclusions

In this work, we developed an efficient FFT full-field model to investigate elasto-viscoplastic properties of polycrystalline materials by interrogating image-based realistic microstructures. The elastic and plastic responses were computed separately. An integrated formulation was also proposed using a particular choice for the elasto-viscoplastic modulus. The predictive capability and computational efficiency of the newly developed CEPFFT method were presented using numerical examples in comparison with a visco-plastic approach and crystal plasticity finite element simulations. Error tests were conducted to show the comparable performance of the basic and augmented Lagrangian algorithms. The multi-grid strategy was implemented to predict the irregular deformation of the microstructure. The self-consistence (convergence with refining discretization) of the CEPFFT method was shown through simulations with increasing resolution of the microstructure. Fatigue properties of Ni-based superalloy microstructures described by fatigue indicator parameters were studied using the CEPFFT method. The main discoveries of this work are as follows:

1. The elastic response of the microstructure is successfully captured by

CEPFFT. Fatigue properties of nickel-based superalloy microstructures can be efficiently investigated using CEPFFT method. The computed results are comparable with those obtained from a crystal plasticity finite element simulation.

2. The equilibrium error in simulations using the main formulation is comparable to the one using the augmented Lagrangian algorithm and depends on the resolution of the input image.

3. The CEPFFT model provides consistent prediction of the homogenized effective mechanical responses and local stress field with the finite element and crystal visco-plasticity fast Fourier transform simulations. The crystallographic texture patterns of microstructures under different deformation modes estimated by the three methods agree well.

4. The local strain fields obtained by the CEPFFT implementation agree very well with visco-plastic results and have similar patterns with the crystal plasticity finite element results.

5. The multi-grid strategy that uses separate computation and material grids is adopted to predict the irregular configuration of deformed microstructure. It is observed that the heterogenous deformation does not result in significant changes in the mechanical response for the tested examples in comparison to the single-grid method.

6. The required computation time of CEPFFT is significantly less than that of crystal plasticity finite element method since the methodology does not require the solution of any matrix equations as in the FEM. This computational efficiency provides significant potential in integrating the FFT approach with stochastic multiscale materials simulations.

7. Various CEPFFT formulations can be introduced. The approach highlighted in this paper computes separately the elastic and plastic fluctuation responses. An integrated form with optimally designed modulus for the homogeneous reference medium may further improve the computational efficiency.

CHAPTER 5

CONCLUSION AND SUGGESTIONS FOR FUTURE RESEARCH

In this thesis, we studied the variability of mechanical properties/responses of polycrystalline systems induced by microstructure uncertainties. The initial given information was a number of microstructure samples generated through certain pre-process and therefore have the same statistical constraints. Linear and nonlinear model reduction techniques were employed to construct the low-dimensional surrogate model of the random microstructure feature space. Taking the surrogate model as the input to the stochastic simulation, new random samples can be efficiently generated and the uncertainty of microstructure-sensitive material properties was quantified with the assistance of proper physics-based deterministic simulations. The achievements of current work include: (1) employment of PCA/KPCA and Isomap methods to construct reduced-order model of random microstructure features at a single material point; (2) development of bi-orthogonal decomposition scheme to resolve the "curse of dimensionality" in stochastic multiscale problems; (3) implementation of conventional crystal plasticity simulators based on Taylor and FE methods; (3) development of an FFT-based full-field crystal plasticity solver to efficiently and accurately evaluate elasto-viscoplastic behavior of realistic microstructures subjected to periodic deformation; (4) investigation of variability of various mechanical properties/responses (stress-strain curve, fatigue indicator parameters, stress distribution, etc.) induced by microstructure variations by solving the stochastic partial differential equations using MC and/or ASGC methodologies.

The developments in the thesis set up the framework for efficient uncertainty quantification of polycrystalline systems. However, there are still many open areas require further research. Suggestions for the continuation of this study are provided next.

5.1 Multiscale modeling of superalloy systems

A multiscale solver integrating mesoscale crystal plasticity constitutive model with macroscale forging simulation has been developed in the current work to study the effect of heterogeneous microstructures on the properties of the final product. However, the mesoscale crystal plasticity model is still based on continuum theory, which does not explicitly model the underlying physical behavior during plastic deformation. In order to make the simulation more realistic, a multiscale framework that takes the microscale discrete dislocation dynamics into consideration can be introduced. Over the past few decades various discrete dislocation dynamics (DD) models have been developed [19, 20, 139, 111, 14]. While early works were limited to two-dimensions (2D), recent research focuses on more realistic 3D simulation with the capability of considering features like multiplication, dislocation intersection, cross-slip, etc., which are crucial for the formation of dislocation patterns. This dislocation dynamics approach is specially beneficial to superalloy systems, since the direct modeling of dislocation structures and precipitates probes the underlying mechanism of the strengthening effect of second phase precipitates. Mohles and co-workers [90, 87, 91, 89, 88] have performed many simulations in which one or more dislocations sweep across a glide plane intersected by many coherent precipitates. Rao et al. followed this work and conducted simulations of a high-

volume-fraction (40%) γ' superalloy [99, 100]. The effects of precipitate shape, volume fraction, and APB energy on the critical resolve shear stress (CRSS), and further the yield strength, were studied. Recently, Vattré et al. [127] extended Rao's work to a higher, up to 70%, precipitate volume fraction. While in the previous studies, the DD simulations were carried out in 2D environment, Vattré's model was set up in 3D. Zbib and co-workers [135] also performed similar simulations based on their 3D multi-scale discrete DD-FEM framework MDDP (multiscale dislocation dynamics plasticity) [138]. The future work could integrate the DD approach into the current continuum simulation for more realistic modeling of the physical system. The behavior of massive dislocations in the precipitate hardened superalloys should be studied. Uncertainties across different scales are interested as well.

5.2 Uncertainty quantification with realistic polycrystalline microstructures

In the current uncertainty analysis, microstructures are represented using topological and crystallographic features such as sizes and orientations of constituent grains. With the development of efficient full-field crystal plasticity fast Fourier transform approach (Section 4) and robust model reduction techniques [126, 12] (e.g. mixtures of principal component analyzers (MoPPCA) [124, 125]), we are able to take realistic microstructures into stochastic simulation, in order to provide more accurate prediction to material properties. However, the complexity of the uncertainty quantification is increased as a trade-off. The key problem is to find an appropriate representation for the realistic microstructure.

The most straightforward representation of a microstructure is pixelized model (here we use pixel for both 2D and 3D models) with each pixel associating with 3 parameters quantifying its crystallographic orientation. A vector that stores the orientation parameters of all pixels becomes a point in the microstructure space. The dimension of this pixelized model depends on its resolution, and is usually very high-dimensional. Meanwhile, several unwelcome features come along with this representation, especially when it is adopted for model reduction. For example, the properties of a microstructure is mostly affected by its morphological and crystallographic features that are determined by the relative position of grains, while the pixelized model describes absolute positions of grains. There is possibility that two microstructures share the same or very close underlying features, such as grain size, shape, spatial distribution, orientation distribution, misorientation distribution, etc., but exhibit different appearance in image representation. These realizations with different appearance are essentially identical in terms of microstructural features and properties. Treating them as different microstructures is a waste of computation resource. The second problem associated with the pixelized representation is that the direct reconstruction of microstructure images from reduced-order samples may give very vague or unrealistic structures. This problems has been observed in two-phase materials [58] and is worsen in the multi-phase (e.g. polycrystalline) situation. The study of these unrealistic microstructures is meaningless and may produce misleading properties. As a result, certain preprocessing needs to be conducted before using the pixelized models in the stochastic simulation, so that the computation is effective and efficient. A reconstruction technique is also needed to find appropriate microstructure realizations corresponding to given reduced representations. Another way of introducing realistic microstructures in the un-

certainty quantification is to extract statistical features (e.g. n-point correlation functions, orientation/misorientation distributions) from the original pixelized model, and use them as the stochastic input. A reconstruction scheme is then needed to produce realistic microstructure samples based on given statistical features during stochastic simulation. The problem of this statistical representation is that the reconstruction error may be large and the reconstruction is not unique. Considering the above issues, introducing realistic microstructure into uncertainty analysis is an open research problem that is of great interest in future research.

5.3 Advanced methodologies for uncertainty analysis, property prediction and material design

Monte Carlo and adaptive sparse grid collocation are employed as the tools to solve the stochastic problems in this thesis. It is known that MC method becomes quickly intractable for complex problems in multiple random dimensions and it has no control on the truncation error. ASGC has good performance for problems with moderate input and output dimensions, but we find that its application to high-dimensional problems (e.g. uncertainty quantification of realistic polycrystalline microstructures) is sometimes problematic. In addition, the model reduction sometimes leads to rapid variability of nearby the microstructures. This large variability induces severe discontinuities in the reconstructed input space which may lead to the fail of sparse grid collocation method. Therefore, developing alternative model reduction techniques and SPDE solvers that are suitable for complex polycrystalline systems with

high-dimensional input and output are of great interest. An idea is to couple the recently developed adaptive high-dimensional model representation approach [79] with ASGC to reduce further the curse of dimensionality in modeling complex systems. Bayesian regression methods [11] can also be considered as an alternative way to give a reliable prediction to the variability of material response/properties. Moreover, the current work focuses on the uncertainty quantification of material properties/reponses induced by microstructure uncertainties. Further research may give more attention to build efficient surrogate models for what-if analysis, which returns the expectation of output properties with possible variance corresponding to given input information. The inverse problem estimating appropriate microstructure and environmental input that result in observed mechanical properties/responses is also interested, as it allows the design of microstructures and manufacture process to produce materials having desired properties.

BIBLIOGRAPHY

[1] A global geometric framework for nonlinear dimensionality reduction. http://isomap.stanford.edu/.

[2] An image-based method for modeling the elasto-viscoplastic behavior of polycrystalline microstructures using the fast fourier transform. *International Journal of Plasticity*.

[3] Swagato Acharjee and Nicholas Zabaras. A proper orthogonal decomposition approach to microstructure model reduction in rodrigues space with applications to optimal control of microstructure-sensitive properties. *Acta Materialia*, 51(18):5627 – 5646, 2003.

[4] B. L. Adams, J. P. Boehler, M. Guidi, and E. T. Onat. Group theory and representation of microstructure and mechanical behavior of polycrystals. *Journal of the Mechanics and Physics of Solids*, 40(4):723 – 737, 1992.

[5] Said Ahzi, Robert J. Asaro, and David M. Parks. Application of crystal plasticity theory for mechanically processed bscco superconductors. *Mechanics of Materials*, 15(3):201–222, 1993.

[6] L. Anand and M. Kothari. A computational procedure for rate-independent crystal plasticity. *Journal of the Mechanics and Physics of Solids*, 44(4):525 – 558, 1996.

[7] R. J. Asaro and A. Needleman. Overview no. 42 texture development and strain hardening in rate dependent polycrystals. *Acta Metallurgica*, 33(6):923–953, 1985.

[8] Nadine Aubry, Rgis Guyonnet, and Ricardo Lima. Spatiotemporal analysis of complex signals: Theory and applications. *Journal of Statistical Physics*, 64:683–739, 1991.

[9] C. Bradford Barber, David P. Dobkin, and Hannu Huhdanpaa. The quickhull algorithm for convex hulls. *ACM TRANSACTIONS ON MATHEMATICAL SOFTWARE*, 22(4):469–483, 1996.

[10] A.J. Beaudoin, A. Acharya, S.R. Chen, D.A. Korzekwa, and M.G. Stout. Consideration of grain-size effect and kinetics in the plastic deformation of metal polycrystals. *Acta Materialia*, 48(13):3409 – 3423, 2000.

[11] Ilias Bilionis and Nicholas Zabaras. Multi-output local gaussian process regression: Applications to uncertainty quantification. *Journal of Computational Physics*, 231(17):5718 – 5746, 2012.

[12] Christopher M. Bishop. *Pattern Recognition and Machine Learning*. Springer, 2006.

[13] A.W. Bowman and A. Azzalini. *Applied Smoothing Techniques for Data Analysis*. Oxford University Press, 1997.

[14] Vasily Bulatov, Wei Cai, Jeff Fier, Masato Hiratani, Gregg Hommes, Tim Pierce, Meijie Tang, Moono Rhee, Kim Yates, and Tom Arsenlis. Scalable line dynamics in paradis. In *Proceedings of the 2004 ACM/IEEE conference on Supercomputing*, SC '04, pages 19–, Washington, DC, USA, 2004. IEEE Computer Society.

[15] P. Ponte Castañeda. Second-order homogenization estimates for nonlinear composites incorporating field fluctuations: I-theory. *Journal of the Mechanics and Physics of Solids*, 50(4):737–757, 2002.

[16] A. Clement. Prediction of deformation texture using a physical principle of conservatiol. *Materials Science and Engineering*, 55(2):203 – 210, 1982.

[17] P. R. Dawson, S. R. MacEwen, and P-D. Wu. Advances in sheet metal forming analyses: dealing with mechanical anisotropy from crystallographic texture. *International Materials Reviews*, 48(2):86–122, 2003.

[18] Vin de Silva and Joshua B. Tenenbaum. Global Versus Local Methods in Nonlinear Dimensionality Reduction. In S. Becker, S. Thrun, and K. Obermayer, editors, *Advances in Neural Information Processing Systems 15*, pages 705–712, Cambridge, MA, 2003. MIT Press.

[19] E Van der Giessen and A Needleman. Discrete dislocation plasticity: a simple planar model. *Modelling and Simulation in Materials Science and Engineering*, 3(5):689–735, 1995.

[20] B. Devincre and L.P. Kubin. Mesoscopic simulations of dislocations and plasticity. *Materials Science and Engineering A*, 234-236:8 – 14, 1997.

[21] J. D. Eshelby. The determination of the elastic field of an ellipsoidal inclusion, and related problems. *Proceedings of the Royal Society of London. Series A, Mathematical and Physical Sciences*, 241(1226):376–396, 1957.

[22] Tony Fast and Surya R. Kalidindi. Formulation and calibration of higher-order elastic localization relationships using the mks approach. *Acta Materialia*, 59(11):4595 – 4605, 2011.

[23] Tony Fast, Marko Knezevic, and Surya R. Kalidindi. Application of microstructure sensitive design to structural components produced from hexagonal polycrystalline metals. *Computational Materials Science*, 43(2):374 – 383, 2008.

[24] Tony Fast, Stephen R. Niezgoda, and Surya R. Kalidindi. A new framework for computationally efficient structurestructure evolution linkages to facilitate high-fidelity scale bridging in multi-scale materials models. *Acta Materialia*, 59(2):699 – 707, 2011.

[25] F. Frank. Orientation mapping. *Metallurgical and Materials Transactions A*, 19:403–408, 1988.

[26] M. Frigo and S. G. Johnson. The design and implementation of FFTW3. *Proceedings of the IEEE*, 93(2):216–231, feb. 2005.

[27] Baskar Ganapathysubramanian and Nicholas Zabaras. Modeling diffusion in random heterogeneous media: Data-driven models, stochastic collocation and the variational multiscale method. *Journal of Computational Physics*, 226(1):326 – 353, 2007.

[28] Baskar Ganapathysubramanian and Nicholas Zabaras. Sparse grid collocation schemes for stochastic natural convection problems. *Journal of Computational Physics*, 225:652 – 685, 2007.

[29] Baskar Ganapathysubramanian and Nicholas Zabaras. A non-linear dimension reduction methodology for generating data-driven stochastic input models. *Journal of Computational Physics*, 227:6612 – 6637, 2008.

[30] Roger Ghanem and P. D. Spanos. *Stochastic Finite Elements: A Spectral Approach*. Springer - Verlag, New York, 1991.

[31] Roger G. Ghanem and Alireza Doostan. On the construction and analysis of stochastic models: Characterization and propagation of the errors associated with limited data. *Journal of Computational Physics*, 217:63 – 81, 2006.

[32] F. Grennerat, M. Montagnat, O. Castelnau, P. Vacher, H. Moulinec, P. Su-

quet, and P. Duval. Experimental characterization of the intragranular strain field in columnar ice during transient creep. *Acta Materialia*, 60(8):3655 – 3666, 2012.

[33] R. Hill. Continuum micro-mechanics of elastoplastic polycrystals. *Journal of the Mechanics and Physics of Solids*, 13(2):89–101, 1965.

[34] J. W. Hutchinson. Elastic-plastic behaviour of polycrystalline metals and composites. *Proceedings of the Royal Society of London. A. Mathematical and Physical Sciences*, 319(1537):247–272, 1970.

[35] J. W. Hutchinson. Bounds and self-consistent estimates for creep of polycrystalline materials. *Proceedings of the Royal Society of London. A. Mathematical and Physical Sciences*, 348(1652):101–127, 1976.

[36] C.E. Krill III and L.-Q. Chen. Computer simulation of 3-d grain growth using a phase-field model. *Acta Materialia*, 50(12):3059 – 3075, 2002.

[37] T. Iwakuma and S. Nemat-Nasser. Finite elastic-plastic deformation of polycrystalline metals. *Proceedings of the Royal Society of London. A. Mathematical and Physical Sciences*, 394(1806):87–119, 1984.

[38] T. P. Gabb J. Gayda and P. T. Kantzos. The effect of dual microstructure heat treatment on an advanced Nickel-base disk alloy. In *Superalloys 2004*, pages 323–329, Warrendale, PA, 2004. TMS.

[39] S. R. Kalidindi, C. A. Bronkhorst, and L. Anand. Crystallographic texture evolution in bulk deformation processing of fcc metals. *Journal of the Mechanics and Physics of Solids*, 40(3):537–569, 1992.

[40] Surya R. Kalidindi. Incorporation of deformation twinning in crystal plasticity models. *Journal of the Mechanics and Physics of Solids*, 46(2):267–290, 1998.

[41] Surya R. Kalidindi and Hari K. Duvvuru. Spectral methods for capturing crystallographic texture evolution during large plastic strains in metals. *Acta Materialia*, 53(13):3613–3623, 2005.

[42] Surya R. Kalidindi, Hari K. Duvvuru, and Marko Knezevic. Spectral calibration of crystal plasticity models. *Acta Materialia*, 54(7):1795–1804, 2006.

[43] Surya R. Kalidindi, Marko Knezevic, Stephen Niezgoda, and Joshua Shaffer. Representation of the orientation distribution function and computation of first-order elastic properties closures using discrete fourier transforms. *Acta Materialia*, 57(13):3916 – 3923, 2009.

[44] J.T. Kent, J.M. Bibby, and K.V. Mardia. *Multivariate Analysis (Probability and Mathematical Statistics)*. Elsevier, 2006.

[45] S.-J. Kim, D. H. Kim, K. H. Oh, A. D. Rollett, R. A. Lebensohn, and H. N. Han. An elastoplastic finite element modeling coupled with orientation image based micromechanical approach. *AIP Conference Proceedings*, 1252(1):103–106, 2010.

[46] Marko Knezevic, Hamad F. Al-Harbi, and Surya R. Kalidindi. Crystal plasticity simulations using discrete fourier transforms. *Acta Materialia*, 57(6):1777–1784, 2009.

[47] Marko Knezevic, Surya R. Kalidindi, and David Fullwood. Computationally efficient database and spectral interpolation for fully plastic taylor-type crystal plasticity calculations of face-centered cubic polycrystals. *International Journal of Plasticity*, 24(7):1264–1276, 2008.

[48] Marko Knezevic, Surya R. Kalidindi, and Raja K. Mishra. Delineation of first-order closures for plastic properties requiring explicit consideration of strain hardening and crystallographic texture evolution. *International Journal of Plasticity*, 24(2):327 – 342, 2008.

[49] U. Kocks and H. Mecking. Physics and phenomenology of strain hardening: the FCC case. *Progress in Materials Science*, 48(3):171–273, 2003.

[50] Babak Kouchmeshky and Nicholas Zabaras. The effect of multiple sources of uncertainty on the convex hull of material properties of polycrystals. *Computational Materials Science*, 47(2):342 – 352, 2009.

[51] Babak Kouchmeshky and Nicholas Zabaras. Modeling the response of hcp polycrystals deforming by slip and twinning using a finite element representation of the orientation space. *Computational Materials Science*, 45(4):1043–1051, 2009.

[52] Babak Kouchmeshky and Nicholas Zabaras. Microstructure model reduction and uncertainty quantification in multiscale deformation processes. *Computational Materials Science*, 48(2):213 – 227, 2010.

[53] E. Kröner. On the plastic deformation of polycrystals. *Acta Metallurgica*, 9(2):155–161, 1961.

[54] E. Kröner. Statistical modelling. In J. Gittus and J. Zarka, editors, *Modelling small deformations of polycrystals*. Elsevier, 1986.

[55] A Kumar and P.R Dawson. Computational modeling of f.c.c. deformation textures over rodrigues' space. *Acta Materialia*, 48(10):2719 – 2736, 2000.

[56] Ashish Kumar and Paul R. Dawson. The simulation of texture evolution with finite elements over orientation space i. development. *Computer Methods in Applied Mechanics and Engineering*, 130(3-4):227 – 246, 1996.

[57] Ashish Kumar and Paul R. Dawson. The simulation of texture evolution with finite elements over orientation space ii. application to planar crystals. *Computer Methods in Applied Mechanics and Engineering*, 130(3-4):247 – 261, 1996.

[58] H. Kumar, C.L. Briant, and W.A. Curtin. Using microstructure reconstruction to model mechanical behavior in complex microstructures. *Mechanics of Materials*, 38(8-10):818 – 832, 2006. Advances in Disordered Materials.

[59] J.T.-Y. Kwok and I.W.-H. Tsang. The pre-image problem in kernel methods. *Neural Networks, IEEE Transactions on*, 15:1517–1525, 2004.

[60] N. Lahellec, J. C. Michel, H. Moulinec, and P. Suquet. Analysis of inhomogeneous materials at large strains using fast Fourier transforms. In C. Miehe, editor, *IUTAM symposium on computational mechanics of solids materials*, pages 247–268, Stuttgart, Germany, August 2001. Kluwer Academic.

[61] Giacomo Landi, Stephen R. Niezgoda, and Surya R. Kalidindi. Multi-scale modeling of elastic response of three-dimensional voxel-based microstructure datasets using novel dft-based knowledge systems. *Acta Materialia*, 58(7):2716 – 2725, 2010.

[62] R. A. Lebensohn, Y. Liu, and P. Ponte Castañeda. Macroscopic properties and field fluctuations in model power-law polycrystals: full-field solutions versus self-consistent estimates. *Proceedings of the Royal Society of London. Series A: Mathematical, Physical and Engineering Sciences*, 460(2045):1381–1405, 2004.

[63] R. A. Lebensohn and C. N. Tomé. A self-consistent anisotropic approach for the simulation of plastic deformation and texture development of polycrystals: Application to zirconium alloys. *Acta Metallurgica et Materialia*, 41(9):2611–2624, 1993.

[64] R. A. Lebensohn and C. N. Tomé. A self-consistent viscoplastic model: prediction of rolling textures of anisotropic polycrystals. *Materials Science and Engineering: A*, 175(1-2):71–82, 1994. NATO Advanced Research Workshop on Polyphase Polycrystal Plasticity.

[65] R. A. Lebensohn, C. N. Tomé, and P. Ponte Castañeda. Self-consistent modelling of the mechanical behaviour of viscoplastic polycrystals incorporating intragranular field fluctuations. *Philosophical Magazine*, 87(28):4287–4322, 2007.

[66] R.A. Lebensohn. N-site modeling of a 3D viscoplastic polycrystal using Fast Fourier Transform. *Acta Materialia*, 49(14):2723–2737, August 2001.

[67] R.A. Lebensohn, O. Castelnau, R. Brenner, and P. Gilormini. Study of the antiplane deformation of linear 2-d polycrystals with different microstructures. *International Journal of Solids and Structures*, 42(20):5441–5459, 2005.

[68] R.A. Lebensohn, P. Ponte Castañeda, R. Brenner, and O. Castelnau. Full-field vs. homogenization methods to predict microstructure-property relationships of polycrystalline materials. In S. Ghosh and D. Dimiduk, editors, *Computational Methods for Microstructure-Property Relationships*, pages 393–441. Springer, 2011.

[69] Ricardo A. Lebensohn, Renald Brenner, Olivier Castelnau, and Anthony D. Rollett. Orientation image-based micromechanical modelling of subgrain texture evolution in polycrystalline copper. *Acta Materialia*, 56(15):3914–3926, 2008.

[70] Ricardo A. Lebensohn, Anand K. Kanjarla, and Philip Eisenlohr. An elasto-viscoplastic formulation based on fast fourier transforms for the prediction of micromechanical fields in polycrystalline materials. *International Journal of Plasticity*, 32-33(0):59 – 69, 2012.

[71] S. B. Lee, R. A. Lebensohn, and A. D. Rollett. Modeling the viscoplastic micromechanical response of two-phase materials using fast fourier transforms. *International Journal of Plasticity*, 27(5):707 – 727, 2011.

[72] Wei Li and Nicholas Zabaras. A virtual environment for the interrogation of 3d polycrystalline microstructures including grain size effects. *Computational Materials Science*, 44(4):1163 – 1177, 2009.

[73] Zheng Li, Bin Wen, and Nicholas Zabaras. Computing mechanical response variability of polycrystalline microstructures through dimensionality reduction techniques. *Computational Materials Science*, 49(3):568 – 581, 2010.

[74] T. H. Lin. Analysis of elastic and plastic strains of a face-centred cubic crystal. *Journal of the Mechanics and Physics of Solids*, 5(2):143–149, 1957.

[75] B Liu, D Raabe, F Roters, P Eisenlohr, and R A Lebensohn. Comparison of finite element and fast fourier transform crystal plasticity solvers for texture prediction. *Modelling and Simulation in Materials Science and Engineering*, 18(8):085005, 2010.

[76] Yi Liu and P. Ponte Castañeda. Second-order theory for the effective behavior and field fluctuations in viscoplastic polycrystals. *Journal of the Mechanics and Physics of Solids*, 52(2):467–495, 2004.

[77] M. Loève. *Probability Theory, fourth ed.* Berlin: Springer-Verlag, 1977.

[78] Xiang Ma and Nicholas Zabaras. An adaptive hierarchical sparse grid collocation algorithm for the solution of stochastic differential equations. *Journal of Computational Physics*, 228:3084 – 3113, 2009.

[79] Xiang Ma and Nicholas Zabaras. An adaptive high-dimensional stochastic model representation technique for the solution of stochastic partial differential equations. *Journal of Computational Physics*, 229(10):3884 – 3915, 2010.

[80] Xiang Ma and Nicholas Zabaras. Kernel principal component analysis for stochastic input model generation. *Journal of Computational Physics*, 230(19):7311 – 7331, 2011.

[81] R. Masson and A. Zaoui. Self-consistent estimates for the rate-dependent elastoplastic behaviour of polycrystalline materials. *Journal of the Mechanics and Physics of Solids*, 47(7):1543–1568, 1999.

[82] D. L. McDowell and F. P. E. Dunne. Microstructure-sensitive computa-

tional modeling of fatigue crack formation. *International Journal of Fatigue*, 32(9):1521–1542, 2010.

[83] Edward L. Melnick and Aaron Tenenbein. Misspecifications of the normal distribution. *The American Statistician*, 36(4):372–373, 1982.

[84] J. C. Michel, H. Moulinec, and P. Suquet. A Computational Method Based on Augmented Lagrangians and Fast Fourier Transforms for Composites with High Contrast. *CMES-Computer Modeling in Engineering & Sciences*, 1(2):79–88, 2000.

[85] J. C. Michel, H. Moulinec, and P. Suquet. A computational scheme for linear and non-linear composites with arbitrary phase contrast. *International Journal for Numerical Methods in Engineering*, 52(1-2):139–160, 2001.

[86] Christian Miehe, Jörg Schröder, and Jan Schotte. Computational homogenization analysis in finite plasticity simulation of texture development in polycrystalline materials. *Computer Methods in Applied Mechanics and Engineering*, 171(3-4):387 – 418, 1999.

[87] V. Mohles. Simulations of dislocation glide in overaged precipitation-hardened crystals. *Philosophical Magazine, Part A*, 81:971–990, April 2001.

[88] V. Mohles. The critical resolved shear stress of single crystals with long-range ordered precipitates calculated by dislocation dynamics simulations. *Materials Science and Engineering A*, 365(1-2):144 – 150, 2004.

[89] V. Mohles and B. Fruhstorfer. Computer simulations of orowan process controlled dislocation glide in particle arrangements of various randomness. *Acta Materialia*, 50(10):2503 – 2516, 2002.

[90] V. Mohles, D. Rönnpagel, and E. Nembach. Simulation of dislocation glide in precipitation hardened materials. *Computational Materials Science*, 16(1-4):144 – 150, 1999.

[91] Volker Mohles and E. Nembach. the peak- and overaged stages of particles strengthened materials: computer simulations. *Acta Materialia*, 49:2405–2417, 2001.

[92] A. Molinari, G. R. Canova, and S. Ahzi. A self consistent approach of the large deformation polycrystal viscoplasticity. *Acta Metallurgica*, 35(12):2983–2994, 1987.

[93] H. Moulinec and P. Suquet. A fast numerical method for computing the linear and nonlinear mechanical properties of composites. *Comptes rendus de l'Académie des sciences. Série II, Mécanique, Physique, Chimie, Astronomie*, 318(11):1417–1423, 1994.

[94] H. Moulinec and P. Suquet. A numerical method for computing the overall response of nonlinear composites with complex microstructure. *Computer Methods in Applied Mechanics and Engineering*, 157(1-2):69–94, 1998.

[95] T. Narutani and J. Takamura. Grain-size strengthening in terms of dislocation density measured by resistivity. *Acta Metallurgica et Materialia*, 39(8):2037 – 2049, 1991.

[96] D. Peirce, R. J. Asaro, and A. Needleman. An analysis of nonuniform and localized deformation in ductile single crystals. *Acta Metallurgica*, 30(6):1087–1119, 1982.

[97] A Prakash and R A Lebensohn. Simulation of micromechanical behavior of polycrystals: finite elements versus fast fourier transforms. *Modelling and Simulation in Materials Science and Engineering*, 17(6):064010, 2009.

[98] Craig P. Przybyla and David L. McDowell. Microstructure-sensitive extreme value probabilities for high cycle fatigue of ni-base superalloy in100. *International Journal of Plasticity*, 26(3):372 – 394, 2010.

[99] S. I. Rao, T. A. Parthasarathy, D. M. Dimiduk, and P. M. Hazzledine. Discrete dislocation simulations of precipitation hardening in superalloys. *Philosophical Magazine*, 84(30):3195–3215, 2004.

[100] S. I. Rao, T. A. Parthasarathy, D. M. Dimiduk, and P. M. Hazzledine. Discrete dislocation simulations of precipitation hardening in inverse superalloys. *Philosophical Magazine Letters*, 86:215–225, April 2006.

[101] Yogesh Rathi, Samuel Dambreville, and Allen Tannenbaum. Statistical shape analysis using kernel PCA. In *Image Processing: Algorithms and Systems, Neural Networks, and Machine Learning*, page 60641B. SPIE, 2006.

[102] Murray Rosenblatt. Remarks on a multivariate transformation. *Ann. Math. Statist.*, 23:470 – 472, 1952.

[103] F. Roters, P. Eisenlohr, L. Hantcherli, D.D. Tjahjanto, T.R. Bieler, and D. Raabe. Overview of constitutive laws, kinematics, homogenization and

multiscale methods in crystal plasticity finite-element modeling: Theory, experiments, applications. *Acta Materialia*, 58(4):1152–1211, 2010.

[104] Sam T. Roweis and Lawrence K. Saul. Nonlinear dimensionality reduction by locally linear embedding. *Science*, 290(5500):2323–2326, 2000.

[105] G. Sachs. Plasticity problems in metals. *Trans. Faraday Soc.*, 24:84–92, 1928.

[106] Sethuraman Sankaran and Nicholas Zabaras. Computing property variability of polycrystals induced by grain size and orientation uncertainties. *Acta Materialia*, 55(7):2279 – 2290, 2007.

[107] Bernhard Schölkopf, Alexander Smola, and Klaus-Robert Müller. Nonlinear component analysis as a kernel eigenvalue problem. *Neural Comput.*, 10:1299–1319, July 1998.

[108] Joshua B. Shaffer, Marko Knezevic, and Surya R. Kalidindi. Building texture evolution networks for deformation processing of polycrystalline fcc metals using spectral approaches: Applications to process design for targeted performance. *International Journal of Plasticity*, 26(8):1183 – 1194, 2010. Special Issue In Honor of Lallit Anand.

[109] M. Shenoy, J. Zhang, and D. L. McDowell. Estimating fatigue sensitivity to polycrystalline ni-base superalloy microstructures using a computational approach. *Fatigue & Fracture of Engineering Materials & Structures*, 30(10):889–904, 2007.

[110] Mahesh Shenoy, Yustianto Tjiptowidjojo, and David McDowell. Microstructure-sensitive modeling of polycrystalline IN 100. *International Journal of Plasticity*, 24(10):1694–1730, 2008. Special Issue in Honor of Jean-Louis Chaboche.

[111] V. B. Shenoy, R. V. Kukta, and R. Phillips. Mesoscopic analysis of structure and strength of dislocation junctions in fcc metals. *Phys. Rev. Lett.*, 84(7):1491–1494, Feb 2000.

[112] S. Smolyak. Quadrature and interpolation formulas for tensor products of certain classes of functions. *Soviet Mathematics, Doklady*, 4:240–243, 1963.

[113] G. Stefanou, A. Nouy, and A. Clement. Identification of random shapes from images through polynomial chaos expansion of random level set

functions. *International Journal for Numerical Methods in Engineering*, 79:127 – 155, 2009.

[114] D. Sulsky, Z. Chen, and H. L. Schreyer. A particle method for history-dependent materials. *Computer Methods in Applied Mechanics and Engineering*, 118(1-2):179 – 196, 1994.

[115] Deborah Sulsky, Shi-Jian Zhou, and Howard L. Schreyer. Application of a particle-in-cell method to solid mechanics. *Computer Physics Communications*, 87(1-2):236 – 252, 1995. Particle Simulation Methods.

[116] V. Sundararaghavan and A. Kumar. Probabilistic modeling of microstructure evolution using finite element representation of statistical correlation functions. *International Journal of Plasticity*, 30-31(0):62 – 80, 2012.

[117] Veera Sundararaghavan and Nicholas Zabaras. Design of microstructure-sensitive properties in elasto-viscoplastic polycrystals using multi-scale homogenization. *International Journal of Plasticity*, 22(10):1799 – 1824, 2006.

[118] Veera Sundararaghavan and Nicholas Zabaras. A multi-length scale sensitivity analysis for the control of texture-dependent properties in deformation processing. *International Journal of Plasticity*, 24(9):1581 – 1605, 2008.

[119] Veera Sundararaghavan and Nicholas Zabaras. A statistical learning approach for the design of polycrystalline materials. *Statistical Analysis and Data Mining*, 1(5):306–321, 2009.

[120] P. Suquet. personal communication, 2011.

[121] P. Suquet, H. Moulinec, O. Castelnau, M. Montagnat, N. Lahellec, F. Grennerat, P. Duval, and R. Brenner. Multi-scale modeling of the mechanical behavior of polycrystalline ice under transient creep. *Procedia IUTAM*, 3(0):64 – 78, 2012. IUTAM Symposium on Linking Scales in Computations: From Microstructure to Macro-scale Properties.

[122] G. I. Taylor. Plastic strain in metals. *Journal of the Inistitute of Metals*, 62:307–324, 1938.

[123] Joshua B. Tenenbaum, Vin de Silva, and John C. Langford. A global geometric framework for nonlinear dimensionality reduction. *Science*, 290(5500):2319–2323, 2000.

[124] Michael E. Tipping and Christopher M. Bishop. Mixtures of probabilistic principal component analyzers. *Neural Computation*, 11(2):443–482, 1999.

[125] Michael E. Tipping and Christopher M. Bishop. Probabilistic principal component analysis. *Journal of the Royal Statistical Society: Series B (Statistical Methodology)*, 61(3):611–622, 1999.

[126] L. J. P. van der Maaten, E. O. Postma, and H. J. van den Herik. Dimensionality Reduction: A Comparative Review. Technical report, Tilburg University, 2009.

[127] A. Vattré, B. Devincre, and A. Roos. Dislocation dynamics simulations of precipitation hardening in Ni-based superalloys with high [gamma]' volume fraction. *Intermetallics*, 17(12):988 – 994, 2009.

[128] Daniele Venturi, Xiaoliang Wan, and George EM Karniadakis. Stochastic low-dimensional modelling of a random laminar wake past a circular cylinder. *Journal of Fluid Mechanics*, 606:339–367, 2008.

[129] H. Wang, P. D. Wu, C. N. Tomé, and Y. Huang. A finite strain elastic–viscoplastic self-consistent model for polycrystalline materials. *Journal of the Mechanics and Physics of Solids*, 58(4):594–612, 2010.

[130] Bin Wen and Nicholas Zabaras. Investigating variability of fatigue indicator parameters of two-phase nickel-based superalloy microstructures. *Computational Materials Science*, 51(1):455 – 481, 2012.

[131] Bin Wen and Nicholas Zabaras. A multiscale approach for model reduction of random microstructures. *Computational Materials Science*, 63(0):269 – 285, 2012.

[132] Dongbin Xiu and George Em Karniadakis. The Wiener–Askey Polynomial Chaos for stochastic differential equations. *SIAM Journal on Scientific Computing*, 24:619–644, 2002.

[133] Dongbin Xiu and George Em Karniadakis. Modeling uncertainty in flow simulations via generalized polynomial chaos. *Journal of Computational Physics*, 187:137 – 167, 2003.

[134] G. Yagawa and H. Okuda. Neural networks in computational mechanics. *Archives of Computational Methods in Engineering*, 3:435–512, 1996.

[135] K. Yashiro, F. Kurose, Y. Nakashima, K. Kubo, Y. Tomita, and H.M. Zbib. Discrete dislocation dynamics simulation of cutting of [gamma]' precipitate and interfacial dislocation network in Ni-based superalloys. *International Journal of Plasticity*, 22(4):713 – 723, 2006.

[136] Nicholas Zabaras and Akkaram Srikanth. An object-oriented programming approach to the lagrangian FEM analysis of large inelastic deformations and metal-forming processes. *International Journal for Numerical Methods in Engineering*, 45(4):399–445, 1999.

[137] André Zaoui and Renaud Masson. Micromechanics-based modeling of plastic polycrystals: an affine formulation. *Materials Science and Engineering: A*, 285(1-2):418–424, 2000.

[138] Hussein M. Zbib and Tomas Diaz de la Rubia. A multiscale model of plasticity. *International Journal of Plasticity*, 18(9):1133 – 1163, 2002.

[139] Hussein M. Zbib, Moono Rhee, and John P. Hirth. On plastic deformation and the dynamics of 3d dislocations. *International Journal of Mechanical Sciences*, 40(2-3):113 – 127, 1998.